Development of a new technique for photoacoustic gas detection based on silicon microelectromechanical resonator.

Wioletta Trzpil

THÈSE POUR OBTENIR LE GRADE DE DOCTEUR DE L'UNIVERSITÉ DE MONTPELLIER

Spécialité : Électronique

École doctorale : Information, Structures, Systèmes

Unité de recherche : Institut d'Électronique et des Systèmes – UMR 5214

Development of a new technique for photoacoustic gas sensing based on silicon microelectromechanical resonator.

Présentée par Wioletta TRZPIL
Le 16 décembre 2021

Sous la direction de Aurore VICET
et Michael BAHRIZ

Devant le jury composé de

Alain BOSSEBOEUF, Directeur de recherche, C2N, CNRS-Université Paris-Sud	Rapporteur
Fabrice STHAL , Professeur, FEMTO-ST, ENSMM, Université Bourgogne - Franche-Comté	Rapporteur
Pascale GALL-BORRUT, Professeur, IES, Université de Montpellier	Examinateur
Raphael LEVY, Responsable de l'unite CMT, ONERA	Examinateur
Vincenzo SPAGNOLO, Professeur, Technical University of Bari	Examinateur
Rose-Marie SAUVAGE, Responsable Innovation AID, DGA	Invitée
Michael BAHRIZ, Maître de conférences, IES, Université de Montpellier	Co-directeur de thèse
Aurore VICET, Maître de conférences, IES, Université de Montpellier	Directeur de thèse

UNIVERSITÉ DE MONTPELLIER

"...I would be an empty universe indeed if it were not for the people I love, and who love me. Without them, the wonder of it all would be lost on me."

Acknowledgement

Throughout the writing of this thesis I have received a great support and assistance from many people who I would like to thank.

First and foremost, I have to thank my research supervisors: Michael Bahriz and Aurore Vicet. Thank you for the opportunity to be part of your project. Without your assistance and dedicated involvement this thesis would never have been accomplished.

My deep gratitude to Michael Bahriz for your openness, constant availability and involvement in every step throughout the process: from theoretical models, through the clean room to the experimental setups. Our stimulating discussions taught me to question every statement, which is absolutely crucial in the scientific world. Your insightful advices allowed me to improve the overall quality of my work. I will not express with my words the amount of gratification for your patients and compassion. I am thankful for a chance to work with you and I feel that the time spent during my PhD was the most fruitful of all my years.

For Aurore Vicet for your practical sense, your advice and your knowledge. I am touched by the trust you placed in me from the start, as well as the freedom I was able to enjoy throughout these three years of research. Your work ethics gives me is a huge source of inspiration for me.

This thesis would not be realized without a support from Rose Marie Sauvage, the head of nanotechnologies scientific domain at DGA “Direction Générale de l’Armement”. Thank you for the trust you put in the project and in me.

I would like to thank Alain Bosseboeuf and Fabrice Sthal for accepting to be my thesis reviewers. I really appreciate your detailed analysis. Your questions and insightful comments helped me to look at the subject from different perspective.

I would like to thank also other members of the jury: Pascale Gall-Borrut, Raphaël Lévy and Vincenzo Spagnolo for accepting to evaluate my work and for your attention to it.

I would like to convey my gratefulness to the M2A group at IES for allowing me to use their equipment. Eric Rosenkrantz deserves special gratitude for facilitating several of the experiments and providing intellectual assistance. Our chats were really beneficial.

I would like to thank Benoit Charlot. Your expertise in technological process is immense. Thank you for help, knowledge, good spirit and all the technological tips.

I want to thank all the group CTM. Special thanks to Jean-Marie Peiris for all your work put in device fabrication. We wouldn't be able to do it without your help. Also, special thanks to Frederic Pichot for your support, good mood, knowledge and valuable discussions.

To all my coworkers form gas sensor group: Kaim Chamassi, Roman Rousseau, Nicolas Maurin, Diba Ayache and Julien Charensol. I really appreciated working with you. I have learned that teamwork is extremely valuable and understanding that "alone I go faster, together we go further".

I would like to thank interns with who I had a chance to work: Alexander Second and Julien Charensol. Thank you for your involvement in this work and the precious time you allowed me to save during my thesis.

To all my coworkers from the NANOMIR group with who I had a chance to work. I will keep all the good memories in my heart.

Getting through my dissertation required more than academic support. I would like to express my gratification to many people for listening and tolerating me at any time. First, Pierre Malbec, who with patience was calming me down every time I panicked. For my best friends: Zeineb Loghmari, Laura Monge-Bartolome, Alicja Olejniczak, and Martin Jedwabny. I cannot express my gratitude and appreciation for your friendship.

None of this could have happened without my family. My parents who always respected my choices and offered encouragement through all the years. To my brothers: Arek Trzpil and Lukasz Trzpil. To Arek for your constant support from the very beginning, for which I am forever grateful. To Lukasz for your continuous humour.

Table of Contents

Motivation and introduction

The gas sensors market is constantly growing. This growth is driven by a wide range of applications (figure 1.1.1) and increasing legislative constraints on air monitoring. Moreover, gas plays a vital role in many aspects of life. The application can be classified into six subgroups presented in figure I1.1:

a) **Industry:** monitoring emissions of toxic gasses, protecting workers from poisonous gases and detections of pipeline leaks (e.g. H_2S, SO_2, NO, HF); this section includes petrochemical;
b) **Air quality:** monitoring emissions of greenhouse gasses (CO_2, CH_4); this section includes automotive;
c) **Security and defence:** monitoring of explosive and toxic substances for life protection (CH_4, NO, Sarin, CO);
d) **Medical:** non-invasive detection of pathologies based on breath analysis (C_2H_4 (ppb), CH_4 (ppm), CO(ppm), NO (ppb), acetone (ppb)) [1]; COVID 19 markers [2][3];
e) **Life science:** microorganism incubators (CO_2), solid analysis (CH_4, CO_2), botanics (C_2H_4), natural landscape emission (CH_4)
f) **Others:** food and beverage preservation as well as quality control (C_2H_4); integration in mobile phones and other wearables for multiple purposes (e.g. personal security).

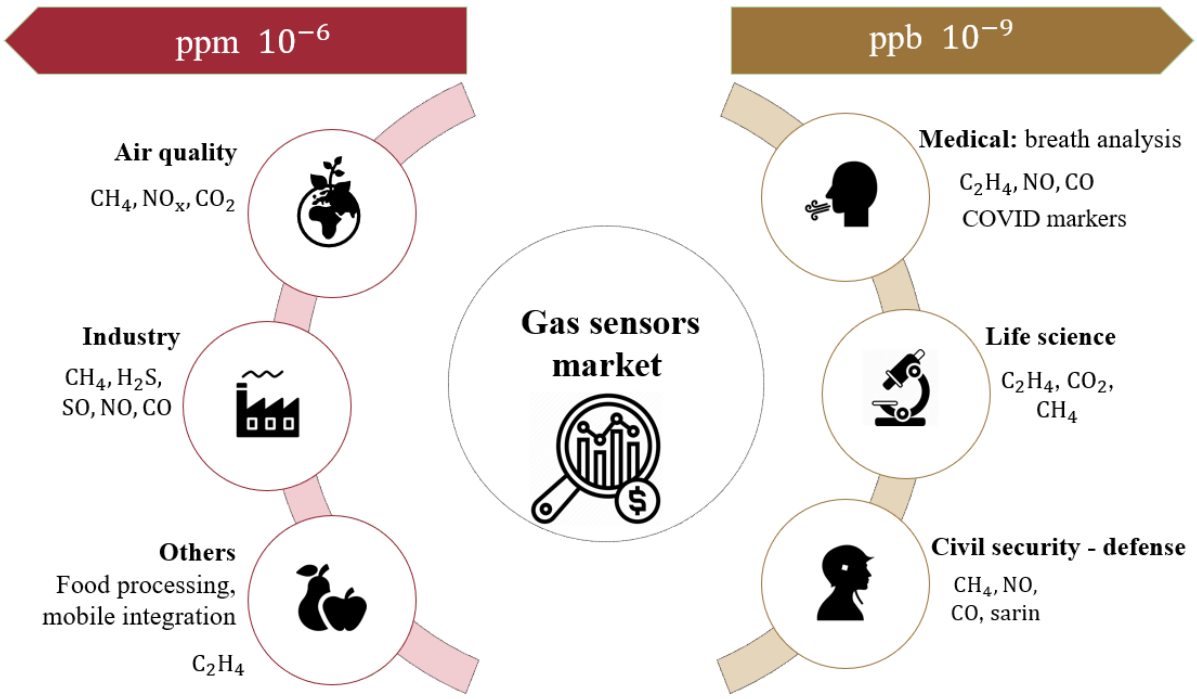

Figure I1.1: Examples of applications for the detection of various gases together with an indication of the level of sensitivity that needs to be reach for each field of application (ppm: part-per-million or ppb: part-per-billion)

For most of these applications, gas sensors need to detect gasses present in small concentrations (ppm, ppb, see figure 1.1.1) and without mistake. Therefore, need to be characterized by excellent selectivity, which means perfectly determine the species among others. Secondly, it should have the ability to detect gasses at low concentrations (ppm, ppb) at a seconds' time scale resolution (e.g. explosive and toxic substances). Moreover, it should give the possibility to perform the measurement continuously. Finally, for real-life applications, it should be compact and characterized by low power consumption.

Despite the wide variety of gas sensors available, it is challenging to find a gas sensor that provides a good balance between all of the features mentioned above. Furthermore, a continuously expanding market demands the development of new solutions that will result in technological innovation.

This thesis is a part of the research project aimed at developing a compact, integrated and portable gas sensor with excellent selectivity, high sensitivity (ppb) providing fast and continuous response. It primarily focuses on the development of an active sensor component that is responsible for compactness and high sensitivity measurement. We also go through the overall design of the sensor. Finally, we propose an innovative approach, which, we believe, will allow to integrate and miniaturize gas sensor while advancing the gas sensor research and market.

In this part of the thesis, we gave an idea of the objective that we want to achieve: gas sensors characterized by excellent selectivity and high sensitivity provided in real-time measurement and combined in a portable and low-cost device. As a result, the first chapter focuses on selecting the appropriate gas detecting method. We describe the most commonly used gas sensing techniques on the market and evaluate them based on four criteria: detection limit, selectivity, stability, and size. From the presented techniques, we chose one: photoacoustic, as it potentially gives the best solution to achieve compact, sensitive, selective and stable gas sensors. Following that, we present state-of-the-art solutions for photoacoustic gas sensors. Finally, we propose an innovative approach based on a silicon microelectromechanical resonator that has been specifically developed for photoacoustic gas sensing with capacitive detection.

Chapter 2 presents detailed working principles of the sensor. Moreover, it addresses issues connected with sensor optimization. It provides an analytic model based on a silicon cantilever, which allows optimizing the cantilever geometry in order to maximize capacitive signal under photoacoustic excitation. The model gives the possibility to increase the signal-to-noise ratio. This model includes a pedagogical and mathematical description together with simulations with a discussion of:

- photoacoustic wave generation;
- different mechanisms degrading the mechanical performances;
- energy conversion between mechanical displacement into an electrical signal via capacitive transduction;

- the influence of the Brownian noise on sensor performances;
- COMSOL study to reinforce the analytic model.

Results of chapter 2 show that sensors based on a simple cantilever with capacitive transduction will not reach state-of-the-art performances. In chapter 4, we propose a solution for this problem.

Chapter 3 presents the development of fabrication procedures for X-resonator (presented in chapter 4) and H-resonator (presented in chapter 5). In this chapter, we discuss the challenges imposed by device fabrication, and we propose solutions. Also, we study and describe the influence of parameters (temperature, concentration) on vertical walls fabrication on (100) oriented silicon using wet chemical etching.

Chapter 4 presents the first successful concept of resonator designed, which decouples photoacoustic wave collection and capacitive transduction. This approach we call the separation-problem concept. We present three generations of resonators. Each generation supposes to address issues that were identified based on the previous generation. The performances were evaluated using Laser Doppler Vibrometer and photoacoustic gas detection with capacitive detection and optical readout mechanism. We describe how to evaluate the sensor performances using Allan variance and normalized noise equivalent absorption coefficient (NNEA).

Chapter 5 chapter presents a simplified design of the X-resonator resonator for photoacoustic gas detection. The design remains the separation-problem concept introduced in chapter 4. We describe the design optimization using COMSOL software. Based on the fabricated sample, we chose one characterized by the best performances over a long time and compared it in photoacoustic gas detection to a bare quartz tuning fork in on-beam configuration.

The work presented in this thesis is a continuation of a PhD thesis submitted in 2018 by Kaim CHAMASSI [4]. The results of the previous work are detailed at the beginning of chapter 4. All the experiments presented in this thesis were held at the Institute of Electronics and Systems (IES) in Montpellier (France) in group NANOMIR. Device fabrication was also performed IES besides one step of device fabrication, detailed in chapter 3, that was performed by FEMTO ST in Besancon (France).

Bibliography

[1] A. Mazzatenta, C. di Giulio, and M. Pokorski, “Pathologies currently identified by exhaled biomarkers,” *Respiratory Physiology and Neurobiology*, vol. 187, no. 1, pp. 128–134, 2013, doi: 10.1016/j.resp.2013.02.016.

[2] W. Ibrahim *et al.*, “Diagnosis of COVID-19 by exhaled breath analysis using gas chromatography–mass spectrometry,” *ERJ Open Research*, vol. 7, no. 3, pp. 00139–02021, 2021, doi: 10.1183/23120541.00139-2021.

[3] H. J. Walker and M. M. Burrell, “Could breath analysis by MS could be a solution to rapid, non-invasive testing for COVID-19?,” *Bioanalysis*, vol. 12, no. 17, pp. 1213–1217, 2020, doi: 10.4155/bio-2020-0125.

[4] K. Chamassi, “Détecteur de gaz multi-espèces par mesure photo-acoustique à effet capacitif,” Ph.D disseration, Institute of Electronics and Systems, Université de Montpellier, Montpellier, 2018.

Chapter 1

1. Introduction of the concept

In this chapter, we present the most frequently used commercial sensing techniques and evaluate them in order to select one that, arguably, best meets the given requirements. Secondly, we present existing state-of-the-art solutions for chosen techniques. Finally, we will propose an innovative approach to reach the objective of the thesis project.

1.1. Choice of the technique

There are a large variety of currently available techniques in gas sensing. Some of them are extremely selective and sensitive; however, they are impossible to apply in portable and compact devices. These techniques are, for instance, mass spectrometry[1] or gas chromatography [2]. Due to the breadth of available techniques, we limit our comparison to those that are already applied in real-life-application. The gas sensing market can be divided into :

- electrochemical gas sensors
- semiconductor gas sensors
- photoionization detector gas sensor
- solid state gas sensors
- catalytic gas sensors
- infrared gas sensors

These sensors are going to be reviewed in the following sections with paying attention to the details concerning advantages, disadvantages, such as sensitivity, stability and compactness.

1.1.1. Solid-state gas sensors

A characteristic of solid-state gas sensors working principle is based on reversible interaction of the gas with the surface of a solid-state material. Solid-state sensors are part of a wide range of sensors that differ from the transduction mechanism (capacitance, work function, thermoresistive, mass, optical characteristics) or reaction energy released by the gas/solid interaction. Here we will discuss only electrochemical and semiconductor sensors as they are the most widely used.

1.1.1.1.Semiconductor gas sensors

Semiconductor gas sensors are made of a gas-sensitive resistive film (usually made of heated oxides, e.g. SnO_2, TiO_2, In_2O_3, WO_3, NiO, etc.) heated with platinum [3]. The typical design scheme is presented in figure 1.1.1 . The gas concentration measurement is conducted via changes of the electrical resistance due to absorbed gas onto the sensitive layer. This change of resistance depends on the physical properties of the resistive film, morphology, geometric characteristics, and temperature at which the reaction occurs. The platinum heater raises the temperature to obtain an optimal sensitivity and response time of the sensor. The pair of electrodes measure the changes of resistance.

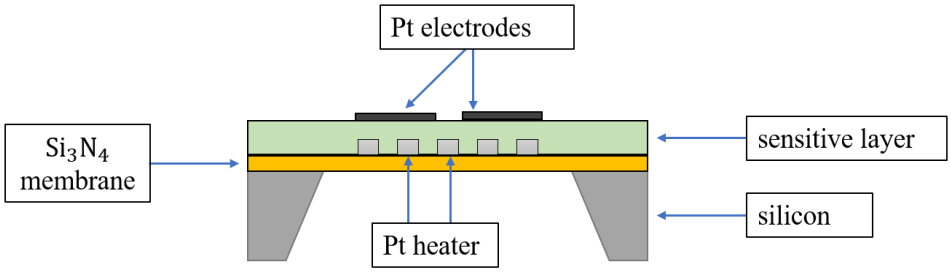

Figure 1.1.1: An illustration of a typical solid-state gas sensor design.

The main advantage of these sensors is stability and long term use. They can be compact, robust, integrated and have a high tolerance to extreme measurement conditions (temperature, humidity).

The main disadvantage is poor selectivity and cross selectivity (reaction to the gasses which interfere with the sensor's response). Besides, to reach a high sensitivity, they are heated to high temperatures. This temperature ranges between 100°C to 500°C depending on the film and characteristic absorption and desorption of the gas. Therefore, they are usually characterized by a high power consumption due to sensitivity dependence on the temperature. Due to high-temperature requirements, the typical power consumption is around 1 W[4]. Finally, they are prone to baseline shifts over time.

1.1.1.2.Electrochemical gas sensors

Electrochemical gas sensors are made of electrodes between which flows current created by an electrochemical reaction. The typical sensor design is presented in figure 1.1.2. The sensor inlet is protected by a membrane (6), which prevents pollution (dust) and water from entering the sensor. The simplest electrochemical sensor is made of two electrodes: working

(2), which undergoes reaction with gas (typically oxidation) and counter (3), which compensates current on the working electrode. A third electrode called the reference electrode (5) can be employed to increase the sensor's efficiency. It measures potential on the working electrode. Electrodes reactions create current (ordered stream of charges). This current is linearly proportional to the gas concentration.

The main advantages of these gas sensors are their low cost, the possibility to create a portable device and its linear response [5].

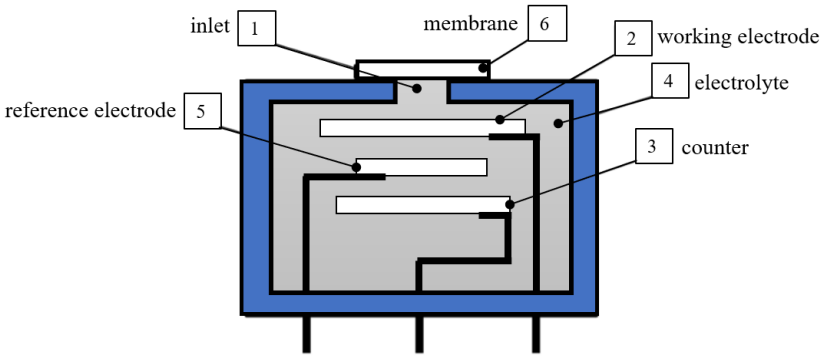

Figure 1.1.2: An illustration electrochemical sensor construction diagram.

Disadvantages are connected with chemical reactions. First of all, the sensor lifetime is limited by the gradual consumption of electrodes and electrolytes. Exposure to extreme humidity (very dry or very humid air) decreases the reliability and lifetime of the sensor. Secondly, the speed of reaction is connected with the temperature. Therefore, these sensors are usually characterized by the lowest range of working temperatures. In addition, cross-sensitivity can occur for some gases, making these gas sensors less selective.

1.1.2. Catalytic gas sensors

Catalytic sensors are used for detecting flammable gases [6]. Their working principle is based on catalytic combustion. The combustible gasses do not burn until reaching a certain temperature. However, due to the reaction with the catalysator, this temperature can be lower down. Catalytic gas sensors (figure 1.2.3) consist of two elements: active and passive, both heated to high temperatures. Both of the elements are made of thin, coiled shape platinum wire. Additionally, the active wire is covered with a catalysator. The temperature on the active wire raises as a result of combustion and changes its resistivity. The reaction is not possible on the passive wire, providing an inert reference that gives excellent stability in environmental

changes. Passive and active elements are integrated into the Wheatstone bridge, which converts resistance changes to tension.

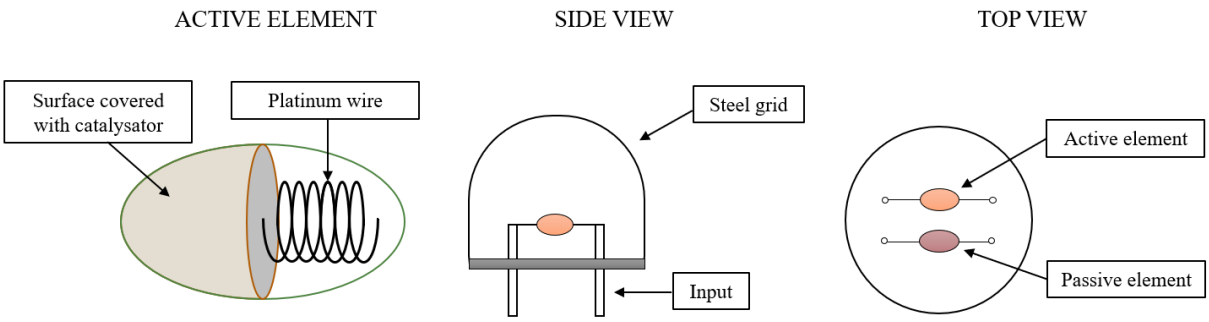

Figure 1.1.3: An illustration of catalytic gas sensor scheme diagram of active element side view and top view.

The main advantage is simplicity, stability and low cost. Initial gas sensors based on this technology were characterized by high power consumption, but they improved thanks to microelectromechanical system (MEMS) technology (microhotplate [7]).

However, these sensors can become poisoned due to contamination of lead, chlorine or silicones. Secondly, they required oxygen for detection, and finally, the long term exposure to high levels of combustible gases may degrade the function of the sensor [8] [3].

1.1.3. Infrared gas sensors

Infrared sensors are based on the interaction of infrared light and gas molecules. This variety of infrared sensors is large [9]. They can differ with a type of detector, e.g. photodetectors [10], pyroelectric, thermoelectric, acoustic[11]; as well as with the type of the infrared source: MEMS-IR emitter [11], laser diode [10], quantum-cascade lasers (QCL) [12] heated wire filament or standard incandescent light [6]. However, all of them are based on the same principle: the interaction of infrared light with gas molecules. Most of the molecules have a well-defined absorption spectrum in the mid-infrared range. Thus, this technique can be highly selective (extended in section 1.3) and immune to contamination or poisoning. Also, they can be extremely sensitive (ppt [13]) and compact [11].

The main disadvantage is that not all the molecules have an infrared spectrum. For instance, this technique cannot be used to detect hydrogen. Another disadvantage is a relatively high cost in comparison to other techniques.

1.1.4. Photoionization detector gas sensors

Photoionization detector (PID) gas sensors work on ionizing the gasses with high energy photons, which result in creating ions (figure 1.2.4). These ions are collected by electrodes in the detector and produce a current proportional to the concentration of ions (and therefore molecules) [14] [15]. They are effective as first responders to gas leaks since their reaction is quick and sensitive (can reach sub part-per-billion). Moreover, they can be compact, low cost and portable.

The main disadvantage of these detectors is that they are not selective as the ionizing lamp will ionize all the compounds with ionization energy equal to or lower than the lamp's power. Secondly, photochemical reactions may produce compounds that coat the PID's interior surfaces, reducing its sensitivity or even triggering device failure. Another issue is that the humidity decreases the sensitivity by introducing leakage current or refracting the UV light. Therefore, they cannot be operated in humid and polluted surroundings.

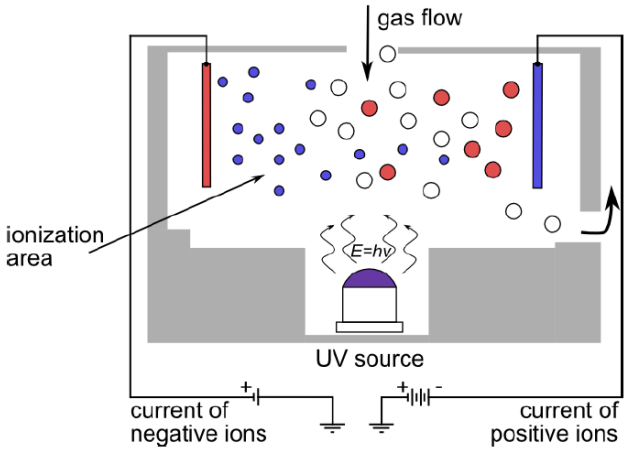

Figure 1.1.4: Illustration of photoionization detector gas sensor working principles. [14]

1.1.5. Comparison and conclusion

Table 1.1.1 summarizes the characteristic of gas sensors presented in previous sections. As can be seen, only infrared-based sensors provide excellent selectivity combined with high sensitivity. Moreover, infrared-based gas sensors offer several advantages over other techniques presented in this thesis. First of all, measurement is based on the fundamental physical properties of molecules. In most cases, there is no direct physical interaction, so no sensor parts can be degraded by the gas during operation. Therefore, the mechanism of failure associated with material based technologies is avoided. They provide a non-destructive way for gas detection since it is a physical analysis method and not a chemical reaction like in the

presented techniques [16]. As a result, the sensor possesses high stability over time and reduced degradation, which minimizes the sensors maintenance cost [17]. Also, they can work without pre-treatment, lack of oxygen (in comparison to catalytic combustion sensors), and accumulation of a gas sample, which might cause the failure of other sensors.

Based on sensors characteristics we decided to use infrared spectroscopic techniques for sensor fabrication.

The biggest disadvantage of IR sensors is cost and compactness. However, the development of new infrared light sources [18] together with detection techniques [19] [20] are driving infrared gas sensors towards low-cost, integrated and compact devices, which is also the goal of our project. Even if the gas sensor will not reach the cost of the semiconductor gas sensors, there are many applications, both scientific and commercial, for which these sensors are irreplaceable.

Table 1.1.1: Comparison of different gas sensor techniques

	sensitivity	**selectivity**	**portable and compact**	**stability**	**durability**	**cost**
electrochemical gas sensors	good (ppm)	good	good	bad	poor	good
semiconductor gas sensors	excellent (ppb)	poor	excellent	good	good	excellent
photoionization detector gas sensor	excellent (sub ppb)	bad	good	poor	poor	excellent
catalytic gas sensors	good	bad	excellent	good	good	excellent
infrared gas sensors	excellent (ppt)	excellent	poor	good	excellent	poor

excellent: perfectly determine one species among the rest
good: determine one species among others; cross-selectivity might occur
poor: selective for some species
bad: not selective

1.2. Infrared gas sensors

Infrared gas sensors, and more generally optical gas sensors, are based on absorption spectrometry: excitation of the molecules from their ground state to excited state through absorption of photons. Due to their distinct characteristics, many organic and non-organic

compounds have unique absorption lines in the infrared (l μm–20 μm) spectral region. That is why IR spectral range is particularly interesting. Figure 1.2.1 depicts spectral lines of some compounds, while figure 1.2.2 presents emitters that cover the spectral range presented in figure 1.2.1.

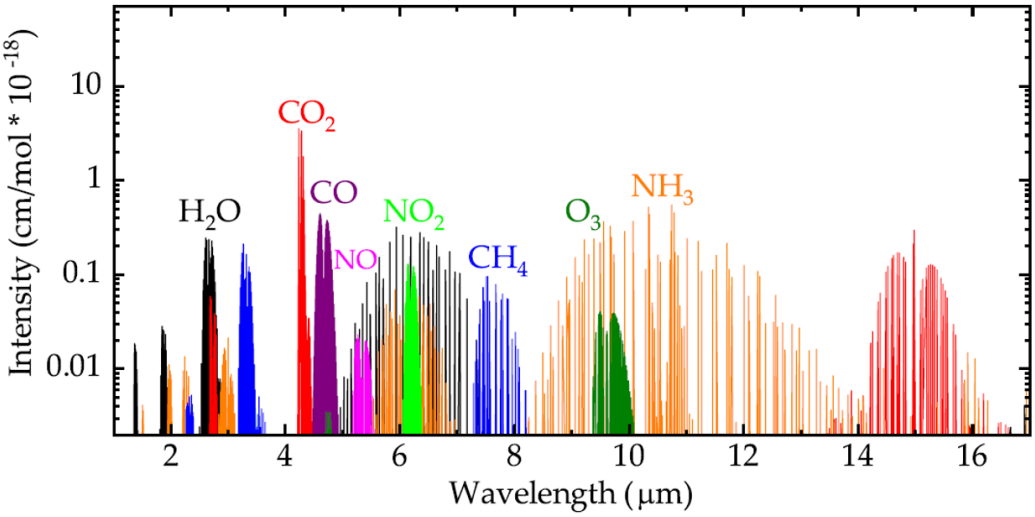

Figure 1.2.1. Mid-infrared absorption spectra of selected molecules with their relative intensities. H_2O: water; CO_2: carbon dioxide; CO: carbon monoxide; NO: nitride oxide; NO_2; nitrogen dioxide; CH_4 methane; O_3: oxygen; NH_3: ammonia. [9]

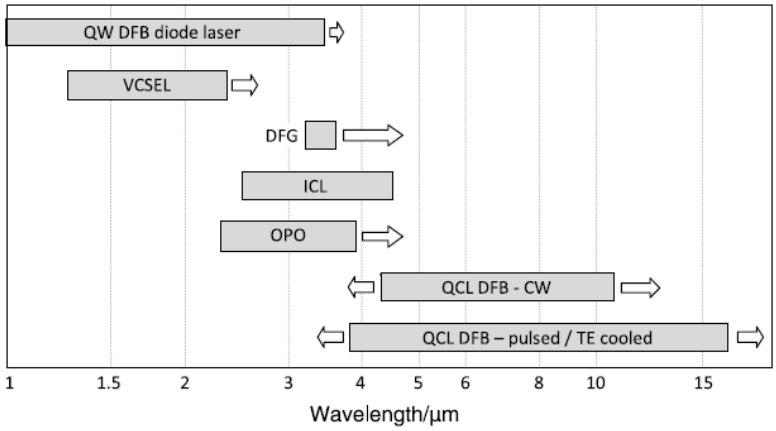

Figure 1.2.2. Wavelength coverages for various light emitters. Arrows show the direction of research activity in a developing field. The abbreviation indicate CW: continuous wave, QW DFB: quantum well distributed feedback, DFG: difference frequency generation, ICL: interband cascade laser, OPO: optical parametric oscillator, QCL: quantum cascade laser. [19]

To be selective, a gas sensor must be able to target a single absorption line. This may be accomplished by applying narrow light emitters such as lasers or broadband emitters with optical devices that filter or disperse the source radiation. Broadband emitters generally have a lower signal-to-noise ratio (SNR), as demonstrated in [19]. As a result, our choice of the emitter will be limited to those with a narrow emission band: lasers. Therefore, we will discuss laser-

based absorption spectroscopy (LAS), which enables the achievement of high selectivity without the need for external components.

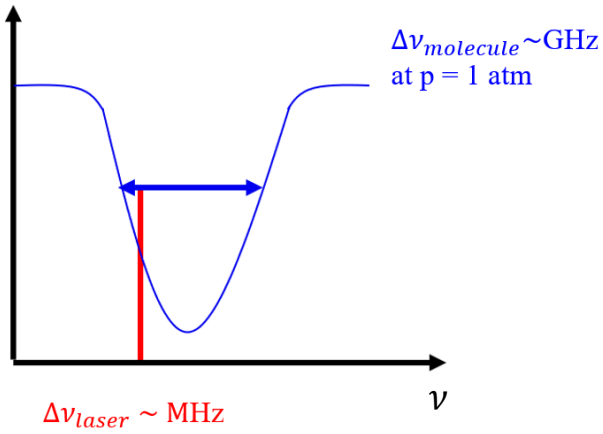

Figure 1.2.3: Schematic illustration of the absorption line of the molecule (blue line) and width of the laser line (red curve).

Typically, the absorption linewidth of the gasses is in the range of few gigahertz (blue curve, figure 1.2.3), while the linewidth of the laser is in the range of few megahertz (red curve, figure 1.2.3). Due to these characteristic width, laser light allows the probing of the individual absorption line, accurately distinguishing between molecules and quantify chemical species.

Depending on the detection technique, LAS can be divided into optical and acoustic [9]. Both of these techniques rely on gas absorption.

1.2.1. Optical - TDLS

One of the most often used LAS techniques, and also one of the most sensitive among optical techniques, is tunable laser diode spectrometry (TDLS). The TDLS configuration is shown in figure 1.3.4. It includes a laser source, a gas chamber, a photodiode, and an electrical readout device that typically includes an amplifier (often a transimpedance or current amplifier) and a lock-in amplifier.

In this technique, the wavelength of the laser is tuned to scan the absorption line of the target gas. The laser can be adjusted by changing either the current or the temperature. The most often used method is the current scan, although both methods may be used to target a specific absorption range.

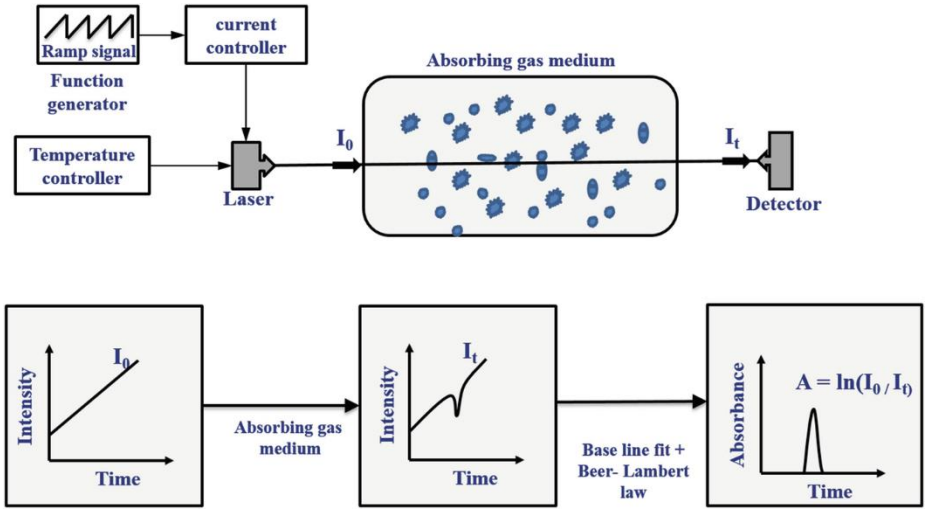

Figure 1.2.4: Schematic illustration of TDLS setup. [21]

Detection of the gas is performed by measuring the light intensity on the photodiode. When light is absorbed by molecules, the light intensity on the photodiode decreases. This drop of the intensity (i.e. the absorbed intensity $I_{abs}(\lambda)$) can be expressed as follow:

$$I_{abs}(\lambda) = \frac{I(\lambda)}{I_0(\lambda)} \tag{1.1}$$

where $I(\lambda)$and $I_0(\lambda)$ are the intensity of the transmitted and initial light, respectively.

According to Beer Lambert's law, the intensity of light passing through the absorbing medium will decrease exponentially as a function of the density of the molecules N [molecules/m^3], optical path x [m], and molecular absorption cross-section $\sigma(\lambda)\left[\frac{m^2}{molecule}\right]$, which can be calculated with the following equation :

$$I_{abs}(\lambda) = \exp(-\sigma(\lambda)Nx) \tag{1.2}$$

The absorption cross-section is individual for each molecule, and it depends on the wavelength and ambient conditions (temperature and pressure). It can be determined using, for instance, the HITRAN database [22]. To calculate the “concentration”, one can use the following equation:

$$C = \frac{N}{N_{tot}} \tag{1.3}$$

where C is a volume mixing ratio (concentration), N is the density of target molecules and N_{tot} is a density of all molecules temperature T [°C] and pressure p [atm], which can be calculated as follow:

$$N_{tot}(p,T) = \frac{p}{T} N_L \tag{1.4}$$

where $N_L = 2.6867811 \cdot 10^{25} \left[\frac{1}{m^3}\right]$ is the Loschmidt constant. Loschmidt constant N_L is number density. It contains information about the number of particles of an ideal gas at a given pressure $p_o = 1\ atm$ and at temperature $T_o = 0°C$ and is determined using the formula below:

$$N_L = \frac{p_o}{k_B T_o} = \frac{p_0 N_A}{RT} \tag{1.5}$$

where k_B= 1.38· 10^{-23} $\left[\frac{J}{K}\right]$ is a Boltzmann constant, $N_A = 6.02214076 \cdot 10^{-23}$ [mol^{-1}] is an Avogadro constant and $R = N_A k_B$ is a gas constant.

The main disadvantage of TDLS is a sensitivity proportional to the length of the optical path, which implies that in order to measure small gas quantities, the optical path needs to be enlarged. This causes TDLS gas sensors rather bulky. Another drawback of this method is that the small intensity changes are measured against a large background. This reduces the detection limit. The final drawback is the high noise level, which occurs as a result of any disturbance to the laser source or optics, causing variations in the output light intensity. To address the noise issue, a method known as modulation spectroscopy can be employed. This method, also used in photoacoustic spectroscopy, is further described in appendix A.

However, it is worth pointing out that research towards achieving compact and integrated (on-chip) technology is constantly in progress for these sensors. For instance, in 2017 Green et al [10] presented first scalable on-chip IR-TDLAS sensor with sub-100 parts-per-million by volume (ppmv) CH_4 sensitivity.

1.2.2. CRDS

Cavity ringdown spectroscopy (CRDS) is a more recent approach for high-sensitivity monitoring based on laser absorption spectroscopy. It is based on cavity-enhanced absorption spectroscopy (CEAS) [23]. The principles are presented in figure 1.3.5. In this technique, a laser pulse is trapped in a highly reflecting detecting cavity (usually R > 99.9 percent). Due to absorption, scattering by the medium within the cell, and reflectivity losses, the light intensity will drop by a specified percentage during each cycle within the cell. The light intensity within the cavity is calculated as an exponential function of time:

$$I(t) = I_0 \exp\left(-\frac{t}{\tau}\right) \tag{1.6}$$

The operating principle is based on measuring decay constant τ, which is the time required for the intensity to drop to 1/e of the initial value. That is why this method is called ringdown. Subsequently, gas concentration C is determined by comparing the time decay for an empty cavity τ_0 to time decay for a cavity filled with gas τ:

$$\frac{\tau_0}{\tau} = 1 + \frac{\alpha l}{1-R} = 1 + \frac{2.303\epsilon l C}{(1-R)} \tag{1.7}$$

where α is an absorption coefficient, l is the cavity length, R is the mirror reflectivity, and $\epsilon$is the molar absorptivity.

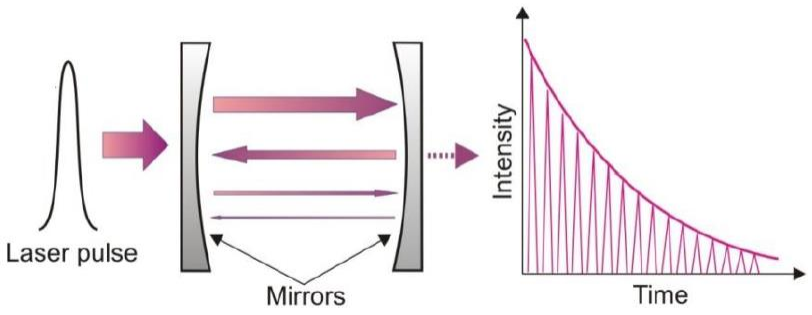

Figure 1.2.5: Schematic illustration of cavity ringdown spectroscopy [24].

The main advantage of this technique is its extremely high sensitivity, immunity to laser intensity fluctuation. Thanks to this immunity, CRDS does not need calibration and comparison to standards. The main disadvantage is that high sensitivity is obtained on km path length. Secondly, the high reflective mirrors with multilayer coating are costly and can be produced for limited wavelength ranges. Finally, this technique requires high responsivity detectors, which at IR wavelength range require cryogenic cooling.

1.2.3. Photoacoustic

Photoacoustic sensors, in comparison to optical, differ in the way absorption of the light is measured. The photoacoustic effect is schematically presented in figure 1.2.6. Molecules after absorption of modulated laser light are moved to an excited state. Relaxation of molecules can occur through:

- A1 radiative deexcitation producing a photon (emission)
- A2 collide with other molecules creating heat
- A3 initiate a chemical event such as bond rearrangement

It can also collide with another molecule bringing it into an excited state.

The photoacoustic wave results from A2 process (heat), which causes synchronized expansion-contraction of the gas (B2, figure 1.2.6). This periodic motion within the gas causes a photoacoustic wave. However, this process is connected with thermal relaxation time unique for each molecules and will determine the efficiency of this process. This discussion will be extended in chapter 2, section 2.2.

Heat (A2 process) can as well cause electromagnetic radiation (B1 process) or phase transition, e.g. plasma (B3 process).

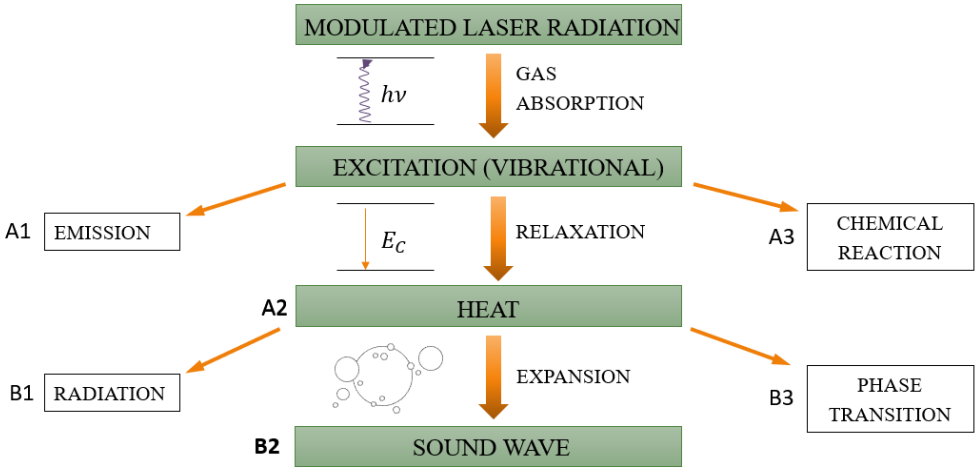

Figure 1.2.6: A scheme of photoacoustic wave creation.

The light intensity needs to be modulated slow enough to assure the thermal relaxation of molecules, which will cause the coherent temperature modulation within the gas. This temperature modulation can be described by a function called heat production rate $H(\vec{r},t)$, extended in chapter 2.

The changes of the temperature within the gas cause the pressure changes based on the ideal gas law:

$$pV = nRT \tag{1.6}$$

where P [Pa], V [m^3] , n [mol], R =8.314 [J K^{-1} mol^{-1}] ,T [K] are pressure, volume, number of atom in substance, an ideal gas constant and temperature, respectively. This periodic change of pressure is an actual acoustic wave, which can be described by wave equation with source (chapter 2).

Generation of the signal is given by :

$$S = k \cdot N \cdot \sigma(\lambda) \cdot P_L \tag{1.7}$$

where k is a system-specific constant, N is the density of target molecules, $\sigma(\lambda)$ is the absorption cross-section and, P_L is the optical power. Equation (1.7) draws important general rules of photoacoustic spectroscopy. Namely, the detected signal is proportional to the gas concentration (linear characteristic). Secondly, the signal is proportional to the power of the laser P_L. The second conclusion gives a huge advantage to improve the photoacoustic sensor's compactness over the optical sensors.

1.2.4. Our choice

The limit of detection, representing the sensitivity of most sensors, can be quantified using the normalised noise equivalent absorption coefficient (NNEA) or Noise Equivalent Absorption (NEA). The technique CRDS is the most sensitive, however not evident to compare with photoacoustic gas sensing technique. This figures of merit allow comparing different techniques without a reference to the specific gas. As presented in figure 1.3.7, the techniques which enable to detect of the lowest concentration of the gas; thus, the one characterized by the minimum NNEA is CRDS (NNEA is reaching 10^{-14} W $\cdot$ cm^{-1} $\cdot$ $Hz^{-1/2}$). However, this sensitivity is achieved due to the long pathways of the detectors. On the other hand, photoacoustic-based gas sensors show outstanding performances for short pathlength [19].

PA gas sensors are characterized by simplicity and highly reliable performances. In comparison to TDLS, photoacoustic gas sensing has several advantages:

a) Photoacoustic measurement is achromatic, which means wavelength independent.
b) The signal is measured only when the absorption occurs. This allows reducing the always appearing background noise in the TDLS technique.
c) The photoacoustic response for changes of concentration is linear.
d) The system's size may be small thanks to the signal proportional to the laser's power.

Thanks to those numerous advantages, which the most important for us seems to be compactness, we chose to work with photoacoustic gas sensing techniques. However, it is not straightforward to determine which method is the best, especially with the increasingly diverse range of technologies. Every technique has advantages and disadvantages. Constantly evolving techniques demonstrates that many of them provide cost and size reduction opportunities. Our ultimate goal is to develop an innovative technique for photoacoustic gas sensing that will enable us to provide even more solutions in a constantly evolving market.

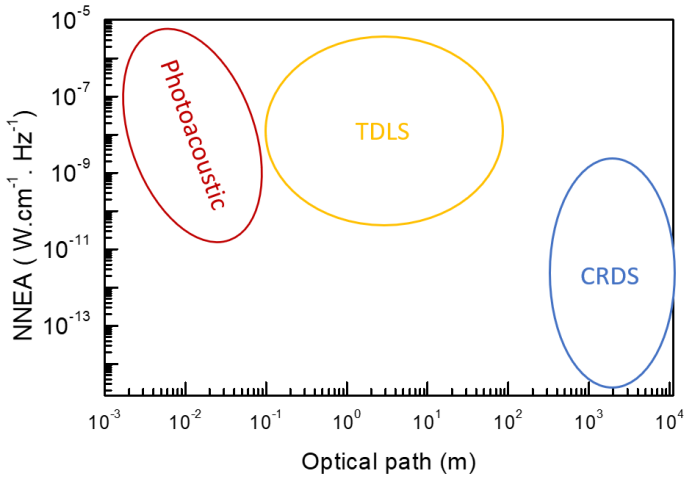

Figure 1.1.7: Normalized noise equivalent absorption (NNEA) for chosen techniques as a function of optical path. PAS – photoacoustic absorption spectroscopy, TDLS – tunable diode laser absorption spectroscopy, CRDS – cavity ringdown spectroscopy [19] [25].

1.3. State of the art in photoacoustic spectroscopy

1.3.1. Introduction

The photoacoustic effect was for the first time reported by Alexander Graham Bell in 1880 [25]. Term photoacoustic was sometimes used as optoacoustic. However, this term was often confused with acousto-optic effect, which is based on the interaction between light and acoustic or elastic waves in crystals.

Beginnings of photoacoustic gas sensors based on microphones reaches just 1938 when Vienegrov, for the first time, evaluated the concentration of the gas species in a gas mixture [27]. Using a blackbody as an infrared source, he was able to measure CO_2 in N_2 down to 0.2% concentration. The measurement was performed via capacitive transduction (voltage measured between two electrodes of the microphone).

In 1939 Pfund used a gas analysis system based on the photoacoustic effect for CO_2 and CO; however, he measured the changes of the temperature using thermopile [28]. The sensitivity obtained by Pfund was similar to the one of Vienegrov.

The notable improvement was made by Luft in 1943 when he described commercial recording automatic gas analyzer based on the photoacoustic effect [29]. This gas analyser employed two photoacoustic cells in a differential design. It minimised background absorption in cell windows and enabled the analysis of a gas mixture of more than two species.

The photoacoustic spectroscopy had its official debut in 70s' with the development of laser sources, photodetectors and theory concerning photoacoustic effect in solids [30].

Nowadays, there exist many different methods to detect a photoacoustic wave in gasses. They differ with the transduction mechanism as well as with its interaction between the device and the photoacoustic force. Below we will discuss the three most commonly used acoustic transducers used in photoacoustic gas sensing :

a) standard microphone (PAS),
b) the quartz tuning fork (QTF), and quartz enhances photoacoustic spectroscopy (QEPAS)
c) cantilever and cantilever enhanced photoacoustic spectroscopy (CEPAS)

We will also shortly present some other possibilities with their pros and cons, and finally, we will propose our solution for the next generation of photoacoustic gas sensors.

1.3.2. Microphone based photoacoustic spectroscopy

As presented in the previous section, microphones were the first acoustic transducers used in photoacoustic gas sensing. In general, microphones are transducers that convert an acoustic wave into an electric signal. However, with this broad definition, both CEPAS and QEPAS come into the terminology of microphones. Indeed, all of these elements respond mechanically to changes in pressure. To be specific, by the term "Microphone based photoacoustic spectroscopy", we refer to diaphragm-like microphones with electrical transduction (not with optical transduction) like condenser or electret microphones.

The majority of microphones are condenser microphones. Here we present the electret condenser microphones (ECMs) and microelectromechanical system (MEMS) microphones (figure 1.4.1 [31]). The working principle for both of them is similar. However, MEMS microphones dominate the market due to miniature package sizes, lower power consumption and excellent temperature characteristics. Condenser microphones are capacitors with one movable electrode (diaphragm or membrane) and one fixed. The electret layer (dielectric with a quasi-permanent electric charge) is introduced between them to decrease the polarization voltage. When the diaphragm moves due to the acoustic force, the capacitance changes, which results in a voltage difference between electrodes [32]. For detecting small gas concentrations in photoacoustic gas sensing, microphones should be sensitive and provide a high signal to noise ratio (SNR) [32]. The main characteristics affecting SNR are its mechanical susceptibility, quality factor, noise characteristics and stability [33]. Mechanical susceptibility

depends on the stiffness of the diaphragm, and viscous damping between the plates called the squeeze film effect. The sensitivity of the condenser microphones is proportional to its surface and inversely proportional to the distance between the electrodes. However, increasing the area increases its mass, while decreasing the distance between the electrodes increases the damping. Thus, there must be a compromise between those two effects. This problem considers all the photoacoustic sensors with capacitive transduction and will be extended in chapter 2. One of the solutions to improve the squeeze film effect is to create holes in the membrane. This solution has been applied in MEMS microphones (figure 1.3.1b).

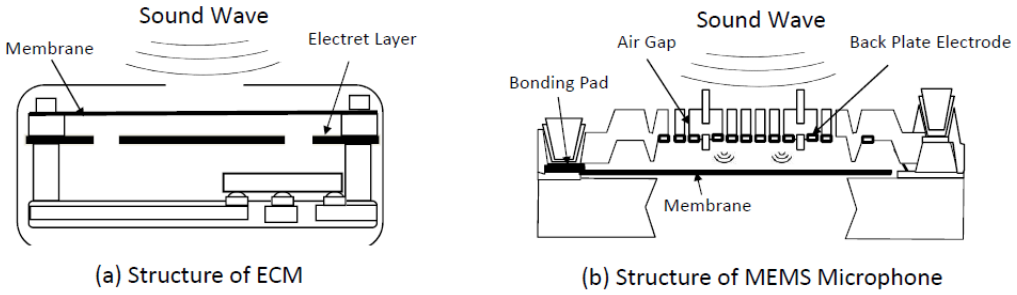

Figure 1.3.1. Scheme of a) electret condenser microphone (ECM) and b) MEMS microphone [27]

The acoustic pressure generated via the photoacoustic effect has weak amplitude. Microphones can be highly sensitive, but their frequency response is generally flat in a large range. As a result, the SNR of a single microphone in photoacoustic gas detection is low. To overcome this problem, acoustic cavities are used to restrict and amplify the pressure wave.

The best sensor based on microphones are characterized by NNEA of $3.1 \cdot 10^{-9}$ $(W \cdot cm^{-1} \cdot Hz^{-1/2})$ [34]. However, several solutions have been proposed in the literature to increase sensitivity, for instance by:

a) **using optical fiber amplifiers:** with this improvement, sensor can reach NNEA of $1.5 \cdot 10^{-9}$ $(W \cdot cm^{-1} \cdot Hz^{-1/2})$
b) **using optical resonant cavities:** this improvement allows reaching NNEA of $2.6 \cdot 10^{-11}$ $(W \cdot cm^{-1} \cdot Hz^{-1/2})$ [35]. However, the calculation of NNEA for photoacoustic gas sensors using optical resonance cavities is not straightforward. To be more precise, we believe that correction should be applied as increasing the number of passes will increase absorbance, increasing the heat production rate. This effect is not included in the calculation of NNEA.
c) **exchanging the capacitive detection with optical:** the main damping mechanism in capacitive like microphones comes from the transduction mechanism itself (small distance between the electrodes). Exchanging the capacitive detection with optical, will allow to avoid an electrod (increase the gap) and therefore can decrease the damping mechanism. This solution has been reported in [36]. Nonetheless, the

optical read this approach is less effective than cantilever-like microphones (section 1.4.4) because a membrane has a strain that causes it less sensitive to movement and generates a nonlinear response [37]. Secondly, optical readout mechanism is rather bulky.

The main advantage of microphones is their maturity of fabrication with an integrated electronic circuit which gives feasibility in developing small and compact systems. Furthermore, they have a well-known operating mechanism as well as more advanced improvements than other approaches. The main disadvantage is their poor quality factor, which makes them susceptible to system noise. Because of this feature, they must be used with an acoustic chamber.

1.3.3. Quartz enhanced photoacoustic spectroscopy – QEPAS

Another improvement in photoacoustic gas sensing was made in 2002 by Kosterev et al. [38]. They proposed to use of the quartz tuning fork (QTF) as a detecting device for photoacoustic wave (see figure 1.3.2). This technique is called quartz enhanced photoacoustic spectroscopy (QEPAS).

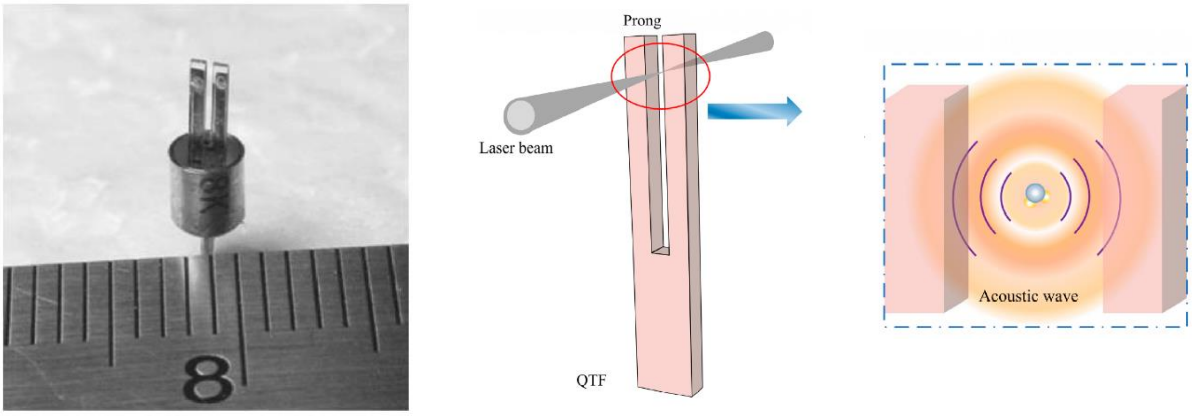

Figure 1.3.2: a) Photograph of a typical wristwatch QTF adopted to PAS next to the scale marker [39] b) Scheme of the QTF with a laser beam in the on-beam configuration, c) Photoacoustic wave created between the prongs on QTF [40]

QTF is a piezoelectric resonator (piezoelectric transduction) distinguished by high quality factor (above 10000 in atmospheric pressure [41]) at its fundamental mode of vibration, which is 32.768 kHz. Initially it was developed for the watch industry as a timekeeper.

In most of the configurations with QTF, a photoacoustic wave is confined between the prongs by focusing the laser beam between the prongs (figure 1.3.2c: bare QTF on-beam configuration) or using a tube-like acoustic resonator (figure 1.3.3). Optimizing the laser spot might be difficult due to the narrow space between the prongs (0.3 mm). Illuminating modulated laser light into the QTF prongs might result in absorption of this light by the quartz crystal. This will cause a photothermal excitation which refers to photothermal noise. To overcome photothermal excitation, an acoustic resonator with different configuration (figure 1.3.3) can be utilized as a solution to overcome photothermal noise.

This photoacoustic wave causes the anti-phase mechanical movement of the prongs, which is further translated into an electrical signal via the piezoelectric effect. Because of the quadrupole electrode pattern, only anti-phase modes will cause the electrical signal. The best NNEA of commercial QTF with acoustic cavity was achieved for an on-beam QTF with acoustic resonator and is equal to $3.3 \cdot 10^{-9}$ $(W \cdot cm^{-1} \cdot Hz^{-1/2})$ [42].

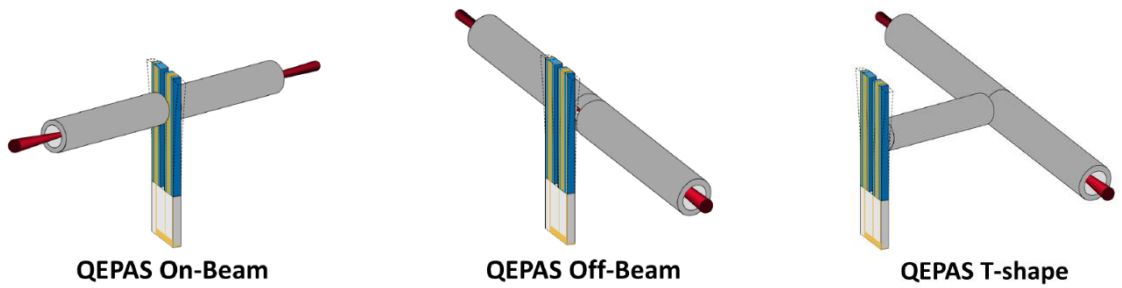

Figure 1.3.3: Different configuration of QEPAS using acoustic mcroresonators with their names. [41]

Acoustic cells are not the only improvement in QEPAS. Currently, existing techniques include:

a) **Custom QTF:** Since the standard QTF was not designed for photoacoustic gas sensing. Several groups fabricated custom QTF [44]–[46] in order to improve the performances of QTF in photoacoustic. Some of these custom QTFs are presented in figure 1.3.4. Most of the improvements focus on increasing the gap between the QTF prongs and decreasing the resonance frequency (chapter 2). The best reported NNEA for custom QTF without external elements (acoustic microresonator) was reported $3.75 \cdot 10^{-11}(W \cdot cm^{-1} \cdot Hz^{-1/2})$ using a terahertz optical source (far-IR range) [47]; and $1.7 \cdot 10^{-8}(W \cdot cm^{-1} \cdot Hz^{-1/2})$ using mid-IR source (1392 nm) [45].

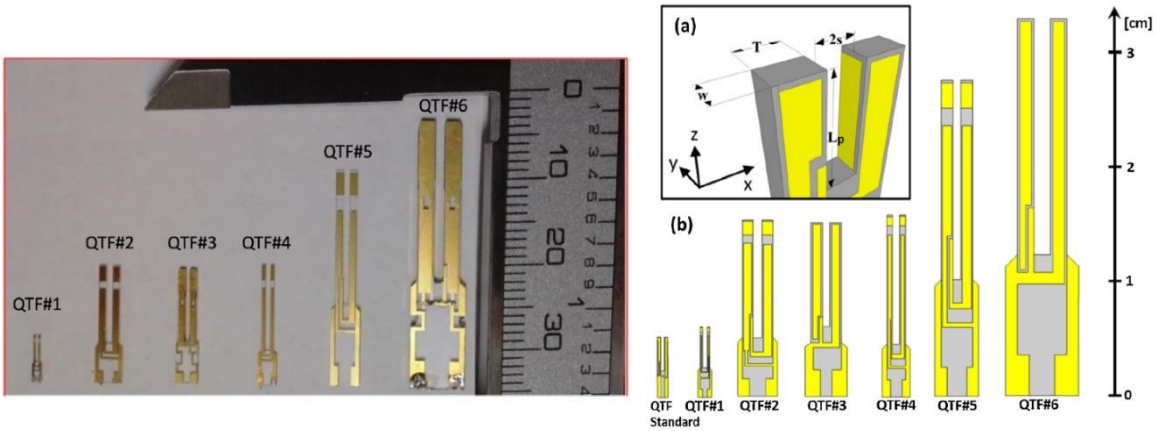

Figure 1.3.4: Picture of different custom QTF (left panel) and scheme of QTFs presented in the left panel (right panel). [46]

b) **Intracavity QEPAS (figure 1.4.5)** : I-QEPAS was proposed in 2014 [48] [49]. The improvement of sensitivity is made by increasing the optical power (probability of photon absorption of the gas). Namely, placing QTF in a laser cavity increases the number of light passes. The best reported NNEA is $3.2 \cdot 10^{-10} (W \cdot cm^{-1} \cdot Hz^{-1/2})$.

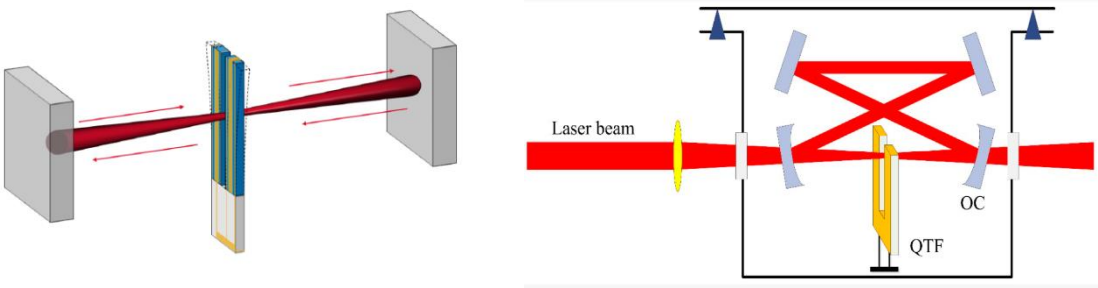

Figure 1.3.5: Scheme of intracavity QEPAS (I-QEPAS) [40] [43]

c) **In-plane configuration (figure 1.4.6):** another important aspect of the QTF was introduced and described in depth in the work of Duquesnoy [25]. According to [25] coupling of QTF with an acoustic source is not optimized. As a solution, they proposed an in-plane configuration presented in figure 1.3.6.

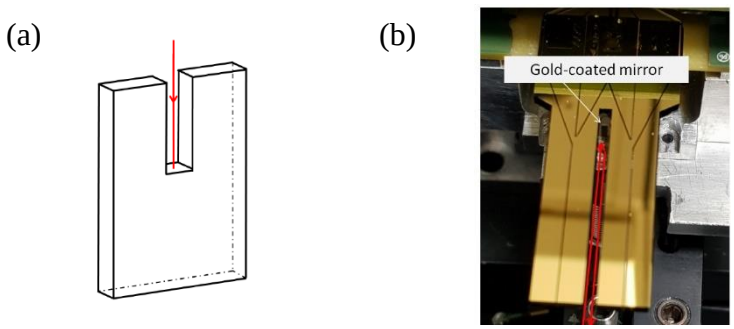

Figure 1.3.6: (a) Scheme of an in-plane configuration of QTF [25]. (b) Picture of custom QTF in in-plane configuration. The laser beam is focused on the gold-coated mirror between the prongs [25]

d) **Radial resonators:** this resonator addresses the same problem presented in point c). In fact, tube-like resonators presented in figure 1.3.3 are not optimized in terms of acoustic-mechanical overlap and lower QTF overall sensitivity. To overcome this problem, Duquesnoy et al. [25] proposed a radial resonator (figure 1.4.7a-c). Custom QTF was combined with a radial cavity (figure 1.4.7a), presenting an NNEA of $3.9 \cdot 10^{-9}(W \cdot cm^{-1} \cdot Hz^{-1/2})$. The beam is focused between the prongs of QTF. The walls of the cavity are at a distance $\frac{\lambda_{ac}}{2}$ from the laser focal point. This technique was lately called Radial-Cavity Quartz-Enhanced Photoacoustic Spectroscopy (RC-QEPAS) (figure 1.4.7d) [50]. Besides increasing overlap between the acoustic force and mechanical mode, it facilitates the laser beam alignment.

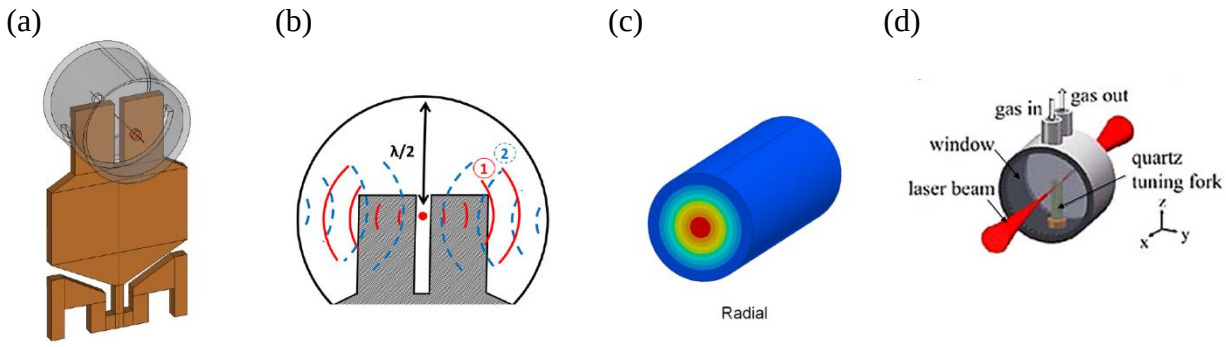

Figure 1.3.7: (a) Scheme of custom QTF with radial resonator [25]. (b) The schematic illustration presents conditions for achieving radial resonance (walls at a distance schematically $\frac{\lambda_{ac}}{2}$ [25]. (c) Radial cavity illustration with red colour representing positive relative pressure and blue representing negative relative pressure [25]. (d) Scheme of Radial-Cavity Quartz-Enhanced Photoacoustic Spectroscopy [50]

QTF's main advantage is high quality factor, which makes it resistant to acoustic noise and allows avoiding acoustic cavities. Furthermore, it is low-cost and compact.

Arguably, one of the biggest disadvantages of QTF is the use of piezoelectric material, which cause further integration in CMOS technology very limited. Furthermore, QTF due to the high quality is highly sensitive to environmental conditions. QTF must work at its resonance frequency in order to achieve maximum sensitivity. In order to follow the resonance, a method is required to recalculate/measure resonance frequency and quality factor with sufficient accuracy in a short time. Nevertheless, to overcome this problem, some solutions have been already proposed [51] [52] and are in constant development.

1.3.4. Cantilever enhanced photoacoustic spectroscopy – CEPAS

In 2004 Kauppinen et al. proposed a new concept for photoacoustic gas sensors [37]. It was based on a silicon cantilever-type acoustic transducer with an optical readout mechanism. The silicon cantilever has typical dimensions of: thickness d = 5 μm, length l = 4 mm and width w = 2 mm (figure 1.4.8). The interferometer detects a cantilever deflection under an acoustic force. This readout mechanism provides extremely high sensitivity (displacement detection well under picometer). In this cantilever like acoustic transducer, the damping effect is significantly reduced in comparison to the microphones discussed in section 1.3.2. As a result, cantilever displacement can be a hundred times higher than microphones' displacement [53]. Furthermore, thanks to the optical read out mechanism, the electric noise is negligible. However, due to the low quality factor (below 100) and the low effective mass, thermal fluctuation noise (Brownian noise) cause significant cantilever displacement even without the gas, thus decreasing its SNR. To make this technique useful, a photoacoustic cell operated at low frequency is applied, as the photoacoustic signal is inversely proportional to frequency (equation (1.7)). In CEPAS, similarly to the microphone based technique, measurement is performed out of the cantilever resonance frequency.

For CEPAS configuration, the best reported NNEA is $1.7 \cdot 10^{-10}(W \cdot cm^{-1} \cdot Hz^{-1/2})$ [54].

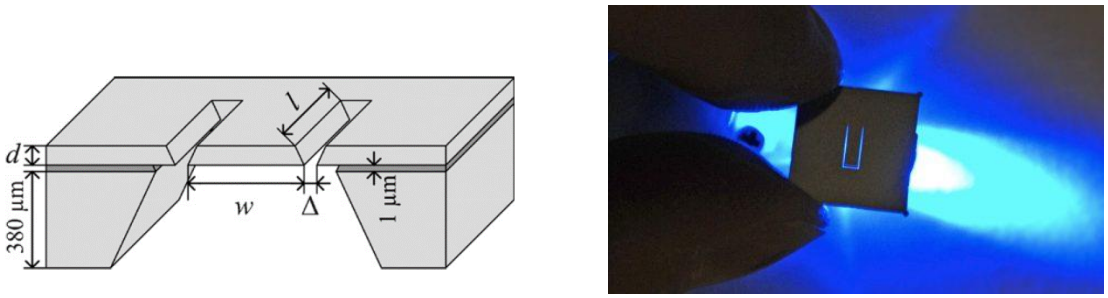

Figure 1.3.8: Scheme of silicon cantilever sensor thickness d = 5 μm, length l = 4 mm and width w = 2 mm, gap between the frame and cantilever Δ = 30 μm [52](left panel). Picture of the cantilever sensor (right panel) [54]

Similarly to advancements in QEPAS, and microphone-based photoacoustic gas sensors, CEPAS sensitivity can be improved by applying an optical cavity [56]. This technique is called Cavity Enhanced Cantilever Enhanced Photoacoustic Spectroscopy (CECEPAS). With this improvement, the NNEA is currently the best reported in atmospheric pressure value. NNEA for CECEPAS is $1.75 \cdot 10^{-11}(W \cdot cm^{-1} \cdot Hz^{-1/2})$.

The main advantage of CEPAS is its high sensitivity and silicon technology which allows it to be integrated. Furthermore, in comparison to MEMS microphones, the fabrication process is simple. The main drawback is the sensor's size due to an optical readout mechanism and the need for an acoustic cavity. In contrary to QTF, in CEPAS the overlap between the

acoustic force and mechanical mode is optimized. Therefore, according to [25], the possibilities of increasing already existing CEPAS sensitivity is limited.

1.3.5. Capacitive silicon micro-resonator enhanced photoacoustic spectroscopy

From all of the presented PA techniques, only QEPAS presents a satisfying NNEA ($8.8 \cdot 10^{-7} (W \cdot cm^{-1} \cdot Hz^{-1/2}$[38]) without using external elements like an acoustic or optical cavity. However, for integrated compact sensors, QTF is quite limited due to the use of piezoelectric material. Precisely, crystal quartz is not compatible with CMOS technology (for the moment). On the other hand, standard microphones photoacoustic gas sensors are gaining interest due to their size and compatibility with CMOS technology.

We see a great perspective in using silicon technology, like in MEMS microphones for photoacoustic, combined together with a resonator of high quality factor, like QTF one. This solution was initially proposed in 2019 by Chamassi et al. [57] and have not been explored by other research teams. To address the lack of the literature concerning this topic and provide an innovative detector for photoacoustic gas sensors, the presented thesis focuses on developing a silicon microelectromechanical (MEMS) resonator with capacitive sensing specifically designed for photoacoustic gas detection. The main advantages of this approach include:

a) **Laser-based infrared technology**: this technique provides excellent selectivity, and the current development of IR lasers on silicon [58] opens up a great opportunity for the sensor's full integration.
b) **Geometry specifically designed for photoacoustic gas sensing**: the resonator, unlike QTF, microphone or cantilever, can have an elaborated geometry which is advantageous for optimization towards photoacoustic gas sensing.
c) **High quality factor:** it allows increasing the SNR without a need of an acoustic cavity.
d) **The simplicity of the fabrication process:** in contrary to MEMS microphones, we propose a simple fabrication process, discussed in chapter 3.
e) **Silicon technology with capacitive readout mechanism:** this approach gives potentially the best possibility for compactness and further integration.

Bibliography

[1] J. H. Gross, *Mass spectrometry: a textbook.* Springer Science & Business Media., 2006.

[2] R. Karasek, E. Clement., W. Francis , *Basic gas chromatography-mass spectrometry: principles and techniques.* Elsevier, 2012.

[3] G. Korotcenkov, "Metal oxides for solid-state gas sensors: What determines our choice?," *Materials Science and Engineering B: Solid-State Materials for Advanced Technology*, vol. 139, no. 1, pp. 1–23, 2007, doi: 10.1016/j.mseb.2007.01.044.

[4] Emerson, "Electrochemical vs . Semiconductor Gas Detection – a Critical Choice," *00870-0200-4928, Rev AA*, pp. 1–6, 2019, [Online]. Available: https://www.emerson.com/documents/automation/white-paper-electrochemical-vs-semiconductor-gas-detection-en-5351906.pdf

[5] M. Bakker, Eric and Telting-Diaz, "Electrochemical sensors," *Bioengineering Innovative Solutions for Cancer*, vol. 74, no. 12, pp. 47–71, 2019, doi: 10.1016/B978-0-12-813886-1.00004-8.

[6] Z. Yunusa, M. N. Hamidon, A. Kaiser, and Z. Awang, "Gas Sensors: A Review," *Sensors & Transducers*, vol. 168, no. 4, pp. 61–75, 2014, [Online]. Available: http://www.sensorsportal.com

[7] L. Xu, T. Li, X. Gao, and Y. Wang, "A high heating efficiency two-beam microhotplate for catalytic gas sensors," in *2012 7th IEEE International Conference on Nano/Micro Engineered and Molecular Systems, NEMS 2012*, 2012, pp. 65–68. doi: 10.1109/NEMS.2012.6196724.

[8] G. Monitors, "Combustible Gas Safety Monitoring : Infrared vs . Catalytic Gas Detectors," *General Monitors White Papers*, 2007.

[9] D. Popa and F. Udrea, "Towards integrated mid-infrared gas sensors," *Sensors (Switzerland)*, vol. 19, no. 9, pp. 1–15, 2019, doi: 10.3390/s19092076.

[10] L. Tombez, E. J. Zhang, J. S. Orcutt, S. Kamlapurkar, and W. M. J. Green, "Methane absorption spectroscopy on a silicon photonic chip," *Optica*, vol. 4, no. 11, p. 1322, 2017, doi: 10.1364/optica.4.001322.

[11] J. Huber, C. Weber, A. Eberhardt, and J. Wöllenstein, "Photoacoustic CO2-sensor for automotive applications," *Procedia Engineering*, vol. 168, pp. 3–6, 2016, doi: 10.1016/j.proeng.2016.11.111.

[12] Rousseau, R., Loghmari, Z., Bahriz, M., Chamassi, K., Teissier, R., Baranov, A.N. and Vicet, A., 2019. Off-beam QEPAS sensor using an 11-μm DFB-QCL with an optimized acoustic resonator. *Optics express*, 27(5), pp.7435-7446.

[13] T. Tomberg, M. Vainio, T. Hieta, and L. Halonen, "Sub-parts-per-trillion level sensitivity in trace gas detection by cantilever-enhanced photo-acoustic spectroscopy," *Scientific Reports*, vol. 8, no. 1, pp. 1–7, 2018, doi: 10.1038/s41598-018-20087-9.

[14] C. M. Zimmer, K. T. Kallis, and F. J. Giebel, "Micro-structured electron accelerator for the mobile gas ionization sensor technology," *Journal of Sensors and Sensor Systems*, vol. 4, no. 1, pp. 151–157, 2015, doi: 10.5194/jsss-4-151-2015.

[15] S. Pyo, K. Lee, T. Noh, E. Jo, and J. Kim, "Sensitivity enhancement in photoionization detector using microelectrodes with integrated 1D nanostructures," *Sensors and Actuators, B: Chemical*, vol. 288, no. January, pp. 618–624, 2019, doi: 10.1016/j.snb.2019.03.045.

[16] T. Aldhafeeri, M. K. Tran, R. Vrolyk, M. Pope, and M. Fowler, "A review of methane gas detection sensors: Recent developments and future perspectives," *Inventions*, vol. 5, no. 3, pp. 1–18, 2020, doi: 10.3390/inventions5030028.

[17] S. Edition, *Woodhead Publishing Series in Electronic and Optical Materials*. 2015. doi: 10.1016/b978-1-78242-221-1.09989-5.

[18] M. L. L. and D. W. D Jung1, S Bank2 *et al.*, "Next-generation mid-infrared sources," *Journal of Optics*, vol. 29, no. xxxx, 2017, doi: 10.1080/14484846.2018.1432089.

[19] J. Hodgkinson and R. P. Tatam, "Optical gas sensing: A review," *Measurement Science and Technology*, vol. 24, no. 1, 2013, doi: 10.1088/0957-0233/24/1/012004.

[20] V. Wittstock, L. Scholz, B. Bierer, A. O. Perez, J. Wöllenstein, and S. Palzer, "Design of a LED-based sensor for monitoring the lower explosion limit of methane," *Sensors and Actuators, B: Chemical*, vol. 247, pp. 930–939, 2017, doi: 10.1016/j.snb.2017.03.086.

[21] K. P. J. Kannan, M., Krishna, Y., Jagadeesh, G., & Reddy, *Temperature measurement in a shock tunnel using tunable diode laser absorption spectroscopy*. Springer Berlin Heidelberg, 2017.

[22] L. S. Rothman *et al.*, "The HITRAN 2008 molecular spectroscopic database," *Journal of Quantitative Spectroscopy and Radiative Transfer*, vol. 110, no. 9–10, pp. 533–572, 2009, doi: 10.1016/j.jqsrt.2009.02.013.

[23] T. Gherman and D. Romanini, "Mode – locked cavity – enhanced absorption spectroscopy," vol. 10, no. 19, pp. 3763–3769, 2002.

[24] J. Wojtas, J. Mikolajczyk, and Z. Bielecki, "Aspects of the application of cavity enhanced spectroscopy to nitrogen oxides detection," *Sensors (Switzerland)*, vol. 13, no. 6, pp. 7570–7598, 2013, doi: 10.3390/s130607570.

[25] M. Duquesnoy, "Tuning forks in photoacoustic spectroscopy: Comparative study and new developments." Ph.D disseration, University of Paris-Saclay, Paris, 2021.

[26] A. G. Bell, “On the Production and Reproduction of Sound by Light.,” *American Journal of Science*, 1880.

[27] M. L. Veingerov, “New Method of Gas Analysis Based on Tyndall-Roentgen Opto-Acoustic Effect,” *Dokl. Akad. Nauk. USSR*, vol. 19, p. 687, 1938.

[28] A. H. Pfund, “Atmospheric contamination.pdf,” *Science*, 1939.

[29] K. F. Luft, “SUR UNE NOUVELLE METHODE DANALYSE PAR ABSORPTION IN FRAROUGE-LA MODULATION SELECTIVE,” *COMPTES RENDUS HEBDOMADAIRES DES SEANCES DE L ACADEMIE DES SCIENCES*, 1954.

[30] A. Rosencwaig and A. Gersho, “Theory of the photoacoustic effect with solids,” *Journal of Applied Physics*, vol. 47, no. 1, pp. 64–69, 1976, doi: 10.1063/1.322296.

[31] C. Yan, G. Zhang, X. Ji, T. Zhang, T. Zhang, and W. Xu, “The Feasibility of Injecting Inaudible Voice Commands to Voice Assistants,” *IEEE Transactions on Dependable and Secure Computing*, vol. 18, no. 3, pp. 1108–1124, 2021, doi: 10.1109/TDSC.2019.2906165.

[32] I. G. Calasso and M. W. Sigrist, “Selection criteria for microphones used in pulsed nonresonant gas-phase photoacoustics Selection criteria for microphones used in pulsed nonresonant gas-phase photoacoustics,” vol. 4569, no. 1999, 2013, doi: 10.1063/1.1150114.

[33] P. R. Scheeper, A. G. H. van der Donk, W. Olthuis, and P. Bergveld, “A review of silicon microphones,” *Sensors and Actuators: A. Physical*, vol. 44, no. 1, pp. 1–11, 1994, doi: 10.1016/0924-4247(94)00790-X.

[34] M. R. Havey, D. K., Bueno, P. A., Gillis, K. A., Hodges, J. T., Mulholland, G. W., van Zee, R. D., & Zachariah, “Photoacoustic Spectrometer with a Calculable Cell Constant for Measurements of Gases and Aerosols,” *Analytical Chemistry*, 2010.

[35] J. C. Phys, M. Hippler, C. Mohr, and K. A. Keen, “Cavity-enhanced resonant photoacoustic spectroscopy with optical feedback cw diode lasers : A novel technique for ultratrace gas analysis and high-resolution spectroscopy Cavity-enhanced resonant photoacoustic spectroscopy with optical analysis and high-r,” vol. 044308, no. 2010, 2014, doi: 10.1063/1.3461061.

[36] T. Yang, W. Chen, and P. Wang, “A review of all-optical photoacoustic spectroscopy as a gas sensing method,” *Applied Spectroscopy Reviews*, vol. 56, no. 2, pp. 143–170, 2021, doi: 10.1080/05704928.2020.1760875.

[37] J. Kauppinen, K. Wilcken, I. Kauppinen, and V. Koskinen, “High sensitivity in gas analysis with photoacoustic detection,” *Microchemical Journal*, vol. 76, no. 1–2, pp. 151–159, 2004, doi: 10.1016/j.microc.2003.11.007.

[38] and F. K. T. A. A. Kosterev, Yu. A. Bakhirkin, R. F. Curl, "Quartz-enhanced photoacoustic spectroscopy," *Optics Letters*, vol. 27, no. 21, pp. 1902–1904, 2002, doi: 10.3969/j.issn.1001-0548.2015.06.025.

[39] A. A. Kosterev *et al.*, "Applications of quartz tuning forks in spectroscopic gas sensing," vol. 043105, 2005, doi: 10.1063/1.1884196.

[40] Y. Ma, "Review of recent advances in qepas-based trace gas sensing," *Applied Sciences (Switzerland)*, vol. 8, no. 10, 2018, doi: 10.3390/app8101822.

[41] P. Patimisco, G. Scamarcio, F. K. Tittel, and V. Spagnolo, "Quartz-enhanced photoacoustic spectroscopy: A review," *Sensors (Switzerland)*, vol. 14, no. 4, pp. 6165–6206, 2014, doi: 10.3390/s140406165.

[42] L. Dong, A. A. Kosterev, D. Thomazy, and F. K. Tittel, "QEPAS spectrophones: Design, optimization, and performance," *Applied Physics B: Lasers and Optics*, vol. 100, no. 3, pp. 627–635, 2010, doi: 10.1007/s00340-010-4072-0.

[43] G. Aoust, "Développements de sources infrarouges et de résonateurs en quartz pour la spectroscopie photoacoustique," 2016. [Online]. Available: http://www.theses.fr/2016SACLX067/document

[44] M. Duquesnoy, G. Aoust, J. M. Melkonian, R. Lévy, M. Raybaut, and A. Godard, "Quartz enhanced photoacoustic spectroscopy based on a custom quartz tuning fork," *Sensors (Switzerland)*, vol. 19, no. 6, pp. 1–10, 2019, doi: 10.3390/s19061362.

[45] H. Zheng *et al.*, "Quartz-enhanced photoacoustic spectroscopy employing pilot line manufactured custom tuning forks," *Photoacoustics*, vol. 17, no. December 2019, p. 100158, 2020, doi: 10.1016/j.pacs.2019.100158.

[46] P. Patimisco *et al.*, "Analysis of the electro-elastic properties of custom quartz tuning forks for optoacoustic gas sensing," *Sensors and Actuators, B: Chemical*, vol. 227, pp. 539–546, 2016, doi: 10.1016/j.snb.2015.12.096.

[47] A. Sampaolo *et al.*, "Improved tuning fork for terahertz quartz-enhanced photoacoustic spectroscopy," *Sensors (Switzerland)*, vol. 16, no. 4, pp. 1–8, 2016, doi: 10.3390/s16040439.

[48] S. Borri *et al.*, "Intracavity quartz-enhanced photoacoustic sensor," *Applied Physics Letters*, vol. 104, no. 9, 2014, doi: 10.1063/1.4867268.

[49] P. Patimisco *et al.*, "High finesse optical cavity coupled with a quartz-enhanced photoacoustic spectroscopic sensor," *Analyst*, vol. 140, no. 3, pp. 736–743, 2015, doi: 10.1039/c4an01158a.

[50] Lv, H., Zheng, H., Liu, Y., Yang, Z., Wu, Q., Lin, H., Montano, B.A.Z., Zhu, W., Yu, J., Kan, R. and Chen, Z., 2021. Radial-cavity quartz-enhanced photoacoustic spectroscopy. *Optics Letters*, 46(16), pp.3917-3920.

[51] R. Rousseau, N. Maurin, W. Trzpil, M. Bahriz, and A. Vicet, “Quartz tuning fork resonance tracking and application in quartz enhanced photoacoustics spectroscopy,” *Sensors (Switzerland)*, vol. 19, no. 24, 2019, doi: 10.3390/s19245565.

[52] R. Levy, M. Duquesnoy, J. M. Melkonian, M. Raybaut, and G. Aoust, “New Signal Processing for Fast and Precise QEPAS Measurements,” *IEEE Transactions on Ultrasonics, Ferroelectrics, and Frequency Control*, vol. 67, no. 6, pp. 1230–1235, 2020, doi: 10.1109/TUFFC.2019.2943388.

[53] V. Koskinen, J. Fonsen, K. Roth, and J. Kauppinen, “Progress in cantilever enhanced photoacoustic spectroscopy,” *Vibrational Spectroscopy*, vol. 48, no. 1, pp. 16–21, 2008, doi: 10.1016/j.vibspec.2008.01.013.

[54] V. Koskinen, J. Fonsen, K. Roth, and J. Kauppinen, “Cantilever enhanced photoacoustic detection of carbon dioxide using a tunable diode laser source,” *Applied Physics B: Lasers and Optics*, vol. 86, no. 3, pp. 451–454, 2007, doi: 10.1007/s00340-006-2560-z.

[55] Gasera, “OPTICAL CANTILEVER MEMS MICROPHONE.”

[56] T. Tomberg, T. Hieta, M. Vainio, and L. Halonen, “Cavity-enhanced cantilever-enhanced photo-acoustic spectroscopy,” *Analyst*, vol. 144, no. 7, pp. 2291–2296, 2019, doi: 10.1039/c9an00058e.

[57] K. Chamassi, W. Trzpil, R. Arinero, R. Rousseau, A. Vicet, and M. Bahriz, “Capacitive silicon micro-electromechanical resonator for enhanced photoacoustic spectroscopy,” *Applied Physics Letters*, vol. 115, no. 8, 2019, doi: 10.1063/1.5098140.

[58] M. Rio Calvo *et al.*, “Mid-infrared laser diodes epitaxially grown on on-axis (001) silicon,” *Optica*, vol. 7, no. 4, p. 263, 2020, doi: 10.1364/optica.388383.

Chapter 2

2. Theoretical model

This chapter is mainly based on Trzpil et al. article [1]; however, some parts have been extended while others improved. The author of this thesis contributes to the article with theory examination, text composition, simulations and data analysis.

This chapter presents the problem given by working principles of photoacoustic gas sensor with capacitive transduction, which was introduced in chapter 1, section 1.4.6. Namely, to keep a good sensitivity in capacitive type microphones, the distance between the electrodes needs to be maintained small and the displacement needs to be maximized. Displacement is related to force (here, photoacoustic force) acting on the membrane and energy losses described by damping. Increasing the photoacoustic force by simply changing the device's geometry consists in increasing the surface used to collect the photoacoustic energy. However, a wide surface will increase viscous damping and particularly squeeze film effect. This creates a dilemma since it is necessary to increase the surface for photoacoustic force enhancements, while for viscous damping optimization, it is necessary to decrease the surface. Therefore, we assert that optimizing a mechanical resonator for photoacoustic force collection exhibits the opposite trend than optimizing for viscous damping reduction. This study addresses a problem of geometry optimization of a cantilever-shaped resonator for photoacoustic gas detection. To solve it, we created an analytic model for a silicon-based microresonator sensor, a cantilever, dedicated to photoacoustic gas sensing with capacitive transduction. This analytic model was implemented in Python programming environment. Optimization aims to determine the geometrical parameters of the cantilever: length L, width b, thickness h, gap d (figure 2.1.1) and its resonance frequency, which would maximize the output electrical signal and the signal-to-noise ratio.

This chapter describes as well a COMSOL simulation used to reinforced the analytic model.

2.1. General description

The working principle of a gas sensor based on photoacoustic spectroscopy using a cantilever as a capacitive transducer is schematically presented in figure 2.1.1. The acoustic pressure generated by laser light absorption applies a force on the cantilever and sets it in motion. To maximize the displacement, the acoustic wave is generated at the cantilever's resonance frequency via the laser wavelength modulation. The silicon cantilever is electrically insulated from the back silicon, forming a capacitor. One of the electrodes of the capacitor is the cantilever itself. The displacements of the cantilever cause the capacitance variations. The

capacitance variations can be converted into a current or a voltage signal depending on the excitation frequency [2].

Performing a trial and error method solely for the sensor's performance optimization is not feasible due to economic and time reasons. Therefore, a computational method is the most reasonable choice.

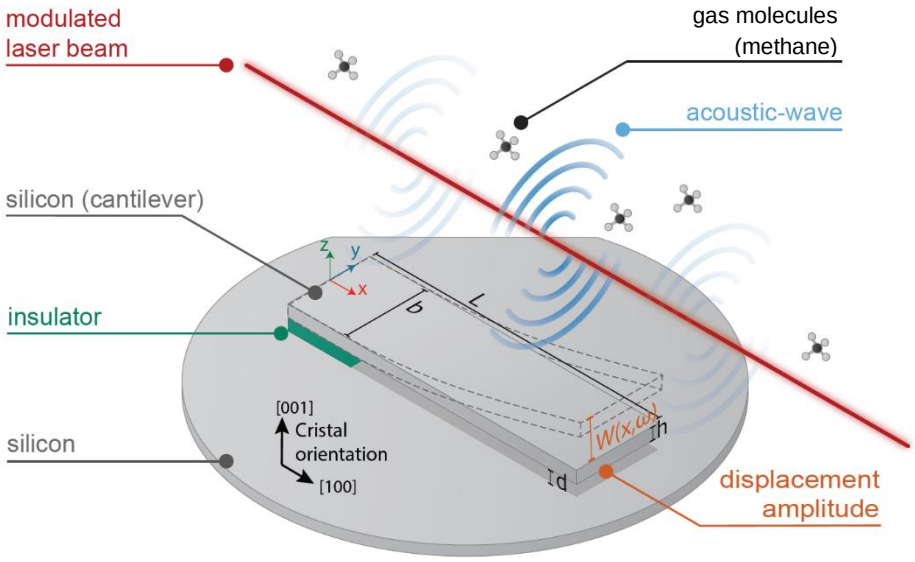

Figure 1.1.1: Sensing scheme of a silicon cantilever based sensor for photoacoustic gas detection with capacitive transduction mechanisms

The sensing scheme imposes multiphysics problems in different domains and can be divided into four parts, presented in figure 1.1.2 : (1) acoustic force, (2) damping mechanisms, (3) mechanical displacement and (4) output signal.

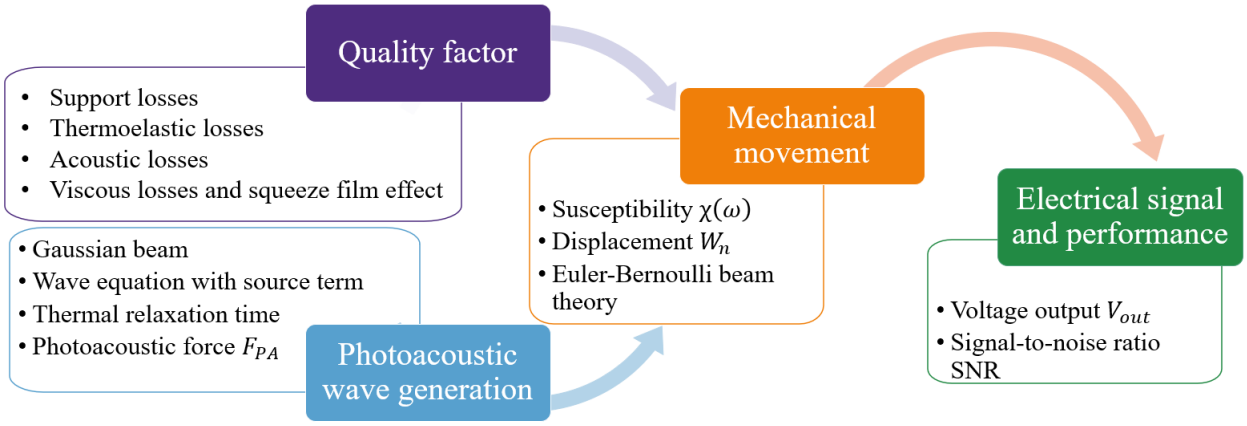

Figure 2.1.2: Scheme presenting multiphysics aspect of analytic model for cantilever capacitive signal enhancement under photoacoustic force.

Many of these problems are not directly coupled; others are characterized by opposite trends in terms of geometry optimization. For this, the cantilever has to be sized to maximize its displacement under acoustic wave exposition while exhibiting a strong capacitance variation. Each subsection will consider one of the following blocks, while the last block is divided into two sections. Finally, we gathered all the calculations to study the effect of the gap (d in figure 2.1.1) on the signal-to-noise ratio optimization.

2.2. Photoacoustic force

This part describes the generation of the photoacoustic wave and its interaction with the cantilever. The purpose of this section is to study the cantilever dimensions (length L, width b, thickness h) and its resonance frequency in order to maximize the acoustic force. This part evaluates the photoacoustic pressure generation and the photoacoustic force applied to the cantilever.

As in TLDS (chapter 1, section 1.3) the acoustic wave is obtained by wavelength modulation technique at the pulsation ω [2], the photoacoustic effect is related to heat production rate, depending on the non-radiative relaxation time of the target gas. The non-radiative relaxation strongly relies on the molecular species, the gas concentration, temperature, pressure and the gas mixture. To obtain realistic values, our numerical estimation is performed on one specific gas: CH_4 diluted in N_2. However, the model is compatible with any gas mixture once the relaxation time is known.

2.2.1. Photoacoustic wave generation

The source of the photoacoustic wave generation lies in periodic gas absorption induced by a modulated laser beam. We consider a Gaussian laser beam that propagates along the x-axis at an altitude $z = z_L$ and centred with respect to the y-axis at $y = y_L$ (figure 2.2.1.)

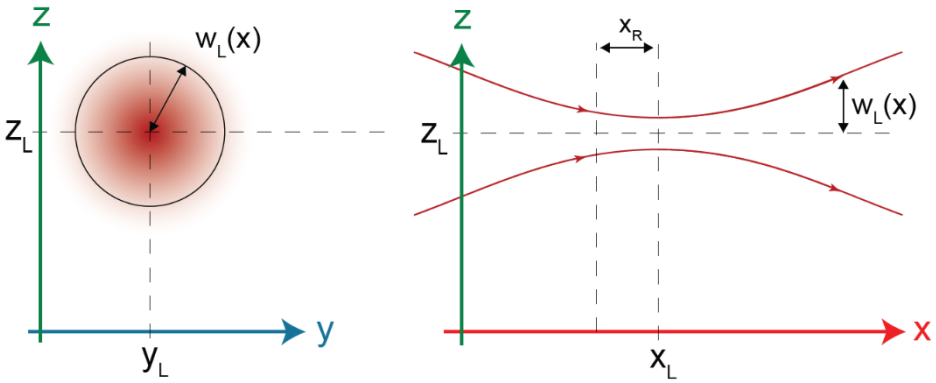

Figure 2.2.1: Gaussian beam profile and its position on the axis in relation to the cantilever microbeam.

The distribution of the light intensity $I(x,y,z)$ is related to the laser power P_L and normalized Gaussian profile $g(x,y,z)$:

$$I(x,y,z) = P_L \cdot g(x,y,z) \tag{2.1}$$

The normalized Gaussian profile depends on the laser radius $w_L(x)$:

$$g(x,y,z) = \frac{2}{\pi\omega_L(x)^2}\exp\left(-2\frac{(z-z_L)^2+(y-y_L)^2}{w_L(x)^2}\right) \tag{2.2}$$

The laser radius is given by the following equation :

$$w_L(x) \quad = w_L(x_L)\sqrt{\left(1+\frac{(x-x_L)^2}{x_R^2}\right)} \tag{2.3}$$

where x_R depends Rayleigh length $x_R = \frac{\pi w_L^2(x_L)}{\lambda_L}$, which depends on the laser emission λ_L and waist of the beam $w_L(x_L)$.

The theoretical model used to describe the pressure and force of the acoustic wave generated by molecular absorption is based on the model developed by Petra et al.[4]. However, our model takes into account the variation of the laser beam radius $w_L(x)$ along the optical axis (x-axis), and the effects of the gas relaxation time constant. The assumptions used in the model are:

a) The wavelength modulation is performed without the modulation of the laser power.
b) Sommerfeld radiation condition: no reflection from any walls of a gas cell, and photoacoustic energy fade in infinity.
c) The photoacoustic pressure is unaltered by the presence of the cantilever.
d) The laser beam radius is smaller than the distance between the cantilever and the optical axis.

To fulfill assumption (c), the acoustic wave wavelength must be at least one order larger than the thickness and width of the cantilever : $\lambda_a \sim 3.5\ cm$ at 10~kHz.

The absorption of the modulated light causes periodic heat changes and subsequently an acoustic wave. The heat production rate H(x,y,z,t) is given by:

$$H(x,y,z,t) = \frac{C_f(\omega)g(x,y,z)}{\sqrt{1+(\omega\tau)^2}}e^{i(\omega t-\arctan(\omega\tau))} \tag{2.4}$$

where ω is the laser modulation frequency, τ is the target gas relaxation time $C_f(\omega)$ is the effective absorption coefficient. Absorption and transmission line shape can be ideally described with a Lorentzian line shape function (appendix A1). The laser emission wavelength scan the absorption line and is modulated around the central wavelength λ_c. The modulated wavelength can be expressed as:

$$\lambda(t) = \lambda_c + \lambda_{amp} \sin(\omega t) \tag{2.5}$$

where λ_{amp} is the modulation amplitude. When the laser wavelength is modulated, the power remains constant and equal to P_L, we can write $C_f\ (\omega) = 0.50\alpha(\omega\ )P_L$, where $\alpha(\omega)$ is the absorption coefficient of the gas. The 0.5 factor is obtained by expansion of the absorption function (Lorentzian) in Fourier series. We consider only the first Fourier component ($a_1 = 0.5$) for the $1f$ detection method. Second Fourier components would result in a coefficient of 0.35 ($a_2 = 0.35$) [4]. More details are provided in appendix A1.

We are looking for a solution of photoacoustic pressure P(x,y,z), which can be through the wave equation with source :

$$\frac{\partial^2 u}{\partial t^2} - c_s^2\ \Delta u = S \tag{2.6}$$

The source of photoacoustic wave generation is related to the heat production caused by light absorption. The expression of photoacoustic pressure $P(x,y,z)$ is given by the wave equation with source:

$$\frac{\partial^2 P(x,y,z,t)}{\partial t^2} - c_s^2\ \Delta P(x,y,z,t) = (\gamma - 1)\frac{\partial H(x,y,z,t)}{\partial t} \tag{2.7}$$

where $c_s = 347.276\, m/s$ is the sound velocity in air and $\gamma = C_p/C_v$ the adiabatic gas coefficient or heat capacity ratio equal to the fraction ratio between heat capacities at constant pressure C_p and volume C_v. Due to the source term, equation (2.7) is the inhomogeneous equation in time. It may be solved by taking a time Fourier transform and expressing the solution as an infinite expansion of the normal mode. By substituting $P(x,y,z,t) = p(x,y,z)e^{i\omega t}$, $H(x,y,z,t) = h(x,y,z)e^{i\omega t}$ and boundary conditions, we can work with steady-state solution of equation (2.7). Based on this, Petra et al. [4] showed that the pressure equation takes the following form:

$$p(x,y,z) = -\frac{\pi A}{2c_s^2\ k_s^2}(Y_0\big(k_s r\ + iJ_0(k_{sr})\big)\int_0^{+\infty} uJ_0(u)\ exp\frac{-2u^2}{k_s^2 w_L(x)^2}du \tag{2.8}$$

where J_0 , Y_0 are the zero-order Bessel function of a first and a second kind, respectively; $k_s = \frac{\omega}{c_s}$is the wave number, $r = \sqrt{(z - z_L)^2 + (y - y_L)^2}$ is the distance between the laser beam and the cantilever and A is the amplitude of photoacoustic pressure :

$$A = -(\gamma - 1)\omega H(x, y, z)\frac{2}{\pi w_L(x)^2} \quad (2.9)$$

Eq. (2.9) shows a crucial distinction between optically produced sound in unbounded space (our consideration) and sound inside an enclosed volume (such as an acoustic resonator). As presented in chapter 1, equation (1.7), the amplitude of the photoacoustic wave in an enclosed cell scales as 1/ω [9].
In the presented model, we consider a cantilever without an acoustic cavity; therefore, the amplitude of acoustic pressure scales proportionally to ω. The reason behind this is that acoustic pressure is proportional to the speed of the optical power variation.

2.2.2. Photoacoustic force

Pressure is defined as the force applied perpendicular to an object's surface per unit area across which that force is distributed. Because the pressure acts on both sides of the cantilever, the force will be defined as a difference between the pressure on the top and bottom side of the cantilever integrated over the cantilever surface:

$$F_{PA} = \int_0^L \int_{-b/2}^{b/2} \big(p(x, y, z) - p(x, y, z - h)\big)\phi_n(x)dxdy \quad (2.10)$$

where $\phi_n(x)$ describes the one-dimension shape of the cantilever mechanical mode n. The shape of the mode contains information about the cantilever deflection and can be found analytically by solving an eigenvalue problem of the Euler-Bernoulli equation. The mode shape for a clamped-free cantilever is given by [5]:

$$\phi_n(x) = \cosh\left(\alpha_n \frac{x}{L}\right) - cos\alpha_n \frac{x}{L} - \frac{\sinh(\alpha_n) - \sin(\alpha_n)}{cosh(\alpha_n) + cos(\alpha_n)}\left(\sinh\left(\alpha_n \frac{x}{L}\right) - sin\left(\alpha_n \frac{x}{L}\right)\right) \quad (2.11)$$

The acoustic force acting on the cantilever is frequency-modulated at the wavelength modulation frequency of the laser source. For a first harmonic detection (1f detection), it is adjusted to the cantilever mode frequency.

In our model, the cantilever vibrates in its fundamental mode-first harmonic $n = 1$ which corresponds to a mode constant $\alpha_1 = 1.875$.

2.2.3. Optimal position of the laser beam

To optimize a photoacoustic force in terms of cantilever geometry, first, we need to optimize the laser beam position to maximize a photoacoustic force acting on the cantilever. For this study, we used a cantilever of a frequency $f_n = 11\ kHz$ and fixed dimensions: width $b = 50\ \mu m$, thickness $h = 100\ \mu m$ and length $L = 3.5\ mm$. Other parameters are detailed in table 2.2.1.

Table 2.2.1: Parameters used in simulation connected with the laser source and acoustic wave

parameter	description	value
λ_L	laser wavelength	1.65 μm
$w_L(x_L)$	laser waist (experimental value)	100 μm
x_L, y_L, z_L	laser beam waist radius position	0.725L, 0, 250mm
P_L	laser power	50 mW
C_{gas}	CH_4 concentration in N_2	1%
α	absorption coefficient	CH_4 0.38 m^{-1}
τ	target gas relaxation time	CH_4 11.5μs [19]
c_s	speed of sound	Air 347.276 m/s
γ	heat ratio capacity	Air 1.4

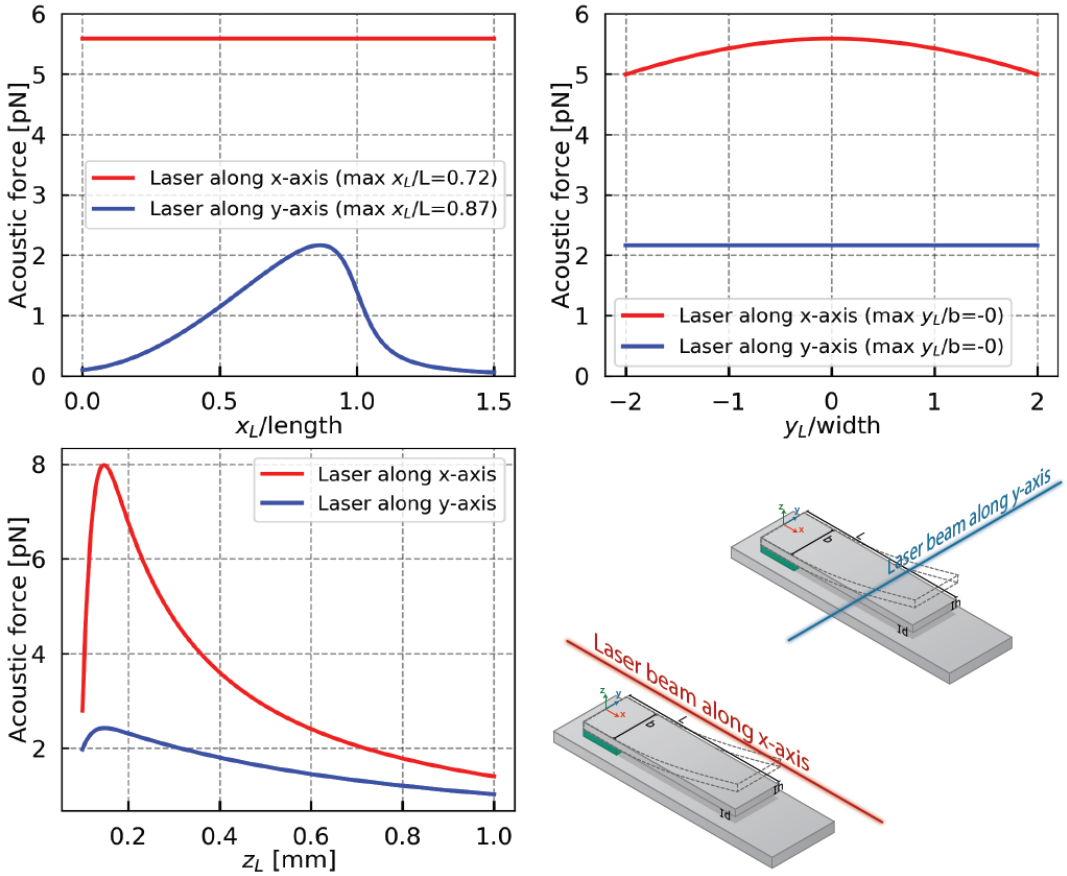

Figure 2.2.2: Amplitude of the photoacoustic force applied on a cantilever as a function of the laser beam position for two configurations: red - laser beam along the x -axis; blue - laser beam along the y-axis. Where $f_n = 11\ kHz$, $b = 50\ \mu m, h = 100\ \mu m$ and $L = 3.5\ mm$, respectively the resonance frequency, the width, the thickness and the length of the cantilever.

We calculated the acoustic force using equation (2.10) as a function of a laser beam position: x_L, y_L, z_L . The simulation was run for two configurations of the laser beam: parallel (red curve figure 2.2.2) and perpendicular (blue curve figure 2.2.2).

Figure 2.2.2. presents results of simulation for beam position optimization. Based on the results, we conclude that photoacoustic force is maximized for a laser position along x-axis with beam position: $x_L = 0.725L$ and $y_L = 0\mu m$ where L is the total length of the cantilever. To fulfil the assumption that laser light does not interfere with the cantilever, we chose $z_L = 250\ \mu m$.

2.2.4. Frequency optimization

Due to the thermal relaxation time, the modulation frequency strongly affects the heat production rate (equation (2.4)) and subsequently the acoustic force. Indeed, to allow the molecules to thermalize efficiently, the laser modulation needs to be lower than the molecules relaxation time.

As mentioned in chapter 1, each molecule exhibits a different relaxation time. To maximize the PA force, optimization needs to be made with respect to one type of gas. We chose CH_4 diluted in nitrogen N_2 for which the relaxation time is equal to 11.5 µs [6]. However, the relaxation time between the molecules might differ by several orders of magnitude. The conducted simulation was obtained for emission wavelength $\lambda_L = 1.65$ µm to target a strong methane absorption line.

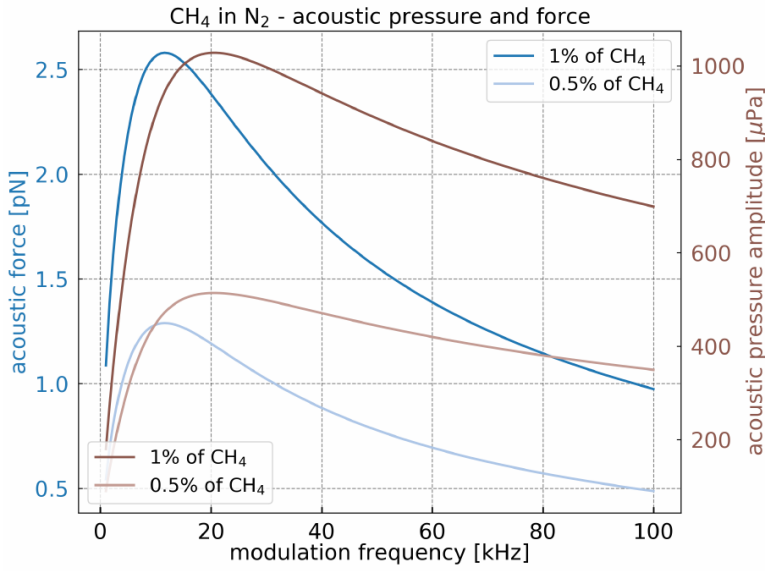

Figure 2.2.3: Acoustic force and acoustic pressure dependency on the modulation frequency for diluted CH_4 at 1% and 0.5% in nitrogen. Cantilever width $b = 25\ \mu m$ and thickness $h = 100\ \mu m$.

Figure 2.2.3 presents the acoustic pressure and force for CH_4 diluted in N_2, 1% and 0.5%, respectively. Only the acoustic force depends on cantilever geometry. To maintain a fixed frequency, the cantilever length is adjusted with the following equation (2.12):

$$f_n = \frac{\omega_n}{2\pi} = \frac{\alpha_n^2}{2\pi\sqrt{12}} \frac{h}{L^2} \sqrt{\frac{E}{\rho_b}} \tag{2.12}$$

where f_n, ρ_b = 2330 $\frac{kg}{m^3}$, E=130 GPa are the resonance frequency of a clamped-free cantilever, the silicon density and silicon Young's modulus in [100] direction [7], respectively.

For each concentration, they increase with the frequency until reaching a maximum of around $20\ kHz$ for the acoustic pressure and around $11\ kHz$ for the acoustic force. This maximum is related to CH_4 relaxation time value. The maximum visible on acoustic pressure in figure 2.2.3 shift to a lower frequency for acoustic force due to the cantilever length which appears only in the acoustic force equation (2.10).

According to equation (2.12), the length of the cantilever is longer for lower frequencies. Therefore, the surface exposed to the acoustic pressure is larger, which subsequently increases the acoustic force at low frequencies. According to equation (2.12), if the width and thickness of the cantilever is fixed, then for low frequencies the length will be longer than for higher frequencies. Thus, low frequencies cantilever are characterized by greater photoacoustic energy collection.

The maximum value of the acoustic force is at 11 kHz. To maximize the force applied on the cantilever, the following numerical simulations of the cantilever geometry (width b, thickness h and length L) are realized at this given frequency. However, the model is adaptable to any frequency with respect to the assumptions.

2.2.5. Geometry optimization towards photoacoustic force enhancement

The objective of this section is to find the geometry of the cantilever to enhance the photoacoustic force. Figure 2.2.4 presents acoustic force for a cantilever of 11 kHz as a function of cantilever width and thickness. The length of the cantilever is adjusted according to equation (2.12). Darker blue indicated higher photoacoustic force.

The figure presents two general trends. Namely, the photoacoustic force increases with the width b and the thickness h. Indeed, the surface enlargement increases the energy collection from the acoustic wave. Secondly, the thickness increment raises the pressure difference between the top and bottom sides of the cantilever, which enhances the acoustic force. In the simulation the thickness is fixed. Thus, to maintained fixed frequency, the length of the cantilever needs to be adjusted according to equation (2.12). Based on this equation one can

see that the cantilever length will increase with thickness to maintain fixed frequency, hence greater photoacoustic force for thicker cantilevers.

The results presented in figure 2.2.4 would change while using different gases, volume mixing ratios and given frequency (figure 2.2.3). Nevertheless, the general trend would remain constant.

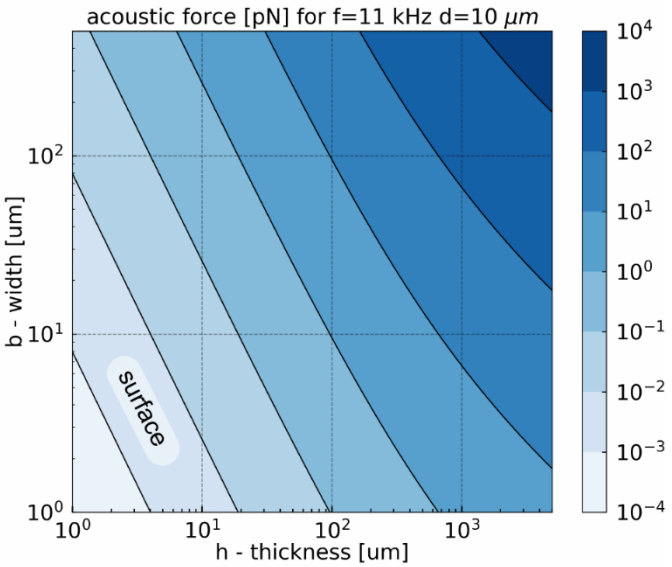

Figure 2.2.4: Acoustic force for 1 % of CH_4 in N_2 as a function of width b and thickness h of the cantilever. For different thicknesses, the length is adjusted to maintain constant frequency: 11 kHz. This frequency was chosen to maximize acoustic force. The area with the weakest acoustic force corresponds to cantilevers with the smallest surface.

2.3. Damping mechanism: the quality factor

This section aims to describe and calculate the following mechanisms of losses: viscous, thermoelastic, support and acoustic damping, as a function of cantilever geometry.

2.3.1. General description

The quality factor Q is a dimensionless number that describes the energy losses in the system. It can be expressed as the ratio between the energy stored in a cycle of vibration E_{stored} and the energy dissipated in a cycle of vibration $E_{dissipated}$:

$$Q = 2\pi \frac{E_{stored}}{E_{dissipated}} \tag{2.13}$$

There are two main mechanisms where the cantilever can lose energy: through internal energy dissipation, like thermoelastic losses and external dissipation, like viscous damping,

support losses or acoustic losses. The total quality factor consists of quality factors originating from different losses and can be calculated using the following equation:

$$Q_{total} = \frac{1}{Q_{viscous}} + \frac{1}{Q_{thermo}} + \frac{1}{Q_{support}} + \frac{1}{Q_{acoustic}} \tag{2.14}$$

2.3.2. Thermoelastic losses

Thermoelastic damping (TED) is a loss mechanism due to the irreversible heat flow in vibrating structures. A temperature gradient occurs between regions under tension (where the temperature drops) and regions under compression (where the temperature rise). This mechanism is schematically presented in figure 2.3.1b.

We use an analytical model proposed by Lifshitz [8][9], where the thermoelastic quality factor is given by:

$$Q_{thermo} = \frac{C_p}{E\alpha_T^2 T}\left(\frac{6}{\xi^2} - \frac{6}{\xi^3}\left(\frac{\sinh(\xi)+\sin(\xi)}{\cosh(\xi)+\cos(\xi)}\right)\right)^{-1} \tag{2.15}$$

C_p, α_T, T, E are specific heat capacity, linear thermal expansion coefficient, temperature, Silicon Young's modulus, respectively. $\xi = h\sqrt{\frac{\omega\rho_p C_p}{2K}}$ represents a dimensionless number where K is the thermal conductivity. The values of all these parameters can be found in table 2.3.1. The maximum of thermoelastic damping [8] occurs for $\xi = 2.225$. This value corresponds to a transition frequency $f_t = \frac{\pi}{2}\frac{K}{\rho_b C_p h^2}$. For a cantilever frequency f_n lower than the transition frequency f_t ($f_n < f_t$), the beam is permanently in thermal equilibrium. In this case, the vibration is called isothermal. On the other hand, when $f_n > f_t$ the cantilever frequency is higher than the transition frequency, the beam does not have enough time to thermally equilibrate, and this vibration is called adiabatic. In both cases, the energy dissipation is low. However, the Q_{thermo} the quality factor is higher in isothermal than in an adiabatic regime [10].

Figure 2.3.1 presents the results for cantilever geometry optimization towards thermoelastic losses minimalization. In the case of the constant-frequency regime, one needs to calculate the thickness giving the maximal damping. Based on the f_t expression, the isothermal zone corresponds to the thin cantilever thickness and the adiabatic zone to the large thickness. For $f_n = 11\ kHz$ the maximal thermoelastic damping, i.e. the lowest $Q_{thermo} = 12500$, corresponds to a cantilever with thickness $h = 90\ \mu m$.

Therefore, for a frequency of 11 kHz, thermoelastic damping is not a limiting factor.

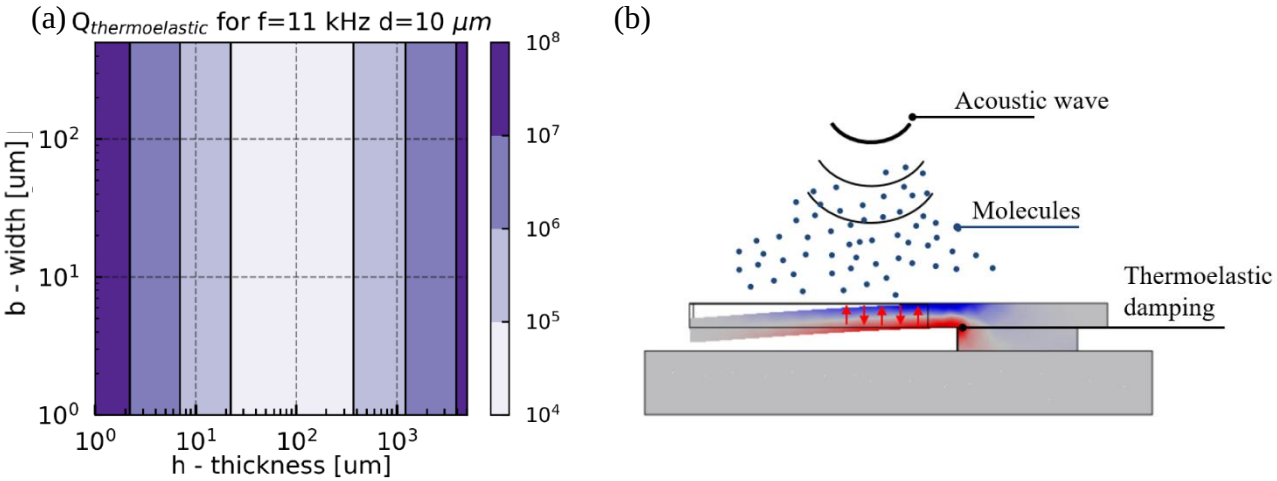

Figure 2.3.1: (a) Thermoelastic quality factor as a function of width and thickness for a cantilever of fundamental resonance frequencies equal to 11 kHz and for a gap between support and cantilever equal to d=10 µm. (b) Schematic illustration of a source of acoustic losses: acoustic wave which is created via the cantilever movement

2.3.3. Acoustic losses

Acoustic losses refer to losses caused by a vibrating structure being a source of acoustic wave radiation, which is schematically presented in figure 2.3.2b. A good approximation of these losses can be expressed with an analytical model for a cantilever with an elliptical cross-section [11] [12] [13]. In this approach, the quality factor related to acoustic losses is given by the following equation :

$$Q_{acoustic} = \frac{256}{\pi}\frac{\rho_b}{\rho_f}\frac{1}{(k_s b)^3}\frac{h\int_0^L \phi_n^2(x)\,dx}{\int_{\varphi=0}^{\pi}\sin^3\varphi\,|\int_0^L \phi_n(x)\exp\left(-ik_s x\cos(\varphi)\right)dx|^2\,\mathrm{d}\varphi} \qquad (2.16)$$

where ρ_f is a fluid density, $k_s = \omega/c_s$ is the acoustic wavenumber, c_s is the speed of sound. Numerical calculations using equation (2.16) are presented in figure 2.3.2a. Based on these results, one can see that losses caused by acoustic radiation are significant when an acoustic wavelength λ_a is comparable or lower than a typical dimension of the cantilever. Therefore, losses are increasing for thin and wide cantilevers. For instance, for a cantilever with a width b=5000 µm and thickness h = 1 µm the acoustic quality factor is equal to $Q_{acoustic} = 605$. Also, acoustic damping it is less significant at low frequencies.

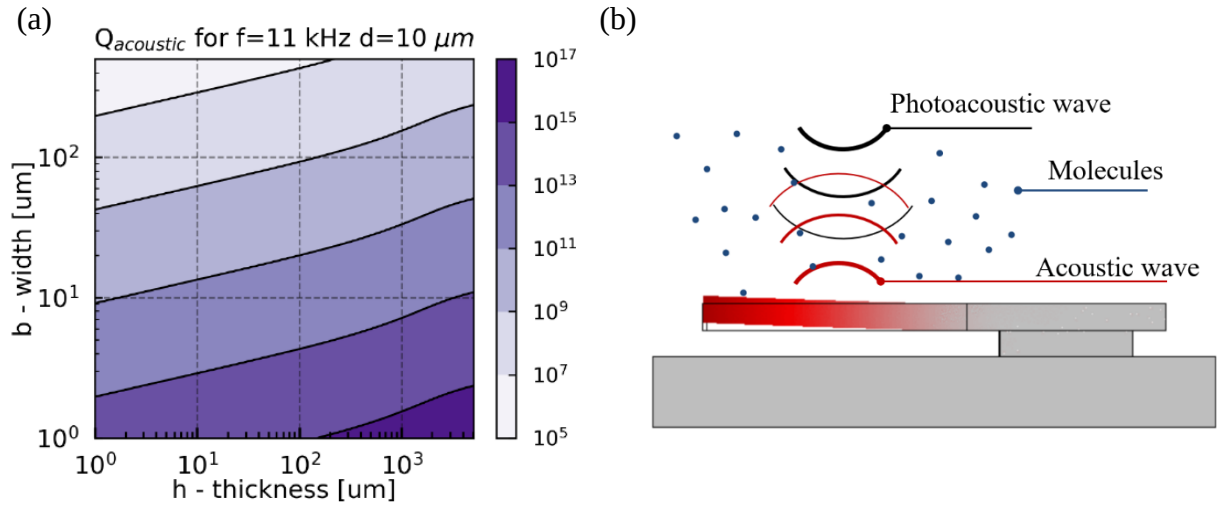

Figure 2.3.2: (a) Acoustic quality factor as a function of width and thickness for a cantilever of fundamental resonance frequencies equal to 11 kHz and for a gap between support and cantilever equal to d=10 µm. (b) Schematic illustration of a source of acoustic losses: acoustic wave which is created via the cantilever movement

2.3.4. Support losses

Support losses are caused by energy dissipation into the support which holds the cantilever. When the cantilever is set in motion, part of its kinetic energy is dissipated into the support. This dissipation is described by the support quality factor. The mechanism of these losses is schematically presented in figure 2.3.3b.

An analytical solution for support losses in the case of a clamped-free cantilever was proposed by Hao [14] and takes the following form:

$$Q_{support} = \left(\frac{0.24(1-\nu)}{(1+\nu)\Psi}\right)\frac{1}{\left(\frac{\alpha_n}{\pi}\chi_n\right)^2}\left(\frac{L}{h}\right)^3 \qquad (2.17)$$

where ν, α_n, χ_n is the Poisson's ratio, a mode constant and a mode shape factor, respectively. For the clamped-free cantilever fundamental mode n=1 and α_1=1.875. Then, the mode shape factor:

$$\chi_1 = \frac{\sin(\alpha_1)-\sinh(\alpha_1)}{\cos(\alpha_1)+\cos h(\alpha_1)} \text{ and } \Psi = 0.336.$$

The results for support losses as a function of cantilever dimensions are presented in figure 2.3.3a. It can be seen from figure equation (2.17) that the energy dissipation from the support is inversely proportional to $\left(\frac{L}{h}\right)^3$. If we look at a fixed frequency, without considering

the length of the cantilever, as it is presented in figure 2.3.3a, then the quality factor of the support is $Q_{support} \propto \frac{1}{\sqrt{\omega_n^3 h^3}}$. The simplest way to understand the reason for support losses increase with the thickness is through energy transfer for this vibration mode. Namely, thick cantilevers will cause higher deformation.

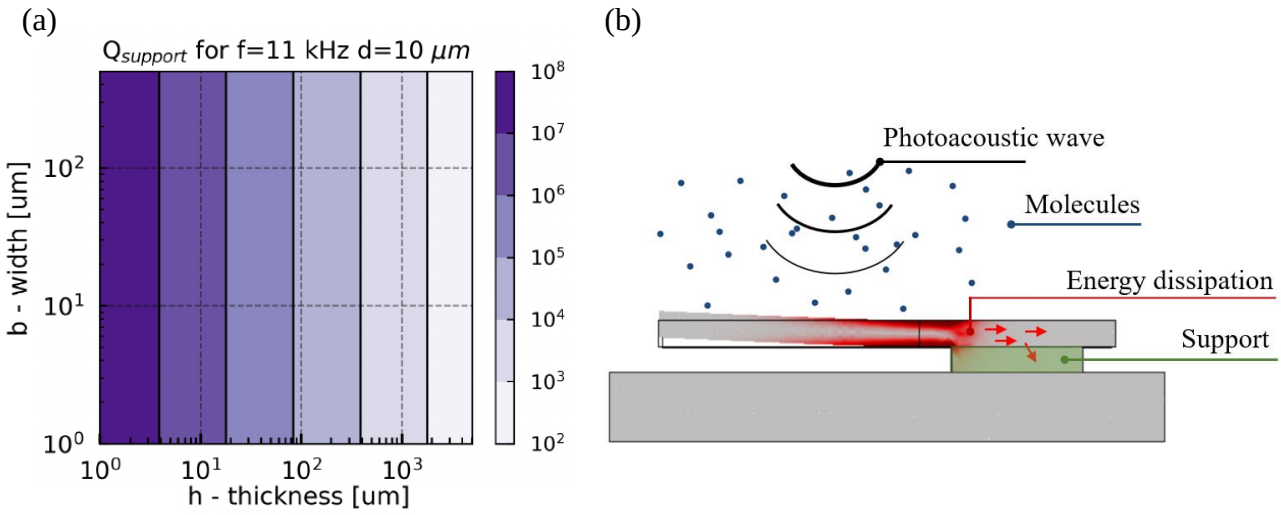

Figure 2.3.3: (a) Support quality factor as a function of width and thickness for a cantilever of fundamental resonance frequencies equal to 11 kHz and for a gap between support and cantilever equal to d=10 μm. (b) Schematic illustration of a source of support losses. The red arrows indicated the energy dissipation into the support.

2.3.5. Viscous losses

Viscous damping originates from fluid resistance. It is considered to be the most significant damping mechanism in MEMS operating in ambient conditions. The exact problem formulation of fluid mechanics alone constitutes a challenge of complexity, and no analytical formula has been yet proposed in the literature. Our study is based mainly on the work of [15] [16] [17].

During the beam excitement in fluid, additional force connected with the medium appears. This force is called further hydrodynamic force $F_{hydro}(x,t)$ and can be described using a normalized time-independent function called hydrodynamic function Γ_{hydro}. Quality factor connected with viscous damping can be analytically expressed using Γ_{hydro} as follow:

$$Q_{viscous} = \frac{\frac{4\rho_b h}{\pi \rho_f b} + \Gamma_{hydro}^R(\omega)}{\Gamma_{hydro}^I(\omega)} \tag{2.18}$$

where ρ_b, ρ_f, Γ^R_{hydro}, Γ^I_{hydro} are the density of the beam, the density of the fluid, real and imaginary part of the hydrodynamic function, respectively. The total hydrodynamic function originates from the linearized Navier -Stokes equation.

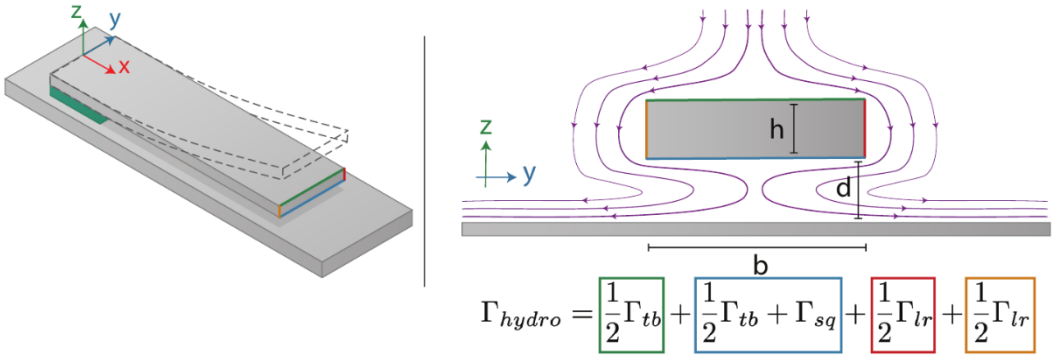

Figure 2.3.4: Scheme of streamlines acting on the cross-section sidewalls of the cantilever oscillating in its first mode of vibration with corresponding hydrodynamic functions. Γ_{tb} is used to describe the forces applied at the top and the bottom of the cantilever, Γ_{lr} relates to the left and right side of the cantilever, while Γ_{sq} is a hydrodynamic force originating from squeeze film effect.

Thus, it can be represented as a linear combination of hydrodynamics functions originating from each sidewall of the beam cross-section [15]. Pictorially it is presented in figure 2.3.4, while mathematically expressed as:

$$\Gamma_{hydro} = \frac{1}{2}\Gamma_{tb} + \frac{1}{2}\Gamma_{tb} + \Gamma_{sq} + \frac{1}{2}\Gamma_{lr}\frac{1}{2}\Gamma_{lr} \tag{2.19}$$

where $\Gamma_{tb}, \Gamma_{sq}, \Gamma_{lr}$ are hydrodynamic functions originating from the top and bottom side of the cantilever, squeeze film, left and right side of the cantilever, respectively.

2.3.5.1. Viscous damping: top and bottom

Γ_{tb} describes the viscous damping on the front and the back of the cantilever. Sader [17] has used the exact analytic solution for a circular-cross section cantilever. Then, he used a multiplicative correction function $\Omega_{sader}(\omega)$ in order to provide a more precise result in the case of infinitely thin rectangular beams. Correction function $\Omega_{sader}(\omega)$ depends on the Reynolds number and, therefore, on the width and frequency of the cantilever. The expression of Γ_{tb} is given in equation (2.20) and Ω_{sader} expression in [17].

$$\Gamma_{tb}(\omega) = \left(1 + \frac{4iK_1\left(-i\sqrt{iR_e}\right)}{\sqrt{iR_e}K_0\left(-i\sqrt{iR_e}\right)}\right)\Omega_{sader}(\omega) \tag{2.20}$$

where K_0, K_1 are modified Bessel functions of the second kind and $Re = \frac{\rho_f \omega b^2}{4\mu_f}$is the Reynolds number, ρ_f is the density of the fluid while μ_f is dynamic viscosity.

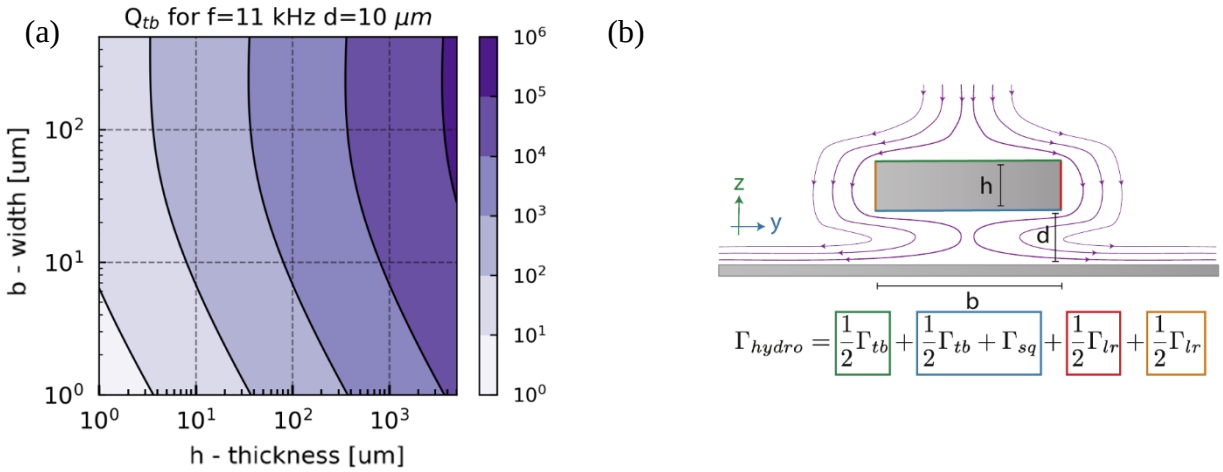

Figure 2.3.5: (a) Quality factor for viscous damping originating from top and side of the cantilever and (b) scheme of streamlines acting on the cross-section sidewalls of the cantilever oscillating in its first mode of vibration with corresponding hydrodynamic functions.

The results of this component as a function of cantilever geometry are presented in figure 4.3.5. Due to the Sader fuction Ω_{sader} it is not straightforward to establish a general trend.

2.3.5.2. Viscous damping: left and right

The theoretical approach of Γ_{lr} can be found in [18] and takes the following form:

$$\Gamma_{lr}(\omega) = \frac{2\sqrt{2}h}{\pi b \sqrt{R_e}}(1+i) \tag{2.21}$$

As explained in [19] this expression doesn't take into account edges and thickness effects but remains a sufficient approximation in our configuration.

The results are presented in figure 2.3.6. We hypothesis that the main contribution comes from the Reynolds number that scale with the width of the cantilever. To support this hypothesis, we plot a Reynolds number as a function of cantilever geometry, which is illustrated in figure 2.3.6b.

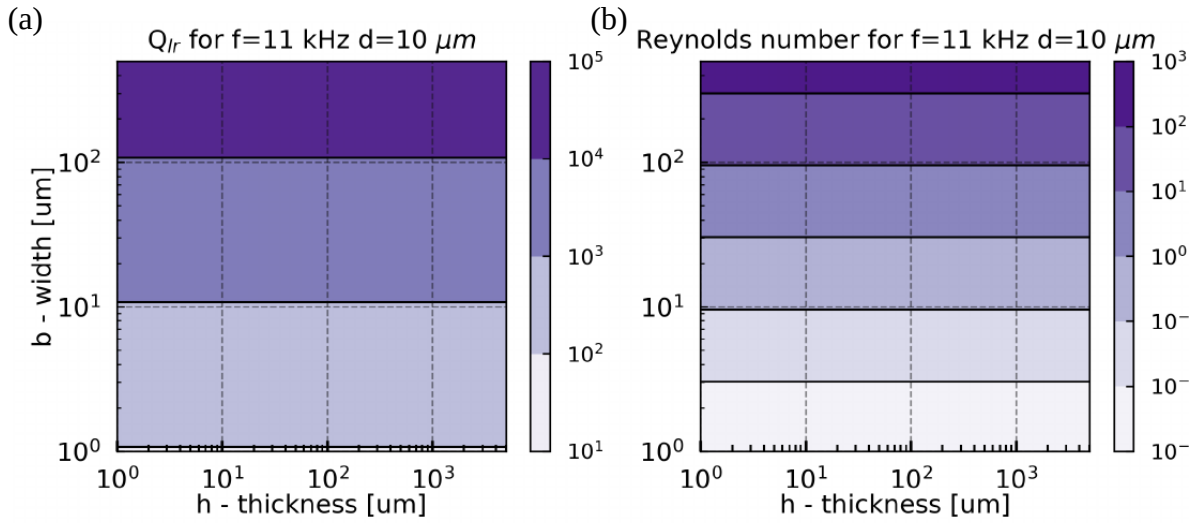

Figure 2.3.6: (a) Quality factor for viscous damping originating from left and right side of the cantilever and (b) Reynolds number as a function of width and thickness of a cantilever. Cantilever's fundamental resonance frequency: 11 kHz, gap between support and cantilever: d = 10 μm.

2.3.5.3. Viscous damping: squeeze film effect

The cantilever creates a parallel-plate capacitor, where one electrode is set in motion by the photoacoustic force and motion is detected by the capacitive changes. Due to the capacitive measurement, the distance between the electrodes is relatively low. Under those circumstances, the squeeze-film damping effect is significant. This phenomenon, presented in figure 2.3.7b, occurs due to the fluid beneath the plate moving rapidly and resisted by the fluid's viscosity. This results in the formation of a pressure distribution beneath the cantilever, which function in our case as a damping force. A mathematical description of squeeze film was given by Bao et al. [20]

$$\Gamma_{sq}(\omega) = -\frac{4P_a}{\pi d b \rho_f \omega^2}\left(f_e(\sigma) - i f_d(\sigma)\right) \tag{2.22}$$

where P_a, d are the surrounding pressure and air gap shown in figure 2.3.4, σ is a squeeze number [20] given by the following equation:

$$\sigma = \frac{12\mu_f \omega L^2}{P_a d^2} \tag{2.23}$$

and $f_e(\sigma)$ and $f_d(\sigma)$ are function introduced by Langlois[20] with the following from:

$$f_e(\sigma) = 1 - \sqrt{\frac{2}{\sigma}} \frac{\sinh\left(\sqrt{\frac{\sigma}{2}}\right) + \sin\left(\sqrt{\frac{\sigma}{2}}\right)}{\cosh\left(\sqrt{\frac{\sigma}{2}}\right) + \cosh\left(\sqrt{\frac{\sigma}{2}}\right)} \quad (2.24a)$$

$$f_d(\sigma) = \sqrt{\frac{2}{\sigma}} \frac{\sinh\left(\sqrt{\frac{\sigma}{2}}\right) - \sin\left(\sqrt{\frac{\sigma}{2}}\right)}{\cosh\left(\sqrt{\frac{\sigma}{2}}\right) - \cosh\left(\sqrt{\frac{\sigma}{2}}\right)} \quad (2.24b)$$

The quality factor originating from the squeeze film damping as a function of cantilever geometry are presented in figure 2.3.7a.

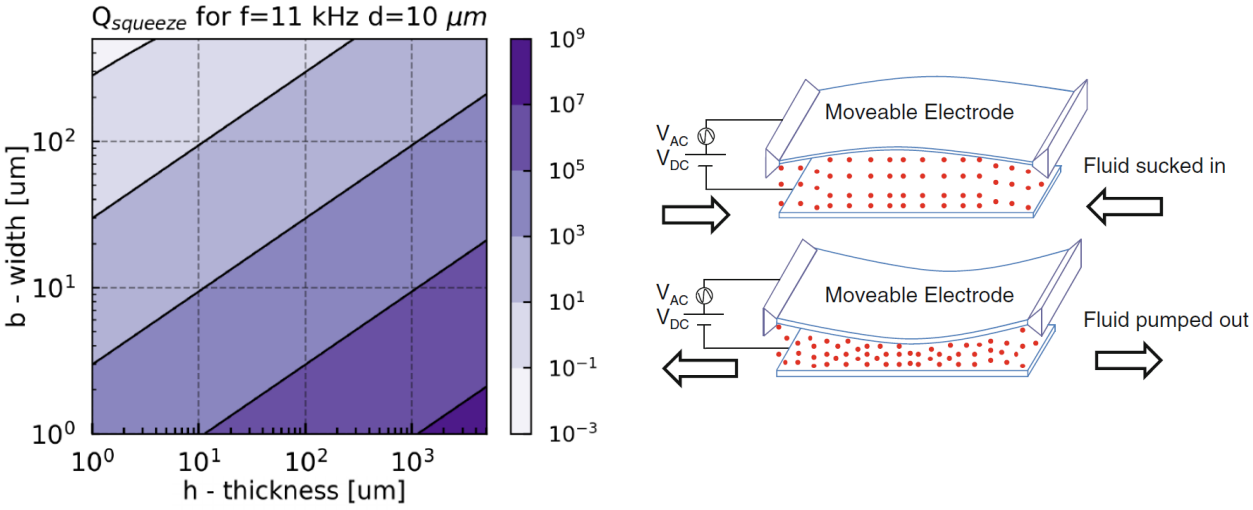

Figure 2.3.7: Schematic illustration of a squeeze film effect (right panel) [21]. Quality factor for squeeze film damping (left panel). Cantilever's fundamental resonance frequency: 11 kHz, gap between support and cantilever: d = 10 μm.

2.3.5.4. Viscous damping: summary

After calculating the quality factor originating from each sidewall of the cantilever, we calculate the quality factor of the viscous damping as a function of cantilever width and thickness. The results are presented in figure 2.3.8.

Indeed, the results show that viscous damping dominates the system. We have identified the areas which correspond to the main limiting mechanism.

For the low width of the cantilever, the limiting damping originates from the left and right side of the cantilever described by Γ_{lr}. Precisely, this damping originates from the low

value of the Reynolds number, which indicates that viscous forces are increasing in comparison to inertial forces.

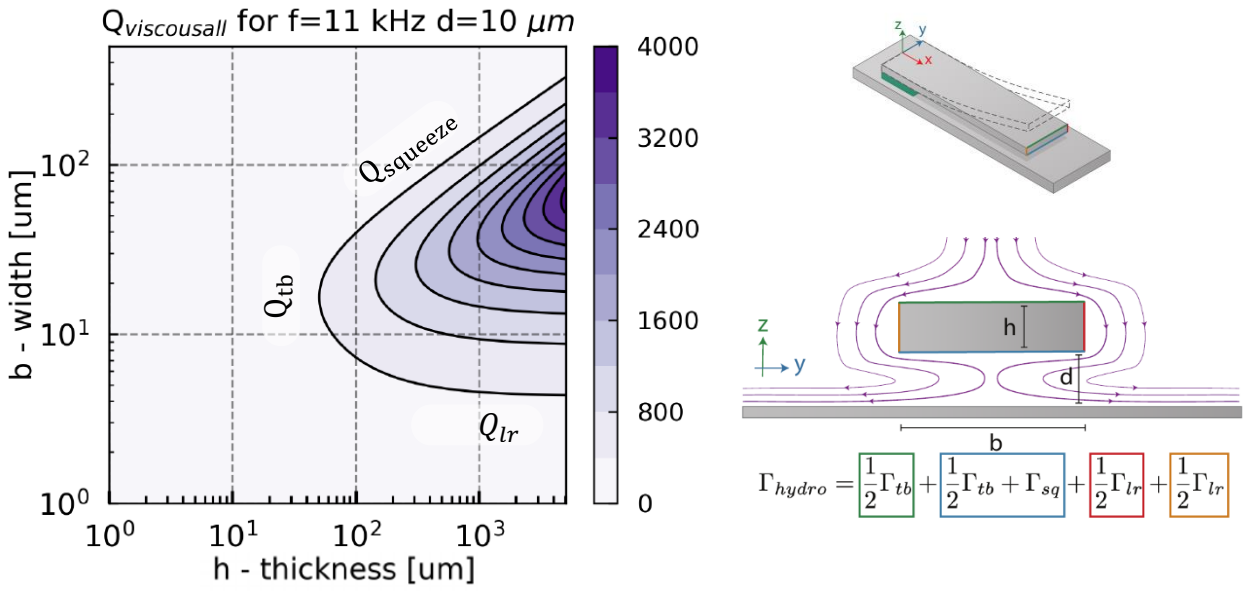

Figure 2.3.8: (a) Viscous quality factor as a function of width and thickness for a cantilever of fundamental resonance frequencies equal to 11 kHz and for a gap between support and cantilever equal to d = 10 µm. (b)

For small thicknesses, damping is strongly influenced by the correction function $\Omega_{sader}(\omega)$ that depends on the Reynolds number in a not straightforward manner [5].

For high thicknesses of the cantilever and small widths, the main contribution to viscous damping originates from the squeeze film effect.

2.3.6. Total quality factor

The next step constitutes combining all the damping mechanisms presented in previous subsections. Thanks to this procedure, we can evaluate if a general trend for quality factor optimization exists. The values of parameters used in this numerical simulation are presented in table 2.3.1. Simulations have been realized at 11 kHz where the acoustic force is maximal and at 60 kHz for comparison. The results are presented in figure 2.3.9.

Despite the lack of a general trend for the quality factor optimization in terms of all losses, it is possible to find the optimal value of the quality factor in terms of geometry for a given frequency. The maximum value is slightly larger at high frequencies, and the most significant effect is the shift of the optimum to the lowest thickness when the frequency increases. As will be detail below, this effect is due to the losses of the mechanical supports.

Table 2.3.1. Parameters used to describe the damping mechanism

parameter	description	value
ρ_b	mechanical resonator density	Si 2330 kg/m^3
ρ_f	fluid density	Air 1.177 kg/m^3
μ_f	fluid dynamic viscosity	Air 1.85 $\times 10^{-5}$ $kg/m/s$
d	air gap	m
P_a	pressure	101325 Pa
T	temperature	300 K
E	Young's modulus	$Si_{<100>}$ 130 GPa
ν	Poisson's ratio	$Si_{<100>}$ 0.28
α_T	thermal expansion coefficient	Si 2.6 $\times 10^{-6}$ $1/K$
C_p	specific heat at constant pressure	Si 700 $J/(kgK)$
K	thermal conductivity	Si 90 W/m/K

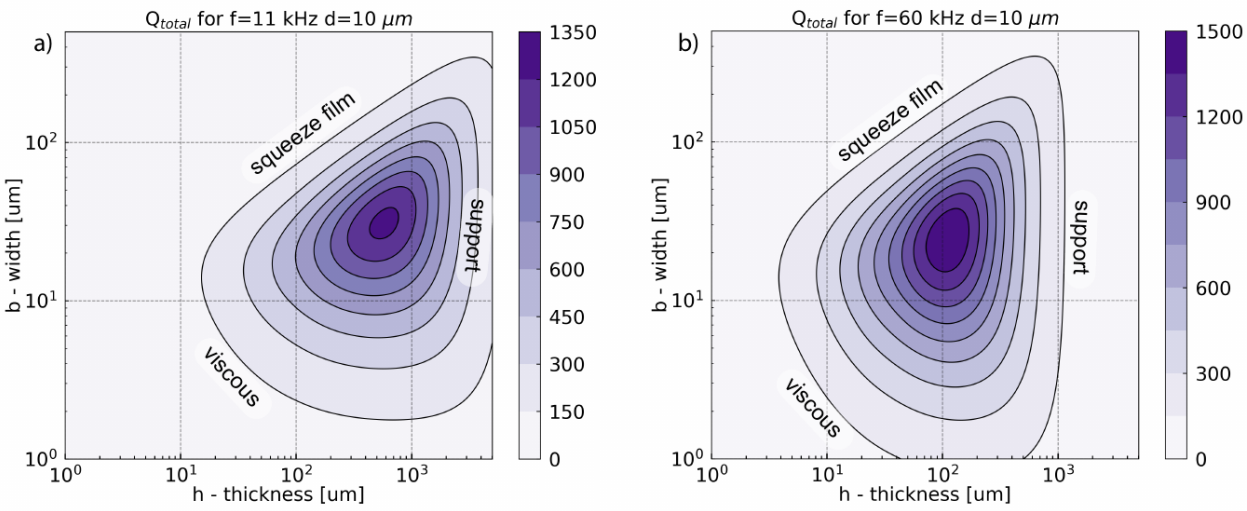

Figure 2.3.9: Total quality factor as a function of width and thickness for a cantilever of fundamental resonance frequencies equal to a) 11 kHz and b) 60 kHz, for a gap between support and cantilever equal to d=10 μm.

In figure 2.3.9, we identified the areas which correspond to the main limiting mechanism. As it was shown $Q_{support} \propto \frac{1}{\sqrt{\omega_n^3 h^3}}$, therefore the limitation for the quality factor with high thickness originates from the damping of the support. The term in $h^3$and ω_n^3 in this equation explains the shift of the optimum to the lowest thickness.

The effect of the squeeze film damping appears for the largest width when the gas is trapped under the cantilever. For the smallest width where the inertial forces are smaller than the viscous forces, the total quality factor is limited by the viscous damping. This area corresponds to the lowest value of the Reynold number.

In this model, neither thermoelastic nor acoustic damping are limiting factors. For all geometries and frequencies, the two associated quality factors are at least one order of magnitude higher than the other damping mechanisms.

2.4. Mechanical displacement

This section aims to describe how the cantilever is set in motion by the acoustic wave, taking into account its susceptibility. The displacement amplitude of the cantilever is described by $W(x,\omega)$ function presented in figure 2.1.1. Further terms describing the cantilever displacement refer to the fundamental vibration mode presented in figure 2.1.1.

2.4.1. Mathematical description

The deflection $W_n(x,\omega)$ at the position x of the n^{th} mode of the beam under a photoacoustic driving force $F_{PA}(\omega)$ is given by:

$$W_n(x,\omega) = \chi_n(\omega)F_{PA}(\omega)\phi_n(x) = w_n(\omega)\phi_n(x) \qquad (2.25).$$

where $\chi_n(\omega)$ is a mechanical susceptibility, $F_{PA}(\omega)$ is the photoacoustic driving force, $\phi_n(x)$ is a mode shape function normalized with $\max(\phi_m(x)) = 1$ and $w_n(\omega)$ is the maximal displacement. For the fundamental mode, $w_n(\omega)$ denotes the displacement amplitude at the extremity of the beam. The mechanical susceptibility $\chi_n(\omega)$ represents the frequency-dependent response of the cantilever under an external force and can be expressed as follow:

$$\chi_n(\omega) = \frac{1}{m_n(\omega_n^2 - \omega^2) + i\left(\frac{\omega_n \omega m_n}{Q_{total}}\right)} \qquad (2.26)$$

where Q_{total} is the total quality factor given in section 2.3, while m_n in an effective mass. The effective mass represents the part of the structure actually involved in the movement.

The structure is subjected to two opposite forces: the photoacoustic force F_{PA}: it is periodic and drives the cantilever into motion (section 2.2) resistance caused by the structure's damping described by Q_{total} (section 2.3)

The effective mass is described with the following equation:

$$m_n = \rho_b hb \int_0^L \phi_n^2(x)dx \qquad (2.27)$$

Effective mass is related to the resistance to changes of motion. Therefore, it decreases mechanical susceptibility and displacement.

2.4.2. Results and discussion

Figure 2.4.1 has been calculated with the mathematical expression of the previous section, equation (2.25). In this section, some approximations will be proposed to explain the shape of the graph.

The mechanical displacement $w_n(\omega_n)$ presented in figure 2.4.1 is the product between the photoacoustic force and the mechanical susceptibility χ_n. At the resonance frequency $2\pi\, f_n = \omega_n$, the susceptibility can be approximated as $\chi_n = \frac{Q}{m_n\, \omega_n^2}$, and the displacement as $w_n(\omega_n) = \frac{Q_{total} F_{PA}}{\omega_n^2 m_n}$.

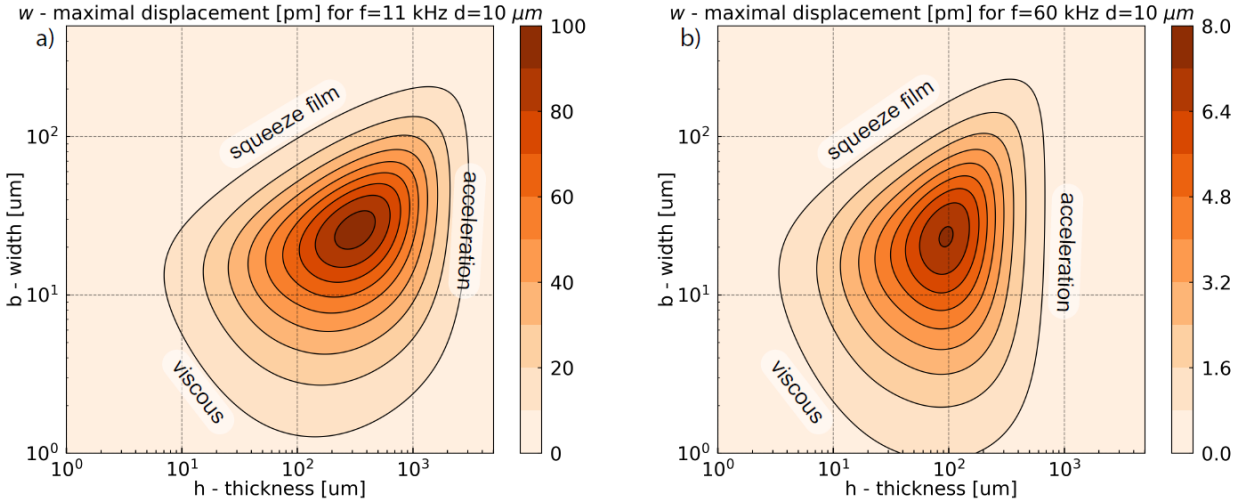

Figure 2.4.1: Total displacement versus width and thickness for a cantilever with fundamental resonance frequency equal to 11 kHz and 60 kHz for a gap between support and cantilever equal to d=10 µm.

For the fundamental mode of the cantilever, we can write the acoustic force as $F_{PA} \simeq 0.39 bL\Delta\, p(b,h)$, where $\Delta\, p(b,h)$ is the pressure difference between the top and the back of the cantilever. The function $\Delta\, p(b,h)$ increases with the thickness h and, in this approximation, remains relatively constant for various widths b. The effective mass of the cantilever's fundamental mode is $m_n \simeq 0.25\rho_b hbL$ (i.e., 25\% of the total mass). The displacement can then be approximated by :

$$w_n(\omega_n) = \frac{Q_{total}\, F_{PA}}{\omega_n^2 m_n} \simeq\ 1.56 \frac{Q_{total}}{\omega_n^2} \frac{\Delta p(b,h)}{\rho_b h} \qquad (2.28)$$

The simulations show that the fraction $\frac{\Delta p(b,h)}{\rho_b h}$ remains quite constant for different widths and is inversely proportional to the cantilever thickness $\frac{\Delta p(b,h)}{\rho_b h} \propto \frac{1}{h}$. Due to its

homogeneity, this term is called "acceleration" in figure 2.4.1. It reduces the maximal displacement when the thickness increases. This area corresponds to weak acoustic force or/and heavy effective mass. Counterintuitively, the simplified expression (2.28) shows that increasing the cantilever surface to collect more photoacoustic energy increases the effective mass, resulting in constant mechanical displacement. Indeed, a simplification by the surface bL appears between the term of the acoustic force and the effective mass.

The other limitations come from the viscous damping introduced by the Q_{total} term, and are similar to those shown in figure 2.3.9.

Figure 2.4.1 shows a large difference in displacement amplitude between a modulation frequency of 11 kHz and 60 kHz. Despite the improvement of the quality factor with increasing frequency, the acoustic force significantly drops at high frequency (figure 2.2.3) and the susceptibility, as it is inversely proportional to ω_n^2 . The results then show that photoacoustic force and susceptibility gain more importance with the change of frequency.

2.5. Voltage output

This section focuses on maximizing the output signal. The output signal represents the energy conversion from mechanical motion to an electrical signal. It gives the relation between the cantilever deflection $W(x,\omega)$, an electrical signal $V_{out}(\omega)$.

2.5.1. Mathematical description

The nominal capacitance $C_0 = Lb\varepsilon_0\varepsilon_r/d$ is the capacitance value without any displacement, where ε_r, ε_0 are the relative permittivity of the media (equal to unity in air) and vacuum, respectively. For the different geometries considered, C_0 may take values between 10^{-4} and $100\,pF$. The expression of nominal capacitance indicates that the change of the distance between two electrodes will cause a capacitance variation.

The dynamic capacitance caused by the deflection of the cantilever is being given by [22]:

$$C(t) = \int_0^L \frac{b\varepsilon_0\varepsilon_r}{d + W_n(x,n)}dx \tag{2.29}$$

The model applies a method called DC bias sensing (chapter 5 in [23]). Figure 2.5.1 presents the sensing scheme. In an electromechanical system, a polarization voltage V_{dc} on the electrodes is required to generate an electrical signal related to the mechanical behaviour of the moving electrode.

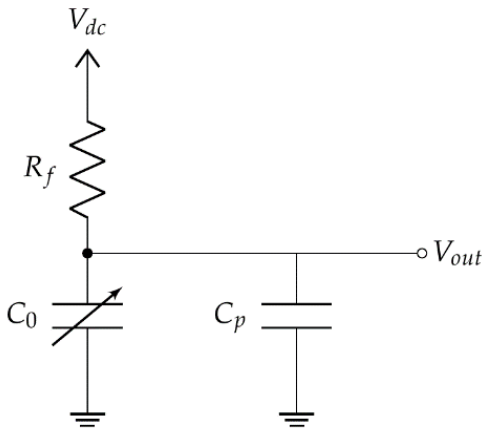

Figure 2.5.1: Sensor conditioning circuit, where : $C_0, C_p, R_f, V_{dc}, V_{out}$ are the capacitance of the cantilever, parasitic capacitance, resistance, polarization voltage and output voltage, respectively.

The application of the force generated by the photoacoustic effect sets the movable electrode in motion. This movement causes the changes of the capacitance from the maximal value C_{max} to the minimal C_{min}. C_{max} and C_{min} correspond to the minimal and maximal distances between the cantilever and support, respectively.

The capacitance variation can take place at a constant charge or voltage [2]. If the time constant $R_f C_0 \gg \frac{1}{\omega_n}$, the electric charge stored in the capacitor remains constant. $R_f \simeq 100\ G\Omega - 10\ T\Omega$ is the value of the resistor placed between the cantilever and the polarization voltage V_{dc}. At constant charge regime, the tension of the measured signal is given by $V_{out}(t) = \frac{C_O V_{dc}}{C(t)}$ while its amplitude is given by:

$$V_{out} = V_{dc} \int_0^L \frac{W_n(x,\omega)}{Ld}\, dx \tag{2.30}$$

2.5.2. Results and discussion

Figure 2.5.2 presents the results obtained for a bias $V_{dc} = 1\ V$. The maximum values follow the tendencies given by the displacement. The values change with the gap d and frequency f_n. Indeed, according to the equation (2.28) the equation (2.30) can be simplified as follows :

$$V_{out} \simeq 0.39 V_{dc} \frac{w_n(\omega)}{d} \tag{2.31}$$

Decreasing the gap d between the two electrodes should lead to an output signal amplitude increase. However, simultaneously it increases the squeeze film damping and reduces the cantilever displacement. The optimization of this parameter will be discussed in the last section.

Equation (2.31) indicates that the signal output does not depend on the area of the capacitor as it would be expected based on equation (2.29). The output signal amplitude is given for an open circuit, without any read-out circuit which can modify the signal. In a complete system, the signal is attenuated by a parasitic capacitor C_p. This parasitic capacitance is the sum of the parasitic capacitance of the resonator itself and the one which comes from the read-out circuit. The output signal attenuation can be estimated with the ratio $\frac{C_0}{C_0+C_p}$ [24] .

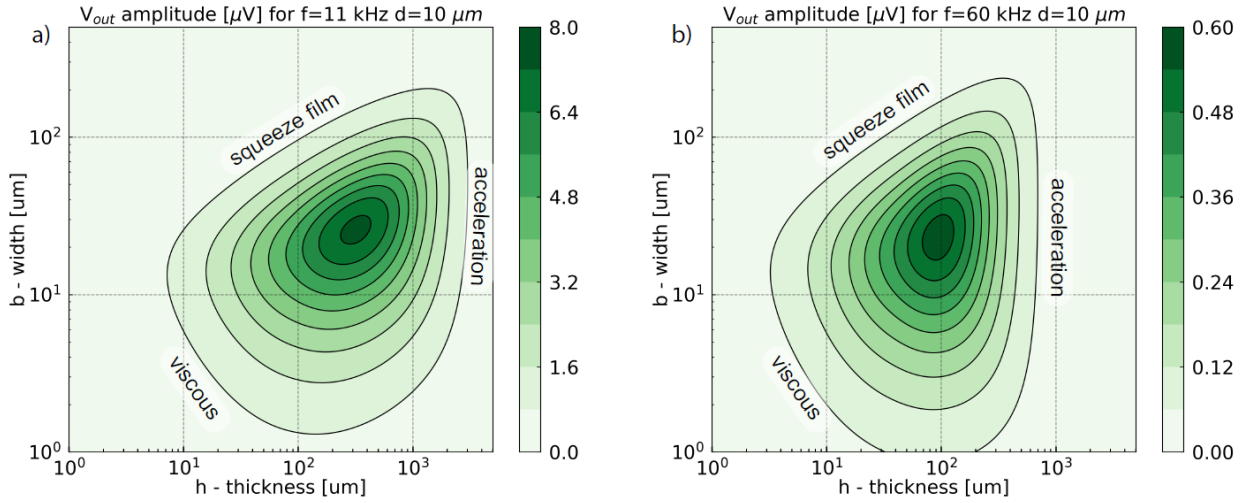

Figure 2.5.2: Amplitude of the output tension versus width and thickness for a cantilever of fundamental resonance frequency equal to 11 kHz and 60 kHz for a gap between the support and the cantilever equal to $d = 10\,\mu m$. The polarization voltage is $V_{dc} = 1\,V$.

2.6. Signal to noise ratio

This section aims to optimize a signal-to-noise ratio (SNR) as a function of cantilever geometry. In this calculation, we include solely thermal fluctuation noise.

2.6.1. Thermal noise

The sensor performance is limited by the unavoidable noise caused by the thermal fluctuations (Brownian movement), which set the resonator in motion. Therefore, it must be considered to construct a high-performance sensor. The maximum displacement of the

cantilever caused by the Brownian noise $w_{noise}(\omega_n)$ [25] is given by the fluctuation-dissipation theorem:

$$w_{noise}(\omega_n) = \sqrt{\frac{4k_bT\Delta fQ}{\omega_n^3 m_n}} = \sqrt{4k_bT\Delta f} \cdot \sqrt{\frac{w_n}{\omega_n F_{PA}}} \quad (2.32)$$

Where k_b, T and Δf are the Boltzmann constant, cantilever temperature and detection bandwidth, respectively. The thermal noise as a function of cantilever geometry is presented in figure 2.6.1.

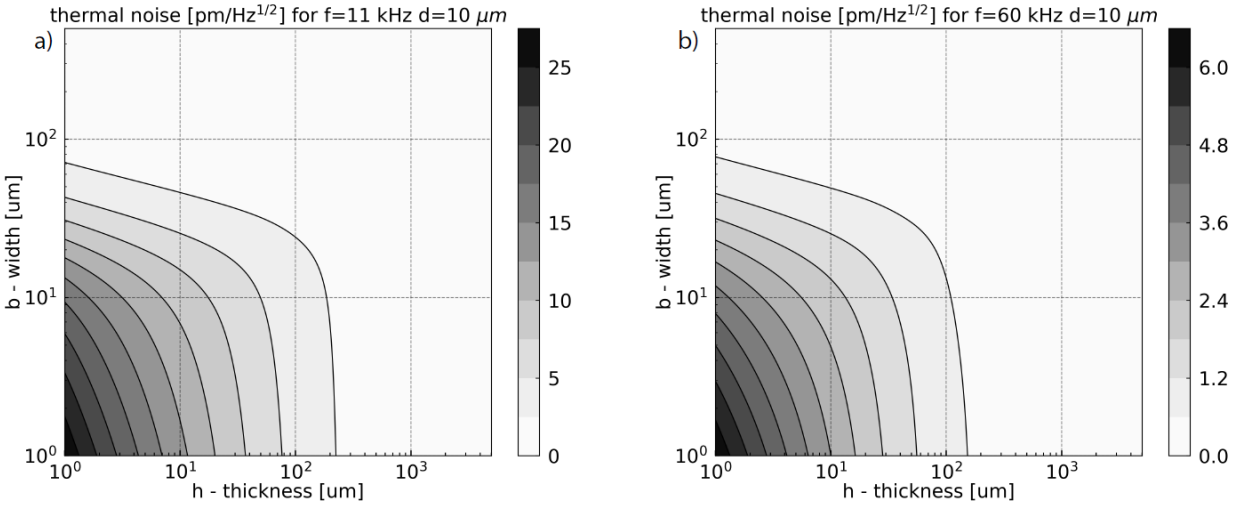

Figure 2.6.1. Thermal noise as a function of width and thickness of a cantilever. Cantilever's fundamental resonance frequency: 11 kHz and 60 kHz, gap between support and cantilever: d = 10 μm.

2.6.2. Signal to noise ratio: results and discussion

Here, the signal-to-noise ratio is defined as a fraction between cantilever displacement caused by the photoacoustic force $w_n(\omega_n)$ and Brownian noise $w_{noise}(\omega_n)$ at the resonance pulsation ω_n:

$$SNR = \frac{w_n(\omega_n)}{w_{noise}(\omega_n)} = \sqrt{\frac{w_n\omega_n F_{PA}}{4k_bT\Delta f}} \quad (2.33)$$

The optimum for the signal-to-noise ratio presented in figure 2.6.2 does not match with the highest output signal amplitude presented in figure 2.5.2. The highest output signal corresponds to the highest mechanical displacement w_n (equation (2.31)). The Brownian noise

can be considered as a force acting on the cantilever. The optimal way to improve SNR is the maximization of the photoacoustic force, which comes down to increasing the surface area for PA pressure collection. Therefore, the optimum signal-to-noise ratio is shifted to greater widths and thickness, where the acoustic force is greater (figure 2.2.4), and the collected energy increases. As in the previous section, the increase of the surface collecting the photoacoustic energy will be limited to the large widths by the squeeze film damping and by the acceleration term for the large thickness.

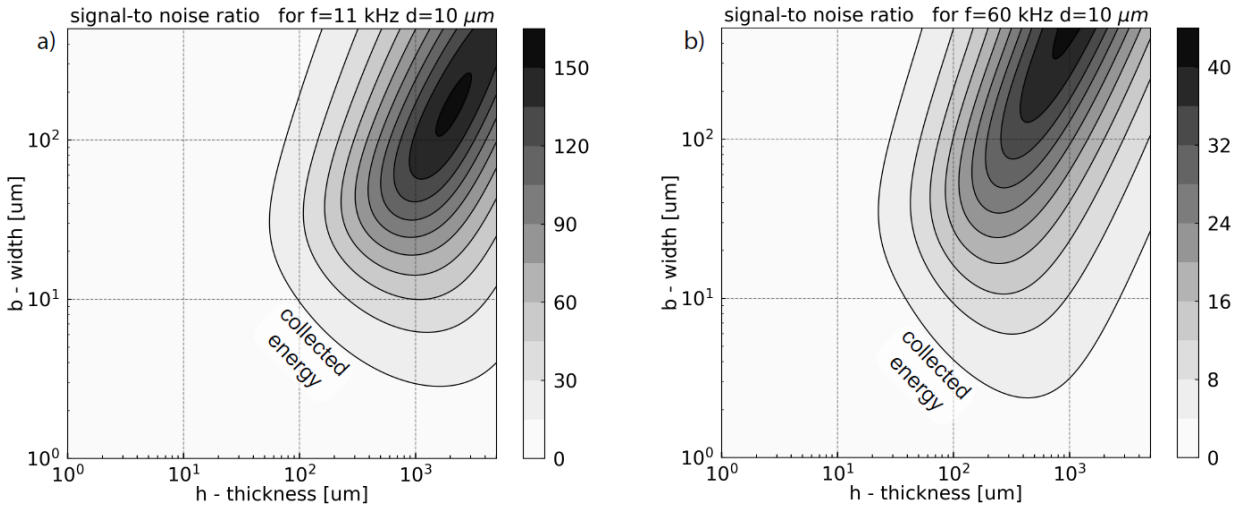

Figure 2.6.2: Signal-to noise ratio for a cantilever of fundamental resonance frequency equal to 11 kHz and 60 kHz, a gap between support and cantilever equal to $d = 10\,\mu m$.

The second significant parameter in the equation (2.33) is the pulsation ω_n. Unlike the previous result, ω_n reduces the difference between low and high frequencies. This is due to the fact that $SNR \propto \frac{1}{\sqrt{\omega}}$, while the amplitude of displacement $w_n(\omega_n) \propto \frac{1}{\omega^2}$.

2.7. Study of the gap effect

This section focuses on the effect of the distance between electrodes d (figure 2.1.1) on the general sensor performance for a constant resonance frequency of 11 kHz. The analytic solutions previously presented (eq. (2.23)) were implemented in a Python programming environment to estimate an optimal value of signal-to-noise ratio for each value of the gap d.

Subsequently, for each optimal SNR value, we get the geometrical parameters of the cantilever (width, length, thickness, figure 2.7.1a) and corresponding to them the output voltage (figure 2.7.1b). Red dot on the figure 2.7.1 illustrates how the maximal value was retrieved.

When d increases, the signal-to-noise ratio increases as the displacement increase due to the decrease of squeeze film damping. At the same time, the signal output voltage decreases due to the increase in the distance between electrodes. This improvement on the SNR can also be explained by the optimized width, which increases with the gap d and which allows collecting more energy. This increase in width is made possible by the decrease in the squeeze film damping for large gap d. Above $d \simeq 200\ \mu m$ the acoustic damping becomes dominant, and some saturation appears on the width curve. The variations on the thickness curve are less important than on the width. The length curve follows the thickness rise to satisfy the constant frequency condition. As for the curve of the width, we can identify using the curves for length and thickness two different regimes probably due to the transition where acoustic damping becomes more important than squeeze film damping.

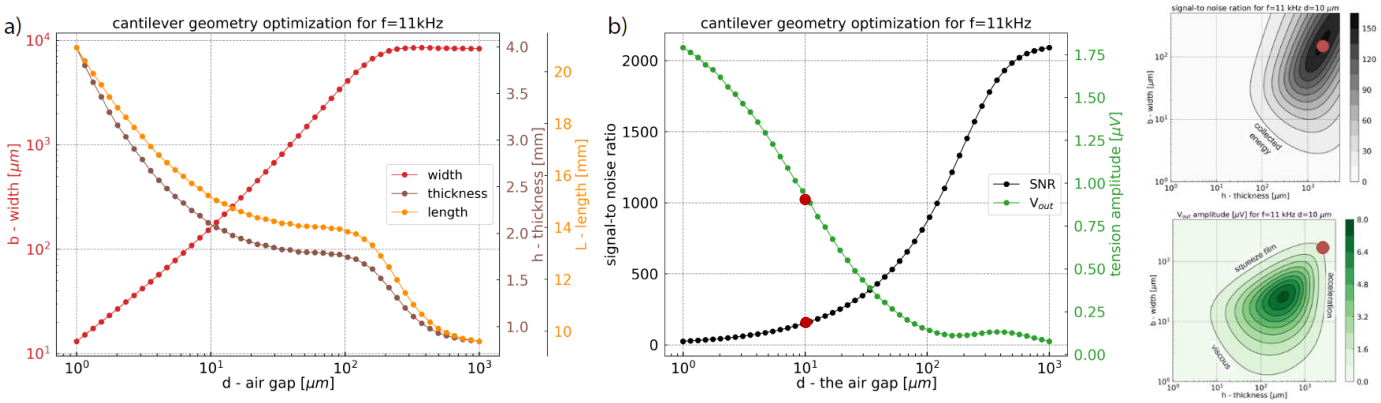

Figure 2.7.1: a) Geometrical values giving the highest signal-to-noise ratio as a function of the gap d between support and cantilever. b) Highest signal-to-noise ratio and its corresponding output amplitude signal as a function of the gap d between support and cantilever. For these simulations, the cantilever fundamental resonance frequency is equal to 11 kHz.

By taking into account the fabrication process issues, a cantilever with a gap d = 10 µm can be realized on a silicon-on-oxide (SOI) wafer. In this case, the signal-to-noise ratio will reach 150, and the amplitude of the output signal should reach 0.9 µV. Depending on the possibilities of the fabrication process, size of the final design and required performance of the device (SNR), figure 2.7.1 can be used as a reference to create a cantilever for optimal photoacoustic gas detection with capacitive transduction mechanisms.

All the calculations presented above can be calculated as well for a clamped-clamped cantilever.

2.8. COMSOL simulation

To study more sophisticated models, for which the analytical solution does not exist or is hard to find, we used COMSOL Multiphysics software based on finite element modelling.

This simulation was used to determine the resonators resonance frequency, mode of vibrations, energy distribution further used to calculate the quality factor for a complex structure (chapter 3), effective mass and displacement for each part of the resonator.

We used ***Solid Mechanics*** module with eigenfrequency study and model designed in 3D. Modes of vibration and frequency were obtained by performing an **eigenfrequency study**.

2.8.1. Effective mass

The total mass of the resonator is calculated using volume integration of density over the resonator geometry:

$$M_{tot} = \int_0^L \int_0^b \int_0^h \rho_{Si} dxdydz \tag{2.35}$$

where ρ_{Si} is a density.

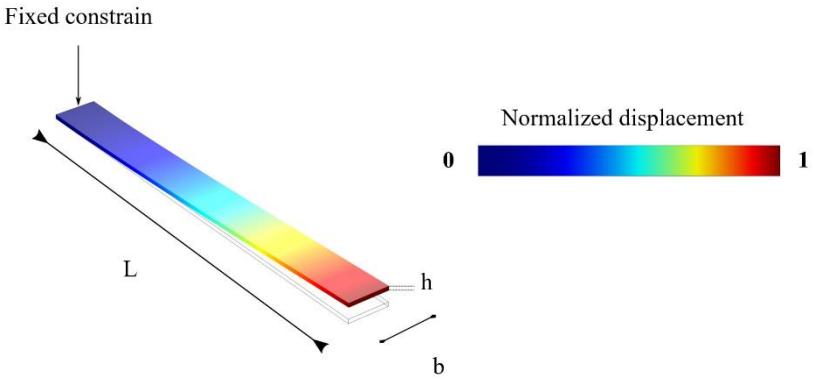

Figure 2.8.1: COMSOL simulation for 1st mode of vibration of a cantilever where the displacement is normalized to 1 (left panel).

To calculate an effective mass using COMSOL, volume integration of density is multiplied by the square power of total displacement over the whole resonator:

$$M_{eff} = \int_0^L \int_0^b \int_0^h (\rho_{Si} \cdot w^2(x,y,z))\, dxdydz \tag{2.36}$$

where w represents a total displacement of the resonator.

One has to notice that this method will be valid if the displacement is normalized in the following manner (figure 2.8.1):

$$\max\left(w(z,y,z)\right) = 1$$

where max is a function that returns the largest value from displacement of the resonator. The model is presented in figure 2.8.1.

2.8.2. Support quality factor

COMSOL simulation allows as well to calculate quality factor for support losses and thermoelastic. To calculate the support losses, we use the general definition of quality factor (equation (2.13)), which is defined as the ratio of the total energy to the losses of energy in a cycle of vibration. The part of dissipated energy in the support is given by $Q_{support}$. To calculate the value of the support quality factor, we used the following approximation:

$$Q_{support} = \frac{2\pi E_{tot}}{E_{dissipated}} \tag{2.37}$$

where E_{tot} is total strain energy of the resonator, while $E_{dissipated}$ the energy dissipated in the support. However, in equation (2.37) we assume that all the energy accumulated in support is lost.

The model is schematically presented in figure 2.8.2.

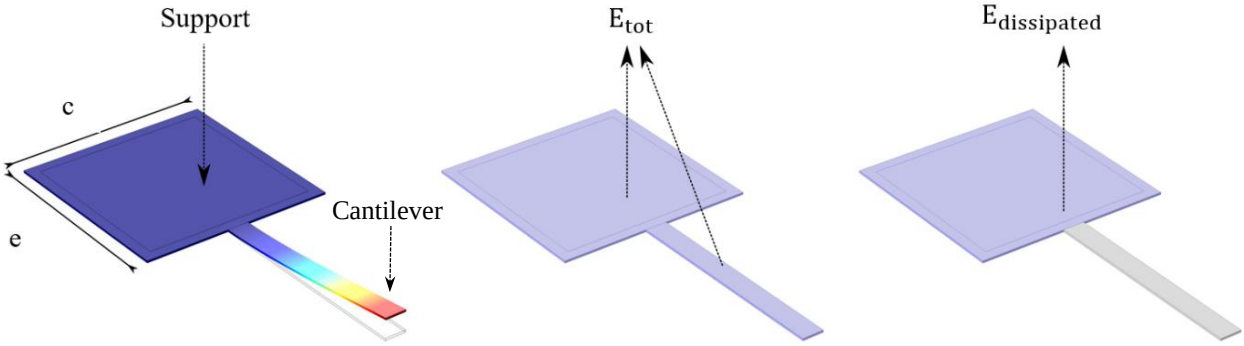

Figure 2.8.2: Schematic illustration of COMSOL model for support quality factor calculation. The middle panel presents the total energy (resonator + support) calculation, while the right panel presents the calculation of dissipated energy into the support.

To calculate E_{tot} [J] we make a volume integration of total strain energy density e_{strain} [J/m^3] (**solid.Ws**) over the whole resonator while $E_{dissipated}$ is elastic energy density total strain energy density integrated over the support:

$$E_{tot} = \int_0^L \int_0^b \int_0^h e_{strain}\, dxdydz + \int_0^e \int_0^c \int_0^h e_{strain}\, dxdydz \qquad (2.38a)$$

$$E_{dissipated} = \int_0^e \int_0^c \int_0^h e_{strain}\, dxdydz \qquad (2.38b)$$

2.8.3. Thermoelastic damping

The COMSOL software incorporates a thermoelastic module, which allows evaluating the thermoelastic quality factor of any geometry. The visualization of thermoelastic damping with COMSOL is presented in figure 2.8.3. To perform the study we chose **Structural Mechanics** and **Thermoelasticity.** Thermoelasticity combines a **Solid Mechanics** interface with a **Heat Transfer in Solids** interface. In the study tree we chose **Thermal Perturbation, Eigenfrequency** study (COMSOL Multiphysics 5.4).

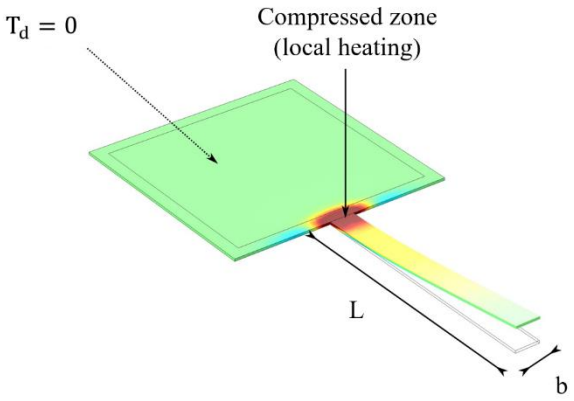

Figure 2.8.3: Modeling of the thermo-elastic effect on COMSOL for a flexural cantilever. During deformation, in the compressed areas the temperature increases, while in the strained regions the temperature drops.

To avoid calculation errors, it is crucial to indicate that the fixed areas, such as the support, have a deviation temperature Td of zero. This condition ensures that the generated gradient temperature comes from displacements of the moving part.

However, as it has been presented in the analytic model, thermal dissipation is not a dominant damping mechanism.

2.9. Conclusions

In this chapter, we presented an analytic model which provides a method to retrieve the optimized cantilever geometry depending on the required size of the sensor and other restrictions which might be imposed by the fabrication process or the sensor conditioning.

The presented analytic model combines multiple physical phenomena, and therefore its optimization is not straightforward. We discussed multiple parameters which affected the sensor performances and analyzed their contributions.

Our model takes into account some optimization for:

a) the acoustic force;
b) the system damping;
c) the mechanical displacement under photoacoustic force considering damping mechanism;
d) the electrical signal under capacitive transduction mechanism;
e) the signal-to-noise ratio.

The model includes the gas relaxation time. We proposed a cantilever geometry optimized for a photoacoustic gas sensor with a capacitive transduction mechanism in the context of CH_4 absorption. However, it can be recalculated for any other gas, knowing the thermal relaxation time of the molecules. The optimal sensor should be created for one specific gas.

The study of the different damping mechanisms shows that viscous damping, and particularly the squeeze film effect, is fundamental. The impact of the squeeze film effect is visible in figure 2.7.1 for d values up to 200 µm. For d above this value, the acoustic damping becomes the limiting damping mechanism.

To improve the SNR, one can increase the gap d and/or the surface collecting the photoacoustic energy. However, increasing the gap d between the two electrodes will decrease the output signal amplitude. Depending on the read-out circuit and the parasitic capacitance, it is possible to obtain a high SNR while maintaining a sufficient output signal. For example, with a gap of $d = 10\ \mu m$ which can be realized on a silicon-on-oxide (SOI) wafer, the signal-to-noise ratio will reach 150, and the amplitude of the output signal will be around $0.9\ \mu V$. For different values of the gap, one can use figure 2.7.1.

While the analytic model can be used for a simple cantilever, it is not sufficient for a complex structure. As it will be presented in the following chapters, COMSOL software is irreplaceable for complex structure calculations. It is a powerful and user-friendly software that we use to evaluate frequency, mass effective, support quality factor and thermoelastic damping for a complex structures. Finally, it also allows to perform quick parametric study for structure optimization.

Bibliography

[1] W. Trzpil, N. Maurin, R. Rousseau, D. Ayache, A. Vicet, and M. Bahriz, "Analytic optimization of cantilevers for photoacoustic gas sensor with capacitive transduction," *Sensors*, vol. 21, no. 4, pp. 1–22, 2021, doi: 10.3390/s21041489.

[2] S. Meninger, J. O. Mur-Miranda, R. Amirtharajah, A. Chandrakasan, and J. H. Lang, "Vibration-to-electric energy conversion," *IEEE Transactions on Very Large Scale Integration (VLSI) Systems*, vol. 9, no. 1, pp. 64–76, 2001.

[3] S. Schilt, L. Thévenaz, and P. Robert, "Wavelength Modulation Spectroscopy: Combined Frequency and Intensity Laser Modulation," *Applied Optics*, vol. 42, no. 33, p. 6728, 2003, doi: 10.1364/ao.42.006728.

[4] N. Petra, J. Zweck, A. A. Kosterev, S. E. Minkoff, and D. Thomazy, "Theoretical analysis of a quartz-enhanced photoacoustic spectroscopy sensor," *Applied Physics B*, vol. 94, no. 4, pp. 673–680, Mar. 2009, doi: 10.1007/s00340-009-3379-1.

[5] H. Yabuno and A. H. Nayfeh, *Nonlinear normal modes of a parametrically excited cantilever beam*. Springer, 2001.

[6] S. Schilt, J.-P. Besson, and L. Thévenaz, "Near-infrared laser photoacoustic detection of methane: the impact of molecular relaxation," *Applied Physics B*, vol. 82, no. 2, pp. 319–328, 2006.

[7] M. A. Hopcroft, W. D. Nix, and T. W. Kenny, "What is the Young ' s Modulus of Silicon ?," vol. 19, no. 2, pp. 229–238, 2010.

[8] R. Lifshitz and M. Roukes, "Thermoelastic damping in micro- and nanomechanical systems," *Physical Review B - Condensed Matter and Materials Physics*, vol. 61, no. 8, pp. 5600–5609, 2000, doi: 10.1103/PhysRevB.61.5600.

[9] F. Lochon, I. Dufour, and D. Rebière, "A microcantilever chemical sensors optimization by taking into account losses," *Sensors and Actuators, B: Chemical*, vol. 118, no. 1–2, pp. 292–296, 2006, doi: 10.1016/j.snb.2006.04.034.

[10] B. le Foulgoc *et al.*, "Highly decoupled single-crystal silicon resonators: An approach for the intrinsic quality factor," *Journal of Micromechanics and Microengineering*, vol. 16, no. 6, 2006, doi: 10.1088/0960-1317/16/6/S08.

[11] W. K. Blake, "The radiation from free-free beams in air and in water," *Journal of Sound and Vibration*, vol. 33, no. 4, pp. 427–450, 1974, doi: 10.1016/S0022-460X(74)80227-0.

[12] R. A. Johnston and A. D. S. Barr, "Acoustic and Internal Damping in Uniform Beams," *Journal of Mechanical Engineering Science*, vol. 11, no. 2, pp. 117–127, Apr. 1969, doi: 10.1243/JMES_JOUR_1969_011_015_02.

[13] P. M. Morse and H. Feshbach, "Methods of theoretical physics," *American Journal of Physics*, vol. 22, no. 6, pp. 410–413, 1954.

[14] Z. Hao, A. Erbil, and F. Ayazi, "An analytical model for support loss in micromachined beam resonators with in-plane flexural vibrations," vol. 109, pp. 156–164, 2003, doi: 10.1016/j.sna.2003.09.037.

[15] G. Aoust, R. Levy, B. Bourgeteau, and O. le Traon, “Sensors and Actuators A : Physical Viscous damping on flexural mechanical resonators,” *Sensors & Actuators: A. Physical*, vol. 230, pp. 126–135, 2015, doi: 10.1016/j.sna.2015.04.004.

[16] R. Cox, “Theoretical Analysis of Laterally Vibrating Microcantilever Sensors in a Viscous Liquid Medium,” 2011.

[17] J. E. Sader, “Frequency response of cantilever beams immersed in viscous fluids with applications to the atomic force microscope,” *Journal of applied physics*, vol. 84, no. 1, pp. 64–76, 1998.

[18] G. Aoust, R. Levy, B. Bourgeteau, and O. le Traon, “Viscous damping on flexural mechanical resonators,” *Sensors and Actuators A: Physical*, vol. 230, pp. 126–135, 2015.

[19] R. Cox, F. Josse, S. M. Heinrich, O. Brand, and I. Dufour, “Characteristics of laterally vibrating resonant microcantilevers in viscous liquid media,” *Journal of Applied Physics*, vol. 111, no. 1, p. 14907, Jan. 2012, doi: 10.1063/1.3674278.

[20] M. Bao and H. Yang, “Squeeze film air damping in MEMS,” *Sensors and Actuators, A: Physical*, vol. 136, no. 1, pp. 3–27, 2007, doi: 10.1016/j.sna.2007.01.008.

[21] M. I. Younis, *MEMS Linear and Nonlinear Statics and Dynamics*, vol. 53, no. 9. Elsevier, 2013.

[22] D. J. Ijntema and H. A. C. Tilmans, “Static and dynamic aspects of an air-gap capacitor,” *Sensors and Actuators A: Physical*, vol. 35, no. 2, pp. 121–128, 1992.

[23] M. Bao, *Analysis and design principles of MEMS devices*. Elsevier, 2005.

[24] P. R. Scheeper, A. G. H. der Donk, W. Olthuis, and P. Bergveld, “A review of silicon microphones,” *Sensors and actuators A: Physical*, vol. 44, no. 1, pp. 1–11, 1994.

[25] B. D. Adamson, J. E. Sader, E. J. Bieske, B. D. Adamson, J. E. Sader, and E. J. Bieske, “Photoacoustic detection of gases using microcantilevers Photoacoustic detection of gases using microcantilevers,” vol. 114510, no. 2009, pp. 1–5, 2014, doi: 10.1063/1.3271157.

Chapter 3

3. Fabrication

This chapter presents the fabrication techniques, the development of the fabrication process, the problems which we have encountered during this development, and how to fix them. Each section aims to explain the parameters that have an impact on successful MEMS fabrication.

3.1. Photolithography mask

We used the top-down approach for microresonator fabrication. In this approach, the material is removed to create devices with a desired shape and size. In the case of our fabrication process, the shape of the resonator is defined by photolithography and, more precisely, by the photomask. The photomask needs to be designed in a way that allows exposure of the UV light on the photoresist only on the desired part of the sample.

To create a mask, we used the gdspy Python library, a free and open-source library. This library allows generating GDSII stream files, which are frequently used in the microfabrication industry.

The advantage of this technique is the Python programming language itself, a robust and reliable tool for mask design. Once the pattern is programmed, the results are exported into the .gds file.

3.2. General description

As introduced in chapter 2, section 2.1, the resonators are fabricated in SOI wafer. Both sides of the wafer are covered with a low-stress mask ($\sigma \sim 0$) of SiN_x [1] deposited with low-pressure chemical vapor deposition (LPCVD) techniques in the Laboratory for Analysis and Architecture of Systems in Toulouse (LAAS).

Steps for sample fabrication presented in figure 3.2.1 are detailed in the following sections. They consist of:

Step 1: Sample preparation such as cleaning and dehydration. Cleaning removes organic and inorganic impurities. It can be done using wet or dry chemical treatment. In most cases, we use both of these treatments.
Step 2: Photolithography on the backside - handle layer of SOI wafer.
Step 3: Mask opening using a reactive ion etching (RIE).
Step 4: Silicon wet chemical etching using KOH on sample's backside (handle layer of SOI wafer).
Step 5: Creating a pattern of the resonator by photolithography process on the device layer.
Step 6: Mask opening using RIE
Step 7: For X-resonator wet silicon etching using KOH solution on the device layer; in case of H-resonator silicon deep reactive ion etching.
Step 8: Etching the buried oxide layer to release the resonator and create a free-standing structure using hydrofluoric acid. Depending on the geometry of the resonator and properties of the SOI wafer, we applied wet or vapor etching technic.
Steps from 2nd to 4th define the shape of sample backetch. Steps from 5th to 7th define the shape of the resonator.

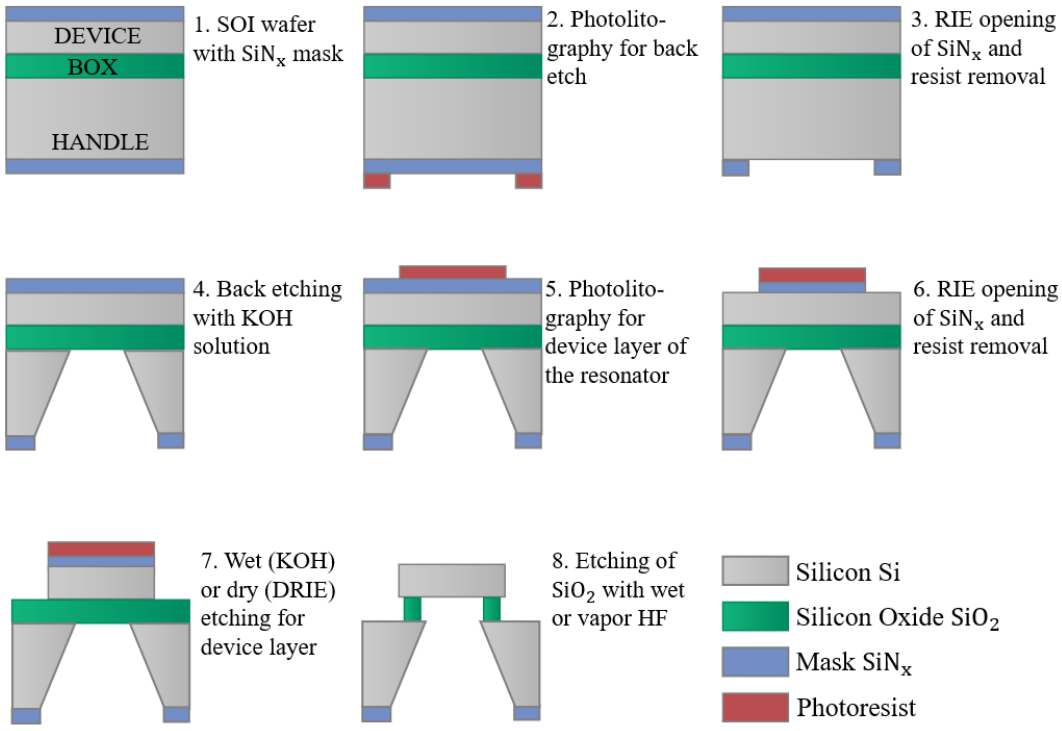

Figure 3.2.1: Steps for the sample fabrication.

3.3. Sample preparation

Sample preparation might consist of several steps like dehydration, cleaning, or surface activation. Cleaning removes both organic and inorganic contamination present on the sample surface. The cleaning techniques can be divided into two categories: a) wet chemical treatment using solvents or acids; b) dry cleaning, for instance, plasma. This step may affect the

lithography process and, consequently, the final design. Initial sample preparation aims to remove mechanically sizable contamination using a nitrogen gun or a steady flow of distilled water.

3.3.1. Cleaning procedure using a wet chemical treatment

The standard wet silicon cleaning is using solvents in the following order:

- 2 min acetone – acetone removes organic impurities
- 2 min ethanol – helps to remove contaminated acetone
- 2 min isopropyl alcohol – helps to remove contaminated acetone
- 1 min of rinsing the sample in a steady flow of distilled water – removes isopropyl alcohol

However, this procedure is often insufficient, particularly for more severe organic origin contamination. For this kind of contamination, one might use the "piranha" solution. "Piranha" solution is known as an excellent removal for all organics residue. The comparison between standard solvent-based cleaning and piranha cleaning is presented in figure 3.3.1. Piranha solution can be used for any silicon sample despite the possibility of developing an oxide layer. The oxide layer created during Piranha cleaning can be removed using a hydrofluoric acid (HF) solution.

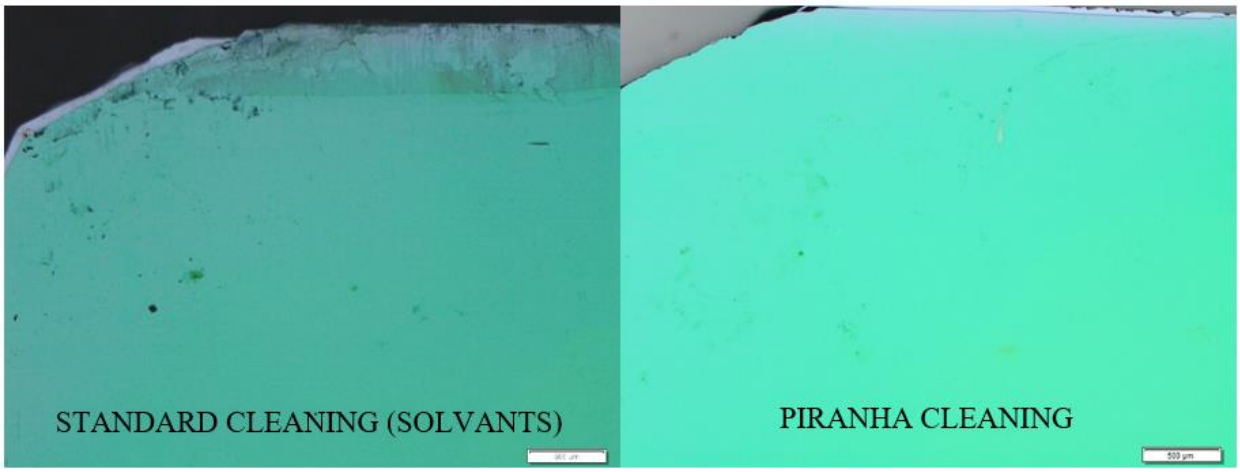

Figure 3.3.1: Comparison of the sample preparation using standard silicon (left panel) and the cleaning procedure with piranha solution (right panel).

The piranha solution used in the presented study consists of 3:1 mixture of sulfuric acid and 30% hydrogen peroxide solution. The preparation of piranha solution is an exothermic process, and the cleaning procedure is the most efficient at high temperatures. Accordingly, the cleaning should be performed as soon as the solution is prepared. The cleaning should last approximately 2 minutes; however, it depends on sample contamination. In the case of our study, a sample can be submerged in the solution for 10 min without damage. Subsequently, samples are washed under running distilled water for around 1 min and dried with compressed nitrogen.

3.3.2. Cleaning procedure using dry cleaning – plasma

Plasma cleaning using argon or oxygen is another way of surface preparation. Plasma oxygen cleans the surface by chemical reaction. It removes organic impurities by breaking bonds of surface contamination (C=C, C-H, C-C, etc.) and by reaction between species created in plasma, like O_2^+, O_2^-, O_3 and organic contamination. This process creates CO_2, CO, H_2O.

Argon plasma cleans the sample through physical ablation and is not selective.

Besides cleaning, plasma activates the sample's surface by creating free bonds on the surface, which consequently promotes resist adhesion (free bonds will bind with oher molecules, here resist, willingly attach to other molecules). This step is usually performed after wet cleaning, before the photolithography process, and after photolithography to remove the residual resist. The complete process of sample preparation is presented in table 3.3.1.

3.4. Photolithography

Photolithography constitutes steps 2 and 5 of the sample fabrication presented in figure 3.2.1. This process creates a geometrical pattern using UV light and photo-sensitive substances (photoresist, as illustrated in the schematic in figure 3.4.1. Through reaction with UV light, photoresist exposed to the UV light remains on the sample (negative resist, figure 3.4.1 e1) or is removed (positive resist, figure 3.4.1 e2) through the use of developer. The steps of photolithography are presented in figure 3.4.1.

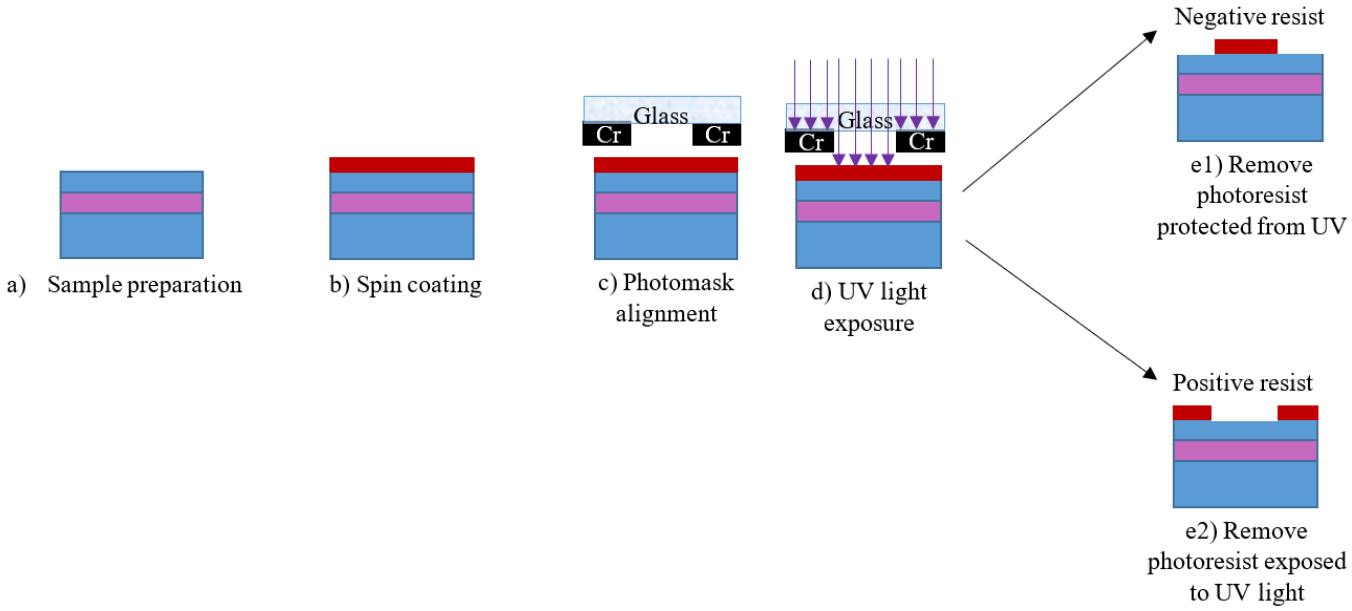

Figure 3.4.1: Simplified illustration for photolithography steps process.

Table 3.4.1: A summary for a photolithography process

step	condition	reason
choice of resist	AZ5214(+/-) AZ1518	Choice of resist type needs to be motivated by the pattern on the photomask and application. For instance, a negative resist is preferable for vertical walls and lift-off.
Sample preparation	Piranha cleaning (optional)	Removes organic impurities
	HF cleaning (optional)	Removes silicon oxide, improves adhesion of the photoresist. Photoresist is characterized by poor adhesion to silica.
	Plasma oxygen	Plasma O2 activates the surface, Ar2 increases the porosity of the surface
	Pre-heating at 145°C for several minutes (5min)	Water desorption. Heating above 150°C decomposes –OH bonding from native silicon oxide, SiO2 and metals.
Spin coating – resist deposition	30 s @ 40000 str	Determine the thickness of the photoresist. Slower speed will result in thicker resist layer.
Soft-baking	1 min @ 115°C	Too short baking/ too low temperature might be insufficient to remove sufficiently the solvent and consequently inferior the resist adhesion. Too high concentration of the solvent might causes N2 bubbles appear during the exposition.
waiting time	1 min/1μm of resist (for thicker resists eg. 30 μm the scale is not linear)	Waiting time between soft baking and exposure for proper water diffusion. Positive resist requires a sufficient water concentration in order provide reasonable development time.
Removing the resist from the sample's edges	60-120 s flood exposure with a sample slightly smaller	Additional step to remove resist on samples edges and corners. Resist on the edges and corners are usually thicker which might create a gap between the sample and mask. This phenomenon increase light diffraction. This step might be important while performing lithography with pattern smaller than 10um
Contact mode	vacuum	Decreasing the distance between the mask and the sample reduces light diffraction on the edges.
Exposition	MJB4: 23 s (6.4 mW/cm^2), EVG: 10 s (15 mW/cm^2)	The exposure time depends on the resist, power density and spectrum of the lamp. In case of positive resist, not sufficient time will cause a low development rate (or incomplete development).
Development	40 s	Should be fixed and exposition time should be adjusted
Water rinsing	~ 1 min	Remove the residual developer.
Plasma O_2	1 min	Removes the residual resist which remains after developer

A successful photolithography process depends on steps summarized in table 3.4.1. If the action affects resist adhesion it is indicated with blue color; if the step has an impact on verticality of the resist walls it is indicated with red color; if step affects both resist adhesion and resist walls verticality, it is marked with a violet color.

3.5. Reactive ion etching

The next step of sample fabrication after photolithography is opening a SiN_x mask with a reactive ion etching. Reactive ion etching is a microfabrication process based on selective removal of materials using chemically reactive plasma (dry etching technique). In this case, the photoresist works like a mask that protects the material from etching. Subsequently, the resist can be removed using a different mixture of gas. The type of etching and selectivity between etching depends on the following parameters :

- pressure
- gas selection
- flow rate
- radio frequency (RF) power
- low frequency (LF) power

All factors listed above play an essential role in the anisotropy of the process. For instance, reduction of the pressure leads to slowing down the process and making it more directional. Secondly, a gas mixture will cause a specific reaction between the etched material and plasma. Two species are presented in the reactive ion etching: radical species and ionic species. The difference between these species with an explanation based on water molecule is illustrated in figure 3.5.1.

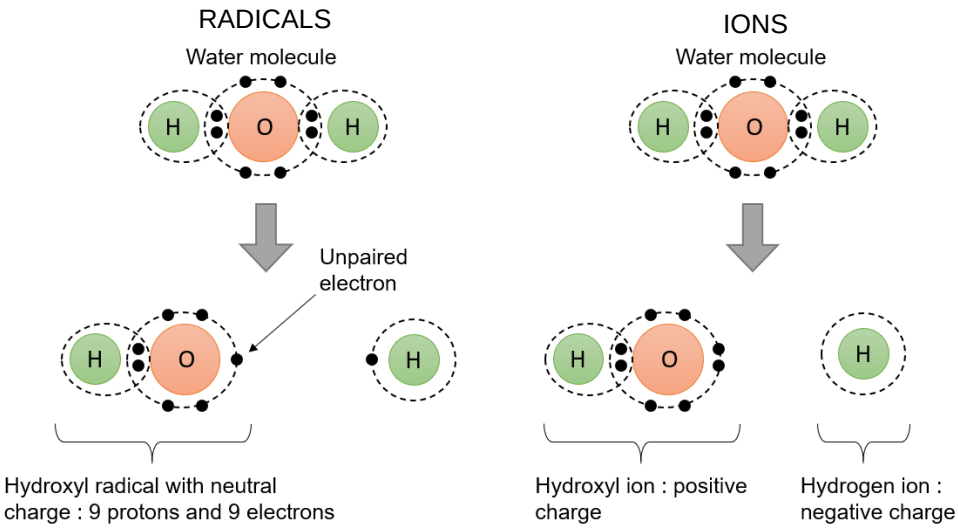

Figure 3.5.1: Scheme representing water molecule forming hydroxyl radical (left panel) and hydroxyl ion (right panel).

Radicals are atoms or molecules with at least one unsatisfied chemical bonding. The etchant gasses are excited by low-frequency LF and radio frequencies RF. LF power is responsible for creating free radicals. Uncharged free radicals are responsible for the isotropic process (reactive etching).

RF excites ions and radicals. It results in a more anisotropic process due to the energetic ion bombardment (ion etching). The scheme for material etching with radical and ionic species is presented in figure 3.5.2. One needs to remember that these are just general rules. All listed parameters are dependent on each other, and the process itself is much more sophisticated. This is discussed below, based on the used recipe.

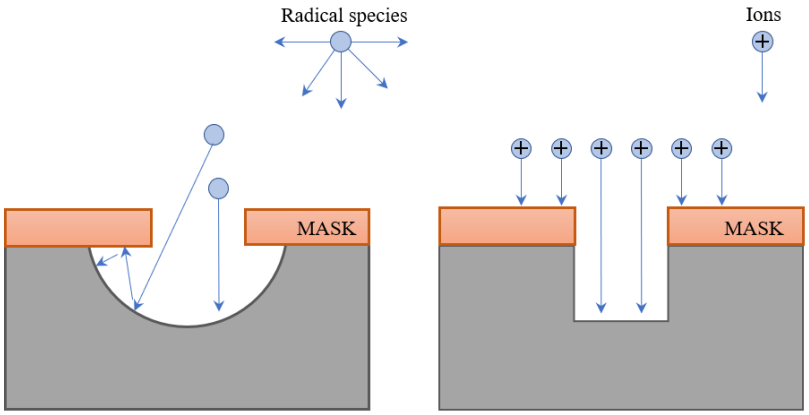

Figure 3.5.2. Scheme representing material etch with radical species (left panel) and ion species (right panel).

Table 3.5.1.Parameters used in RIE for specific etching layer.

etching layer	gas type	Gas flow (sccm*)	LF power (Watt)	RF power (Watt)	Working pressure (mTorr)	Etching rate	Explanation
SiN	O2/ 100sccm	35	400	40	13	120nm/min	Low RF power and low flow of oxygen gives excellent selectivity between etching of SiN and resist
	CHF3/ 200sccm	100					
Resist	O2/ 100sccm	90	600	0	15	300nm/min	The use of high power oxygen plasma efficiently removes the resist

*sccm – standard cubic centimeter per minute (cm^3/min) ; unit of flow measurement given in standard conditions.

In the recipe for etching SiN layer (table 3.5.1) we use two gasses: O_2 and CHF_3 (fluoroform). Fluoroform is an etchant for SiN. The reaction between the etching material and CHF_3 creates, among the others, fluorocarbon particles. Oxygen flow is used to avoid surface contamination with fluorocarbon particles. However, the oxygen flow rate needs to be carefully adjusted as it influences the etching selectivity between photoresist and etching material. Other parameters which influence the etching selectivity are LF and RF power. In the recipe for SiN etch, we used low RF power ($RF \leq 0$). This treatment was aimed to increase the selectivity between the SiN_x layer, Si and SiO_2.

3.6. Wet etching

To define the back hole of the resonator and device layer in some of the resonator's designs, we use a wet etching technique. Wet etching is a process of removing material using liquid phase etchants. To obtain a certain design, the mask with the desired pattern needs to be deposited on the material's surface (wafer). This deposition is usually achieved through photolithography. Etching occurs on the material which is not protected by the mask. In the presented work, we focus on silicon etching.

Wet etching can be divided into isotropic and anisotropic (Figure 3.6.1). For isotropic etching of silicon etchant like HNA mixture (Hydrofluoric Nitric Acetic), can be applied. During the isotropic etching with agitation, the shape resembles a sphere as in perfect case the etching rate for all crystallographic planes is equal. For isotropic etching without agitation, a flatter bottom is exposed due to a diffusion-limited etching rate.

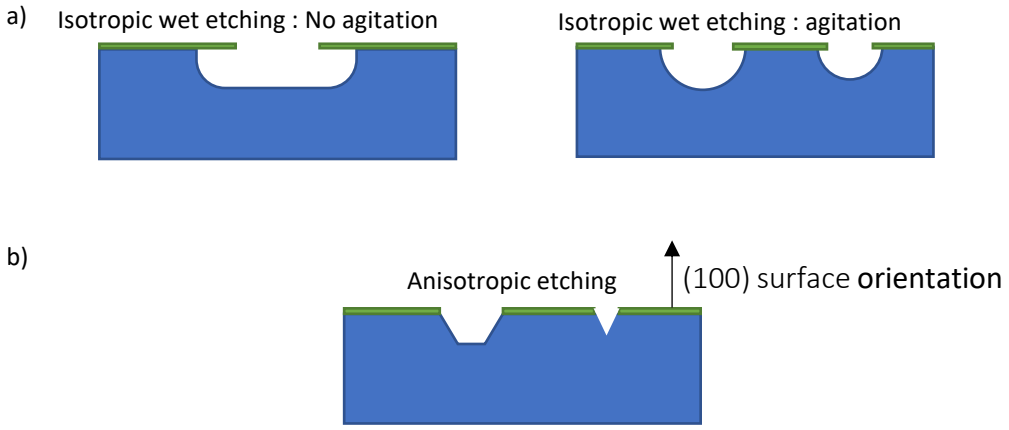

Figure 3.6.1: Scheme of possible etching of bulk silicon using (a) isotropic wet etchant (b) anisotropic wet etchant etched into (100) oriented silicon prepared based on [2]

Anisotropic etching is related to various etching rates for different crystal planes. Commonly used anisotropic etchant for silicon are alkaline solutions (KOH, NaOH), TMAH

(Tetra Methyl Ammonium Hydroxide), EDP *(ethylenediamine pyrocatechol). The difference between the etchants will be discussed later.*

Two factors define anisotropic etching:

1. geometrical – related to the with crystal structure and bond configuration
2. chemical – associated with the etching solution's composition and etching parameters.

The geometry of the etching structure can be fully anisotropic to fully isotropic with all the stages in between. Geometry will be defined through the as well as etching conditions, silicon's doping type and concentration, mask, and even shape of the mask.

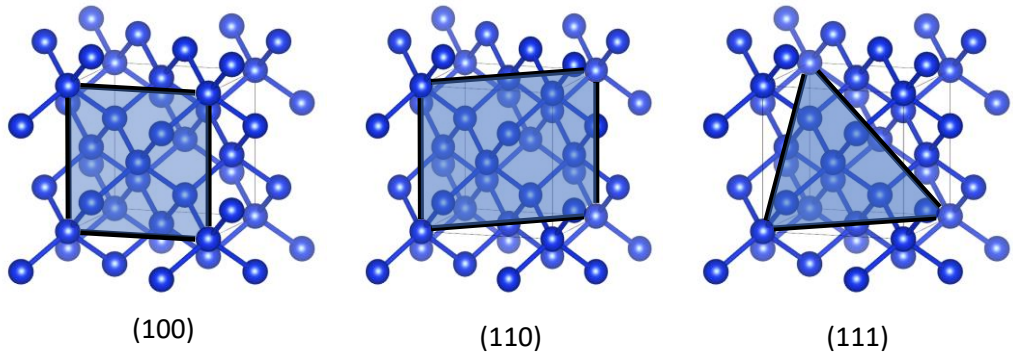

Figure 3.6.2: Diamond structure of silicon with some of the crystal planes. Figure was created based on VESTA [3] software and American Mineralogist crystal structure database [4]

Silicon crystallizes in two structures: diamond (cubic) or lonsdaleite (hexagonal). The diamond structure is less packed and thermodynamically more stable. Therefore, naturally, silicon crystallizes in cubic form. The structure of the diamond consists of two face-centered cubics (FCC cell) move by the vector (¼,¼,¼). The structures of silicon crystallized in a diamond structure are presented in figure 3.3.6 with some of the crystal planes.

In cubic silicon crystal plane (100), (110), and (111) are distinguished by extremely different chemical bond configurations. Generally, there are three basic types of bond configuration. They are presented in figure 3.6.3. and will be designated as bond types A, B, and C [5]. The bonds of type A and C are removed with a constant rate independently on the plane they are situated, whereas atoms with B bond configuration remove the slowest. These kinds of atoms (B-bond configuration) are located on the plane (111), which results in the low etching rate for this plane - etching rate assumed to be 0 [5]

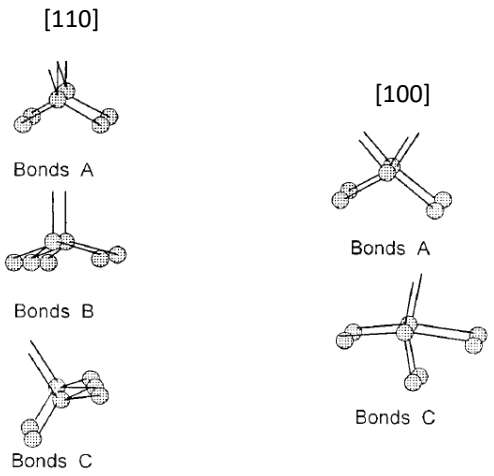

Figure 3.6.3: Basic bond types: A, B, and C. View from direction [110] (left panel) and [100] (right panel) [5].

3.6.1. Back etch and under etch

First, we discuss back etch (cavity etch), which is the 4th step of the sample fabrication (figure 3.2.1 stages from 1 to 6). In table 3.6.1 we compared different silicon etchants. We choose to work with KOH solution as it brings excellent selectivity between silicon and silicon nitride (mask), low sample's roughness, no problem with etching doped silicon, low cost, and low toxicity.

Table 3.6.1: Comparison between typical silicon etchant used in wet-etching method [2]; Where: HNA - Hydrofluoric Nitric Acetic mixture, KOH – potassium hydroxide, NaOH – sodium hydroxide, EDP - ethylenediamine pyrocatechol, TMAH - Tetra Methyl Ammonium Hydroxide.

	HNA	Base (e.g. KOH, NaOH)	EDP	TMAH
Anisotropy	no	yes	yes	yes
Si Roughness	low	low	low	variable
Nitric etch	low	low	low	1 to 10 nm/min
Oxide etch	10 to 30 nm/min	1 to 10 nm/min	1 to 80 nm/min	≈1 nm/min
Al selective	no	no	no	yes
Au selective	likely	yes	yes	yes
Cost	low	low	moderate	moderate
Safety	moderate	safe* and no toxic	low	safe* but toxic

*safe reffers to safety of usage: eg. no explosive, high evaporation temperature

The back etch needs to have well defined and precise size. There are several reasons why the cavity size must be correct :

1. It can increase the pressure difference between the top and bottom of the resonator (chapter 2, ref to equation for photoacoustic force)
2. To avoid opposite capacitive signals in phase opposition (chapter 4, figure 4.3.3c)
3. To avoid overlap of the support (zone 1) with the back etch (chapter 4, figure 4.4.14c). This overlap might cause a collapse of the structure or change the mechanical parameters of the resonator (for instance, frequency).

To predict the back etch's final size, we use properties of anisotropic etching and angle between crystal planes. As pointed out previously, in an anisotropic wet etching, the etching rate depends on the crystal plane. The etching rate is the slowest on the plane (111) (Figure 3.3.7); therefore, the plane (111) is exposed during the wet chemical etching (Figure 3), and it implies that the shape and size of the back etch can be predicted. The angle between the (111) plane to the surface, which is the (100) plane, amounts to 54.7° [4] (Figure 3b). The relation between the mask dimension *D*, etch depth *h*, and the final size *d* can be express by the following equation:

$$d = D - \left(\frac{2h}{\tan(54.7°)}\right) \tag{3.1}$$

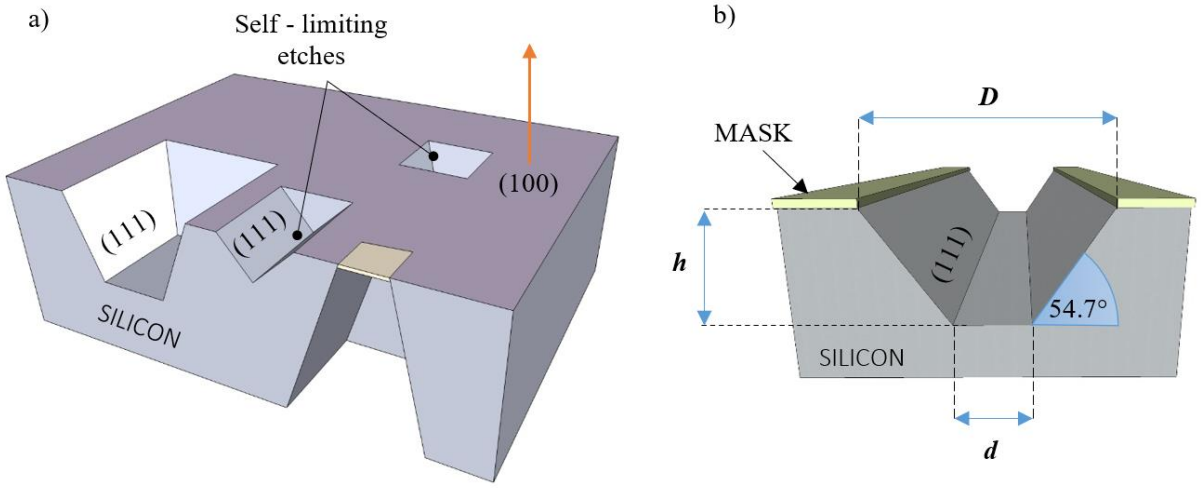

Figure 3.6.4: Schematic etching of silicon with an alkaline solution on the (100) oriented substrate.

We have observed that the opening size (***d*** *in* Figure 3.6.4 b) does not fit the theoretical calculation (based on equation 3.1). Some of the results are presented in figure 3.6.5. The pattern on the mask (***D*** on Figure 3.3.7 b) for all the samples was equal to 300 μm.

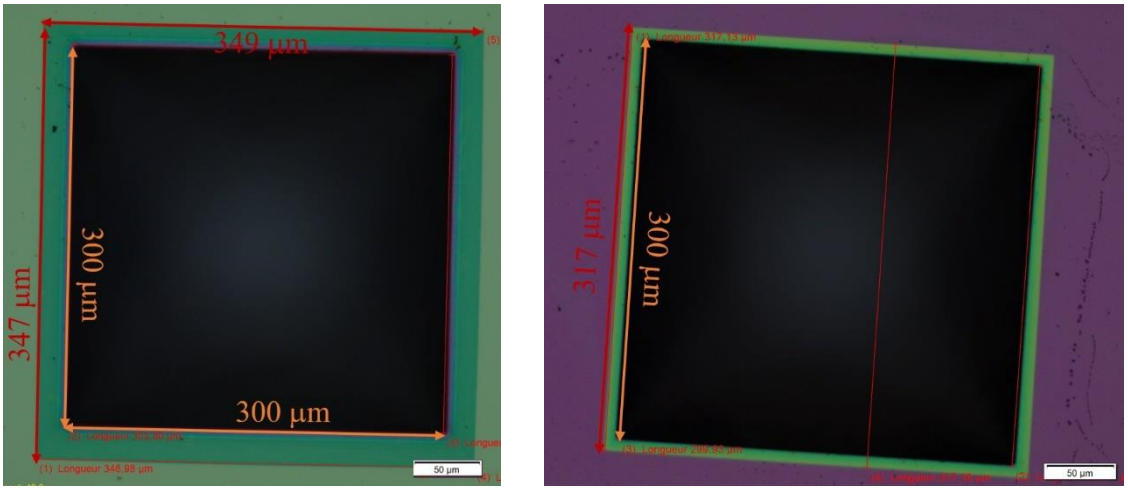

Figure 3.6.5. Optical microscope pictures of the back etch for two selected samples.

The final size of the pattern is different than calculated with equation (1). In all the cases, we noticed a surrounding mask undercut around the etching square, which is visible in both pictures presented in figure 3.6.5.

Based on our investigation (figure 3.6.5) and literature [6] [7], we suspect that the silicon under the mask is etched, which is schematically presented in figure 3.6.6 (right panel). This mask undercut varies between 20 µm to 50 µm and needs to be taken into account to estimate the final size of the back etch (d in figure 3.6.6). The origin of the mask undercut is unknown, but we have found some explanation in the literature [6] [7].

First of all, it was reported in [6] that under etch depends on the mask alignment. The misalignment causes exposure of high-index planes, which subsequently leads to under-etch. To ensure minimal under etching, the mask needs to be aligned with the highest possible precision.

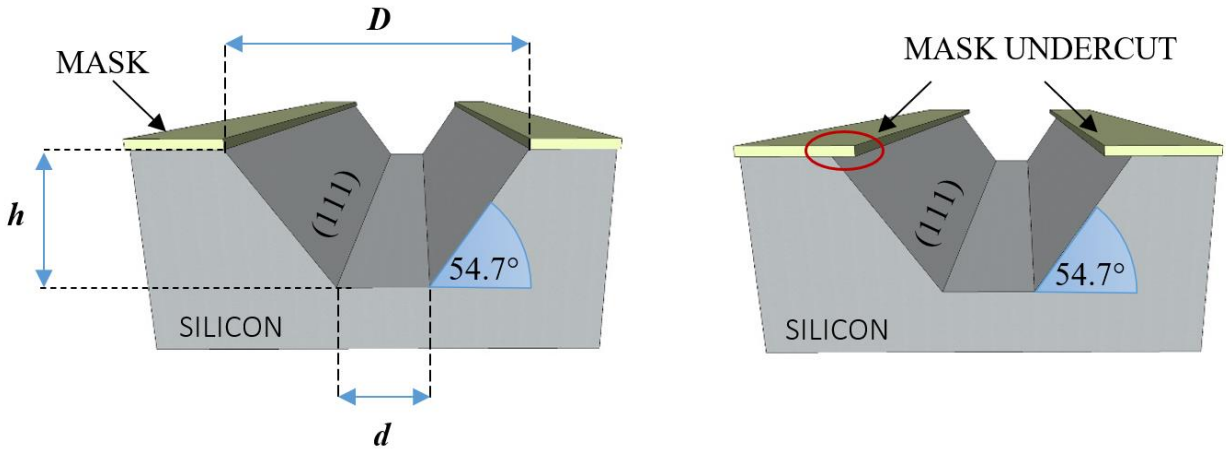

Figure 3.6.6. Schematic etching of silicon with the alkaline solution on the (100) oriented substrate without mask undercut (left panel) and with mask undercut of the mask (right panel).

Secondly, the higher mismatch between the final and predicted size of the back etch will be evident for very deep etching since the under etch will grow with the etching time. For fabricated samples, the etching depth ***h*** in figure 3.6.6 varies between 400 μm and 500 μm depending on the SOI wafer used for MEMS fabrication.

This mask undercut is then a consequence of the anisotropic properties of silicon etching and will change with etching conditions. The etching rate V_{hkl} of individual planes (hkl) is strongly related to the reagent's type, concentration, and temperature (figure 3.6.7 left panel). It is worth noting that this mask undercut can be used to determine the etching rate for some planes. Undercut etch occurs during the etching of the high-index planes (like (331) plane). Thus, the objective is to decrease the etching rate for high index planes. It has been reported in [6] that high-index planes are etched more rapidly than (100) planes in pure alkaline solution. In contrast, for solutions, KOH+IPA high-index planes are much less etched than in pure alkaline solutions (figure 3.6.7 right panel). In the case of our study, the mask undercut does not exceed 50 μm. The minimal precision we need to reach is 100 μm; therefore, it fits in alignment precision.

Table 1
Orientation-dependent etch rates (μm min^{-1}) as a function of KOH concentration at an etching temperature of 70°C. In parentheses are normalized values relative to (110)

Crystallographic orientation	KOH concentration		
	30%	40%	50%
(100)	0.797 (0.548)	0.599 (0.463)	0.539 (0.619)
(110)	1.455 (1.000)	1.294 (1.000)	0.870 (1.000)
(210)	1.561 (1.072)	1.233 (0.953)	0.959 (1.103)
(211)	1.319 (0.906)	0.950 (0.734)	0.621 (0.714)
(221)	0.714 (0.491)	0.544 (0.420)	0.322 (0.371)
(310)	1.456 (1.000)	1.088 (0.841)	0.757 (0.871)
(311)	1.436 (0.987)	1.067 (0.824)	0.746 (0.858)
(320)	1.543 (1.060)	1.287 (0.995)	1.013 (1.165)
(331)	1.160 (0.797)	0.800 (0.619)	0.489 (0.563)
(530)	1.556 (1.069)	1.280 (0.989)	1.033 (1.188)
(540)	1.512 (1.039)	1.287 (0.994)	0.914 (1.051)
(111)	0.005 (0.004)	0.009 (0.007)	0.009 (0.010)

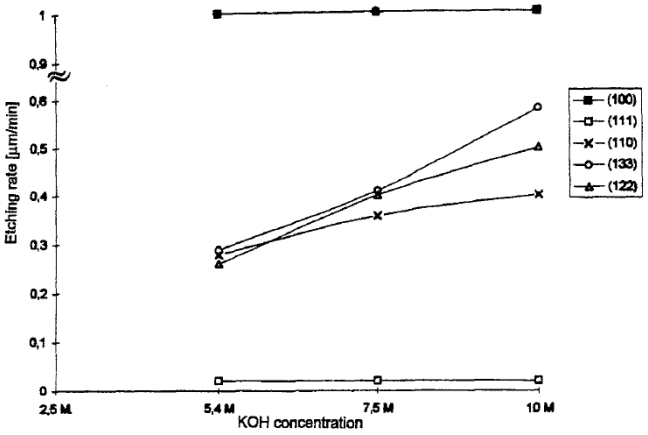

Fig. 5. The etching rates of some Si planes versus etchant (KOH + IPA) concentration, 80°C.

Figure 3.6.7: Table of orientation-dependent etching rates in KOH solution (left panel) [7], and graphic representation of orientation-dependent etching rates in KOH (right panel) [6].

3.6.2 Vertical etch of resonator and micromorphology

The resonator's microfabrication requires a smooth surface and vertical etch. Vertical etch is necessary to decrease the squeeze film effect, as the anisotropic etching will result in larger bottom surface (particularly width). As described in chapter 2, squeeze film effect increase with the width. Therefore, larger bottom surface of the resonator will cause higher damping. During silicon etching in KOH solution, plane (111) will be naturally exposed as it

was explained at the beginning of section 3.6. To obtain a vertical etch, it is necessary to block the exposition of the (111) plane. To achieve it on a silicon wafer with orientation (100), the design needs to be rotated 45° to the direction [110] [8], as it is presented in the figure 3.6.8. However, one needs to remember (beginning of section 3.6) that the etching rate of planes (100), (010), and (001) is equal; therefore, presented here vertical etching will always cause the mask undercut marked in figure 3.6.9.

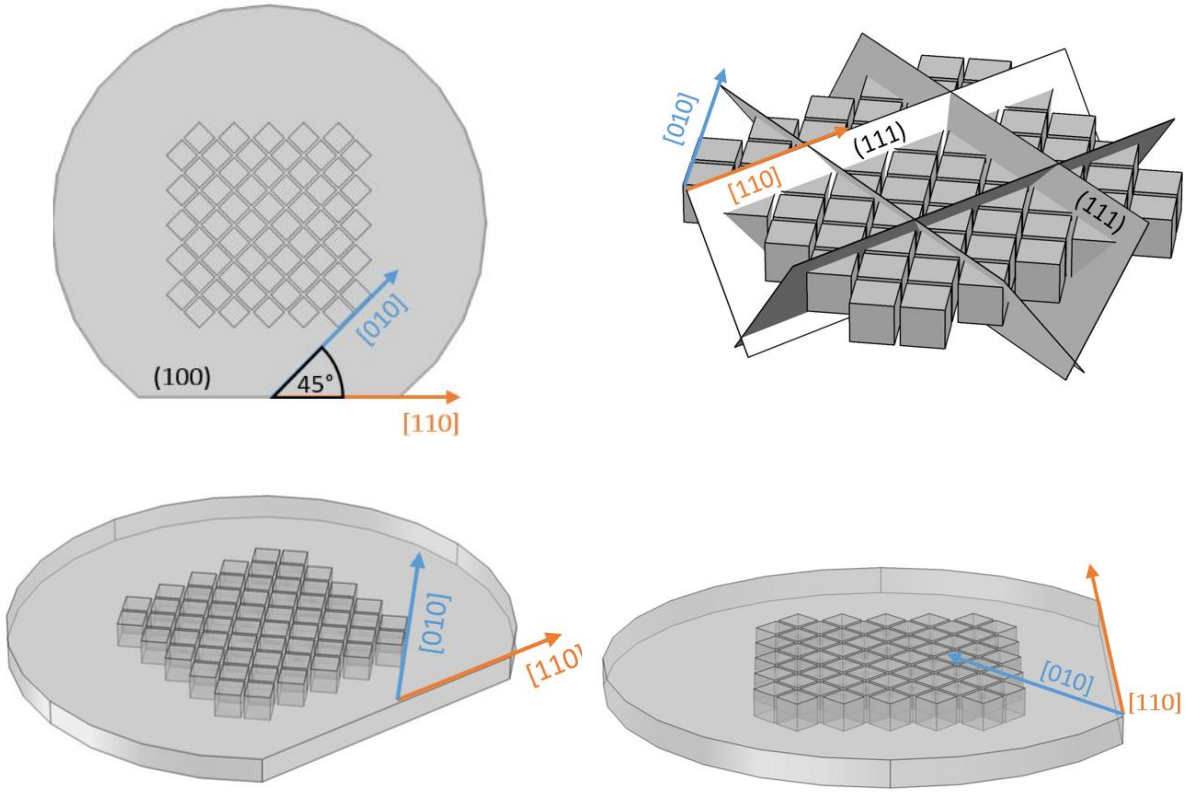

Figure 3.6.8. Scheme of wet anisotropic etching of silicon with crystallographic planes and crystal orientation [9]

During our research on the verticality of the resonator's walls, we encountered some problems resulting in the micro-morphology of the silicon surface (hillocks, protruding edges).

We have observed two main surface corrugations connected with surface micro-morphology, marked in figure 3.6.9:

1. hillocks
2. protruding edges

To study the surface corrugation, a double side polished SOI wafer with (100) orientation was used with a device thickness of 40um, oxide thickness of 4um, and handle thickness of 400um. Different KOH concentrations were studied. Setup was used without agitation, which decreases the homogeneity of the etching. The samples were sized to the square of 1cm x 1cm.

Patterns differ with the size between 40 mm and 250 mm. Samples were layed inside the beakers with the handle facing the bottom of the beaker. However, only the top side was protected by the mask made of either SiO_2 or $SiNi_x$, respectively, to the sample (detailed below).

The objective was to reach the silicone oxide layers with minimal defects on the surface, and a vertical etch.

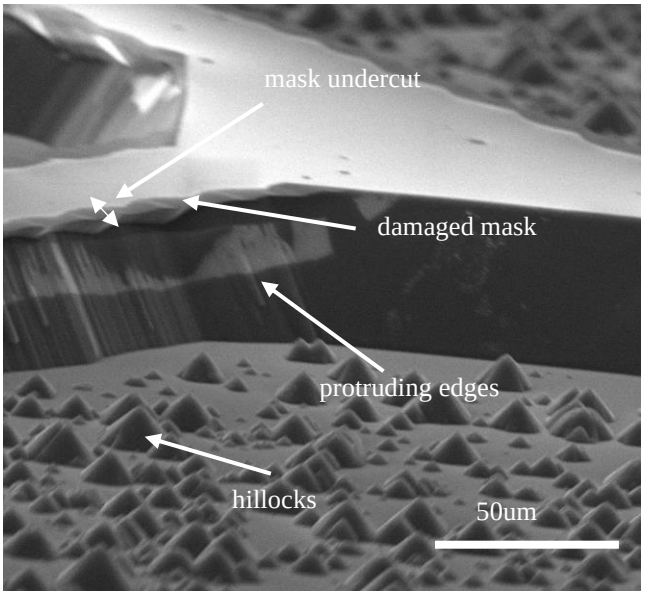

Figure 3.6.9: Scanning electron microscopy picture of silicon etch using KOH solution with marked surface corrugations and mask undercut.

Figure 3.6.10 presents the study of the different etching conditions: temperature and concentration. Based on the figure, one can see that we did not achieve a perfect vertical etch. The closest to the vertical etch is the sample HRE.Y3, for which the KOH concentration was the highest. However, the mask has been removed, which indicates that the high temperature of the etching damages the mask.

Moreover, for XRE.Y4, there is a visible wavy surface and protruding edges. Hillocks are visible only for low temperature and medium KOH concentration which is consistent with the study of Van Veenendaal et al. [10], which claims that the number of hillocks should increase in low concentration and low temperature.

In order to be more consistent with Van Veenendaal et al. [10] study, we investigated samples at different etching stages. Results are presented in figure 3.6.11. As expected, the number of hillocks grows with the etching time. During the KOH etching SiO_2 mask is getting etch creating silica particles that can form a micro-masking. Secondly, the damaged mask falls on the substrate creating another mask layer. In higher temperatures, hillocks are not visible as

more bubbles present in the etching solution evacuate silica particles and mask pieces so they do not adhere to the substrate.

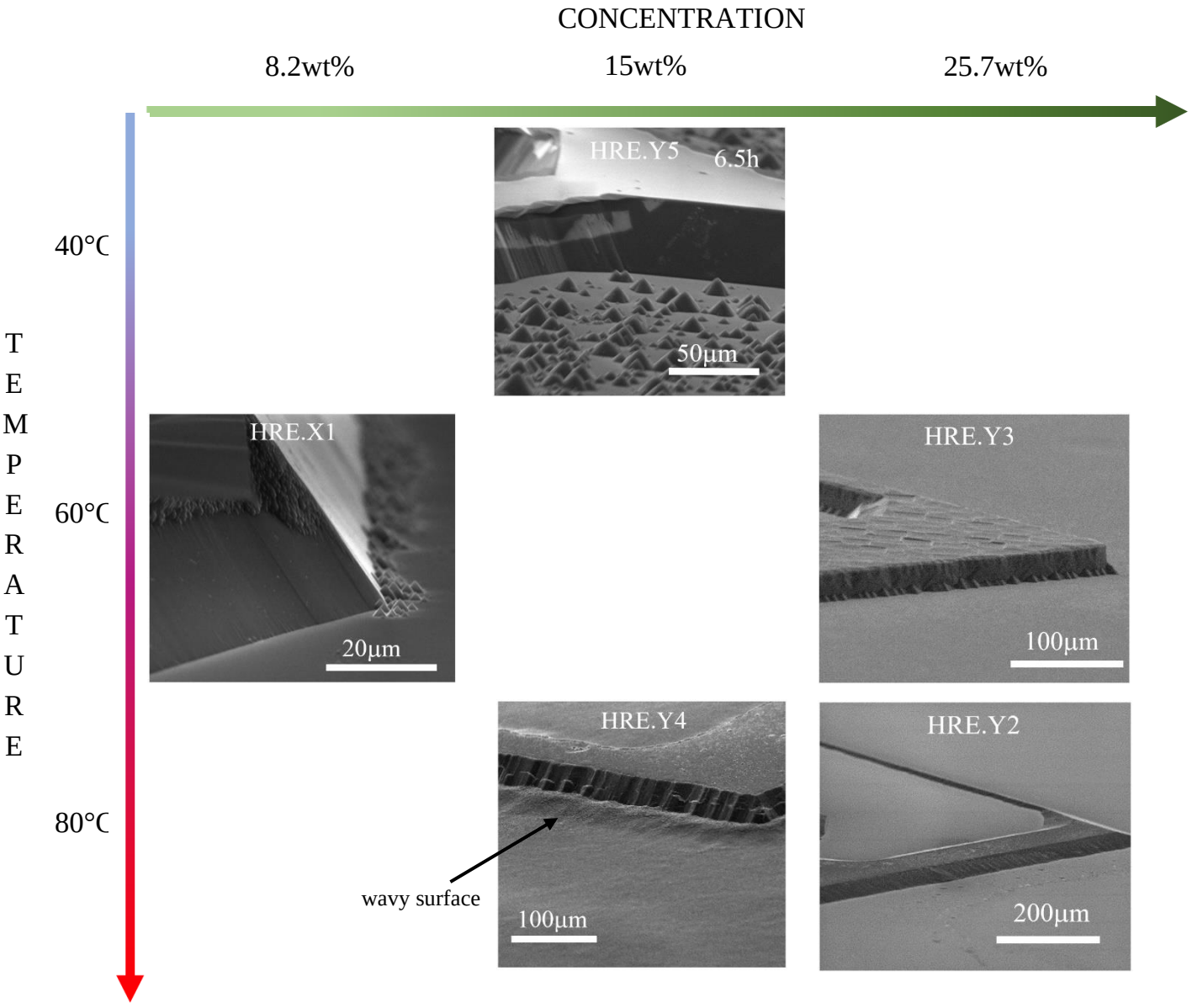

Figure 3.6.10: SEM pictures of samples etched with different etching conditions. Sample HRE.X1 has a 600nm thick SiO_2 mask deposited with the PECVD technique; the rest of the samples have a 400nm thick SiO_2 mask deposited with the same technique.

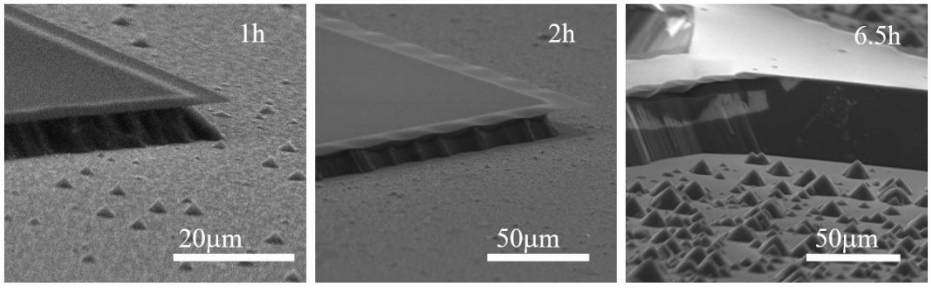

Figure 3.6.11: Effect of the etching time on hillocks formation.

Due to the vertical etch presented in the sample HRE.Y3 we decided to investigate the effect of the SiO_2 mask thickness. The results are presented in figure 3.6.12.

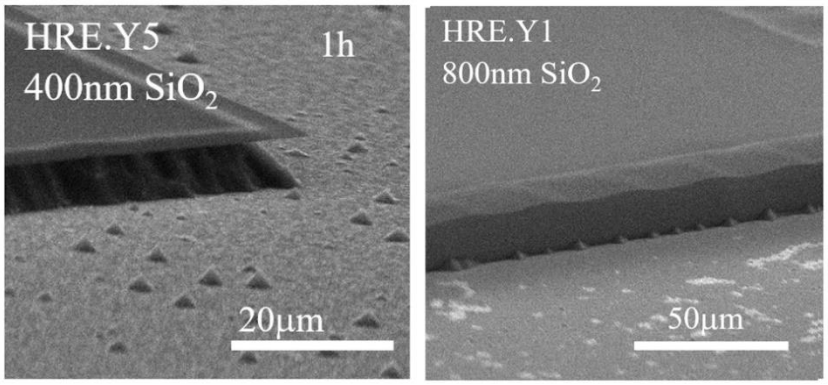

Figure 3.6.12: Thickness effect of SiO2 mask on the vertical etch of silicon. Etching conditions: 15wt% KOH solution, temperature 40°C.

The condition for samples HRE.Y1 and HRE.Y5 were the same; however, the mask thickness has changed. It results in a vertical etch, no hillocks but slightly protruding edges in the case of sample HRE.Y1. Sample HRE.Y1 was the first sample with a mask SiO2 for which we obtained a successful vertical etch. assumed that success was given employing the thicker layer of the mask.

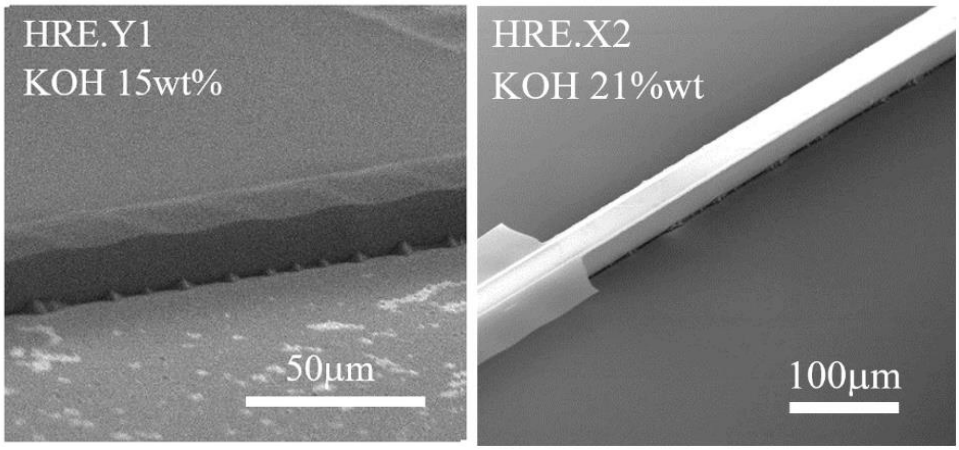

Figure 3.6.13: Effect of KOH concentration on the vertical etch of silicon. Etching temperature 40°C, mask : 800nm thick SiO2.

To verify this hypothesis, we used the same mask thickness: 800nm (XRE.X2, figure 3.6.13) with a higher concentration of KOH. The results are presented in figure 3.6.13. The masked remained during the whole device etching providing a clean vertical etch. As a consequence of observation, we hypothesize that masks play an essential role in etching verticality. Namely, we believe that the reason is the stress of the mask, microdamage of the mask and material of the mask itself.

To verify its credibility, we have tested the etching conditions with a different mask, namely, 500 nm thick low stress (σ~0) silicon nitride SiN_x [2] deposited with techniques low-pressure chemical vapor deposition (LPCVD) in Laboratory for Analysis and Architecture of Systems, Toulouse (LAAS). Figure 3.6.14 presents relatively opposite etching conditions. In both cases, we have obtained a vertical etch, which confirms our hypothesis connected with the role of the mask in the verticality of the etching.

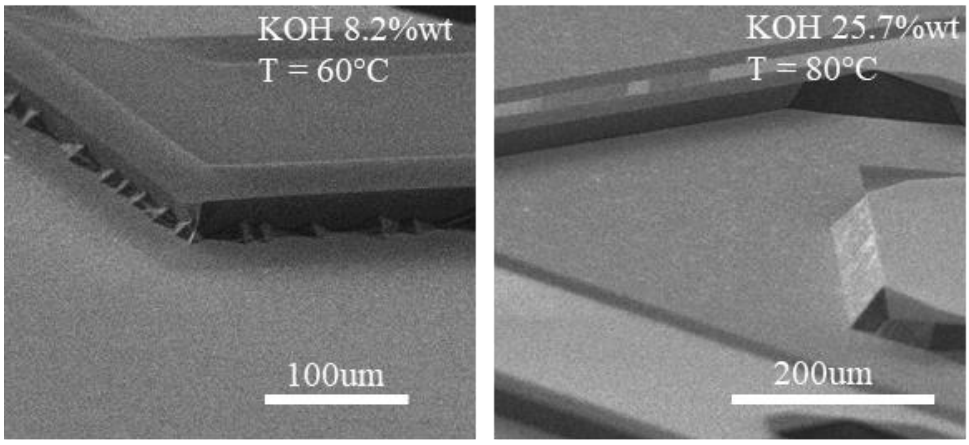

Figure 3.3.14: Scanning electron microscopy picture of silicon etches using 8.2%wt KOH solution at temperature 60°C (left panel) and 25.7%wt KOH solution at temperature 80°C (right panel). In both cases, there is 500 nm thick mask of low-stress SiNx.

We have observed another factor that influences the surface micro-morphology during the conducted study: sample cleaning. The effect of mentioned additional cleaning treatment is presented in figure 3.3.15. It consists of cleaning with piranha solution between mask opening and etching of the device layer with KOH solution (between steps 6 and 7 presented in figure 3.2.1).

Piranha solution is known as an excellent remover for all organic pollution, including a photoresist. The RIE technique used for resist removal is not ideal due to the higher thickness of the photoresist in the corner of the sample. As a result, some photoresist resist residue remains after RIE etching. We suppose that this contamination causes the effect of edge protrusion visible in Figure 3.6.15a (KOH etching without additional cleaning treatment). The treatment of the sample with piranha solution before KOH etching results in the smooth vertical etch (figure 3.6.15b).

To fabricate the X-resonator, we chose 24.3wt% KOH solution at a temperature of 70°C. This concentration and temperature provide a relatively high etching rate (~2 μm/min), allowing obtaining a rapid fabrication process.

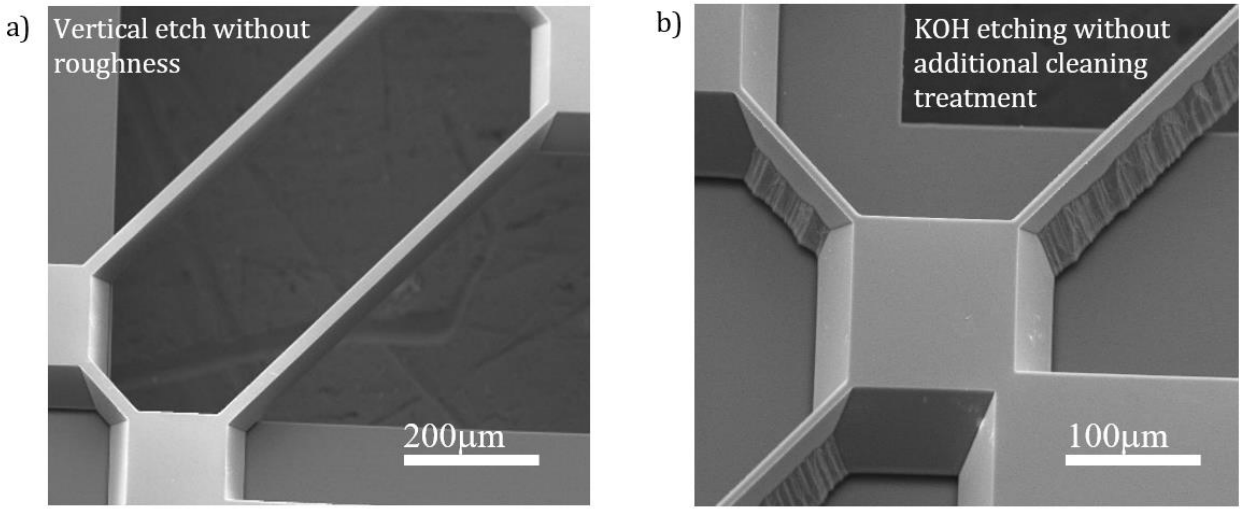

Figure 3.3.15: a) Scanning electron microscopy picture of X-resonator obtained wet etching technique using 25%wt KOH solution at temperature 70°C with an additional cleaning using piranha solution (left panel) and b) 25.7%wt KOH solution at temperature 80°C without cleaning with piranha solution (right panel).

3.6.3. Conclusions

Hillocks are visible only at low temperatures; however, more experimental data should support this observation. The creation of the hillocks is connected with the type and thickness of the mask. Samples with thicker SiO_2 as well SiN mask are characterized by lower hillock concentration. We believe that the creation of the hillock might be connected with mask damage/decomposition as the number of hillocks increases for the longer time of etching. It has been reported [10] that silicate particles might be a velocity source that creates hillocks. Velocity source refers to the region where the etching rate is accelerated due to mechanical or kinetic boundary conditions. The hypothesis regarding silicate particles fits with our observations. The thicker mask of SiO_2 is more stable and less likely to get damage, fall on the substrate, and create micro-masking.

Secondly, the most significant factor for vertical etch comes from the mask type. Typically, it is better to use SiN_x low-stress mask than SiO_2 mask deposited by PECVD. There are two reasons: 1) SiN_x is more resistant in KOH solution – we decrease the time for sample fabrication 2) the etching rate is shorter for SiN_x, and the stability is higher, which decreases the surface roughness and protrusion. However, it is possible to obtain a vertical etch with SiO_2 deposited by PECVD. In this case, the mask should be thicker. Our results do not support the

theory concerning surface tension and verticality of the walls presented in the work of Brockmeier et al. [8] nonetheless, they neither contradict it.

3.7. Deep reactive ion etching

For the fabrication of some resonators, we used deep reactive ion etching. Deep reactive ion etching for silicon was invented in Bosch laboratory in 1996 [12], [13]. Deep etching of silicon is essential to etch a thick silicon layer with high anisotropy. It uses two reactive etching process mechanisms: chemical-isotropic reaction and physical - using ions accelerated in an electric field. The vertical etching is obtained independently of the silicon crystallographic orientation. The main advantage of this process is high anisotropy of the etching, excellent selectivity, and lack of mask undercut, which cannot be avoided in the case of vertical etching using the wet etching technique.

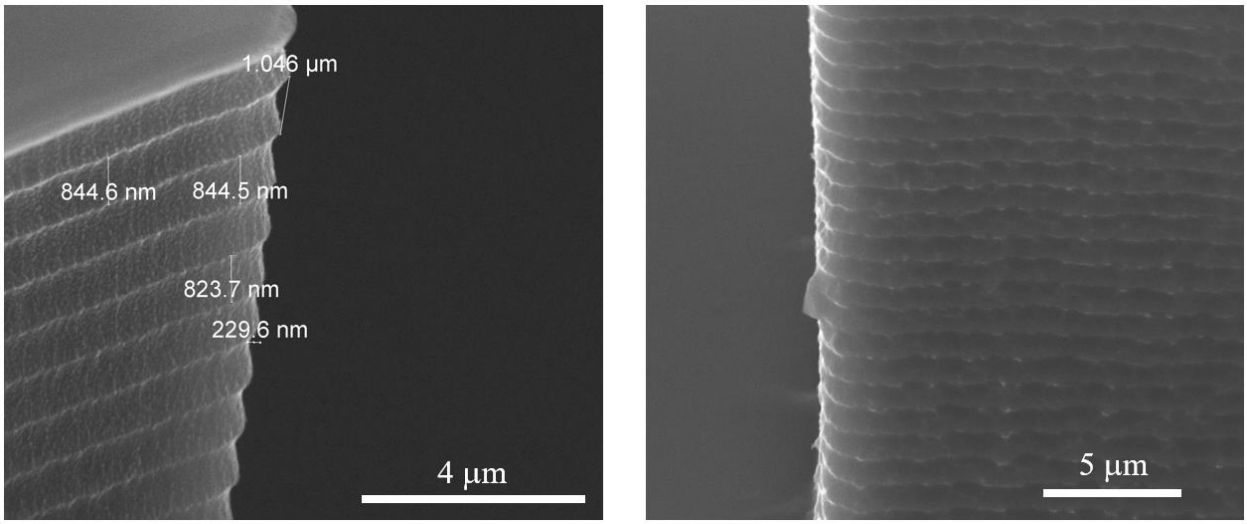

Figure 3.7.1: Scanning electron microscope pictures of H-resonator with visible scalloping.

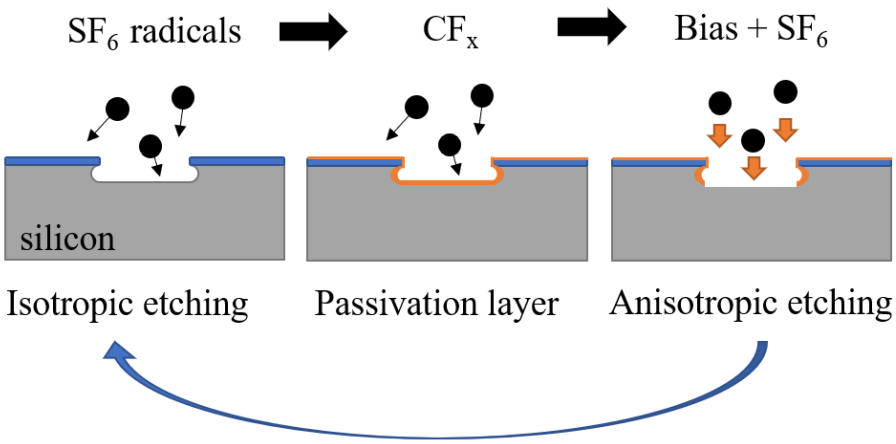

Figure 3.7.2: The principle of the Bosch process.

The Bosch process is schematically presented in figure 3.7.2. The first step of the process is the isotropic removal of the material using SF_6. Secondly, the polymeric passivation layer made of C_xF_x is deposited on the sample. The sample is then bombarded with ions, causing the polymer at the bottom to be removed, and the whole process repeats. As a result, the depth of the structure increases without lateral etching. However, this process results in scalloping, which in some cases might be unwanted. Scalloping is presented in figure 3.7.1. The vertical surfaces from DRIE will never be as smooth as surfaces as achieved with wet anisotropic etching. Table 3.7.1 presents parameters used in the DRIE process and their impact on the process [14] (p.444).

Table 3.7.1: Parameters used in DRIE and their impact on etching based on [14] (p.444)

Parameter	Main effect
Pressure	Uniformity, etch rate, selectivity, etch profile
Platen power	Profile, etch rate, selectivity
Coil power	No effect in 500-900 W range
SF_6 flow	Mask undercut, etch rate
SF_6 time	Etch profile, mask undercut, etch rate
C_4F_8 flow	Mask undercut, etch rate
C_4F_8 time	Etch profile, mask undercut
Exposed Si area	Etch rate, etch uniformity

3.8. HF etching

To create a free-standing structure, it is necessary to remove a part of sacrificial silicon oxide located under the device layer in the SOI wafer – step 8 in figure 3.2.1., section 3.2. The most common method to remove the buried oxide is the use of hydrofluoric acid (HF). HF is the only etchant for SiO_2, assuring an etch at a relatively high rate (1μm/min for 49% solution of HF in ambient temperature and decrease with concentration and temperature). The etching rate also depends on the structure of silica, and therefore etching rate might slightly differ between samples.

The reaction of etching is [15]:

$$SiO_2 + 6HF \rightarrow H_2SiF_6 + 2H_2O \tag{3.2}$$

It is worth pointing out that using the wet etching of silicon oxide might lead to the stiction of the device to the support. The term ***stiction*** refers to unwanted contact between a flexible device layer of SOI wafer and substrate, which results in the device layer collapsing. The effect of stiction, presented in figure 3.8.1, is mainly caused by capillary forces but also hydrogen bridging and Van de Waals forces which will from now on be called adhesive forces [16].

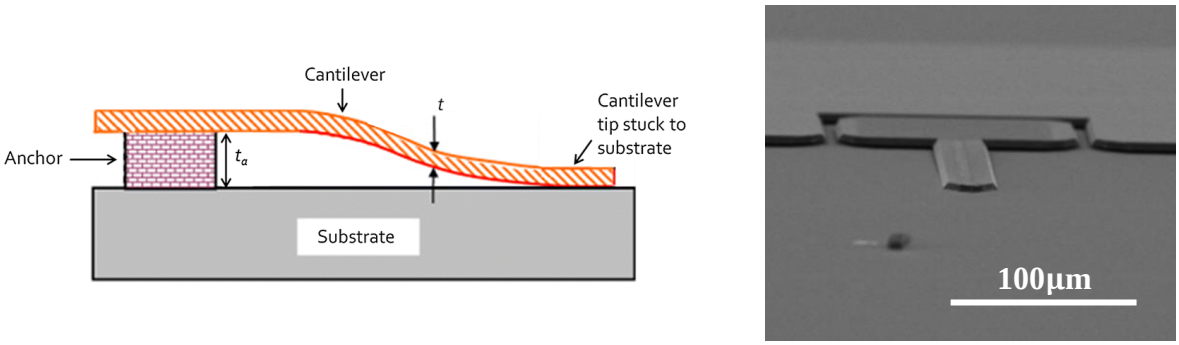

Figure 3.8.1: (a) Schematic illustration of stiction effect [17] (b) SEM picture of collapsed silicon cantilever.

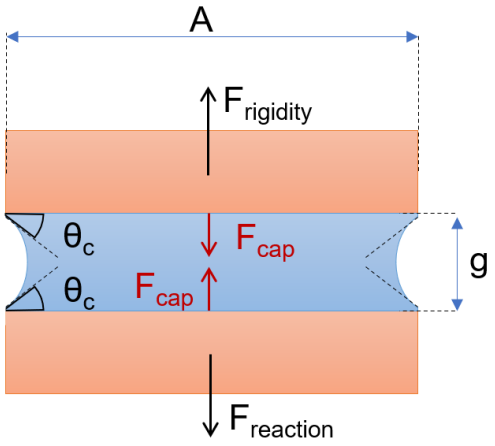

Figure 3.8.2: Between two plates, a thin film of liquid acts as an attractive force. Θ_c is the contact angle between the liquid and solid in the air, g is the thickness of the liquid layer, and A is the wetted area. To maintain equilibrium, a force $F_{reaction}$ and $F_{rigidity}$ is applied. $F_{reaction}$ originates from the support.

Figure 3.8.2 explains the capillary forces F_{cap}. To avoid stiction between the cantilever and the substrate, rigidity $F_{rigidity}$ of the structure needs to be higher than capillary forces F_{cap}. The capillary force will act as an attractive force between two surfaces if the contact angle between the liquid and solid Θ_c is less than 90° [16]. This attractive force F_{cap} will increase with increasing the contact surface A (wetted area) and decreasing the distance g between two surfaces, according to the following equation:

$$F_{cap} = -A\frac{\gamma_{la}}{r} \tag{3.3}$$

where $\gamma_{la}$is a surface tension at the interface and $r = -\frac{g}{2\cos\Theta_c}$ is a radius (connected with radius of the meniscus). The sign for radius is positive for convex meniscus and negative for concave. Therefore, it will be more significant for a long structure (such as long cantilever vs. short) separated with a smaller gap.

For X-resonator, the stiction problem occurred only with the 3rd generation (X5) due to a higher contact area between the liquid and solid than the previous generation. To avoid the stiction effect, several solutions might be applied [18]:

1. immersing the sample in solution characterized by low surface tension, as indicates equation 3.3. We used isopropanol to release X-resonator of 1st and 2nd generation
2. use of vapor HF – discussed in section 3.8.2.
3. phase change at a liquid-gas interface, e.g., freeze-dry technique

3.8.1. Liquid HF etching

The etching rate using liquid HF solution depends mainly on the HF concentration and temperature of the solution.

For fabrication of X-resonator of 1st and 2nd generation (chapter 4) etching of SiO_2 was carried out in Teflon beaker using a 40% aqueous HF solution under the hood in the cleanroom at ambient temperature (~24°C). The procedure is summarized in table 3.8.1 in section 3.8.3. The etching rate depends on the temperature and concentration. Under cleanroom condition (~24°C), the etching rate amounts to 0.7 μm/min

3.8.2. Vapor HF etching

Compared to liquid HF, the method using vapor HF is characterized by a slightly higher complexity of the setup. However, this method seems reasonable in structures where isopropyl alcohol usage is insufficient to avoid stiction.

The setup for conducted etching was created based on the work of [18] and is presented in figure 3.8.3.

However, one needs to remember that water acts as a catalyst in the silicon oxide etching process. The too high temperature on the sample's surface will result in a lack of water

molecules and a prolonged etching rate. Based on the work of [18] an optimal temperature exists around 40°C.

Our study presents similar results to [18], although we used slightly lower temperatures for our process, namely 36°C. The water condensation was not observed. As presented at the beginning of section 3.8, stiction will increase with the structure's length and decrease with the oxide layer thickness (equation 3.3). During the calibration procedure, the oxide layer was at least three times smaller than the oxide layer in the wafer used for the micro-resonator.

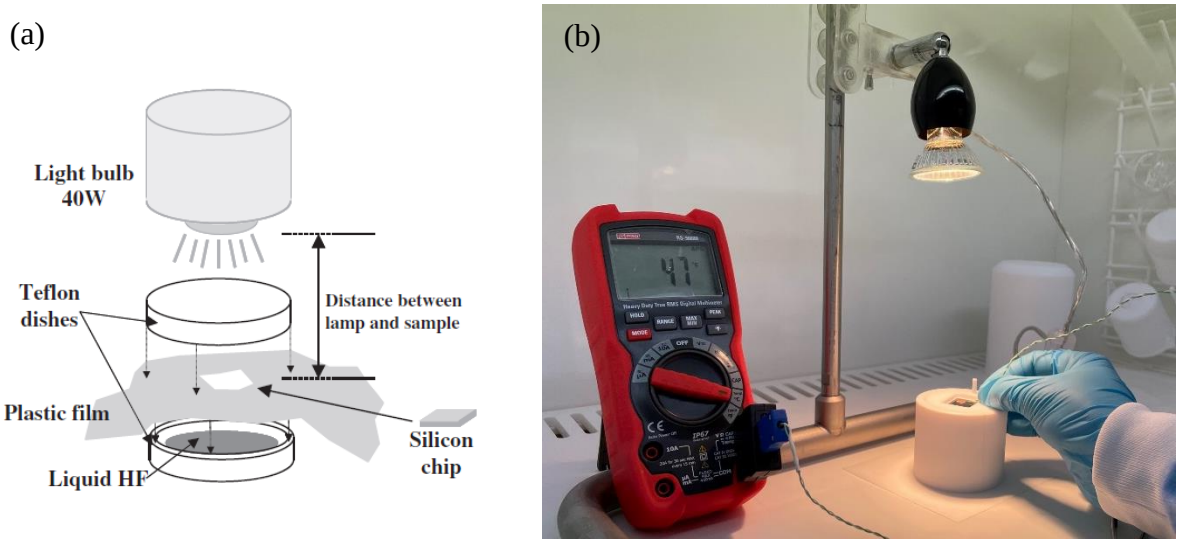

Figure 3.8.3: (a) schematic illustration of setup for vapor HF (b) picture of a setup for vapor HF etching.

For reliability reasons, the etching was performed using the same Teflon beaker with the same volume of HF solution (20mL).

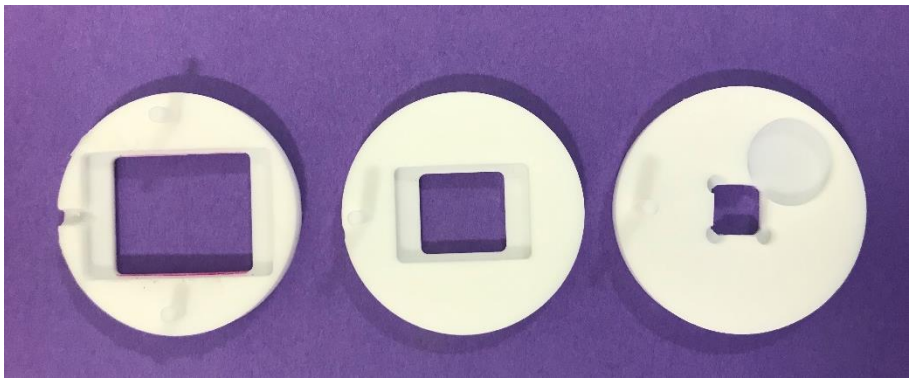

Figure 3.8.4: Picture of Teflon supports for vapor HF.

For our process, we used Teflon supports with several dimensions presented in figure 3.8.4. and for different sizes of samples. As the setup temperature depends on the support and sample size, the distance between the sample and lamp must be verified and adjusted to obtain a constant temperature.

Depending on the sample size, Teflon support, and distance between the lamp and sample, the thermalization time changes between 6 to 13 minutes. Thermalization time refers to the time after which the temperature of the sample is stabilized at a fixed distance between the lamp and sample.

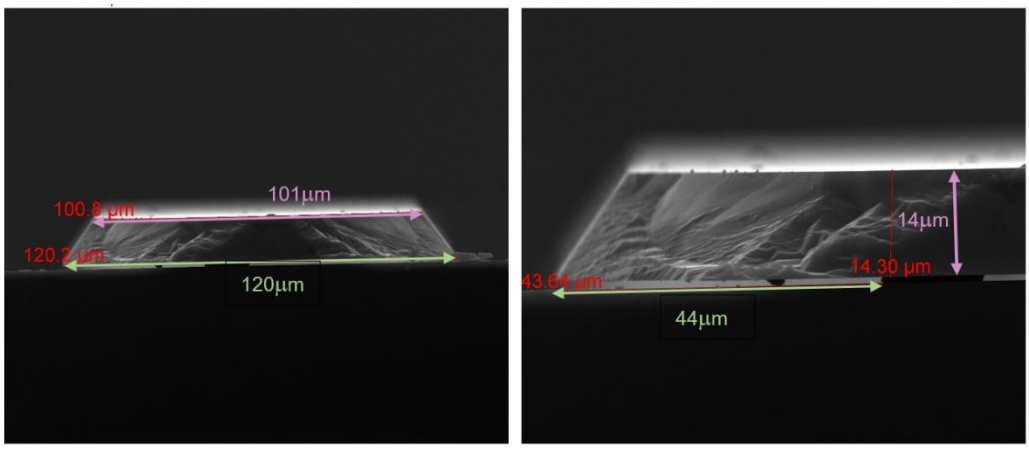

Figure 3.8.4. SEM pictures from vapor HF calibration performed with the following conditions: 36°C for 2h20min.

The calibration of the etching rate was conducted on the SOI wafer with device thickness 15 µm, oxide 1000 Å, and handle 350 µm. The pattern of parallel lines of 100 µm width separated with a gap of 400 µm was obtained with a procedure presented in section 3.6 using wet etching technique with 22wt% KOH solution at temperature 70°C. The time was adjusted to reach the oxide layer.

The sample was thermalized for 15min at a fixed distance between the lamp and sample: 17.5cm, reaching the temperature of 36°C. The undercut was measured using scanning electron microscopy after 2h20 min of etching. Results are presented in figure 3.8.5. As visible from SEM pictures, the undercut after 2h20min amounts to 43.6 µm, which gives the etching rate of 0.3 µm/min. The process should depend on temperature and HF concentration and thus should be linear. We did not observe water condensation.

3.8.3. Process comparison

Table 3.8.1: Comparison of the silicon oxide etching using liquid and vapor HF.

Liquid	vapor
stiction	avoid stiction
high etching rate – fast fabrication process	low etching rate
isotropic and homogeneous	water condensation might disturb the homogeneity

Table 3.8.2: Procedure summary of the silicon oxide etching using liquid and vapor HF.

	Liquid HF	Vapor HF
Sample preparation	immersing in water	15min of sample thermalization using lamp of 40W. Distance between the light and sample around 20cm*
Etching	etching rate depends on temperature: at 23°C, etching rate amounts to 0.7 μm/min	The etching rate depends on sample temperature; at 36°C etching rate amounts to 0.3 μm/min.
homogeneity	isotropic, homogeneous	isotropic, homogeneity depends on water condensation on the sample
post-etching procedure	rinsing sample with water, after immersing the sample in isopropyl alcohol (to avoid sample stiction)	sample thermalization to remove the residue of HF from the sample's surface.

* Temperature varies depending on the sample and support size; therefore, the distance has to be adjusted to reach temperature of 40°C

3.9. Conclusions

The goal of this chapter focuses on a detailed presentation of the fabrication process. It supposed to address the issue which could be encountered during the fabrication process, as well as their origin and solution. First, it starts with the wafers preparation, then the definition of the resonator pattern using a photolithography process and etching methods of silicon. Precisely, it touches on a subject connected with vertical etching of silicon wafer with (100) orientation, using:

a) wet etching with KOH solution (section 3.6)

b) deep reactive ion etching (section 3.7)

The results from section 3.6 show work that allowed to achieve a vertical etching of the silicon using KOH solution and identify the crucial parameters influencing etching.

Then, section 3.7 presents the principles of deep reactive ion etching. However, this part of the thesis was not expanded as the development process of deep reactive ion etching was not a part of this thesis.

The last subsection (section 3.8) of the chapter briefly introduces methods of SiO_2 etching while extending methods that include HF solution.

Using the fabrication process presented in this chapter, we managed to successfully fabricate devices, which will be presented in the following chapters.

3.10. Bibliography

[1] P. Temple-Boyer, C. Rossi, E. Saint-Etienne, and E. Scheid, "Residual stress in low pressure chemical vapor deposition SiNx films deposited from silane and ammonia," *Journal of Vacuum Science & Technology A: Vacuum, Surfaces, and Films*, vol. 16, no. 4, pp. 2003–2007, 1998, doi: 10.1116/1.581302.

[2] G. T. A. Kovacs, N. I. Maluf, and K. E. Petersen, "Bulk micromachining of silicon," *Proceedings of the IEEE*, vol. 86, no. 8, pp. 1536–1551, 1998, doi: 10.1109/5.704259.

[3] K. Momma and F. Izumi, "VESTA 3 for three-dimensional visualization of crystal, volumetric and morphology data," *Journal of Applied Crystallography*, vol. 44, no. 6, pp. 1272–1276, 2011, doi: 10.1107/S0021889811038970.

[4] R. T. Downs and M. Hall-Wallace, "The American Mineralogist crystal structure database," *American Mineralogist*, vol. 88, no. 1, pp. 247–250, 2003, doi: 10.5860/choice.43sup-0302.

[5] I. Zubel, "The Model of Etching of (hkl) Planes in Monocrystalline Silicon," *Journal of The Electrochemical Society*, vol. 150, no. 6, p. C391, 2003, doi: 10.1149/1.1568940.

[6] I. Zubel and I. Barycka, "Silicon anisotropic etching in alkaline solutions I. The geometric description of figures developed under etching Si (100) in various solutions," *Sensors and Actuators, A: Physical*, vol. 70, no. 3, pp. 250–259, 1998, doi: 10.1016/S0924-4247(98)00141-1.

[7] K. Sato *et al.*, "Characterization of orientation-dependent etching properties of single-crystal silicon: Effects of KOH concentration," *Sensors and Actuators, A: Physical*, vol. 64, no. 1, pp. 87–93, 1998, doi: 10.1016/S0924-4247(97)01658-0.

[8] A. Brockmeier, F. J. S. Rodriguez, M. Harrison, and U. Hilleringmann, "Surface tension and its role for vertical wet etching of silicon," *Journal of Micromechanics and Microengineering*, vol. 22, no. 12, 2012, doi: 10.1088/0960-1317/22/12/125012.

[9] O. Adljuy, “Crystallography Orientation.” 2011.

[10] E. van Veenendaal, K. Sato, M. Shikida, and J. van Suchtelen, “Micro-morphology of single crystalline silicon surfaces during anisotropic wet chemical etching in KOH: Velocity source forests,” *Sensors and Actuators, A: Physical*, vol. 93, no. 3, pp. 232–242, 2001, doi: 10.1016/S0924-4247(01)00653-7.

[11] and A. S. Schröder, H., E. Obermeier, “Micropyramidal hillocks on KOH etched { 100 } silicon surfaces : formation , prevention and removal,” 1999.

[12] F. Laermer, A. Schilp, K. Funk, and M. Offenberg, “Bosch deep silicon etching: Improving uniformity and etch rate for advanced MEMS applications,” *Proceedings of the IEEE Micro Electro Mechanical Systems (MEMS)*, pp. 211–216, 1999, doi: 10.1109/memsys.1999.746812.

[13] F. Laermer, A. Schilp, and Robert Bosch GmbH, “Method of anisotropically etching silicon,” *US Patent 5501893*, p. US5501893 A, 1993, [Online]. Available: https://patents.google.com/patent/US5501893A/en

[14] B.-Y. Kononchuk, Oleg and Nguyen, *Silicon-On-Insulator (SOI) Technology*. Elsevier, 2014.

[15] H. P. Gianchandani, Yogesh B and Tabata, Osamu and Zappe, *Comprehensive microsystems*. Elsevier Amsterdam, 2008.

[16] N. Tas, T. Sonnenberg, H. Jansen, R. Legtenberg, and M. Elwenspoek, “Stiction in surface micromachining,” *Journal of Micromechanics and Microengineering*, vol. 6, no. 4, pp. 385–397, 1996, doi: 10.1088/0960-1317/6/4/005.

[17] M. Cauchi, I. Grech, B. Mallia, P. Mollicone, B. Portelli, and N. Sammut, “Essential design and fabrication considerations for the reliable performance of an electrothermal MEMS microgripper,” *Microsystem Technologies*, vol. 0123456789, 2019, doi: 10.1007/s00542-019-04363-w.

[18] Y. Fukuta, H. Fujita, and H. Toshiyoshi, “Vapor hydrofluoric acid sacrificial release technique for micro electro mechanical systems using labware,” *Japanese Journal of Applied Physics, Part 1: Regular Papers and Short Notes and Review Papers*, vol. 42, no. 6 A, pp. 3690–3694, 2003, doi: 10.1143/jjap.42.3690.

Chapter 4

4. X – resonator

This chapter presents the first successful concept of resonator design, which decouples photoacoustic wave collection and capacitive transduction. The resonators presented in this chapter were developed and studied using COMSOL, a finite element software. Resonators were fabricated using the wet etching technique extended in chapter 3. Then, a frequency response analysis was performed to determine the resonators' mechanical parameters: resonance frequency and quality factor. Finally, some of the resonators were implemented in photoacoustic gas sensing.

4.1. Concept

The concept of a photoacoustic gas sensor based on silicon micro-mechanical resonator specially designed for photoacoustic gas sensing with capacitive transduction was for the first time proposed by Chamassi et al. in 2018 [1]. This first successful design, named 8-resonator, is presented in figure 4.1.1a. Compared to the standard cantilever presented in chapter 2, 8-resonator has been designed to increase the quality factor of the anchor and the overlapping area between the photoacoustic force and the resonator. The 8-resonator consists of two support made of two large squares marked with yellow color in the figure 4.1.1a They were moved maximally from the center moving part, where the mechanical displacement is maximum.

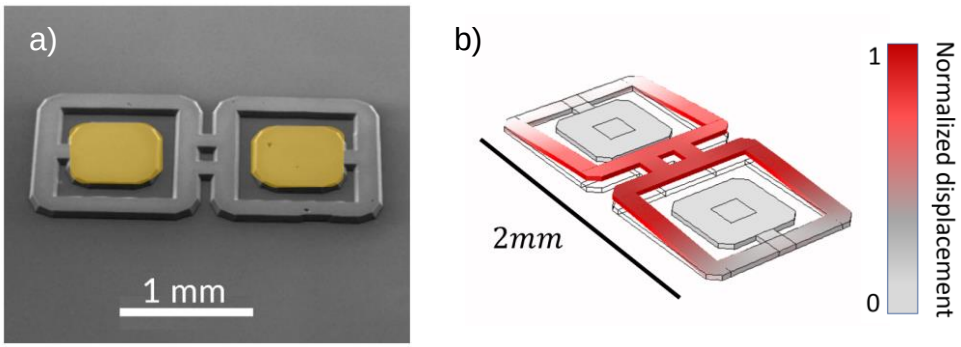

Figure 4.1.1: a) Scanning electron microscopy picture of the 8-resonator with support marked with yellow. b) COMSOL simulation demonstrating deflection of the 8-resonator for first mode of vibration which occurs at 15 kHz.

This sensor stands as a promising solution. However, its performance differs significantly from that presented by the state-of-the- art gas sensing techniques, and particularly the QEPAS technique. Namely, 8-resonator is characterized by Normalized Noise Equivalent Absorption (NNEA) coefficient of value $8.9 \cdot 10^{-6}$ [$cm^{-1} \cdot W/\sqrt{Hz}$) and LOD($1\sigma$) of 1100 ppmv for CH_4 @10s of integration time with a laser of power 7 mW emitting at 1.63 µm. The reason for the poor limit of detection (LOD) and NNEA of the sensor shown by Chamassi et al. in 2018 [1] comes from the capacitive transduction mechanism. As presented in chapter 2, in capacitive sensing, the distance between two electrodes needs to be small as the capacitive signal is inversely proportional to the distance between the electrodes: $\mathrm{d}C(t) \propto \frac{1}{d}$ where $\mathrm{d}C(t)$ is a variation of the capacitance and d distance between electrodes. This proximity increases the viscous damping of the mechanical resonators, which lowers their sensitivity. That is why a low-quality factor characterizes the 8-resonator [1]. This damping can be minimized by decreasing the resonator's surface. As introduced in chapter 2, the voltage output from the capacitive signal is proportional to the displacement, therefore decreasing the surface will not affect the voltage output from the resonator movement. However, based on the model presented in chapter 2, decreasing the surface (thin arms) reduces the energy collected from the acoustic wave and thus the sensor's sensitivity. In the case of 8-resonator, the area for photoacoustic energy collection is large (table 4.3.3). Nonetheless, this large surface and proximity of the two electrodes decreases the quality factor and thus the displacement of the 8-resonator. Chapter 2 demonstrates that an optimum between these two opposite tendencies can be found for a simple cantilever. Despite this improvement, a simple cantilever based on SOI (silicon on insulator) wafers would not achieve the same performance as the state-of-the-art photoacoustic gas sensors. Therefore, to reach the objective, a different approach needed to be applied.

The approach proposed in this thesis focuses on the separation of the problems through dividing the resonator into sections; each performs a specific function. Thanks to this approach, each part can be optimized independently. The resonator manages two main functions:

- photoacoustic energy collection
- electrical transduction

The shape of the resonator must be constructed in such a manner that the above-mentioned functions are separated. Furthermore, the geometry must ensure an excellent coupling between the sections and low support losses.

To reach this aim, we created a complex mechanical resonator design, presented in figure 4.2.1. It is made up of several mechanical zones that are linked together. Some of these zones are in charge of the capacitive transduction, while others are in charge of the photoacoustic energy collection. The design and contribution of each zone of the resonator, called X-resonator, will be discussed in the next section.

4.2. General description and working principles

This section introduces the operating principles and describes the resonator's geometry. The explanation is done using the scheme of the X-resonator's 1st generation. All of the resonators in this chapter are characterized by the same zone configuration and general shape. Figure 4.2.1 depicts the resonator's design. The device was created on a SOI wafer, similar to that described in chapter 2. The resonator itself creates a mobile electrode, while the substrate is a fixed electrode. We used a highly doped silicon, to avoid any metal deposition. The electrical contacts are made by micro soldering using aluminum wires. Energy from the photoacoustic wave is collected by zone 3. Zone 2 represents the part of the resonator where the displacement is converted into the electrical signal.

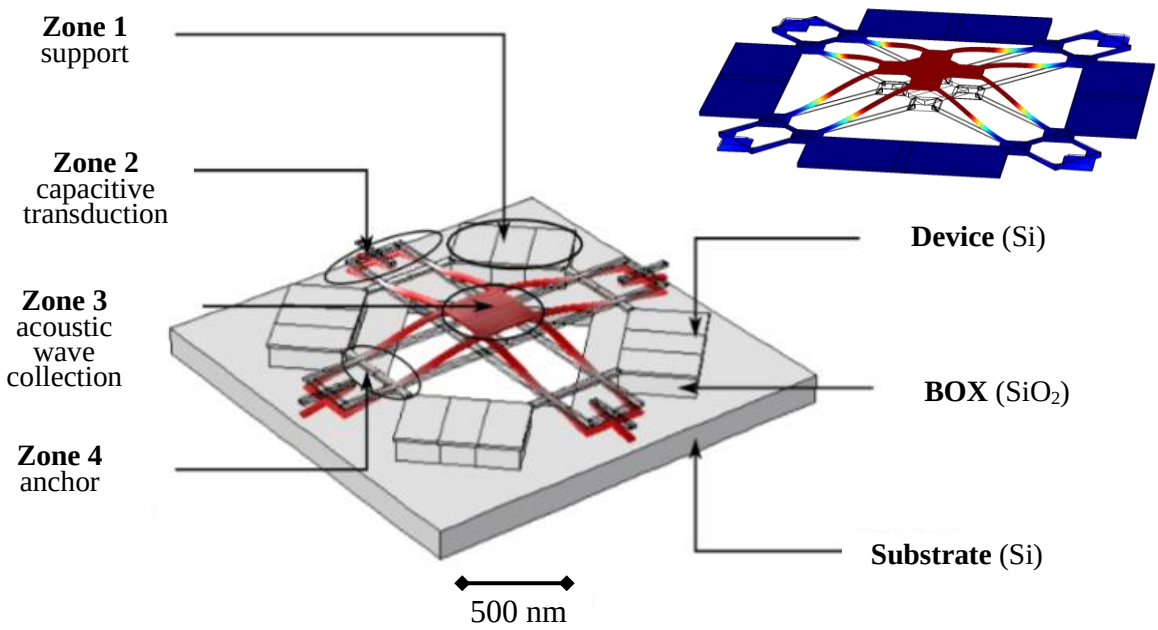

Figure 4.2.1. Geometry scheme of X-resonator with its four zones created on SOI wafer [2] together with picture form COMSOL simulation demonstrating the vibration mode of interest.

Zone 3 is the mobile part of the resonator designed to be the photoacoustic transducer. Its function is to maximize the harvesting of photoacoustic force in order to set the whole resonator in motion. The cantilever geometry optimization for this was presented in chapter 2, section 2.2. The results indicate that the surface area should be increased while also considering acoustic damping (chapter 2 figure 2.7.1).

The hole under zone 3, from now on called back etch, fulfills two functions:

a) **Avoid squeeze film effect** to get higher quality factor and displacement.

b) **Decrease the effect of an opposite displacement originating from zones 3 and 2.** Zone 3 moves in phase opposition to zone 2. Thus, capacitive changes from zone 2 will be opposite to capacitive changes in zone 3. These contradictory motions will result in capacitive signals in **phase opposition** and will decrease the overall capacitive signal.

Zone 2 is mobile and represents part of the device where the mechanical movement is converted into the electric signal via capacitive transduction. We target the mode of vibration presented in figure 4.2.1, as it will bring the highest capacitive signal because all extremities in zones 2 are moving in phase, creating a constructive interference. The geometry resembles thin cantilevers connected to each other. These thin cantilevers with vertical walls implemented in X-resonator decrease the contribution of the squeeze film effect in comparison to the 8-resonator. The capacitive signal depends on several factors. As presented in chapter 2, optimization of capacitive signal for a cantilever follows the trend for displacement (chapter 2, figure 2.4.1 and 2.5.2), which means that together with increase of the displacement, capacitive signal will increase in accordance with the following formula (chapter 2 equation (2.30)):

$$V_{out}(x,\omega) = V_{dc}\int_0^L \frac{W_n(x,\omega)}{Ld}\,dx \tag{4.1}$$

where $W_n(x,\omega)$ represents the displacement (chapter 2, figure 2.2.6 equation 2.30), d the distance between electrodes, L the length of the cantilever and V_{dc} the polarization voltage. Based on the same model, the displacement mainly follows the total quality factor trend with a shift towards smaller thicknesses due to the acceleration term (chapter 2, figure 2.3.9 and 2.4.1). For the small distance between electrodes, the quality factor is limited by viscous damping, and more particularly, the squeeze film effect. Optimization for zone 2 focuses on the minimization of this damping. It can be calculated with the model presented in chapter 2.

Zone 4 defines the coupling between zone 3 and 2 as well as coupling between zone 1 and all the resonators. Its position relative to zones 2 and 3 will determine the effective mass and the ratio of displacement between zones 2 and 3. This zone influences the quality factor of the support. To decrease the support losses, one needs to optimize the position and the width of zone 4. Compared to the 8-resonator, the support losses should significantly reduce by adding a zone 3, which spatially isolates the moving part (zone 1 and 2) from the support (zone 4).

Zone 1 holds the resonator. It needs to be sufficiently large to maintain the structure; however, increasing its size will increase the parasitic capacitance.

4.3. X-resonator 1st generation

This section presents the characterizations, simulations and gas sensing experiments for the first generation of designs, which decouples photoacoustic sensing from electrical transduction.

We have created several designs that differ among themselves with frequencies, thicknesses of the arms, and sizes of zones 1, 2, 3, and 4. The resonators' frequencies must be in the range 1-45 kHz [3] due to the thermal relaxation time of the molecules. The resonators with geometrical parameters are given in appendix A2.1. Variation of the arm's thicknesses aimed to study the squeeze film effect. Frequencies and zone 3 variation aimed to investigate photoacoustic force acting on the resonators. The first generation of the X-resonator sought to enhance photoacoustic gas sensing performance over 8-resonator. It was the first prototype of a resonator that decouples photoacoustic detection and capacitive sensing. This non-optimized design was a learning tool for the manufacturing process difficulties, understanding the physics, and proving the concepts. Subsequently, it was used for further designs optimization.

4.3.1 Characterization – Laser Doppler Vibrometer

This section introduces the tools that allowed us to evaluate resonators performances.

A high performance resonator should be characterized by high quality factor. First of all, to minimize energy losses. Secondly, to act as a band pass filter and finally to increase the mechanical susceptibility, which is directly connected to the displacement. Therefore, the quality factor was a criterion to compare the first generation of resonators among themselves.

The quality factor and resonance frequency can be retrieved by studying the frequency response of the resonator. Frequency response study is based on measurement of the resonators spectrum in response to a stimulus. We need a technique that allows dynamic analysis with a high resolution. Therefore, we chose to perform a frequency response study using Laser Doppler Vibrometer (LDV) as it is dynamic, real-time, and non-invasive. The measurement is performed on the focal point of the LDV laser spot, of size 3 μm (with a 10x microscope objective). Thus, compared to other techniques, LDV allows verifying the deflection and modes of vibration in different points of the resonator. For the measurements presented in this thesis, we used a Polytec Vibrometer OVF-5000 with a velocity decoder VD-06. Decoder VD-06 provides the best resolution for resonator's frequency range.

Presented in figure 4.3.1 setup for characterization includes a Laser Doppler Vibrometer, a camera, a vacuum chamber, a lock-in amplifier that also works as a function generator, and a piezoelectric element. The helium-neon laser beam from LDV is split by beam splitter BS1 into the reference and test beam, both of frequency f_{laser}. The test beam is then focalized onto the vibrating MEMS after passing through the second beam splitter BS2. The

beam is then reflected from the vibrating MEMS, adding a Doppler shift to the beam frequency due to the reflection from the vibrating object. This Doppler shift is equal to $f_D = \frac{2v(t)\cos(\alpha)}{\lambda}$, where $v(t)$ is a time dependent velocity of the MEMS, α is an angle between the velocity vector and the laser beam, and λ is a wavelength of the laser beam. The reflected beam, now of frequency $f_{laser} + f_D$ is redirected by BS2 onto a third beam splitter, BS3. The reference beam from BS1 passes through an acousto-optic modulator (AOM), which shifts its frequency by f_{AOM}. Following that, both beams are combined and directed toward a photodetector detector which responds to the beat frequency between two beams. Output from the photodetector is a standard frequency modulated FM signal with acousto-optic modulator frequency as carrier frequency and Doppler shift as modulation. This signal is subsequently demodulated to determine the MEMS' velocity in time.

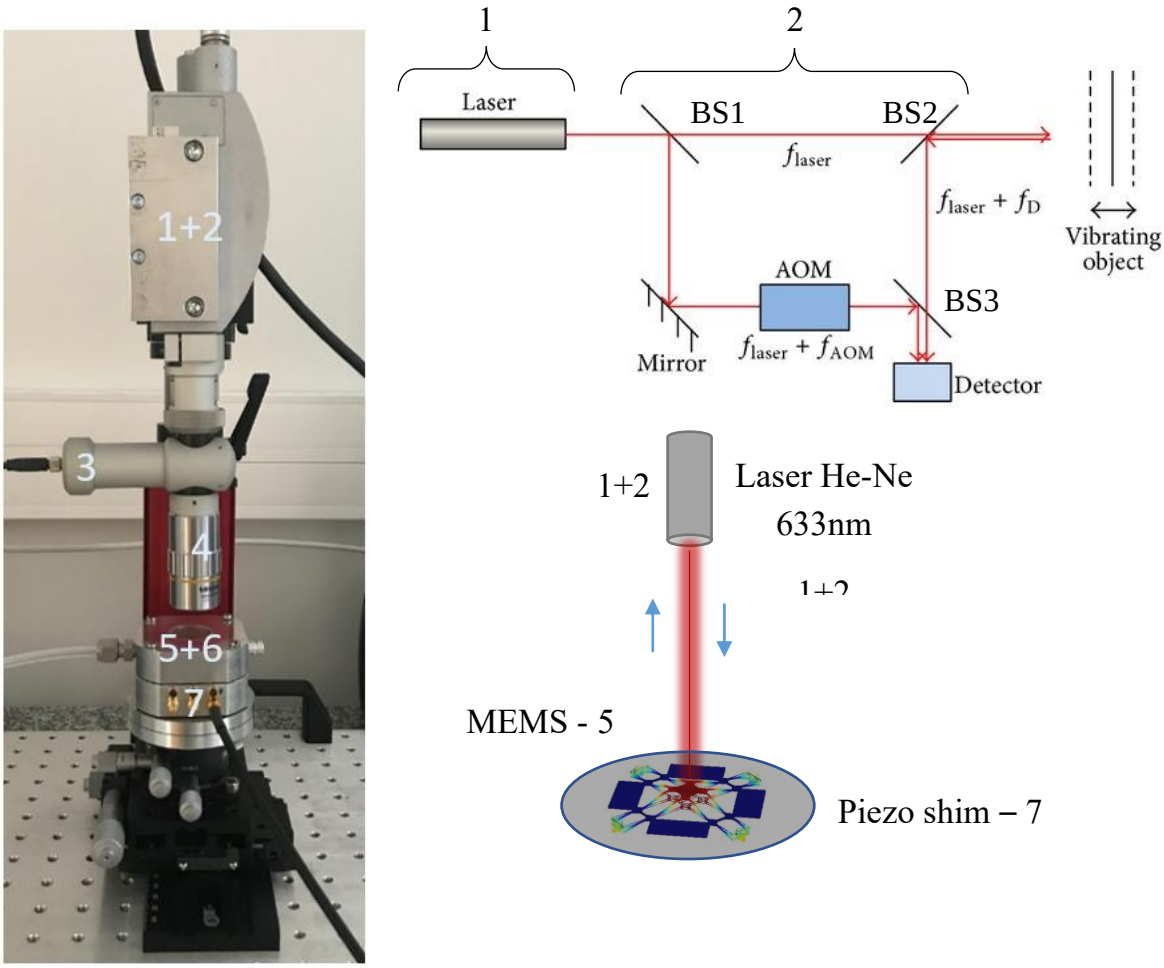

Figure 4.3.1: Setup for MEMS characterization. 1 – Laser, 2 – interferometer, 3 - camera, 4 – optical objective 10x, 5 – MEMS; 6 – chamber for characterization under vacuum or in the presence of certain gas (like for PA measurement), 7 – piezo element for MEMS excitation.

Primarily, the resonator needs to be set in motion. For this, we used a piezoelectric crystal on top of which we mounted the MEMS. A Lock-in amplifier sends an electric signal at a fixed frequency and voltage, causing vibration of the piezo shims at a chosen frequency. Subsequently, the vibrating piezo element causes the vibration of the MEMS.

The resonator's response is expected to be characterized by a Lorentzian line shape. As an example, figure 4.3.2 illustrates the frequency response from sample XRE.F6 retried via LDV. Plot (figure 4.3.2) was made using a Python programming environment. Violet points represent the experimental data, the green curve a Lorentzian fit, and the yellow lines cross the point for which the bandwidth Δf was calculated.

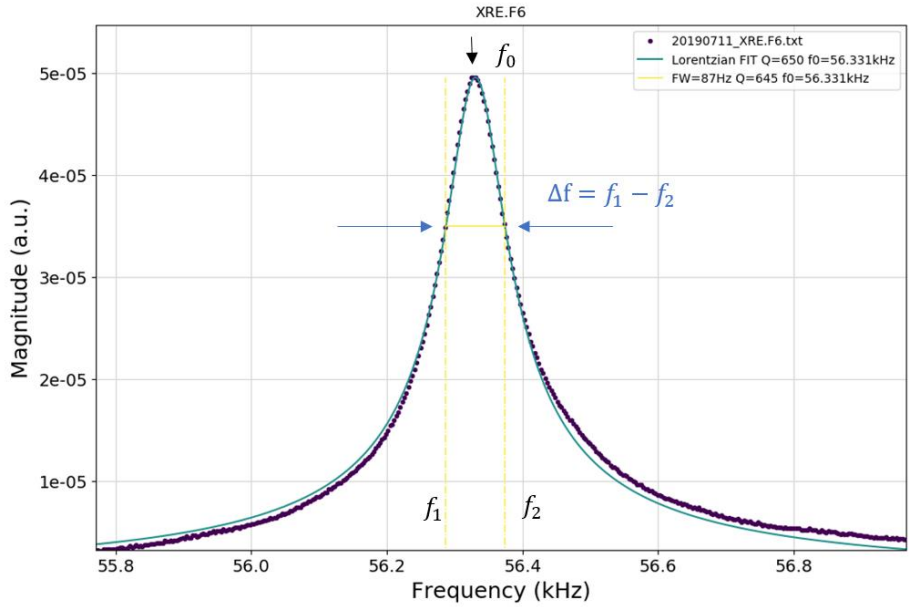

Figure 4.3.2: LDV measurement at 1atm using velocity decoder VD-06, sensitivity 2mm/s/V, excitation voltage 100 mVpk. Violet points represent experimental data, the green line represents a Lorentzian fit, and the yellow lines are the crossing points, thanks to which we calculated the bandwidth Δf.

The experimental data are fitted with a Lorentzian profile (green curve, figure 4.3.2) using the following equation [4]:

$$|L(\omega)| = \frac{w_{max}}{\sqrt{\left(\sqrt{\omega_0^2 - \omega^2}\right)^2 + (2\xi\omega_0\omega)^2}} \qquad (4.2)$$

Where ξ is a damping coefficient, ω_0 the resonance pulsation, $w_{max} = L_{max} 2\xi\omega_0\omega$, where $L_{max}$is an amplitude. Based on the fit, the quality factor Q is calculated in Python code using the following formula:

$$Q = \frac{1}{2\xi} \tag{4.3}$$

The yellow lines in figure 4.3.2 are used to calculate the quality factor numerically using the equation :

$$Q = \frac{f_0}{\Delta \mathrm{f}} \tag{4.4}$$

where f_0 is the resonance frequency and Δf is a frequency bandwidth. The program works in the following manner:

1) It determines the maximum of the curve, retrieves its index and y value. The value of the maximum on the x-axis corresponds to the resonance frequency f_0.
2) The maximum value L_{max} is divided by $\sqrt{2}$, $\frac{L_{max}}{\sqrt{2}}$. The indexes for a value equal to $\frac{L_{max}}{\sqrt{2}}$ correspond to f_1 and f_2 and $\Delta f = f_2 - f_1$

Frequency response measurements were performed on Polytec Vibrometer OVF-5000 using a velocity decoder VD-06. Decoder VD-06 provides the best resolution (0.01 μm/s) for resonator's frequency range (1-100kHz). The quality factor calculated by Lorentzian fit is 650, while the quality factor calculated with equation (4.4) is 645. Thus, the relative uncertainty between the two methods in the case of the presented measurement is less than 1%. This uncertainty depends on a number of points, time constant set on the lock-in amplifier, and waiting time between two measurement points. To obtain reliable values for the device characterization using the frequency sweep technique, the distance between two points needs to be relatively close while the time constant is relatively high [5]. The quality factor of the resonator dictates these exact parameters. For instance, to have a fair accuracy, the number of points in bandwidth Δf should be at least 50. Therefore, the distance between the two closes points δf will be given by: $\delta f = \frac{f_o}{50Q}$. The time constant between the measurement of each point should be at least three times higher than the resonator's response time calculated with the following equation: $\tau = \frac{Q}{2\pi f_0}$. For instance, for QTF of the quality factor of 10000 and resonance frequency 32.73 kHz $\tau \approx 490\, ms$ and $\delta f \approx 0.07 Hz$; while for a resonator of quality factor 650 and resonance frequency 53 kHz (figure 4.3.2) $\tau \approx 2\, ms$ and $\delta f \approx 1.6\, Hz$.

4.3.3.1. Reliability of measurement

Besides the choice of the piezo shim, other factors influence the reliability of the MEMS characterization using LDV:

1) **Excitation voltage:** high excitation voltage might cause high displacement which will bring non-linear effects. To avoid this effect, one needs to use low excitation voltage (<100mV).
2) **Modes of vibration for piezo element:** in our study, a piezoelectric material is in the shape of a membrane. Like any membrane, it has its mode of vibration, which indicates that the middle part represents a different frequency response than the extremities. To reduce the uncertainty of this effect, the sample should always be placed in the same area on the piezo element. In the case of the X-resonator, the sample size is 1cm x 1cm, while the MEMS itself is centred in the middle.

4.3.3.2. Results and discussion

We have created designs, families of the resonator with arms sizes in the range between 5um (XRE.F) to 50 μm (XRE.R 40 μm, XRE.G 21μm), the total length of the resonator (figure 4.3.3 red arrow) in the range between 1700 μm to 3900 μm, support size (ZONE 1) in the range 600 μm to 1300 μm, frequency range 31kHz to 85kHz, and variation of the zones 2, 3 and 4. Appendix A2.1 contains information about geometrical parameters different resonators.

Table 4.3.1. Table summarizing the sample characteristic and process. Appendix A2.1 contains information about the manner of naming samples and expected dimensions.

SAMPLE	Process report	Characteristic		Capacitive signal
		Resonance frequency f_0	Quality factor Q	
XRE.D1	Part of resonator damaged during releasing of the device with liquid HF	-	-	-
XRE.V1	It was damaged during the fabrication process.	-	-	-
XRE.G1	It was damaged during the fabrication process.	-	-	-
XRE.R1	Sample released, characterized, damaged during characterization process.	34.5 kHz	64	NO
XRE.S1	Damaged during fabrication process.	-	-	-
XRE.C1	Sample over etched with KOH solution	-	-	-
XRE.F1	Sample released, characterized and damaged during characterization process.	37 kHz	430	-

XRE.F3	Sample released and characterized	57.9 kHz	300	NO
XRE.F4	Damaged during the fabrication process.	-	-	-
XRE.F5	Sample released and characterized	53.1 kHz	710	YES
XRE.F6	Sample released and characterized	56.4 kHz	650	-
XRE.C2	Sample released and characterized	70.7 kHz	400	NO
XRE.G2	Sample released and characterized	59.8 kHz	440	YES
XRE.R2	Sample released and characterized	35.4 kHz	60	NO
XRE.E2	Sample released and characterized	89.8 kHz	270	NO

Data from the characterization of resonators have been ordered chronologically and presented in table 4.3.1. The first half of the entire sample set are test samples based on which we discovered some difficulties imposed by the fabrication process: back etch and vertical etch. Subsequently, we have found a way to overcome these difficulties, which is seen in the second half of the entire sample set, for which we got 88% of success in the fabrication process. The fabrication process is presented in chapter 3.

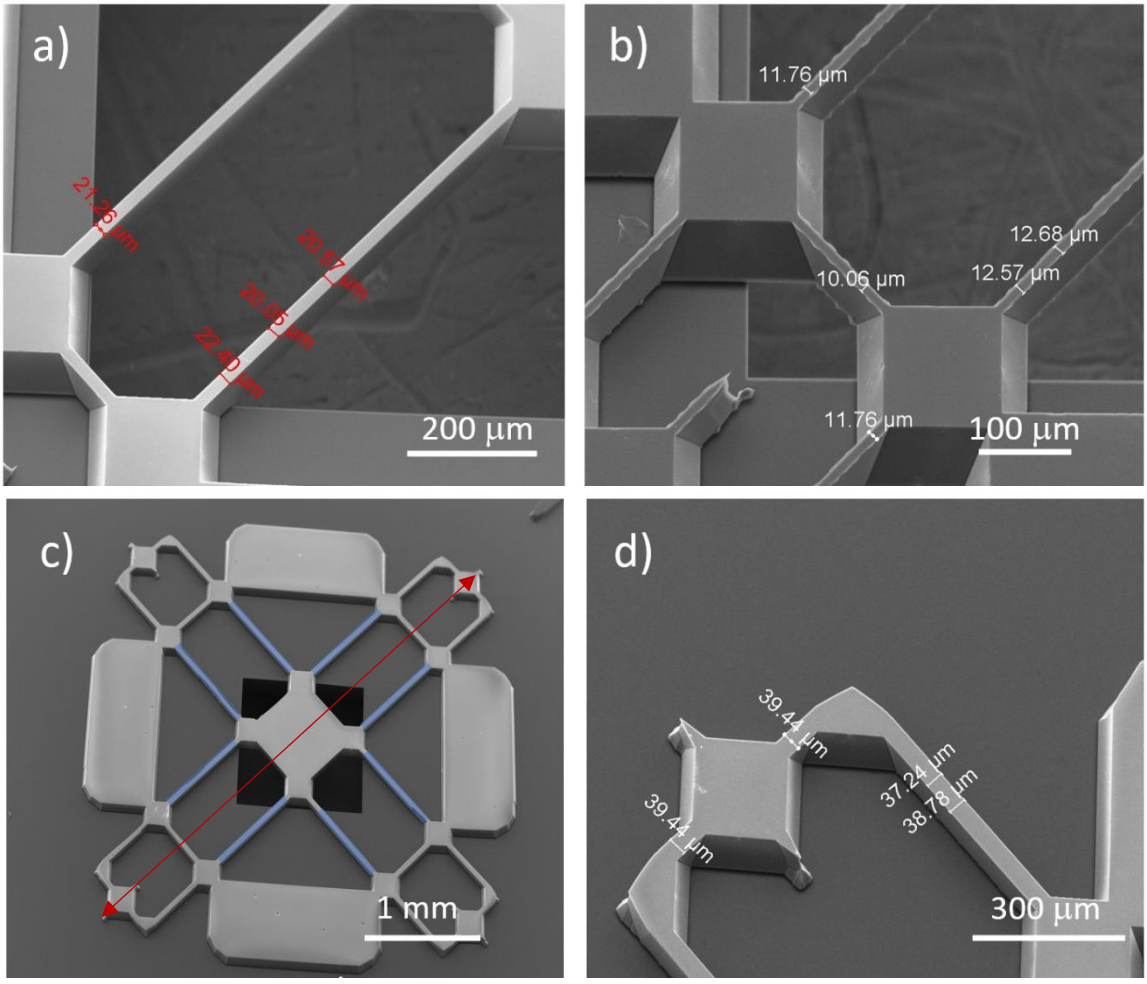

Figure 4.3.3: Scanning electron microscope picture of a) XRE.G2, b) XRE.C2, c) d) XRE.R2

The differences between the quality factors between different families (XRE.G: figure 4.3.3a; XRE.C: figure 4.3.3.b; XRE.R: figure 4.3.3.c,d) is connected with the width of the arms and total size of the resonator, which is visible in figure 4.3.3. As presented in figure 4.3.3 R-family (figure 4.3.3.c,d) is characterized by the widest arms. As we might have some issues with smooth walls in the case of F- family, it can be seen that XRE.G and XRE.R (figure 4.3.3a and b) are characterized by smooth vertical walls, which were obtained thanks to piranha cleaning (chapter 3).

Misalignment between the back etch, and the device and the size of the back etch is another cause of variance in the quality factor. Figure 4.3.3c shows an example of misalignment as well as an issue with the size of the back etch. The structure is not well centered relative to the back etch, which is referred to a misalignment issue. On the other hand, a too small back etch presented in figure 4.3.3c will cause more damping. A blue mark was placed on the resonator in figure 4.3.3c to indicate where the squeeze film might be avoided by using an appropriate size of the back etch.

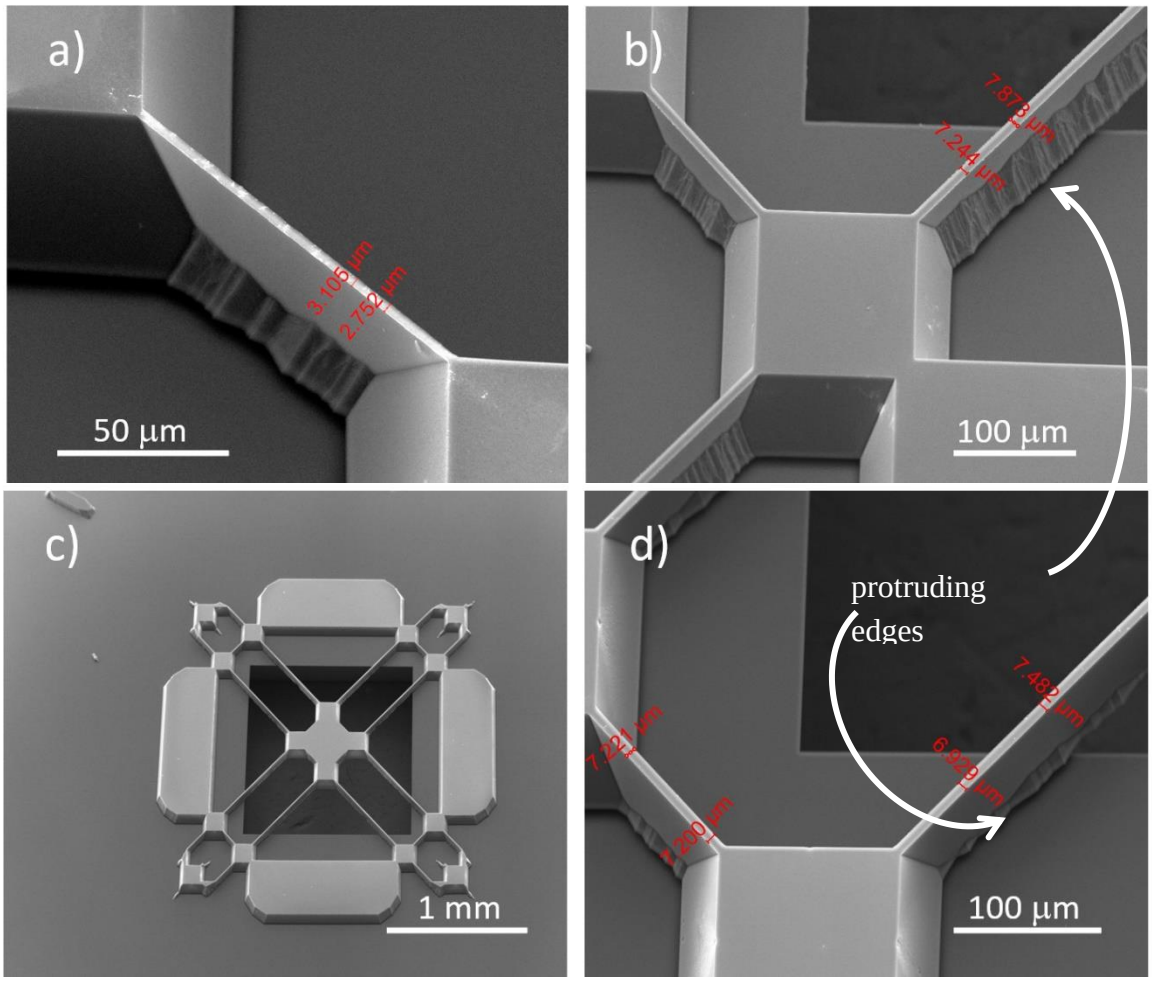

Figure 4.3.4: Scanning electron microscope picture of a) XRE.F1, b) XRE.F3, c) d) XRE.F5

Unfortunately, the collected data present high frequency and quality factor discrepancy for the same resonator's family. We analyzed the pictures from scanning electron microscopy in an attempt to identify a reason for these differences. Figure 4.3.4 depicts images of the F-family. The problem with differences between the frequencies seems to be connected with the reproducibility of the fabrication process. Namely, samples from the same family vary in terms of arm thickness. For instance, XRE.F3 (figure 4.3.4b) is distinguished by the thickest arms and the most prominent protruding edges (chapter 3, section 3.6). As a result, the surface area of the device's bottom side is increased by the protruding edges, and more air is trapped between the electrodes, increasing the squeeze film effect. This squeeze film effect leads to a decrease in the quality factor of the resonator. To summarize, variations between the quality factors and frequencies among one family of resonators is caused by inhomogeneity and repeatability issues.

Due to a large amount of data, we will only discuss results from designs that have provided considerable insight into device performance and physics cognition. Therefore we decided to present further data only from XRE.F5 and consider only this design for further optimization. The choice of XFRE.F5 was dictated by the high quality factor and the fact that we could get the capacitive detection. The characterization of XRE.F5 is presented in figure 4.3.5.

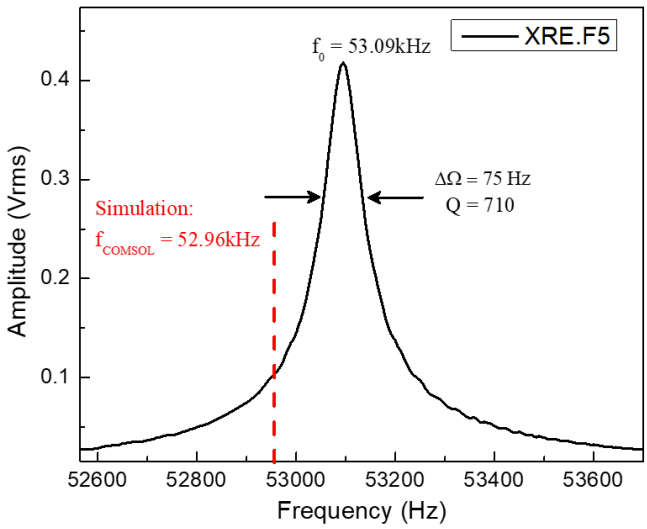

Figure 4.3.5: Frequency response of XRE.F5 obtained via LDV measurement with a piezoelectric excitation. The red line represents the frequency of the resonator from the COMSOL simulation.

4.3.2. COMSOL simulation

To calculate the mechanical susceptibility, the quality factor of the support and to create a tool for further optimization, we performed a theoretical study of the mechanical parameters of the resonator. For this, we used COMSOL software (chapter 2, section 2.8). Frequencies, effective masses and support losses have been examined concerning vibration modes.

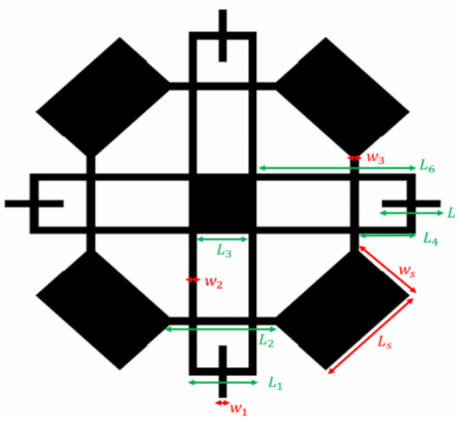

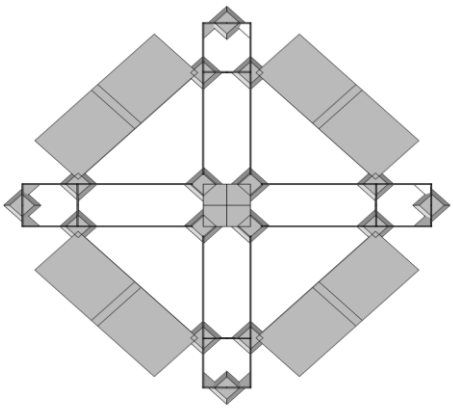

symbol	mask [um]	after fabrication
w_1	9.8	square ~160um
w_2	9.8	7um
w_3	9.8	~ 120um
L_1	315	330
L_2	608	-
L_3	295	315
L_4	364	245
L_5	402	
L_6	1180	
L_s	1061	
w_s	260	

Figure 4.3.6: a) Geometry scheme of XRE.F presented on the photolithography mask and b) geometry scheme which represents XRE.F after fabrication. Figure presented on the right panel was created using COMSOL Multiphysics Software.

The results of the mechanical parameters from the COMSOL simulation are presented in table 4.3.2.

4.3.2. Characteristic of XRE.F5 resonator calculated using COMSOL Multiphysics Software.

Type	Frequency [kHz]	Mass [μm]	Effective mass [μm]	Q support	Area for PA energy [mm^2]
XRE.F5	52.96	0.226	0.0173	17735	0.1

Figure 4.3.7. shows resonators' modes of vibrations and their corresponding frequencies. We are working on a fundamental mode of vibration located at 52.96kHz. Compared to other modes, this one provides the most efficient convertion of mechanical movement to the capacitive signal due to the arms moving in phase. This movement in phase will create a constructive interference between capacitive signals originating from each of the extremities. Other modes are localized above 100kHz.

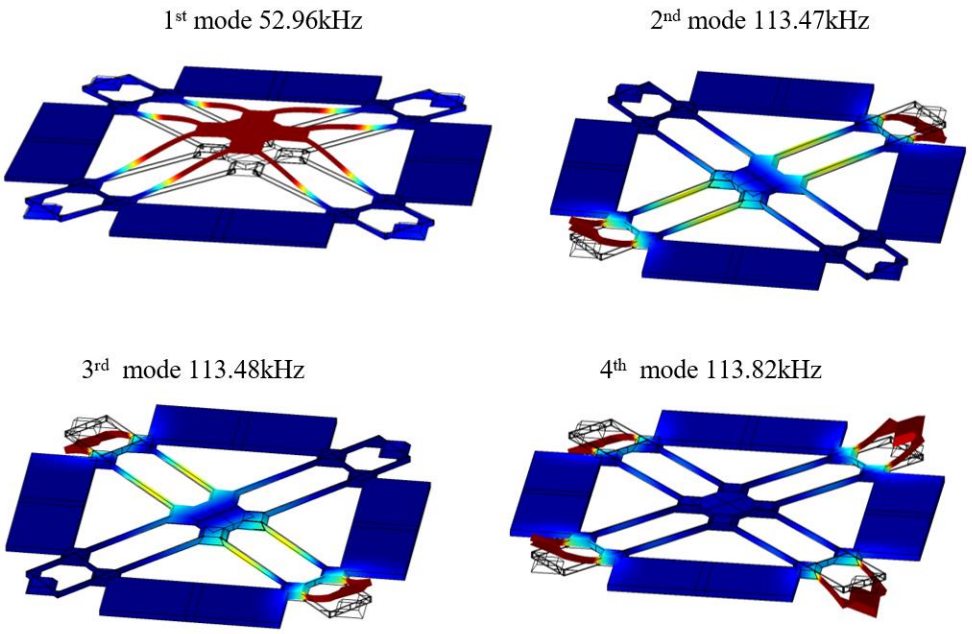

Figure 4.3.7: Modes of vibration for XRE.F with the corresponding frequencies calculated using COMSOL Multiphysics Software.

The conducted simulation presents a fair agreement with the experimental data (figure 4.3.5). This ensures a reliable estimation of effective mass and support quality factor. Higher modes are located far from the fundamental mode, preventing crosstalk between the fundamental and higher modes.

4.3.3. Gas detection

The goal of the research is to create a photoacoustic gas sensor with capacitive transduction characterized by superior performances over 8-resonator [1]. Therefore, the next step is the implementation of the fabricated resonators in gas sensing with capacitive transduction. This section aims to present the results from gas detection obtained with XRE.F5.

4.3.3.1. Setup

Figure 4.3.8 illustrates the setup, which includes a laser source controlled by a laser driver with a temperature controller that regulates the laser's current and temperature. The laser light is collimated in the gas chamber above the resonator. If the modulation laser light is absorbed by the gas, the interaction between the laser and gas creates a photoacoustic wave that causes the resonator's mechanical movement.

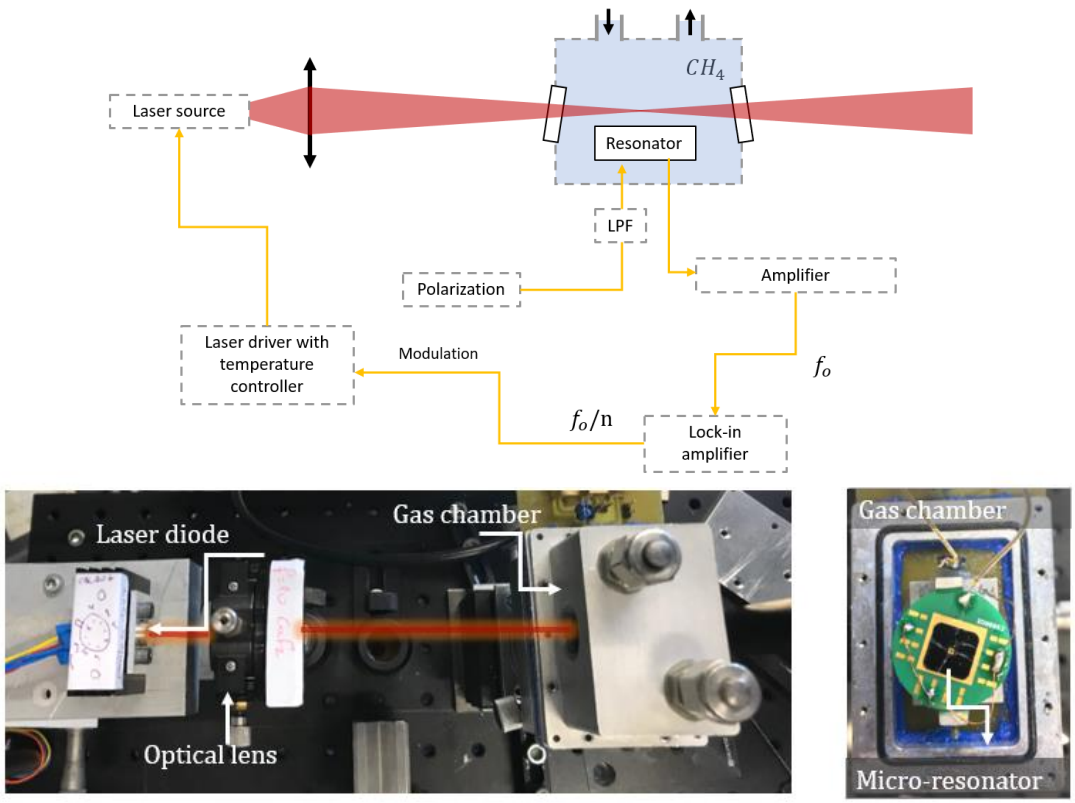

Figure 4.3.8: Scheme of the experimental photoacoustic setup with capacitive detection. The laser current is modulated at n-harmonic (n=1 for 1f detection, n=2 for 2f detection). The signal from the resonator is amplified and demodulated by the lock-in amplifier. LPF indicates a low pass filter.

To generate the electrical signal from the mechanical movement of the resonator via capacitive transduction, the resonator must be polarized [6]. In our experiments we used the voltage in range between 15 V and 27 V. Current from the resonator is amplified and converted into a voltage using current amplifier LCA-100K-50M. The signal is demodulated at the laser modulation frequency using a lock-in amplifier.

4.3.3.2. Laser

To detect one of the methane lines, we use an Eblana (EP1653-7-DM-TP3901) commercial distributed feedback laser (DFB) with an emmited wavelength of 1.63 μm operating in a continuous regime in ambient temperature.

In an ideal DFB laser, the central spectral peak contains all the power produced by the device. In reality, the laser signal includes some power in the side peaks, also known as side modes. A DFB laser's side-mode suppression ratio (SMSR) describes the amplitude difference between the main and largest side modes in decibels. A SMRS value for DFB laser is greater than 30 dB and it indicates that most of the power is in the main mode.

SMSR of Eblana laser is 53dB. Its threshold is 20 mA and it reaches a power of 7 mW for 120 mA. The tunability based on the datasheet is estimated to be 0.01nm/mA at 22°C. Figure 4.3.9a presents the tunability of the laser for different temperatures. This tunability is sufficient to scan the absorption line of the methane localized at 1.6537 µm, illustrated in figure 4.3.9b (HITRAN [7] database). To target the methane absorption localized at 1.6537 µm, the temperature on the laser driver is fixed at 25°C.

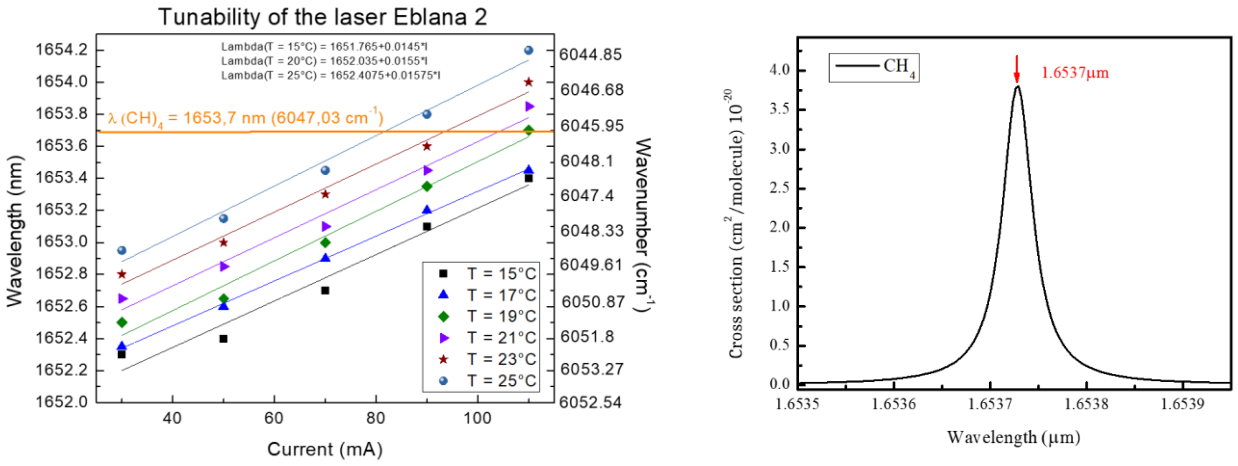

Figure 4.3.9. (a) Wavelength and tunability of the Eblana DFB laser as a function of temperature and injected current. (b) Methane cross-section centered at 1.6537 µm at atmospheric pressure obtained using HITRAN database [7]

4.3.3.3. Conditioning circuit

The resonator's vibration causes capacitive variation that must be detected using a conditioning circuit called DC bias [8]. Figure 4.3.10. presents a conditioning circuit. The charges are injected into the MEMS by bias V_{DC}. Any real DC source is burden with AC noise. This noise originates from stray mutual inductance and stray capacitance, and it might cause severe problems in circuits. To prevent the noise from reaching MEMS, we apply a low-pass filter (figure 4.3.10 green box) that will cut the noise localized above the cut-off frequency $f_c\ (Hz)$, according to

$$f_c = \frac{1}{2\pi R_f C_d} \tag{4.5}$$

The value of cut-off frequency f_c needs to be much smaller than the resonance frequency of the resonator f_o: $f_c << f_o$. For this, values of resistance R_f and decoupling capacitor C_d need to be adjusted. The cut-off frequency f_c is connected with the time constant $\tau_c = \frac{2\pi}{f_c}$. τ_c must be small enough to cut maximum of the noise and simultaneously charge the capacitor (resonator)

in a reasonable time. The relation between the voltage across the resonator V_R, at any time t of charging period is given with equation :

$$V_R = V_{DC}(1 - e^{\left(-\frac{t}{\tau_c}\right)}) \tag{4.6a}$$

The time to reach 99% of the polarization voltage ($V_R = 99\% \cdot V_{DC}$) can be calculatred with:

$$0.99 = 1 - e^{\left(-\frac{t}{\tau_c}\right)} \tag{4.6b}$$

$$t = -\ln(0.01)\,\tau_c \tag{4.6c}$$

where t is the time required to reach charge on the resonator 99% of the polarization voltage.

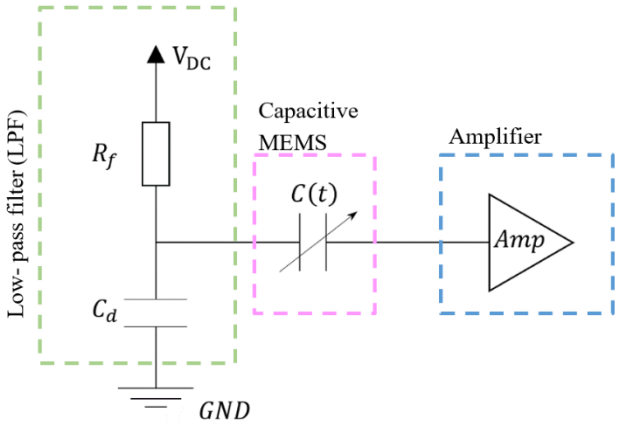

Figure 4.3.10: Sensor conditioning circuits: V_{DC}, R_f, C_d, C(t), Amp, GND are the polarization voltage, resistance, decoupling capacitor, variable in time MEMS capacitance, amplifier, and ground, respectively. R_f = 2 MΩ, C_d = 100 nF, V_{DC} change in range between 15V to 27V

We used R_f = 2 MΩ and C_d = 100 nF (f_c=0.8 Hz, τ_c = 4.6 s, t = 18s) for the measurement presented in the following section. C(t) marked in figure 4.3.10 is a capacitance of the MEMS, which varies in time in response to the resonator movement.

4.3.3.4. Characterization

This section shows the characterization of the resonator using photoacoustic wave as the excitation source. Subsequently, the movement of the resonator is converted into an electric signal and detected via capacitive variation.

The results from the photoacoustic characterization of XRE.F5 with capacitive read-out mechanism is presented in figure 4.3.11. The phase change visible on the right panel confirms the resonance. The quality factor calculated based on the Lorentzian fit is 710.

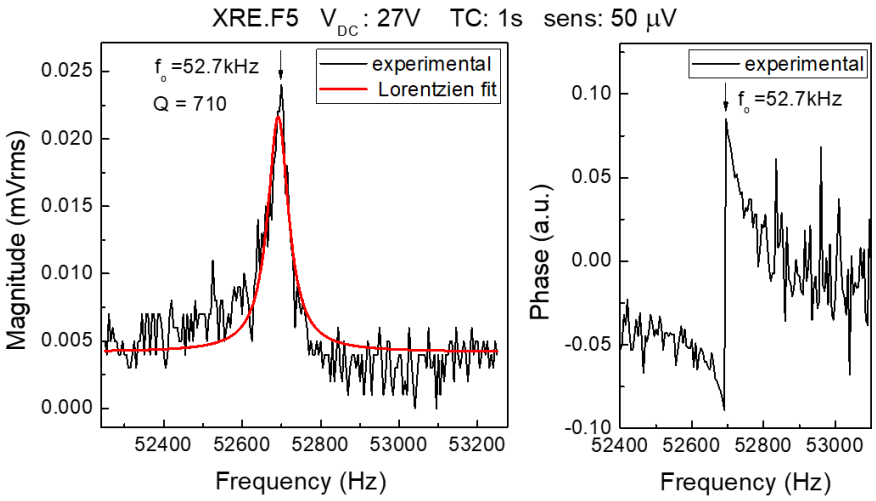

Figure 4.3.11: Capacitive measurement XRE.F5 resonator frequency response with 100% CH_4 for polarization voltage V_{DC} = 27V. The red curve represents a Lorentzian fit. The time constant on lock-in amplifier TC: 1s, sensitivity on the lock-in amplifier sens: 50 µV.

4.3.3.5. 1f detection

The micro-resonator is sensitive to photothermal noise. This implies that even in the absence of the target gas, the resonator may be set in motion, resulting in the generation of an undesired electric signal. This photothermal signal originates from the absorption of the laser light by silicon. To prove the photoacoustic effect and identify the gas, we use wavelength modulation spectroscopy WMS (appendix A1). In this method, laser light scans the absorption line linearly by changing the output wavelength λ(t) of the laser through the current sweep.

These techniques generate a modulated signal $\tilde{L}(t)$ (appendix A1), which consists of periodic components with the modulation frequency f_m and higher harmonics of the spectrum. Scanning the absorption line allow identification of the gas and proves the photoacoustic detection. The signal can be later on demodulated using a lock-in amplifier. The signature of the measured signal in 1f detection corresponds to 1st derivate of the absorption spectrum and is presented in figure 4.3.12.

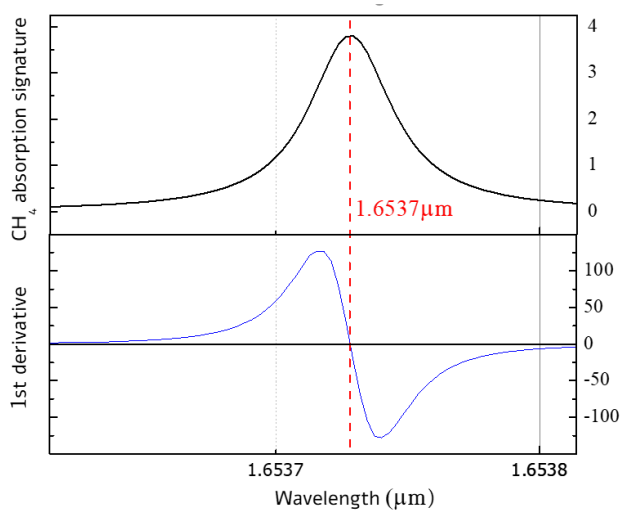

Figure 4.3.12: Signature of methane absorption (upper panel) and the first derivative of methane absorption (bottom panel).

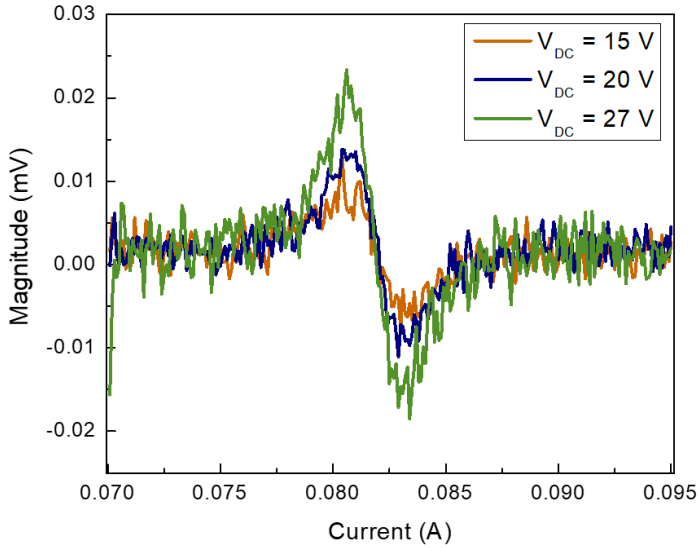

Figure 4.3.13: Capacitive measurement XRE.F5 resonator of the first harmonic. Signal obtained by absorption of 100% CH_4 at atmospheric pressure for different polarization voltage. Eblana DFB laser emitting at 1.63 µm with an output power 2.5 mW for a current of 80 mA. Conditions of the measurement: time constant 500 ms, sensitivity set on the lock-in amplifier: 50 µV

The 1f signature of the CH_4 absorption (figure 4.3.13) was identified by performing a spectral scan through tunning of the driving current. According to equation (4.1) the voltage output should be proportional to the polarization voltage. The results for XRE.F5 are depicted in figure 4.3.13 present clear 1f signature. Moreover, as expected, the signal increases with the polarization voltage, which is a proof of capacitive detection. The amplitude of the signal is expected to grow linearly with polarization voltage. Nevertheless, estimation of the signal amplitude based on figure 4.3.13 is not reliable due to the significant noise.

4.3.4. Discussion and conclusions

We have designed and fabricated a set of resonators that decouples photoacoustic sensing and capacitive transduction. Thanks to decoupling and fabrication process, we managed to reduce the squeeze film effect. We have chosen a resonator with the highest quality factor: XRE.F5 and implemented it in photoacoustic gas sensing using a capacitive transduction mechanism.

4.3.3. Selected features of Selected resonators.

RESONATOR	8-resonator	XRE.F5
f_0 [kHz]	14,7	52,96
Q-factor	140	810
Effective mass [μg]	47	17
Susceptibility [s^2/kg]	$1.37 \cdot 10^{-2}$	$1.7 \cdot 10^{-2}$
Capacitive signal [μV]	200 (for polarization voltage 30V)	22 (for polarization voltage 27V)
Area for photoacoustic $A_{PA}[mm^2]$	1.5	0.1
Acoustic pressure p_{PA} [μPa] (for CH_4 1%) (chapter 2, figure 2.2.3)	2.6	1.6
Acoustic force [pN]	3.9	0.16
Capacitive area A_0 $[mm^2]$	2.4	0.17
Support area A_p $[mm^2]$	0.7	0.65

Table 4.3.3 contains characteristics of the XRE.F5 and 8-resonator. We compared the resonators based on the criteria which are connected with the sensor performances:

- photoacoustic force
- effective mass,
- quality factor,
- high susceptibility

Because of the anisotropic etching of silicon, the capacitive area in the 8-resonator is greater than the photoacoustic area (chapter 3, section 3.6). In spite of improving the quality factor, effective mass and mechanical susceptibility, XRE.F5 is characterized by a ten times lower capacitive signal from photoacoustic gas detection than 8-resonator (CH_4 concentration 100% and same laser). The results are comparable due to the same conditioning of the experiments. We identified two reasons for a low and noisy capacitive signal from XRE.F5 (figure 4.3.12 and figure 4.3.13):

a) Low photoacoustic force: 8-resonator is characterized by a higher surface for photoacoustic energy collection and lower resonance frequency. Because of the difference in area and resonance frequency, the photoacoustic force is approximately 18 times higher for the 8-resonator than for the XRE.F5. The

acoustic force was calculated using equation chapter 2, section 2.2 equation (2.10). However, in the calculation, we did not take into account a mode shape. Thus, we suppose that photoacoustic force in case of the 8-resonator was overestimated.

b) Low attenuation factor: the attenuation factor may potentially be the reason for a low capacitive signal in the case of XRE.F5. The voltage output is multiplied by a factor known as the attenuation factor S_A, represented by the equation below [9]:

$$S_A = \frac{C_0}{C_0 + C_p} \tag{4.7}$$

where C_0 and C_p are nominal and parasitic capacitance, respectively. The capacitance is a function of the electrodes overlapping area A, the distance between the plates d, the permittivity of the media ε_r and the permittivity of the vacuum ε_r : $C = \frac{\varepsilon\varepsilon_r A}{d}$. The dielectric constant of the air and silica differs with a factor 3: $\varepsilon_{SiO_2} \approx 3\varepsilon_{air}$. Distance between the electrodes remains constant. Therefore, equation (4.7) can be simplified to:

$$S_A \approx \frac{1}{1 + \frac{3A_p}{A_0}} \tag{4.7b}$$

where A_p is the area of the parasitic capacitance and A_0 is the area of nominal capacitance. In the case of the 8-resonator, A_0 is roughly four times higher than for XRE.F5. The accurate calculation of the attenuation factor is complicated due to the tricky estimation of silicon oxide under etch below zone 4. The dielectric constant of silica is about three times greater than the dielectric constant of air; thus, underestimating the area of the oxide layer will result in a significant difference in attenuation factor. For the same area $C_p = 3C_0$. To avoid a misestimation of the attenuation factor, we solely compared areas for nominal A_0 and parasitic capacitance A_p.

Despite quality factor improvement in XRE.F5 in comparison to 8-resonator, the capacitive signal from photoacoustic gas detection via capacitive transduction was ten times better for 8-resonator than for X-resonator. This comparison helped us to identified weaknesses of XRE.F5 in comparison to 8-resonator. Namely, low photoacoustic force (due to the surface and resonance frequency) and low attenuation factor S_A.

It is worth noting that the 1st generation was more a tool to prove the concept of problem separation, leading to quality factor improvement, overcoming the fabrication challenges, understanding the physics and issues. Based on this design, we created a new generation of X-resonators. The family of X-resonators 2nd generation is presented in the next section. The designs from each family aimed to address a solution for one problem identified with 1st generation of X-resonator.

4.4. X-resonator 2nd generation – F-family

The second generation of X-resonators is an evolution of the first generation of X-resonator. Thanks to this design, we increased Q factor and introduced decoupling of problems, which led to a measurement of the capacitive signal under photoacoustic gas excitation. For that reason, we focused on this geometry. We attempted to improve this design by slightly modifying its geometrical parameters: increasing the number of arms (zone 2) and changing the size of the middle part (zone 3). As a result, we created three families presented in figure 4.4.1.

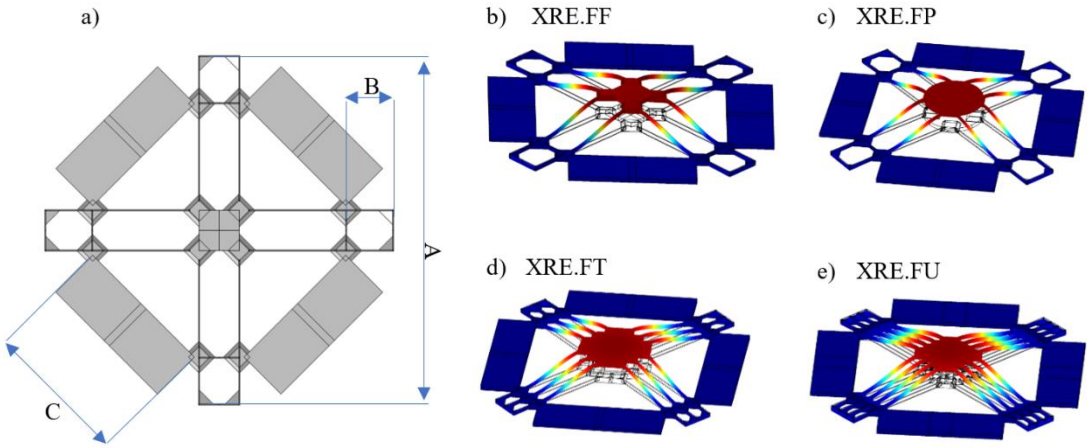

Figure 4.4.1: a) Geometry scheme of XRE.FF created in COMSOL Multiphysics Software. For XRE.F, XRE.FF, XRE.FP, XRE.FT and XRE.FU dimensions A, B and C are equal. First mode of vibration modelized using COMSOL Multiphysics Software for resonator: b) XRE.FF, c) XRE.FP, d) XRE.FT, e) XRE.FU

Dimensions A, B, and C marked on the figure are constant. Each family is supposed to address a different issue concerning XRE.F5

a) FF family –This geometry is addressed to fix the issue caused by the squeeze film effect at the extremities of the resonator XRE.F5. Therefore, we eliminated the extra arm in zone 2 (a square resulting from anisotropic etching).
b) FP family - geometry is addressing the photoacoustic energy collection. It is a variation of FF family, characterized by a higher surface for photoacoustic energy collection: we increased the size of the zone 3 compared to the FF family.
c) FT, FU family – is supposed to address the issue of capacitive sensing and more precisely aims to increase the attenuation factor S_A. We have focused on increasing the nominal capacitance to improve the attenuation without significant change of the geometry. Therefore, the difference between this family and others relies on the numbers of arms – the area of zone 2 increased compared to FF and FP families. In FT family, each of the 4 extremities are divided into 3, resulting in 12 moving arms. In FU family, each of the four extremities is divided into four, resulting in 16 moving arms.

Table 4.4.1 summarizes a study conducted on 2nd generation of X-resonators using COMSOL software. An eigenfrequency analysis was used to determine the vibration modes and frequencies.

Table 4.4.1: Characteristic of some of the resonators calculated using COMSOL Multiphysics Software.

Type	Frequency [kHz]	Mass [µg]	Effective mass [µg]	Q support	Area for PA energy [mm^2]	Capacitive area A_0 [mm^2]
XRE.F	52.96	226	17.3	17735	0.16	(0.4)
XRE.FF	52.98	218	17.2	18185	0.16	0.33
XRE.FP	43.02	200	18.7	17936	0.31	0.33
XRE.FT	53.04	246	35	13852	0.16	0.4
XRE.FU	62.64	247	24.7	8050	0.17	0.58 (0.8)

4.4.1. Quality factor enhancement

FF family of 2nd generation of X-resonator was designed to increase the quality factor in comparison to XRE.F5. Figure 4.4.2. present the SEM picture of both resonators. The part responsible for high squeeze film damping is marked in red (figure 4.4.2.).

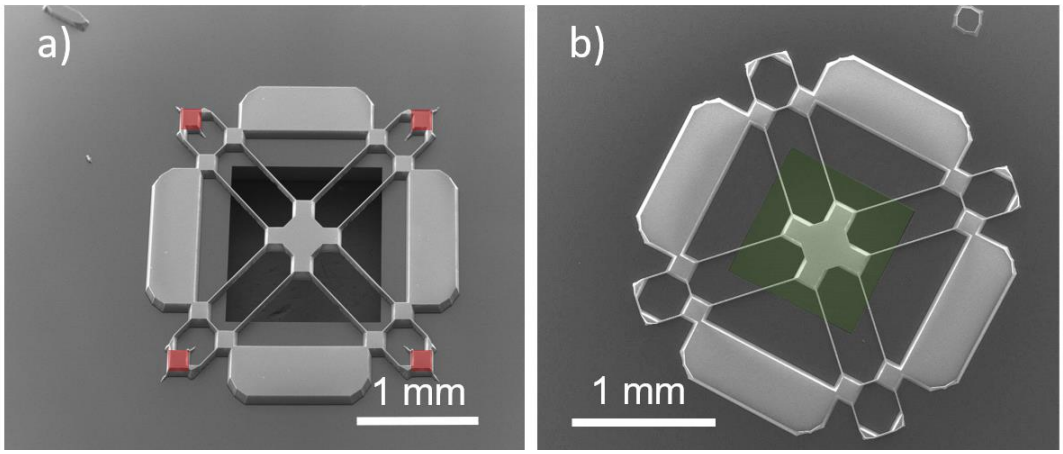

Figure 4.4.2. Scanning electron microscope picture of a) XRE.F5, b) XRE.FF2.

In the FF family, here XRE.FF2, we removed it. This treatment should decrease the squeeze film effect and consequently increase the quality factor of XRE.FF(figure 4.4.2b) in comparison to XRE.F (figure 4.4.2 a).

We have characterized them by performing a frequency response. The results are presented in figure 4.4.3. Indeed, we managed to increase the quality factor; thus, our hypothesis was correct. Moreover, we believe that the quality factor of XRE.FF2 could be increased even more by increasing the back etch, marked in green in figure 4.4.2, as in XRE.F5 the back hole is bigger than in the case of XRE.FF2.

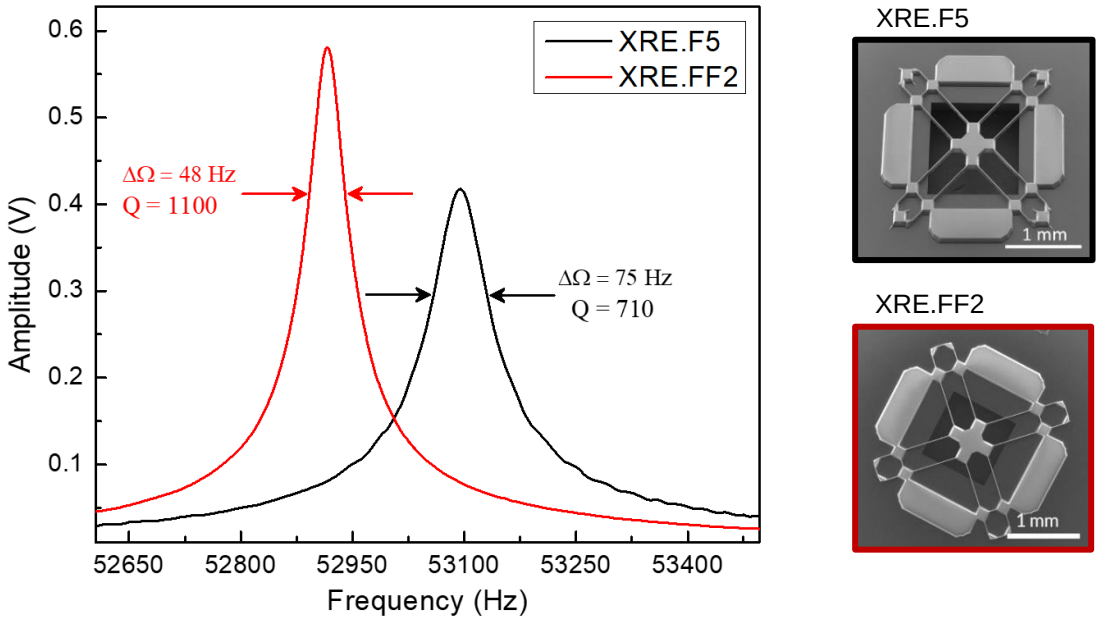

Figure 4.4.3. Frequency response of XRE.F5 (black curve) and XRE.FF2 (red curve) from resonator obtained via LDV measurement with piezoelectric excitation. The quality factor of XRE.FF2 improved in comparison to XRE.F5 by 55%.

4.4.2. Photoacoustic energy collection enhancement

FP family of 2nd generation of X-resonator was designed to increase the photoacoustic energy collection comparing to XRE.FF2. The reason for increasing the photoacoustic energy collection is to raise the displacement of the resonator, which is directly connected with the output signal. To increase the photoacoustic energy collection, we enlarged the surface responsible for collecting photoacoustic pressure. Figure 4.4.4. present the SEM picture of both resonators. The enlarged part responsible for photoacoustic energy collection is marked with yellow (figure 4.4.2.).

We needed to develop a method for verifying the deflection of a resonator under the photoacoustic force excitation. For this, we created a photoacoustic sensor system with an optical read-out mechanism called LDV for this purpose. Interferometric measurement is a fast and straightforward method to verify the movement of the resonator. With LDV we can determine the displacement of the resonator, as it is proportional to the voltage output.

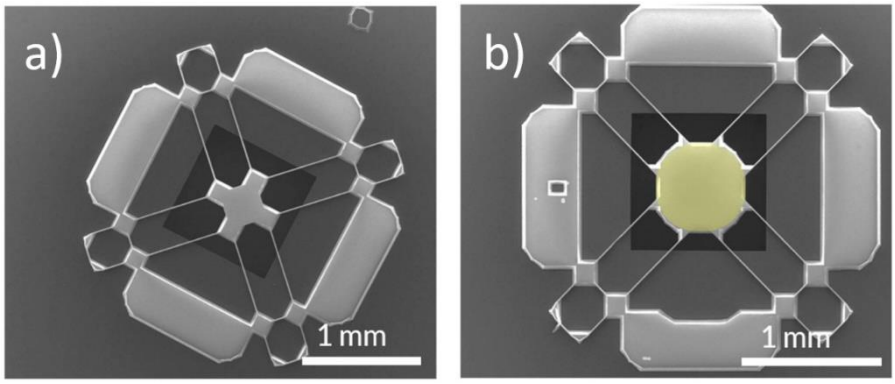

Figure 4.4.4. Scanning electron microscope picture of a) XRE.F5, b) XRE.FF2

In this section, we present results from LDV using photoacoustic waves as an excitation source. Secondly, we conducted 1f detection to ensure that the resonator movement was caused by photoacoustic excitation and not thermal. Finally, we calculated the Allan-Werle deviation, which gives information about the limit of detection (LOD) and enables the calculation of Normalized Noise Equivalent Absorption (NNEA).

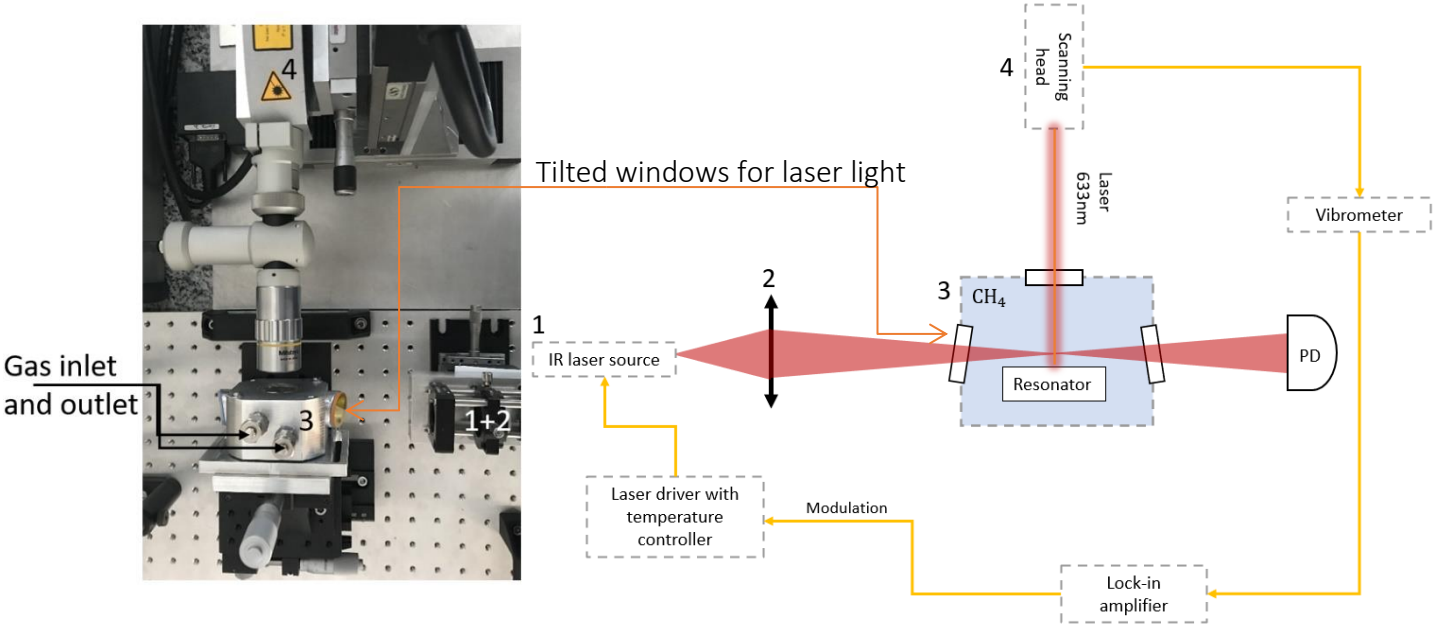

Figure 4.4.5. Setup for photoacoustic measurement and Characterization of methane using resonator with optical read-out mechanism based on LDV. 1– laser source, 2 – focal lens, 3 – gas chamber, 4 – LDV.

The setup for characterization with photoacoustic excitation is illustrated in figure 4.4.5. It includes a laser ($\lambda = 1.6$ μm), presented in section 4.5.1, a gas chamber with inlet, outlet, and three windows: one on the top made from sapphire for optical read-out mechanism, and two infrared transmission windows made of CaF_2. The windows for the infrared laser are tilted by 20° to prevent feedback into the laser. The laser light is collimated above the resonator. The photoacoustic wave created due to the interaction between laser light and gas causes the mechanical movement of the resonator. LDV detects the mechanical movement. A signal from

the vibrometer is demodulated at the laser's modulation frequency by the MFLI lock-in amplifier.

In spite of 3.5 times lower quality factor, sample XRE.FP is characterized by higher displacement than XRE.FF2, as can be seen in figure 4.4.6. Both of the resonators should be characterized by a similar quality factors as the only parameter which has changed is the size of the middle part (zone 3). We hypothesize that the cause of the lower quality factor for XRE.FP2 is a broken symmetry. There is a noticeable hole in the resonator support, and one arm is thinner in one section. According to the model presented in chapter 2, the displacement should increase with increase of the quality factor.

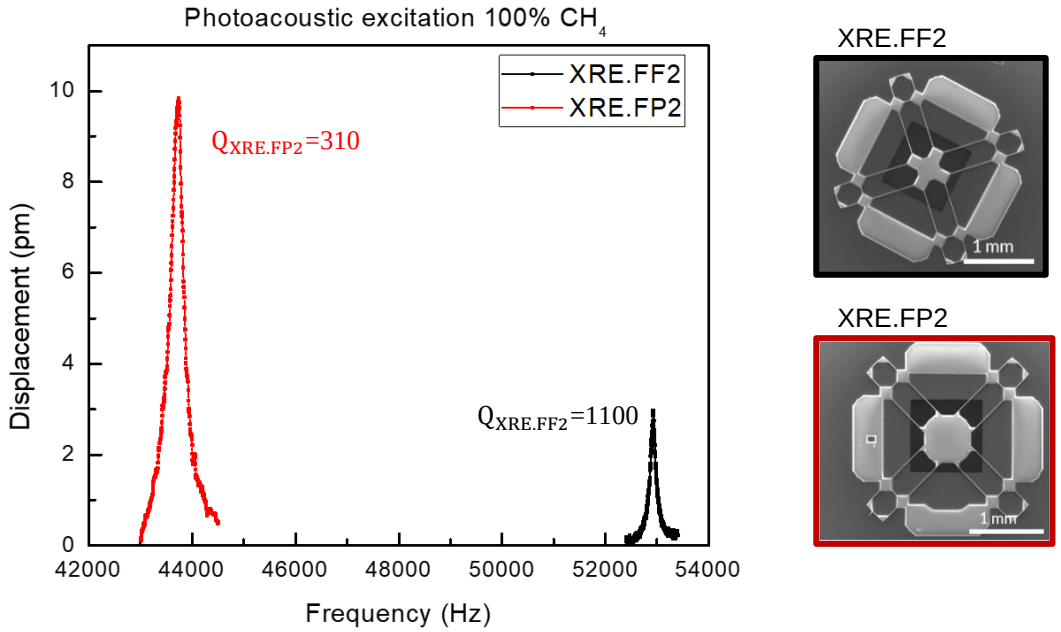

Figure 4.4.6. Displacement of XRE.FP (red curve) and XRE.FF (black curve) under photoacoustic excitation created through methane absorption. Displacement extracted from LDV measurement. Decoder VD-06, range 2mm/s/V, 100% of CH_4. Quality factor is 310 and 1100 for XRE.FP2 and XRE.FF2, respectively.

Presented measurement of frequency response study, even if performed with gas, does not necessarily indicate a photoacoustic excitation. As mentioned previously, a microresonator is susceptible to photothermal excitation. To check photoacoustic excitation and identify methane, we performed 1f detection, as presented in section 4.3.4.3. The results for both resonators are presented in figure 4.4.7.

Form 1f detection it can be seen that signal for XRE.FP is only four times smaller, while the concentration is one hundred times smaller than in the case of the XRE.FF. The signal from the resonator is assumed to be linear. Following this assumption, for the same methane concentration, the signal from XRE.FP2 should be 350 times higher than the one presented by XRE.FF2. For XRE.FP2 quality factor is lower and mass effective higher. This indicated lower mechanical susceptibility for XRE.FP2. Therefore, we assume that the higher displacement of XRE.FP over XRE.FF2 is caused by photoacoustic force (chapter 2, equation (2.28)), and more

precisely area for photoacoustic energy collection which is higher for XRE.FP2. This conclusions will be extended in section 4.4.2.4.

Because XRE.FP2 looks promising as a photoacoustic transducer, we decided to verify the limit of detection (LOD) performed on XRE.FP with optical read-out mechanism. This limit of detection will be used to calculate Normalized Noise Equivalent Absorption (NNEA) coefficient. NNEA is a criterion that allows comparing performances of different techniques used in photoacoustic gas spectroscopy. A mathematical description with results for LOD and NNEA calculation is presented in the next section.

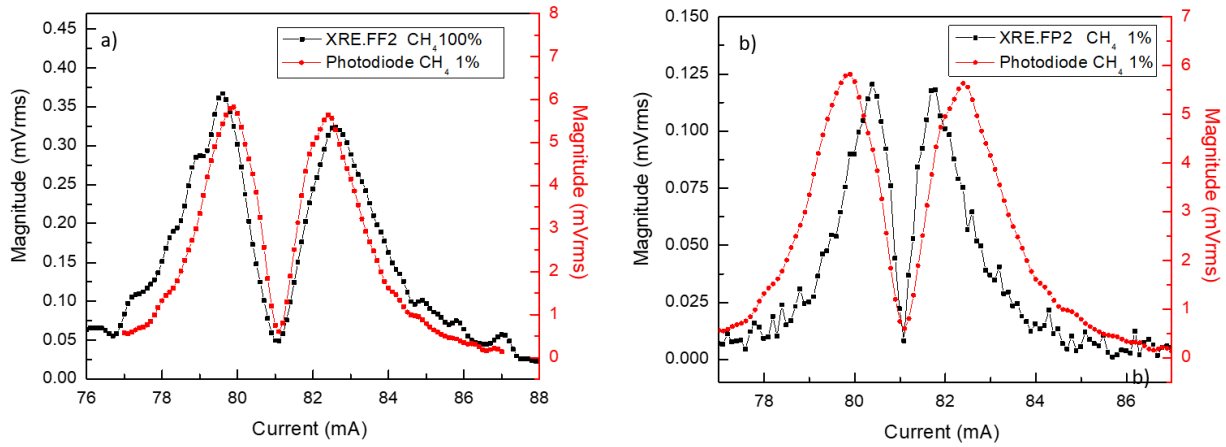

Figure 4.4.7. The absolute value of the first harmonic – WMS signal from the resonator a) XRE.FF2 (black curve) and photodiode (red curve) b) XRE.FP2 (black curve) and photodiode (red curve). Signal from resonator was obtained using optical read-out mechanism. Signal obtained by absorption of a) 100% CH4 and b)1% at atmospheric pressure using Eblana DFB laser emitting at 1.63 µm with an output power 2.5 mW for current of 80 mA. Time constant 500ms, sensitivity on LDV 2 mm/s/V, vibrometer laser spot focalized in the resonator center.

4.4.2.1. Limit of detection and Allan Variance

The limit of detection (LOD) is the lowest detectable quantity of a compound that can be distinguished from its absence. It is strongly correlated with the signal-to-noise ratio. In most cases, LOD is calculated for 1σ or 3σ, which gives the value of the detection for SNR 1 and 3, respectively.

Sample averaging is a technique for increasing the signal-to-noise ratio and consequently the LOD for a species. The integration of the sample over time results in noise removal and an improvement in the SNR. However, there exists an optimal integration time due to the system's instability. System's instability might be caused by temperature fluctuations, conditions inside a cell including gas leak, Poisson noise introduced by quantized nature of emitted photons by laser, or noise originating from electronics devices. The optimum integration time maximizes SNR and, therefore, LOD.

A statistical tool called Allan-Werle deviation can be applied to estimate an optimal integration time and study the system's stability. This method may be used to analyze the stability of any physical parameter over time. In 1993 Werle [10] successfully introduced it in the optical gas sensor development and it is currently widely used in laser spectroscopy.

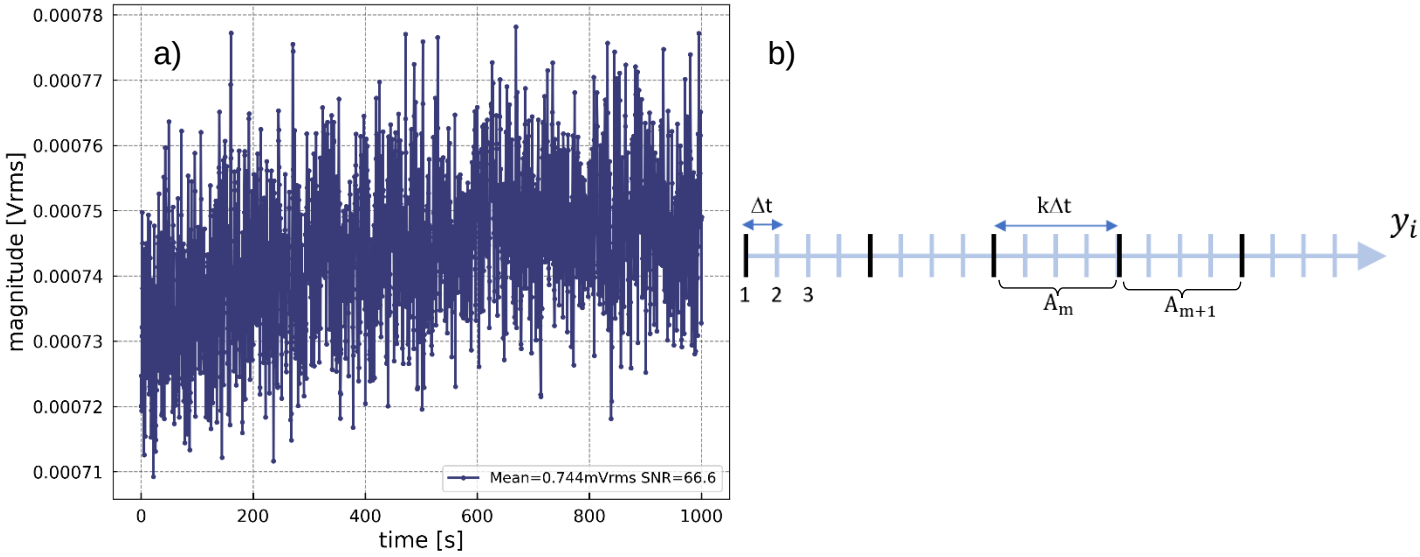

Figure 4.4.8. a) Rough signal in time form photoacoustic measurement made on the resonator H75R45F4.1 with a time constant set up on lock-in amplifier 100 ms. b) The scheme of the creation of the Am subsets from the initial data points y_i from measurement presented on the left panel.

In the experimental setup of the Allan variance, a signal from the sensor is measured at a constant concentration every step time Δt. As a consequence, we get a set of N-points of the value y_i. These points are represented in figure 4.4.8a and schematically figure 4.4.8b.

The set of N points is divided into M subsets distanced from each other with a timestep $\tau = k\Delta t$, where k indicates the number of samples in one subset.

The average of each subset A_m will be given by following equation:

$$A_m(\tau) = \frac{1}{k}\sum_{i=1}^{k} y_{(m-1)k+i} \tag{4.8}$$

Allan variance is given by:

$$\sigma_A^2(\tau) = \frac{1}{2(M-1)}\sum_{m=1}^{M}[A_m(\tau) - A_{m-1}(\tau)]^2 \tag{4.9}$$

while Allan deviation will be defined as a $\sigma_D = \sqrt{\sigma_A^2}$

SNR can be defined as a ratio between the average value $\bar{x}$ of the variable x_i to the square root of Allan variance:

$$SNR(\tau) = \frac{\bar{x}}{\sigma_A(\tau)} \tag{4.10}$$

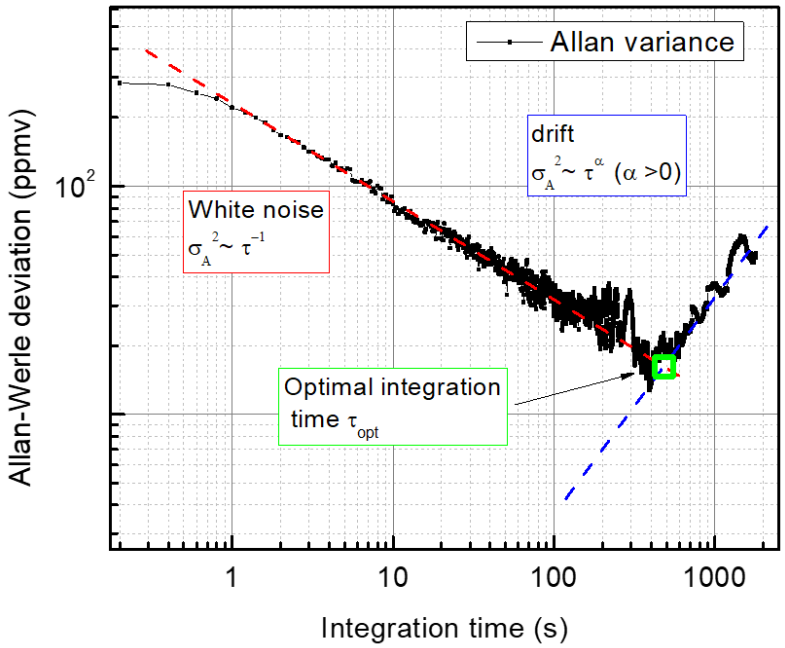

Figure 4.4.9. Allan – Werle deviation calculated for XRE.FP from 30 min acquisition for 1f detection with 1% of CH_4. Time constant 200 ms, optical read-out mechanism. White noise is dominating when $\sigma_A^2 \propto \tau^{-1}$ (red slope), drift dominated region occurs for $\sigma_A^2 \propto \tau^{\alpha}$ (where $\alpha > 0$, blue slope). Beyond the drift noise and white noise exist an optimal integration time τ_{opt}.

4.4.2.2. Allan variance – results and comparison

As mentioned previously, the concept of photoacoustic gas sensor based on silicon micro-mechanical resonator, specially designed for photoacoustic gas detection with capacitive transduction, called 8-resonator, was for the first time proposed by Chamassi *et al.* [1]. Our work focuses on reaching the same or superior limit of detection, stability and NNEA. To calculate the LOD for different resonators and consequently be able to compare them using NNEA, we performed Allan Variance evaluation described in the previous section. Figures: 4.5.10, 4.5.11, and 4.5.12 present the outcomes from the Allan-Werle deviation, which were subsequently used to calculate LOD and NNEA.

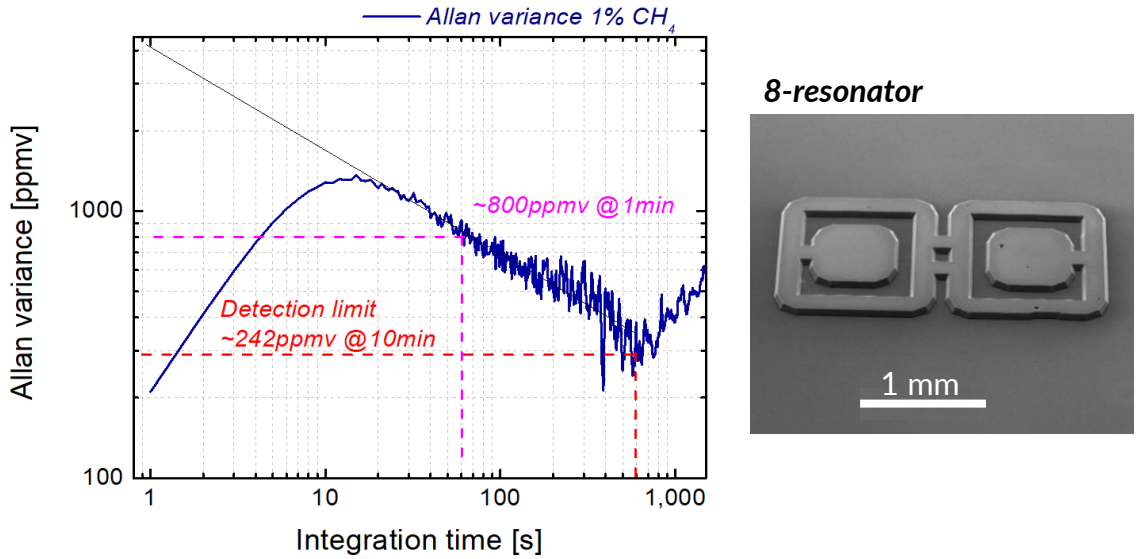

Figure 4.4.10. Allan – Werle deviation (left panel) calculated for 8-resonator from a 60 min of acquisition for 1f detection with 1% of CH_4. Time constant set up on the lock-in amplifier 2 s, capacitive read-out mechanism with polarization voltage 30V. SEM picture of 8-resonator (right panel).

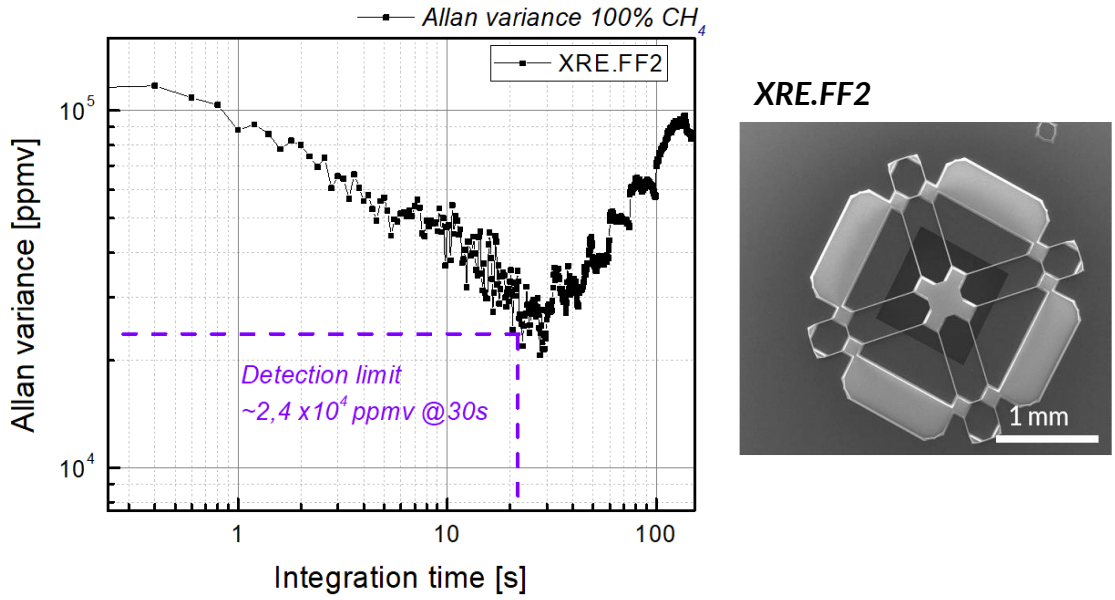

Figure 4.4.11. Allan – Werle deviation calculated for XRE.FF2 from 30 min acquisition for 1f detection with 1% of CH_4. Time constant set up on the lock-in amplifier 200 ms, optical read-out mechanism. SEM picture of XRE.FF2 (right panel).

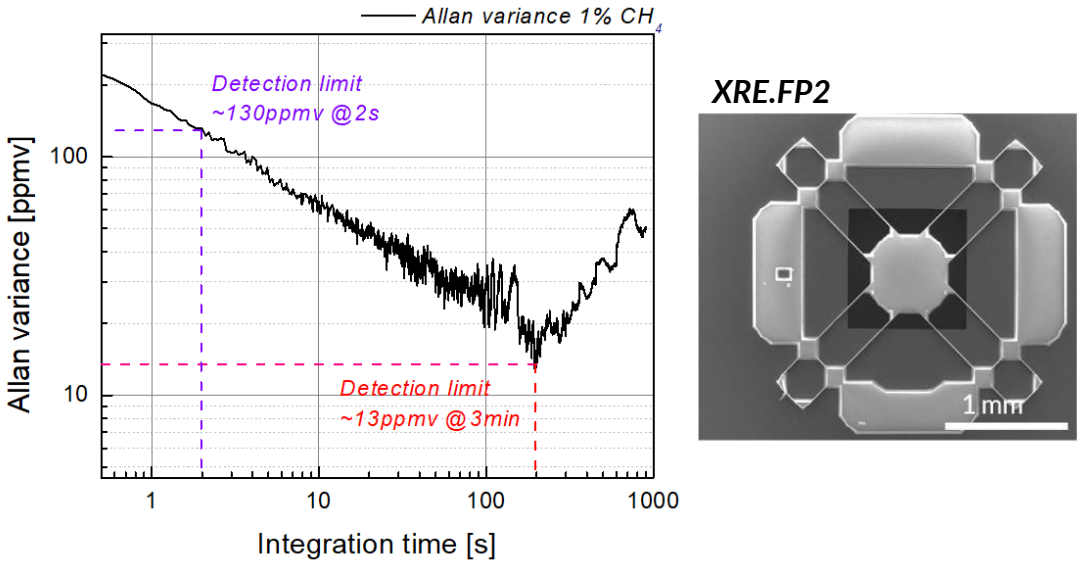

Figure 4.4.12. Allan – Werle deviation calculated for XRE.FP2 from 30 min acquisition for 1f detection with 1% of CH_4. Time constant set up on lock-in the amplifier 200 ms, optical read-out mechanism. SEM picture of XRE.FP2 (right panel).

The results of LOD for different resonators are summarized in table 4.4.2. XRE.FP is characterized by the lowest LOD. LOD of XRE.FP2 in 1 s of integration time is roughly 24 times better LOD of 8-resonator for the same integration time. For 10 s of integration time XRE.FP2 is characterized by 27 times lower LOD than for 8-resonator and 629 times higher than for XRE.FF for the same integration time. The discussion and explanation of the differences are given in section 4.4.2.4.

Presented here results were made with the same laser and gas. We have tried to performed LDV measurement with 8-resonator, but we did not achieve any signal. However, LOD is not a good criterion for comparing different resonators, as it does not consider a laser intensity or the intensity of the absorption window. Another method is needed that allows comparing various sensing approaches, regardless of measurement circumstances. One of the existing criteria discussed in the following section is Normalized Noise Equivalent Absorption (NNEA).

Table 4.4.2. Limit of detection for selected resonator and selected integration times based on Allan-Werle Deviation.

Integration time	Limit of detection		
	8-resonator	XRE.FF2	XRE.FP2
1s	4000 ppmv (from interpolation)	88 000 ppmv	167 ppmv
2s	3100 ppmv	75 000 ppmv	130 ppmv
10s	1700 ppmv	39 000 ppmv	62 ppmv
30s	1100 ppmv	24 000 ppmv	38 ppmv
Minimum	242ppmv @ 10min	24 000 ppmv @ 30s	13ppvm @ 3min

4.4.2.3. NNEA

The sensitivity of the sensor can be qualified using Normalized Noise Equivalent Absorption (NNEA)[$\frac{W}{cm\sqrt{Hz}}$]. NNEA is a criterion that allows comparing performances of different techniques used in photoacoustic gas spectroscopy (e.g. QEPAS, CEPAS) as it takes into account the power of the laser P_L , absorption cross-section of molecules $\sigma(\lambda)$ and electrical bandwidth Δf . NNEA can be calculated using the following equation:

$$NNEA = \frac{\alpha_{LOD} P_L}{\sqrt{\Delta f}} \tag{4.11}$$

where α_{LOD} is the absorption coefficient detection limit. To calculate α_{LOD} one can use the following formula:

$$\alpha_{LOD} = \alpha_{1ppmv} c_{LOD} \tag{4.12}$$

where c_{LOD} is a concentration of a target gas in ppmv calculated based on the Alan-Werle deviation for a given integration time $T = \frac{1}{\Delta f}$ and α_{1ppmv} is the absorption coefficient for concentration of 1 ppmv which can be retrieved using HITRAN database.

4.4.2.4. Discussion and Conclusions

Table 4.4.3 summarizes the properties of the resonators. NNEA was calculated for 1s of integration: bandwidth Δf =1 Hz, laser power P_L = 2.5 mW and absorption coefficient α_{1ppmv}=3.87·10^{-7} cm^{-1} (based on HITRAN database: figure A2.2.1 in appendix A2).

In spite of XRE.FF having the highest susceptibility, the displacement and LOD achieved through this resonator is the smallest of those resonators presented in the table. One explanation is the area for photoacoustic energy collection, which is the smallest for XRE.FF2 and the greatest for XRE.FP2. It is worth noticing that it was impossible to get a signal from 8-resonators using the LDV technique.

The best LOD was achiever by XRE.FP2 and amounts 38 ppmv in 1 s of integration. However, comparing the performances between the resonators is not straightforward as photoacoustic gas detection with 8-resonator was performed via capacitive detection, while for two others with optical transduction. NNEA is a criterion that allows us to compare different

techniques of detection. As can be seen, NNEA for XRE.FP2 is equal to $1.6{\cdot}10^{-7}$. Additionally, the NNEA of XRE.FP2 is reaching the performances of the state-of-the-art sensors, as it has been marked in figure 4.4.13. These findings demonstrate that the X-resonator is an effective photoacoustic transducer.

Table 4.4.3: Selected features of Selected resonators.

RESONATOR	8-resonator	XRE.FF2	XRE.FP2
f_0 [kHz]	14,7	52,9	43.7
Q-factor	140	1100	310
Effective mass [μg]	47	17	19
Susceptibility [s^2/kg]	$1.37{\cdot}10^{-2}$	$2.1{\cdot}10^{-2}$	$0.9{\cdot}10^{-2}$
Area $[mm^2]$	$11{,}8{\cdot}10^{-7}$	$1{,}6{\cdot}10^{-7}$	$3{,}1{\cdot}10^{-7}$
Area for photoacoustic wave collection $[mm^2]$	1.5	0.1	0.31
Acoustic pressure [μPa] (for CH_4 1%)	2.6	1.6	1.7
Acoustic force [pN]	3.9	0.16	0.53
Detection limit (@30s)	1000ppm	2,4%	38ppmv
Detection	Capacitive	Optical	Optical
NNEA (for 1s) [$cm^{-1}{\cdot}W/\sqrt{Hz}$]	$8.9{\cdot}10^{-6}$	$8.5{\cdot}10^{-5}$	$1.6{\cdot}10^{-7}$

It is worth noticing that XRE.FP is characterized by a relatively low quality factor. According to the hypothesis, when the quality factor improves, displacement and deflection should rise, and so should mechanical susceptibility and NNEA. For example, raising the quality factor to 800 should increase a mechanical susceptibility by factor two. Despite a low quality factor, results of NNEA and LOD confirm the potential for this resonator as a photoacoustic transducer.

Nevertheless, our goal is to achieve photoacoustic gas sensing with capacitive transduction. Therefore, XRE.FP2 does not fulfil our requirements. In fact, all fabricated resonators are poor capacitive transducers. We assume that the reason behind the poor transductor is that most of the movement of the resonator is centralized in the middle part (zone 3), which is responsible for photoacoustic energy collection.

To overcome this drawback we present a new design in section 4.5

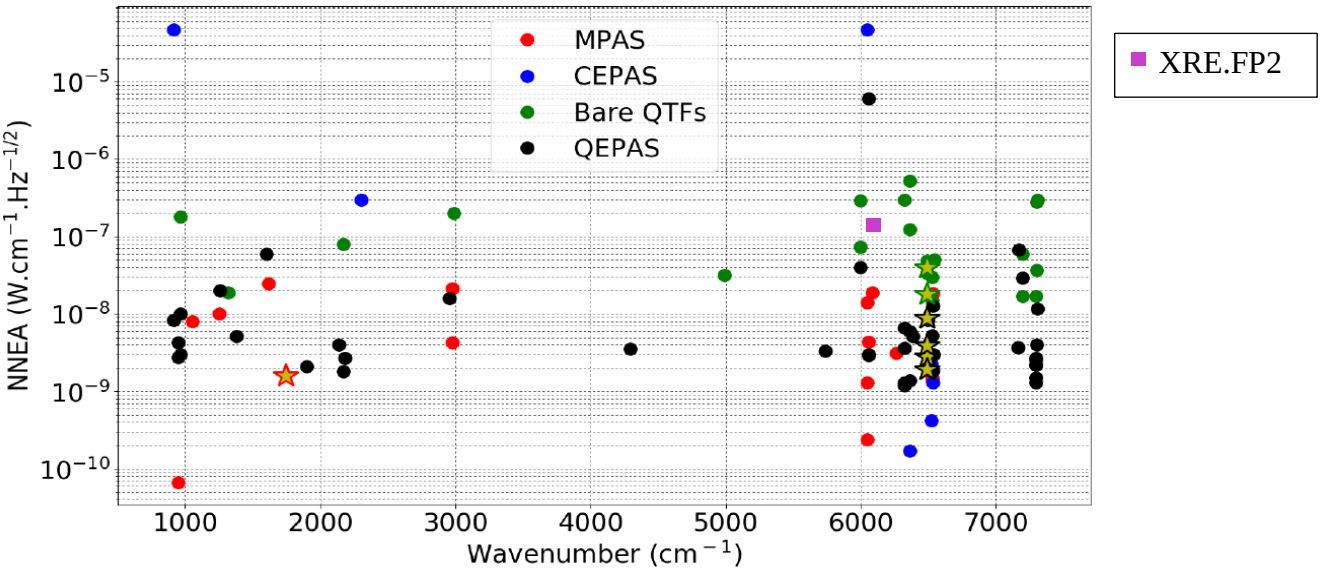

Figure 4.4.13. Review the various NNEA values published in the literature for different techniques [11]. MPAS, CEPAS, Bare QTF and QEPAS stands for Microphone Photoacoustic Spectroscopy, Cantilever Enhanced Photoacoustic Spectroscopy, photoacoustic spectroscopy with quartz tuning fork without acoustic cavity and Quartz Enhanced Photoacoustic Spectroscopy. The work provided in [11] is represented by the stars.

4.4.3. Capacitive signal enhancement

FT and FU family of 2nd generation of X-resonator was designed to increase the attenuation factor S_A given by equation (4.7) in section 4.3.5 and consequently increase the capacitive signal. To enhance the attenuation signal, we focused on improving the nominal capacitance by increasing the number of arms. We wanted to compare the resonators among themselves; thus, we avoided creating an entirely different geometry. The resonators are presented in figure 4.4.14.

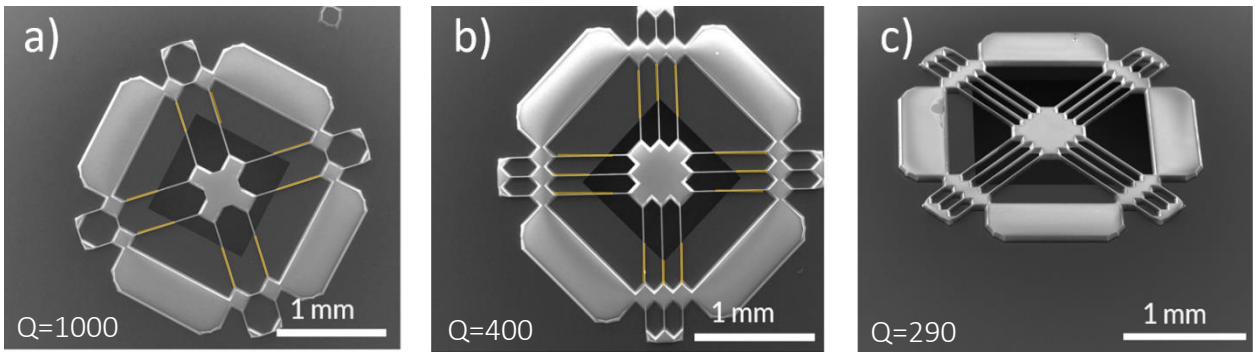

Figure 4.4.14. Scanning electron microscope picture of a) XRE.FF, b) XRE.FT, c) XRE.FU. The characterization of the resonators is presented in figure 4.4.15. The quality factor of XRE.FT is 400 while XRE.FU 290. The low quality factor of XRE.FU (in comparison to XRE.FF) is caused by the misalignment with a back etch visible in figure 4.4.14c. Parts marked in yellow bring a capacitive signal in phase opposition to the desired signal.

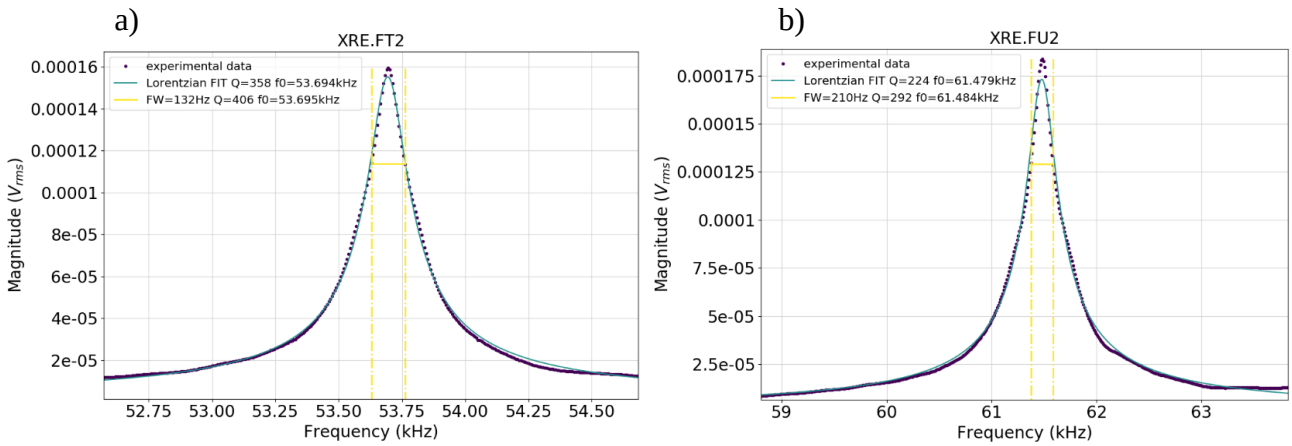

Figure 4.4.15. LDV measurement at 1atm using velocity decoder with sensitivity 2mm/s/V and at excitation 1mVpk for sample a) XRE.FT2 for which f_0 = 53.7kHz, Q factor around 400 and b) XRE.FU2 for which f_0 = 61.5 kHz, Q factor around 290. In both cases the spot is focalized in the middle of the resonator.

In spite of our efforts, resonators from this family were unsuccessful, which means we did not manage to get a capacitive signal. However, based on this design, we identified another problem: low ratio of displacement between the middle part (zone 3) and extremities (zone 2). Ratio of displacement w_{ratio} informs about the ratio of displacement between extremities of the arms w_{end} (zone 2) and the middle part of the resonator w_{mid} (zone 3), which in mathematical form can be expressed as follows:

$$w_{ratio} = \frac{w_{end}}{w_{mid}} \tag{4.14}$$

w_{ratio} was calculated using COMSOL multiphysics software. Indeed, to be an efficient capacitive transducer, a resonator needs to be characterized by high displacement in the zone responsible for converting the mechanical movement into an electric signal. The values of w_{ratio} for different X-resonators 2nd generation are presented in section 4.4.4.

The lack of the capacitive signal might also be caused by the capacitive signals in phase opposition. Marked in yellow (figure 4.4.14) parts of the resonator will bring a capacitive signal in phase opposition to the desired signal.

4.4.3.1. Discussion and conclusions

We have created a family of resonator with enhanced nominal capacitance. This variation aimed to increase the voltage output. In spite of the nominal capacitance improvement, the capacitive signal was not obtained. Table 4.4.4 shows some of the

characteristics of the resonators discussed previously. We have identified two possible reasons for the lack of capacitive signal :

a) low ratio of displacement between zone 2 and the middle part of the resonator zone 3 (w_{ratio});
b) capacitive signal in phase opposition.

Table 4.4.4: Selected features of Selected resonators.

RESONATOR	XRE.FT2	XRE.FU2
f_0 [kHz]	53.7	61.5
Q-factor	410	290
Area for photoacoustic $[mm^2]$	0.17	0.18
Acoustic pressure [μPa] (for CH_4 1%)	1.6	1.4
Acoustic force [pN]	0.27	0.29
Capacitive area	0.4	0.54

4.4.4. Conclusions for 2nd generation of X-resonator

With the second generation of X-resonator, we have improved quality factor and photoacoustic sensing. Despite efforts to improve the performances of the X-resonator, we did not manage to obtain a capacitive signal. However, XRE.FP2 is a good photoacoustic transducer as it is proven with NNEA under optical read out mechanism. We assume that maximization the displacement in zone 2 and increasing the nominal capacitive is needed to improve the capacitive transduction. Table 4.4.4 presents some characteristics of previously presented resonators.

We suppose that the reason why we obtained a capacitive signal from XRE.F5 and not from other is that the w_{ratio} . It is the highest for XRE.F5 (table 4.4.5). Also, area for nominal capacitance in case of the XRE.F5 and XRE.FT is similar, which might lead to a similar attenuation factor.

To summarize, we have achieved a design characterized by good photoacoustic energy collection and poor capacitive transduction. On a basis of theses results we conclude that X-resonator, can be a good photoacoustic transducer. On the other hand we did not manage to obtain a good capacitive signal. We have identified three possible reasons

a) capacitive signal with a phase opposition;
b) low attenuation factor S_A (section 4.3.5, equation (4.7)): low ratio between nominal capacitance and parasitic capacitance;
c) low displacement in zone 2.

To improve the drawback of this design we created a new, 3rd generation of the X-resonators, presented in the following section.

Table 4.4.5: Selected features of Selected resonators.

Type	Frequency [kHz]	Mass [μg]	Effective mass [μg]	Ratio of displacement w_{ratio}	Q support	Area for PA energy [mm^2]	Capacitive area A_0 [mm^2]
XRE.F5	52.96	226	17.3	0.11	17735	0.16	0.4
XRE.FF	52.98	218	17.2	0.068	18185	0.16	0.33
XRE.FP	43.02	200	18.7	0.068	17936	0.31	0.33
XRE.FT	53.04	246	35	0.076	13852	0.16	0.4
XRE.FU	62.64	247	24.7	0.086	8050	0.17	0.58

4.5. X-resonator 3rd generation

The third generation of the X-resonator, presented in figure 4.5.1, is an evolution of the previous generations of X-resonators. Information and issues from earlier designs were collected. Similarly to X-resonator of 1st generation, we created a set of resonators that differs among themselves with different sizes of zones 1, 2, 3 and 4, as well as frequencies. As a result, we optimized all zones of the resonator simultaneously and created a set of devices with:

a) Increased and rotated zone 3 by 45° to optimize the size for photoacoustic energy collection with a wet etching. Zone 3 is responsible for photoacoustic energy collection. The surface for photoacoustic energy collection for this generation is in the range between 0.4 mm^2 to 0.71 mm^2
b) Increased surface of zone 2: A_0, that creates a nominal capacitance. Raise of nominal capacitance will improve the attenuation factor (S_A) and subsequently output signal. Area for nominal capacitance in 3rd generation was in the range 0.17 mm^2 to 0.28 mm^2.
c) Decreased zone 1 that reduces the energy dissipation into the support and consequently increase the support quality factor. The quality factor of the support for this generation is in the range between 5200 to 38500. Decreasing zone 1 also increases the attenuation factor by reducing parasitic capacitance in comparison to previous generations.
d) Optimized position of zone 4. This position was chosen to minimize the displacement of zone 3 (photoacoustic energy collection) and maximize displacement in zone 2 (capacitive transduction). This procedure reduced the effective mass, which for this generation is in the range between 0.01 μg to 0.013 μg, and increased a w_{ratio} which for this generation is in the range between 22 and 193. w_{ratio} has a direct connection to voltage output.
e) Removed capacitive signal in opposite phases, as the back etch is optimized to the resonator (figure 4.5.1b and figure 4.5.2b).

The designed resonators also differ among themselves, with a frequency in the range between 19kHz to 50kHz.

4.5.1. COMSOL simulation

We performed finite element modelling to optimize the structure and get the mechanical parameters, like frequencies, masses, effective masses, ratio of displacement or support losses. Figure 4.5.1a presents a scheme of geometry after etching, while figure 4.5.2b illustrates the COMSOL simulation using the thickness of the arms 10 μm. It depicts that w_{ratio} is increased in comparison to previous generations.

Table 4.5.1. gather information for some of the X5 resonators. Resonators X5A40L50A.1 and X5A40S50A.1 differ in support size (zone 1). Compared to the previous generations, the ratio of displacement has been increased by a factor ranging from 200 to 514, while the area for photoacoustic energy collection ranges from 1.3 to 2.5. The nominal capacitance in most cases increased while the effective mass decreased. Moreover, due to the reduction of support size (zone1), the parasitic capacitance decreased. Therefore, we expect that the mechanical susceptibility, attenuation factor and consequently voltage output should grow.

Table 4.5.1: Characteristics of some of the resonators calculated using COMSOL Multiphysics Software.

Type	Frequency [kHz]	Mass [μm]	Effective mass [μm]	Ratio of displacement w_{ratio}	Q support	Area for PA energy [mm^2]
X5A40L50A.1	48.9	94	11	35	5222	0.4
X5A40S50A.1	45.6	97	11.3	22	8989	0.4

The nominal capacitance after etching amounts 430fF.

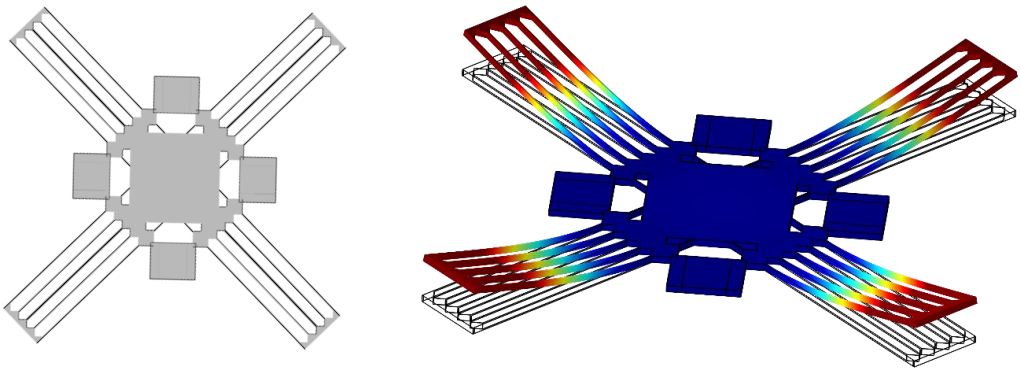

Figure 4.5.1: Geometry scheme of X5 resonator (left panel) and simulation based on COMSOL Multiphysics Software (right panel).

4.5.2. Characterization

With 3rd generation of X-resonators we were aimed to increase ratio of displacement w_{ratio} and quality factor. As presented in COMSOL simulation, the w_{ratio} should increase. To study the displacement ratio, we used LDV with a velocity decoder. Subsequently, we focalized an LDV laser spot on different parts of resonator, as illustrated in figure 4.5.2b. To present the data, we chose two samples similar with geometries, for which the fabrication process was the most successful.

The expected resonance frequency should be localized around 50kHz for both resonators. However, figures 4.5.2 and 4.5.3 present a lack of a clear resonance. We identified regions for both resonators where a resonance-like peak is visible. These regions are circled in red. We expect these regions to be correct as the displacement is characterized by higher amplitude in the arms than in the centre. However, the range of this region significantly deviates from that provided on the basis of the COMSOL simulation. Moreover, the maximal ratio of displacement reaches factor 12 $w_{rato} = 12$ for sample X5A40L50A.1, which is also inconsistent with COMSOL simulation.

Based on the results presented in figure 4.5.2 and 4.5.3 we have identified the following issues :

- no clear resonance
- different magnitude of arms displacement
- low quality factor
- discrepancy between COMSOL simulations and experimental results.

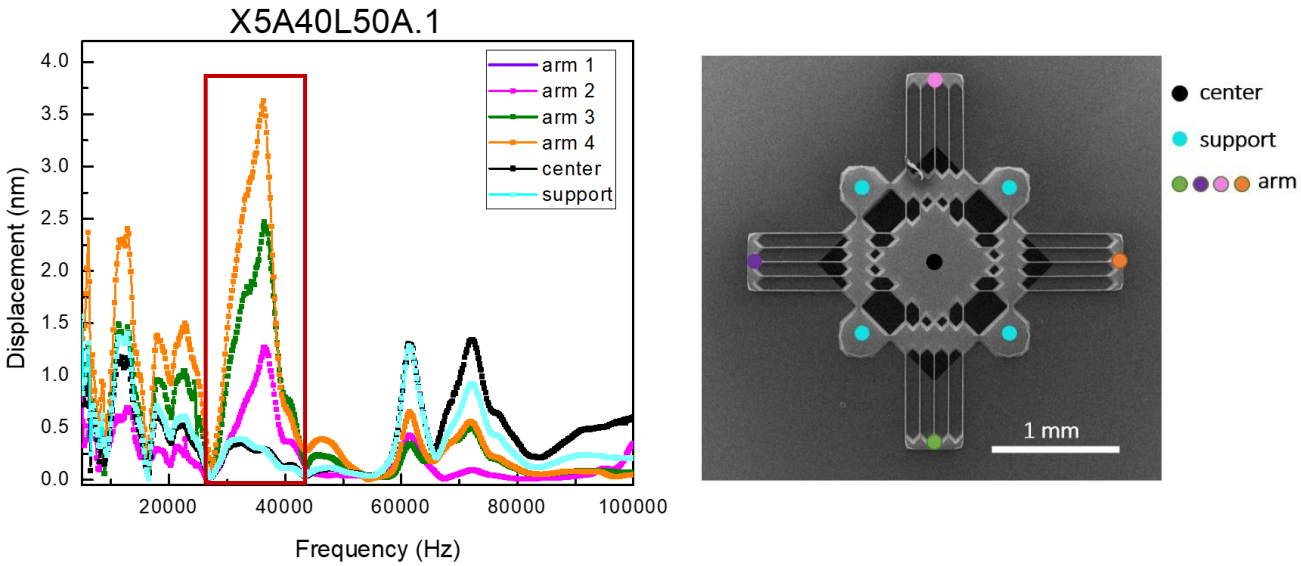

Figure 4.5.2: a) LDV measurement at 1atm using velocity decoder with sensitivity 2mm/s/V and at excitation 100mVpk. Characterization presents no clear resonance. b) SEM picture of X5A40L50A.1 with marked the focalization points of the LDV laser.

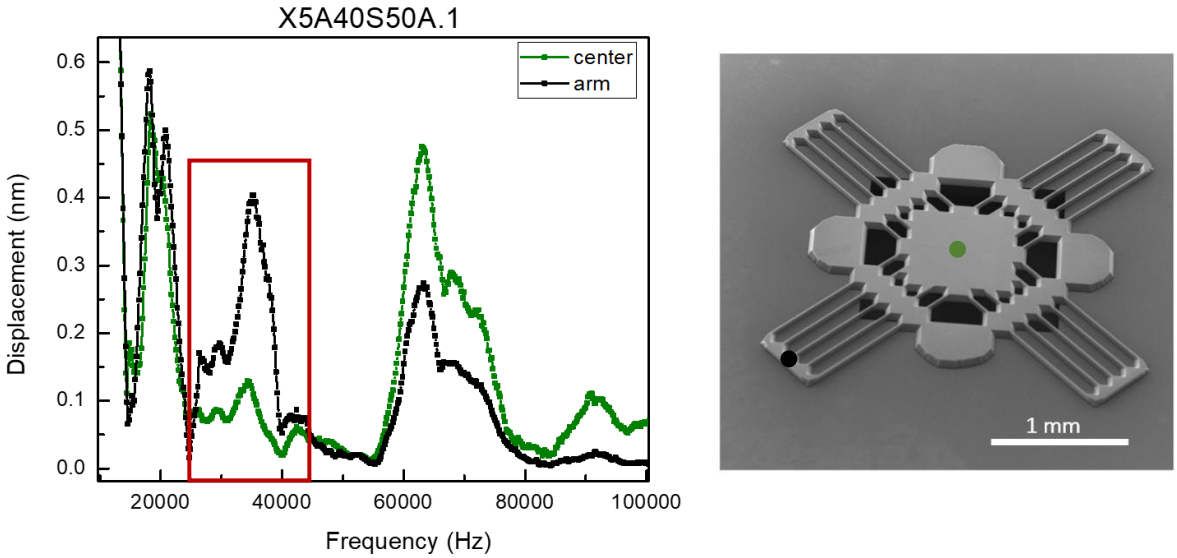

Figure 4.5.3. a) LDV measurement at 1atm using velocity decoder with sensitivity 2mm/s/V and at excitation 100mVpk. Characterization presents a lack of a clear resonance. b) SEM picture of X5A40S50A.1

SEM image shows massive resonators extremities (zone 2). They are a result of wet anisotropic etching of silicon. We hypothesize that a significant amount of air is trapped at the extremities, increasing viscous damping and, in particular, the squeeze film effect. As a result, we conducted a measurement in a vacuum to estimate the quality factor from viscous damping.

4.5.2.1 Characterization under vacuum

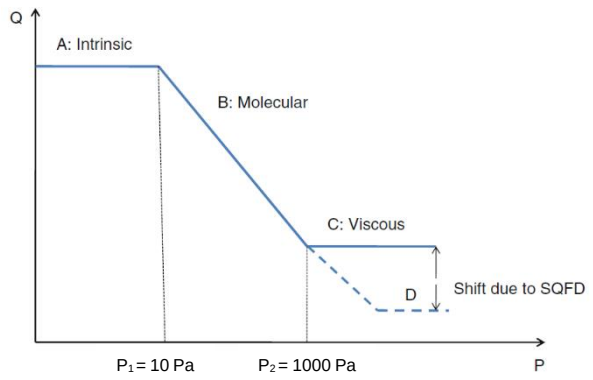

Figure 4.5.4. Scheme of Newell's categorization of the quality factor's dependency on pressure [12]. SQFD refers to squeeze film damping. The illustration was adapted from [4].

As presented in chapter 2, the highest energy losses are caused by viscous damping, particularly the squeeze film effect. To estimate the viscous quality factor and whether the low quality factor of the 3rd generation X resonator is caused by viscous damping, we conducted a measurement in a vacuum. Before starting these tests, it is necessary to understand how the damping and quality factors change under pressure. In 1968 [10], Newell, based on his study conducted on miniaturizing cantilever resonators, introduced three different regions which describe the structure quality factor depending on the pressure. These regions are presented in figure 4.4.16. In general, at low pressure (first region) P_1<10 Pa [4], the structure's quality

factor is unaffected by pressure and is determined by its intrinsic damping. The second region concerns the pressure values between 10 to 1000 Pa. In this region, the air damping is dominant, and the quality factor strongly depends on the pressure. The third region concerns pressure above 1000 Pa. In this region, air acts like a viscous fluid. If the structure is isolated from other surfaces, the quality factor does not depend on the pressure. However, in the case where the structure is near the surface, additional damping called the squeeze film effect occurs. This damping was introduced in the chapter 2 section 2.3 and it causes the shift marked in figure 4.4.16 with a letter D.

Fabricated resonators are operating in the atmospheric pressure. Secondly, squeeze film damping will always occur due to capacitive transduction. Thus, characterization of the resonators presented in section 4.4.4. concern the region D marked in figure 4.4.15

To characterize the viscous damping and calculate the quality factor that comes from support losses and intrinsic damping, one needs to perform a characterization below 10 Pa (0.1 mbar).

The setup for MEMS characterization under vacuum is based on the one presented in figure 4.4.1, section 4.4.1. It is equipped with a vacuum chamber, pressure gauge, and turbopomp. The usage of turbopump allows conducting measurement below 10Pa. For this value of pressure, the viscous damping can be neglected.

To calculate a viscous quality factor, we use a modified equation (2.14) presented in chapter 2, section 2.3:

$$Q_{viscous} = \frac{1}{(\frac{1}{Q_{tot}} - \frac{1}{Q_{vacuum}})} \tag{4.15}$$

Figures from 4.4.17 to 4.4.20 present frequency response from the MEMS obtained through LDV measurement for various resonators. Data from measurements are collected in table 4.4.1.

Measurement in the vacuum allows calculating the viscous quality factor and distinguishing modes of vibration that were not visible in ambient conditions. The quality factor of samples X5A40L50A1.1 and X5A40S50A1.1 for each of the modes amounts to at least 5000. The Q-factor for the structure is high in vacuum and low in ambient conditions indicated significant viscous losses, which confirmed our hypothesis concerning the impact of the viscous damping. We hypothesize that this viscous damping originates from two sources:

a) a large area on the extremities caused by wet anisotropic etching;
b) long arms and high ratio of displacement w_{ratio}.

Thanks to this measurement, we identified various modes of vibration for samples X5A40L50A1.1 and X5A40S50A1.1. The proximity of the modes results from increasing w_{ratio}, and more specifically, the rigidity of the arms. Longer arms will be manifested with a

larger degree of freedom, and therefore, more modes will be visible. These kinds of modes were already presented in section 4.3.2 figure 4.3.8 with XRE.F5. However, in the case of XRE.F5 those modes were shifted in high-frequency regime (in comparison to fundamental mode) due to the short length of the arms (zone 2).

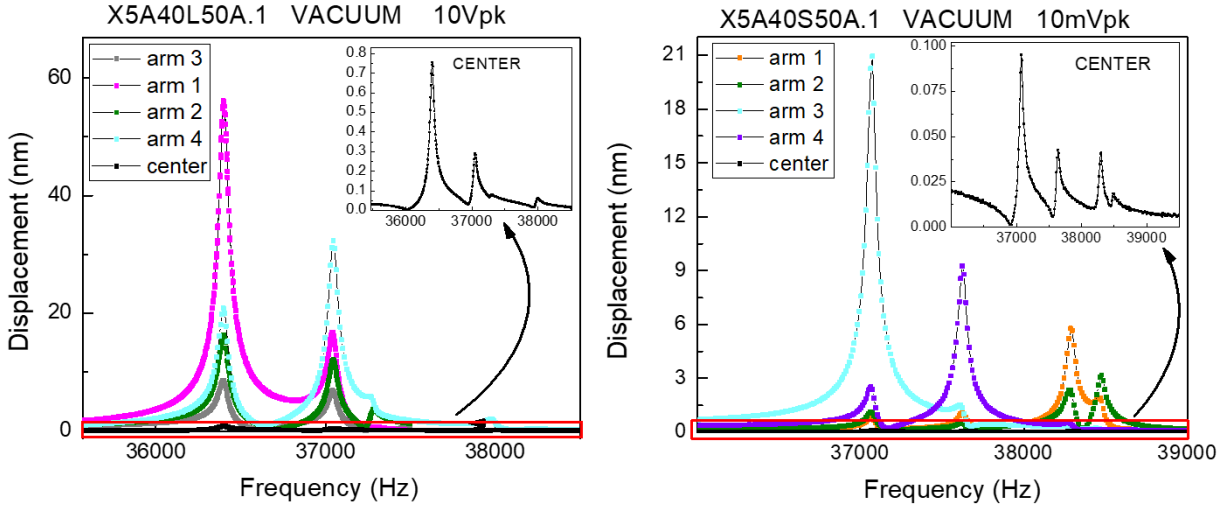

Figure 4.5.5. LDV characterization measurement on sample X5A40L50A1.1 (left panel) and X5A40S50A.1 (right panel) under vacuum ($3.1 \cdot 10^{-3}$ mbar and $1.5 \cdot 10^{-3}$ mbar, respectively). Sample characteristic: Q=1800, f_0=53.83 kHz, FWHM= 30 Hz. Measurement performed with excitation voltage of the piezo shim 50 mVpk, range on LDV equal to 10 mm/s/V and MFLI Zurich amplifier. Quality factor of the modes ≥ 5000.

However, the extremities of XRE.F5 are also characterized by the large surface where the squeeze film might occur. To demonstrate why XREF5 resonators exhibit clear resonance and a high quality factor while X5 resonators does not, in the next section we introduce the theory for calculating the quality factor of a complex structure.

4.5.2.2 Calculation of quality factor of a complex structure

Calculation of the quality factor for a complex structure is not straightforward. This section aims to introduce the tool to calculate a quality factor for a complex structure. As a model, we use a resonator, presented in figure 4.5.6, which can be approximated with two cantilevers.

Let's introduce a coefficient $0 \leq \alpha_A \leq 1$ and $0 \leq \alpha_B \leq 1$ which are the defining contributions of each part of the resonator (A and B) to total energy E_{total} and $\alpha_A + \alpha_B = 1$

Coefficient α_A defines the contributions of the A part of the resonator to the total energy. Mathematically it can be expressed with the following equation:

$$\alpha_A = \frac{E_A}{E_{total}} \tag{4.16}$$

where E_A is the energy (kinetic and strain) accumulated in part A of the resonator.

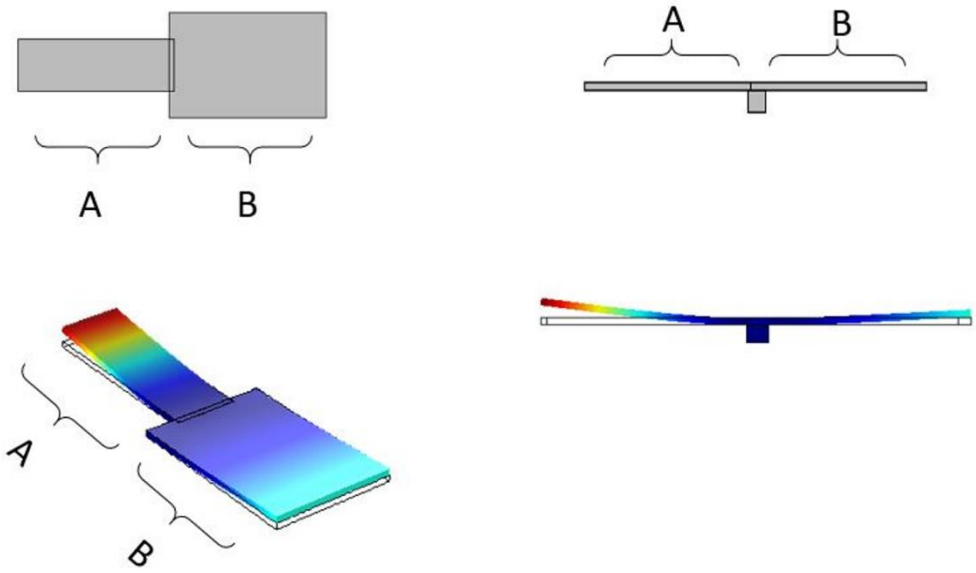

Figure 4.5.6. Sketch of a resonator which can be considered as a two cantilever: A, B.

Respectively, coefficient α_B defines the contributions of the B part. The sum of α_A and α_B is equal 1:

$$\alpha_A + \alpha_B = 1 \tag{4.17a}$$

$$E_A + E_B = E_{TOTAL} \tag{4.17b}$$

The general definition of quality factor can be expressed with the equation:

$$Q = 2\pi \frac{E_{TOTAL}}{E_{LOSS}} \tag{4.18}$$

The total losses of energy consist of the losses from part A: $E_{LOSS}(A)$, and part B: $E_{LOSS}(A)$. Thus, eq. can be rewritten as follow:

$$\mathrm{Q} = 2\pi \frac{\mathrm{E_{TOTAL}}}{\mathrm{E_{LOSS}}(A) + E_{LOSS}(B)} \tag{4.19}$$

Moreover,

$$\mathrm{E_{LOSS}}(A) = 2\pi \frac{\alpha_\mathrm{A} \mathrm{E_{TOTAL}}}{Q_A} \tag{4.20a}$$

$$\mathrm{E_{LOSS}}(B) = 2\pi \frac{\alpha_\mathrm{B} \mathrm{E_{TOTAL}}}{Q_B} \tag{4.20b}$$

$$\alpha_\mathrm{A} + \alpha_\mathrm{B} = 1 \tag{4.20c}$$

Therefore, the total quality factor will be defined as follow:

$$\mathrm{Q} = \frac{\mathrm{Q_A} Q_B}{Q_A(1-\alpha_A) + \alpha_A Q_B} \tag{4.21}$$

To check the validity of the equation, one can assume that whole the energy is located in part A. In this case $\alpha_A = 1$. The total quality factor should be then given only by part A, which is consistent with the equation for the total quality factor $\mathrm{Q} = \frac{\mathrm{Q_A} Q_B}{Q_B} = Q_A$.

COMSOL simulation allows retrieving coefficient α_i, and therefore approximate the total quality factor for a complex structure. To calculate the quality factor for parts A and B, we approximate each of them with a cantilever. Subsequently, the quality factor is calculated separately for each part using the analytic model presented in chapter 2. As the viscous damping is dominant (chapter 2), we will take into account only this damping in the calculation.

Using the analytic model presented in chapter 2, we can calculate the viscous quality factor separately for extremities (zone 2) and the middle part (zone 3) of the resonator. The middle part of XRE.F5 has Q_A =1820. The quality factor at the extremities is $Q_B = 7$. With the COMSOL simulation, we get the $\alpha_A = 0.997$. Therefore, based on equation (4.21), the viscous quality factor for XRE.F5 should be $Q_{XRE.F5} = 1020$.

Respectively for X5 resonator, the quality factor of the middle part (zone 3) is $Q_A = 1740$. The quality factor for the extremities of the resonator is $Q_B = 18$. With the COMSOL simulation, we get the $\alpha_A = 0.0065$. Therefore, the total viscous quality factor of the X5 resonator is $Q_{X5} = 18.2$.

It should be noted that this calculation contains several approximations, and we anticipate that the actual quality factor from viscous damping will be much different from the

calculated one. However, we could explain the variations in quality factor between the first and third generations of the X-resonator using this model.

With X5 resonator, most of the movement is concentrated in zone 2 (low α_A), which brings a lot of viscous damping ($Q_B = 18$). Zone 2 is characterized by a low quality factor, and it will mainly contribute to the total quality factor of a whole structure as most of the movements occur in zone 2 (α coefficient). In contrast, for XRE.F5 the movement was concentrated in zone 3 (high α_A), where no squeeze film effect occur, and the quality factor is much higher than for zone 2.

4.5.3. Discussion and conclusions

For 3rd generation of X-resonator, the capacitive signal was not obtained despite improvements in photoacoustic force, attenuation factor, and support quality factor. The reason was a low quality factor for the whole structure, which is a result of the substantial contribution of zone 2 to the total quality factor. Zone 2 is characterized by a low quality factor due to the squeeze film effect and contributes significantly to the total quality factor due to its high displacement ratio.

To understand the discrepancies between COMSOL simulation and experimental results, we studied and measured the dimensions of the X5 resonator. Figure 4.5.7 presents some measurements on the arms of the X5 resonator performed on two different extremities. As can be seen, the thicknesses bring roughly 24% of the difference between two arms. Based on the pictures, we identified another problem concerning wet etching: inhomogeneity.

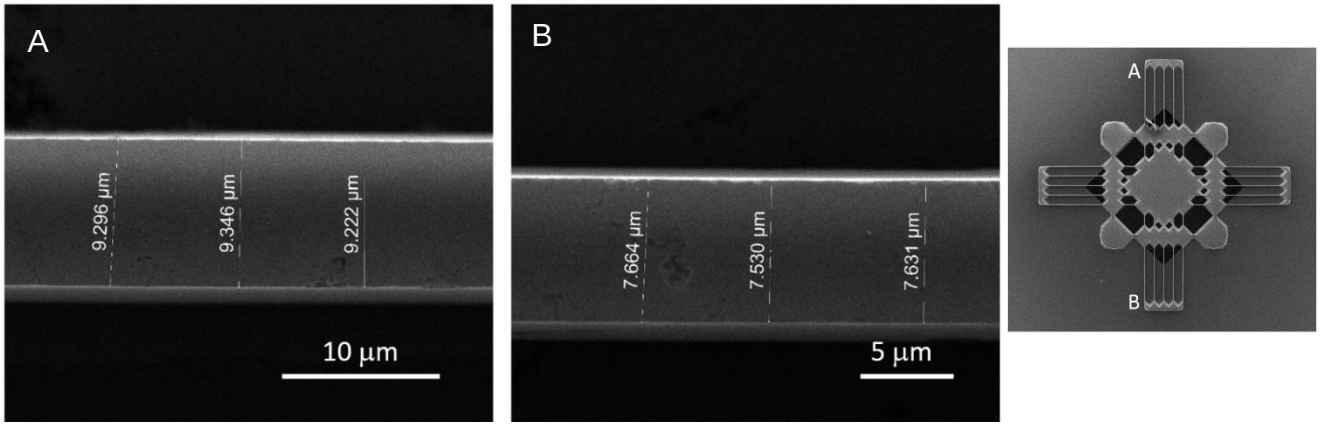

Figure 4.5.7. SEM pictures form sample X5A40S50A1.1 with measurement of the arm thickness on two opposite extremities: A and B. This picture indicates a problem with etching homogeneity.

After precise measurement of the resonator's dimensions, we have modelled these exact geometries and run a COMSOL simulation. A simulation that considers the resonator's exact geometry allowed us to find the origin of different modes presented in figure 4.5.8. Moreover,

the simulation explains the varying amplitudes of displacement for different arms and modes. As presented in figure 4.5.8, for each mode, one arm, which is characterized by a higher displacement. However, the results of the COMSOL simulation in comparison to experimental data were less accurate than in the case of previous resonators. We believe this is related to the lengthy arms. In the case of XRE.F5 the arms were short and had less degrees of freedom. Therefore, the solver had fewer options, and calculation was more straightforward.

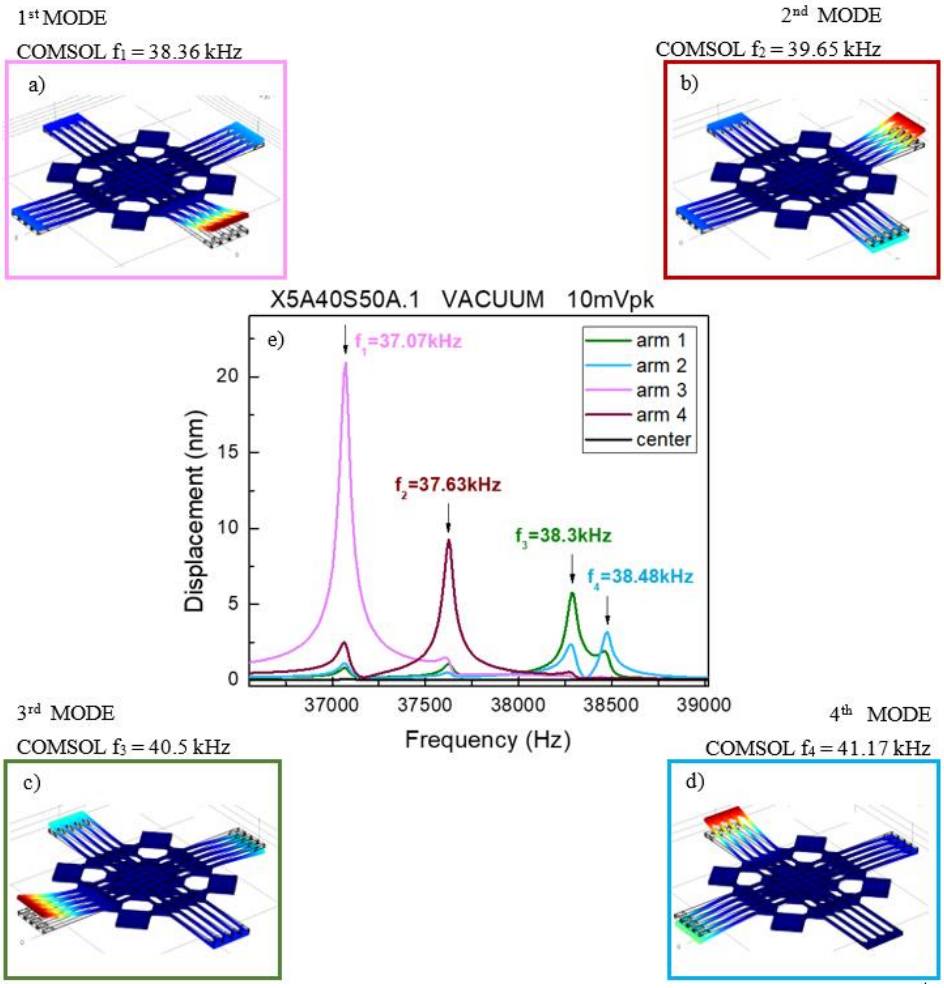

Figure 4.5.8: a) 1st b) 2nd c) 3rd d) 4th mode of vibration obtained by COMSOL simulation. The frame color corresponds to the same color peak presented in figure e). e) LDV characterization measurement on sample and X5A40S50A.1 under vacuum $1.5 \cdot 10^{-3}$ mbar, with piezoelectric excitation velocity decoder and sensitivity of the measurement 10mm/s/V.

This simulation demonstrates that wet etching inhomogeneity has a substantial influence on the frequencies and modes of vibration. It is true especially for the resonators with zone 2 defined by a high degree of freedom (long arms). To build a high-performance structure, the modelling and fabrication procedures must be extremely precise.

4.6. Conclusions and perspectives

We began this chapter by presenting a set of resonators that decouples photoacoustic energy collecting from capacitive transduction. The first set of resonators was called 1st generation of X-resonator. Based on their characterization, we have chosen the resonator characterized by a high quality factor: XRE.F5. We successfully demonstrated photoacoustic gas detection via capacitive transduction on XRE.F5. Using findings from the first generation of X-resonator in comparison to the 8-resonator design, we discovered the following issues:

a) high damping at the extremities caused by anisotropic etching and squeeze film damping;
b) low area for photoacoustic energy collection;
c) low area of nominal capacitance.

To fix the problems listed above, we created a second generation of X-resonators, which consisted of three families. Each family is supposed to address one issue. We have fixed the issue a) and b) with a set of the second generation of X-resonators. Specifically, we enhanced the quality factor from 710 to 1100 and increased photoacoustic energy collection, as measured by NNEA, which rose by a factor of 55 in contrast to the 8-resonator.

However, 2nd generation of the design did not solve the problem with poor capacitive transduction. We made a hypothesis, confirmed in theory, that capacitive transduction was poor due to the low ratio of displacement w_{ratio} between zone 2 and 3. Therefore, we designed the third generation of X-resonators (X5), which is supposed to address issues connected with a low displacement ratio. Additionally, with the X5 resonators, other parameters were improved: quality factor of the support, photoacoustic force collection and attenuation factor. Nevertheless, X5 resonators suffer from a lack of clear resonance. We hypothesized that the absence of resonance is due to excessive viscous damping generated by the large extremities. The measurement under vacuum proved this hypothesis. Nonetheless, it did not explain the discrepancies between X5 resonator and XRE.F5, which was also characterized by the high surface at the extremities. To explain these results, in section 4.5.2.2 we introduce the theory for calculating quality factor for a complex structure. Thanks to this model we calculated the total quality factor for both resonators, which despite of high degree of approximation fits fairly with the experimental data and allows to explain the differences between quality factor for different generations of resonators.

To summarize, we have encountered following problems with X-resonator: inhomogenity caused by wet etching; no clear resonance caused by multimode behavior and viscous damping and no capacitive signal.

Bibliography

[1] K. Chamassi, W. Trzpil, R. Arinero, R. Rousseau, A. Vicet, and M. Bahriz, "Capacitive silicon micro-electromechanical resonator for enhanced photoacoustic spectroscopy," *Applied Physics Letters*, vol. 115, no. 8, 2019, doi: 10.1063/1.5098140.

[2] K. Chamassi, "Détecteur de gaz multi-espèces par mesure photo-acoustique à effet capacitif," 2018.

[3] S. dello Russo *et al.*, "Quartz-enhanced photoacoustic spectroscopy exploiting low-frequency tuning forks as a tool to measure the vibrational relaxation rate in gas species," *Photoacoustics*, vol. 21, p. 100227, 2021, doi: 10.1016/j.pacs.2020.100227.

[4] M. I. Younis, *MEMS Linear and Nonlinear Statics and Dynamics*, vol. 53, no. 9. Elsevier, 2013.

[5] R. Rousseau, N. Maurin, W. Trzpil, M. Bahriz, and A. Vicet, "Quartz tuning fork resonance tracking and application in quartz enhanced photoacoustics spectroscopy," *Sensors (Switzerland)*, vol. 19, no. 24, 2019, doi: 10.3390/s19245565.

[6] S. Meninger, J. O. Mur-miranda, R. Amirtharajah, A. P. Chandrakasan, and J. H. Lang, "Vibration-to-Electric Energy Conversion," vol. 9, no. 1, pp. 64–76, 2001.

[7] L. S. Rothman *et al.*, "The HITRAN 2008 molecular spectroscopic database," *Journal of Quantitative Spectroscopy and Radiative Transfer*, vol. 110, no. 9–10, pp. 533–572, 2009, doi: 10.1016/j.jqsrt.2009.02.013.

[8] M. Bao, *Analysis and design principles of MEMS devices*. Elsevier, 2005.

[9] P. R. Scheeper, A. G. H. van der Donk, W. Olthuis, and P. Bergveld, "A review of silicon microphones," *Sensors and Actuators: A. Physical*, vol. 44, no. 1, pp. 1–11, 1994, doi: 10.1016/0924-4247(94)00790-X.

[10] P. Werle, R. Mücke, and F. Slemr, "The limits of signal averaging in atmospheric trace-gas monitoring by tunable diode-laser absorption spectroscopy (TDLAS)," *Applied Physics B Photophysics and Laser Chemistry*, vol. 57, no. 2, pp. 131–139, 1993, doi: 10.1007/BF00425997.

[11] M. Duquesnoy, D. Marris-morini, and W. Schade, "spectroscopie photoacoustique : Étude comparative et nouveaux développements Tuning forks in photoacoustic spectroscopy : Thèse de doctorat," 2021.

[12] W. E. Newell, "Miniaturization of Tuning Fork," *Science*, vol. 161, no. 3848, pp. 1320–1326, 1968.

Chapter 5

5. H-resonator

This chapter presents a simplified design of the X-resonator for photoacoustic gas detection. The design remains the separation-problem concept introduced in chapter 4. Design optimization was performed in terms of physical parameters using the analytic model provided in chapter 2 and COMSOL simulation. The resonators were fabricated using a deep reactive ion etching (DRIE). The characterization was done using LDV with both piezoelectric and photoacoustic excitation. Among the fabricated resonators, we chose a resonator characterized by the highest capacitive signal under photoacoustic excitation. Subsequently, we implemented the chosen resonator in methane detection and evaluated the sensor's performance using the Allan variance introduced in chapter 4. We compared the results to bare QTF in on-beam configuration to demonstrate that the resonator provides a state-of-the-art performance. We optimized the setup for this comparison to guarantee that both sensors (QTF and H-resonator) were subjected to identical circumstances.

5.1. Concept

This section presents the new resonator design, which was created to address issues we encountered with the last generation of X-resonator. The objective of the research is to create a high-performance silicone microresonator for photoacoustic gas detection with capacitive transduction. By high performance, we imply that it works as a good photoacoustic and capacitive transducer. The photoacoustic force causes the resonator's mechanical movement, converted to an electric signal via capacitive transduction. This conversion depends on multiple parameters discussed in chapters 2 and 3.

The primary issue with the last design (X-resonator, 3rd generation) was its low quality factor. This low quality factor was caused by the high contribution of the squeeze film effect due to the high ratio of displacement. However, keeping this high ratio of displacement is necessary to effectively convert photoacoustic force into an electric signal. Capacitive signals and the ratio of displacement are inextricably linked (chapter 2, equation (2.30),(2.31)).

Another important problem is the multimode behaviour, for which we establish two sources: the inhomogeneity of the wet etching and the design itself.

As a solution for all the above-mentioned problems, we propose a new design called H-resonator. This concept is fabricated with a deep reactive ion etch (DRIE) presented in

chapter 3. Thanks to the fabrication process, we avoid inhomogeneity and optimize the part where the squeeze film effect occurs.

The resonator's design itself has the most important role in avoiding multimode behaviour and increasing reproducibility. We followed the same strategy as in the case of the X-resonator: we divided the resonator's functions into distinct parts. Figure 5.1.1 depicts the design.

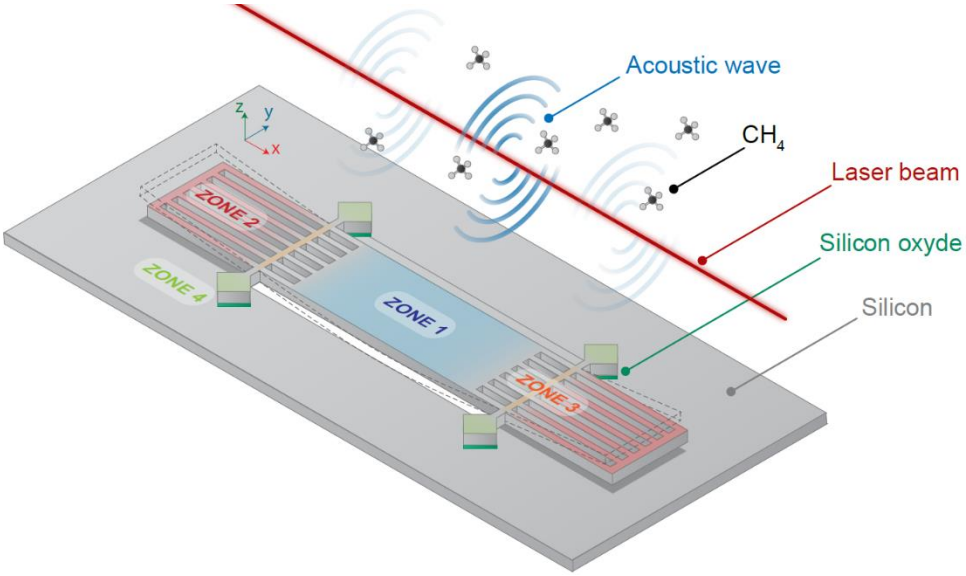

Figure 5.1.1: H-resonator design with the schematic representation of deflection under PA excitation. The laser beam is focused above the resonator's center and is aligned along the resonator's x-axis. The absorption of modulated light generates an acoustic wave all along the beam.

The laser beam is focused above the center of zone 1 and is aligned along the resonator. The absorption of modulated light generates an acoustic wave along the resonator when the laser wavelength matches a target absorption line (methane in our study). The device is manufactured on an SOI wafer (Silicon-on-Insulator).

Zone 1 is responsible for photoacoustic energy collection. This collected photoacoustic energy sets the whole resonator in motion. Zone 2 is the place where the mechanical movement is converted into an electric signal, zone 3 connect zone 1 and zone 2, while zone 4 holds all the structure.

5.2. Optimization

The design needs to be optimized to assure the good performance of the sensor. A good sensor should be characterized by high photoacoustic force, efficient conversion of photoacoustic energy into mechanical movement and efficient conversion of mechanical motion into an electrical signal. Thanks to the separation of the zones, we can simplify the problem of the structure's optimization. We focused on optimization of physical parameters, namely:

a) photoacoustic force
b) energy losses minimalization
c) capacitive signal enhancement

The following sections will expand the structure optimization in terms of these physical parameters.

5.2.1. Photoacoustic force

The X-resonator collects energy in the center, which is not ideal since a photoacoustic wave is created all along the beam. The H-resonator gathers photoacoustic force along the beam, which maximizes the energy collection.

Zone 1 presented in figure 5.1.1 is responsible for photoacoustic energy collection. For efficient photoacoustic energy collection, the surface of zone 1 needs to be large, thick and characterized by significant overlapping between the mechanical mode and acoustic wave (chapter 2, section 2.2). The large surface of zone 1 in close contact with another surface will result in high squeeze film damping. To avoid this effect, we added a hole (back etch) beneath zone 1.

Device thickness and resonance frequency are other essential characteristics to consider while optimizing photoacoustic force. As discussed in chapter 2, the photoacoustic force is affected by modulation frequency. For methane detection, it would be ideal to set the resonance frequency at 11 kHz and simultaneously increase the device thickness. However, in order to make a thick device at low frequency, the length must be increased. Increasing the length increases the resonator's fragility and complexity of the fabrication process. To provide a good compromise between the fabrication process challenges and device performances, we have chosen to work with an SOI wafer characterized by the following parameters: 400 μm thick substrate with a resistivity of 0.01~0.02 $\Omega.\,cm^{-1}$, a 3 μm thick SiO_2 layer, and a 75 μm thick device layer with a resistivity of 01~0.02 $\Omega.\,cm^{-1}$.

5.2.2. Energy losses minimization

The objective in decreasing the energy losses is to convert all the photoacoustic energy into a mechanical movement. There are two main factors in the minimalization of energy losses:

a) total quality factor
b) crosstalk between mechanical modes

The total quality factor from the definition is telling about losses of energy per cycle. However, the total quality factor does not consider losses of energy caused by the multimode behaviour. Crosstalk with the mechanical mode of interest can appear for a mechanical mode with a low quality factor. This crosstalk will spread the energy between the mechanical modes participating in crosstalk. Therefore, our objective is to convert all the photoacoustic energy into one mode of vibration.

The mechanisms of energy losses were covered in chapter 2. Zone 1 is optimized to decrease viscous damping through the employment of back etch. Zone 2 is optimized to decrease the squeeze film effect through the employment of DRIE, respectively. To improve the support quality factor, zone 4 should be properly shaped and reduced to a size that can hold the entire structure. As a result, green zone 4 marked in figure 5.1.1 is a 250 μm x 250 μm square rotated by 45° to decrease the strain energy in the support and therefore to increase the support quality factor (study with COMSOL simulation).

One way to reduce multimode behaviour is to have most of the movement in the center, as the center has a lower degree of freedom. However, our objective is to increase the capacitive signal, thus have a maximum of displacement in zone 2. We hypothesize that responsible for the multimode behaviour and ratio of displacement between zone 1 and zone 2 is mostly the position of zone 3, marked in orange in figure 5.1.1. This hypothesis will be evaluated and verified using the COMSOL simulation in section 5.3.

5.2.3. Capacitive signal enhancement

For capacitive signal optimization, we target a mode of vibration that will bring the highest capacitive variance and, therefore, the highest electrical output. This mode of vibration is presented in figure 5.1.1.

After choosing the best mode of vibration, the capacitive signal enhancement will consist of two parts :

a) increasing the displacement of the part responsible for capacitive transduction
b) increasing the attenuation factor S_A (chapter 4, section 4.3.5, equation (4.7))

To enhance the displacement of zone 2, the ratio of displacement w_{ratio} (chapter 3, section 4.4.3, equation (4.14)) needs to be maximized.

In case of H-resonator, ratio of displacement is defined as a ratio between the displacement at the extremity of zone 2 (w_{end}) and displacement of the middle part of zone 1 (w_{mid}), according to:

$$w_{ratio} = \frac{w_{end}}{w_{mid}} \tag{4.1}$$

Increasing w_{ratio} will improve the mechanical susceptibility as the effective mass m_{eff} will decrease. The limit of growing mechanical susceptibility in this situation will be determined by the squeeze film damping. This conclusion is a consequence of the model concerning the calculation of quality factor for a complex structure presented in chapter 4, section 4.5.2.2. A high ratio of displacement will indicate that the arms give the highest contribution to the quality factor. On the other hand, zone 2 (arms) exhibits a lower quality factor than the middle part of the resonator (zone 1) due to the squeeze film effect.

To increase the attenuation factor, we focus on improving the nominal capacitance and simultaneously decreasing parasitic capacitances. For this, we increase the surface of zone 2 and reduce the size of zone 4, respectively. To increase the surface of nominal capacitance without increasing the squeeze film effect, zone 2 is made up of multiple thin clamped free cantilevers spaced apart by 100 µm. To minimize the squeeze film effect, the width of the cantilever was calculated based on the model presented in chapter 2. The optimal width is 11 µm.

5.3. COMSOL simulation

This section presents the results from simulations for different anchor positions, center size and the number of arms (figure 5.3.1) that allows retrieving optimal values to:

a) avoid a multimode behaviour
b) optimize the surface for photoacoustic energy collection
c) decrease the effective mass m_{eff}
d) optimize the ratio of displacement w_{ratio}
e) increase attenuation factor S_A: the surface ratio between nominal and parasitic capacitance

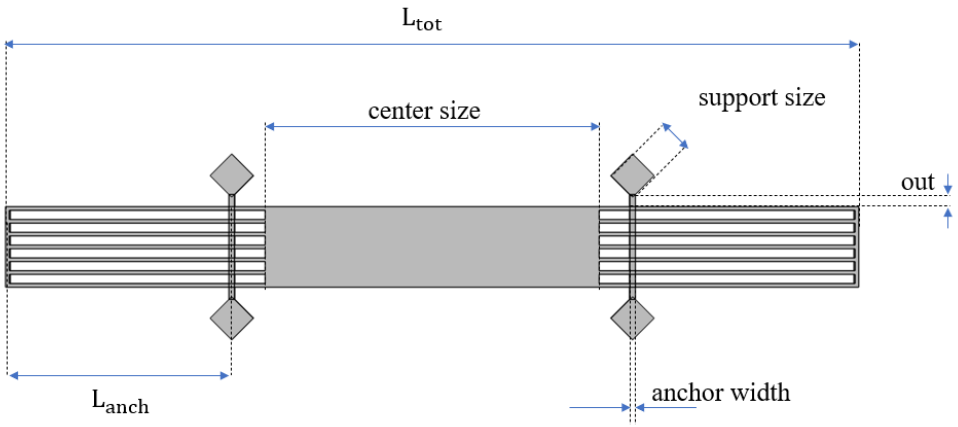

Figure 5.3.1: Sketch of H-resonator with the parameters used for the simulation

Figure 5.3.1 shows a drawing of an H-resonator with the parameters altered during the simulation. The following sections present the impact of these parameters on the mechanical properties of the resonator. We have also studied different thicknesses of devices and the number of arms. Due to the vastness of the results, we present only part of it that we found essential to further comprehension.

5.3.1. Anchor position

Simulations in this section aim to study the parameters which influence the sensor performance as a function of anchor position. We focus on increasing the ratio of displacement, decreasing the effective mass, and increasing the support's quality factor while avoiding anchor positions for which the distance between the main mode and others is less than 1 kHz.

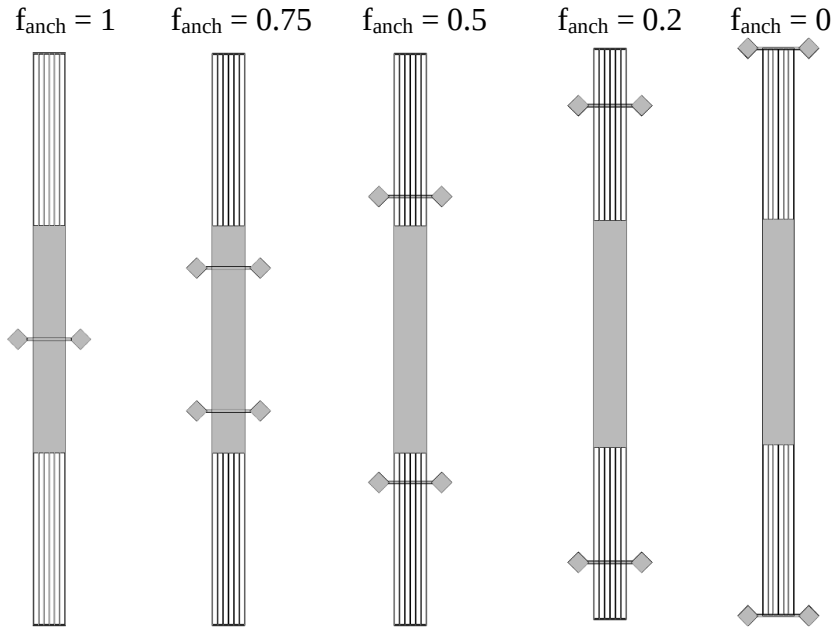

Figure 5.3.2: Graphic depiction of anchor position using a factor f_{anch}.

We expect to work with the particular mode of vibration presented in figure 5.1.1. To begin, we demonstrate that resonators have a wide variety of vibration modes. Secondly, we evaluate our hypothesis connected with anchor position (zone 3) and multimode behavior. For easier visualization of the results, we used f_{anch}, representing the anchor position (figure 5.3.2). This factor is calculated as follow:

$$f_{anch} = \frac{L_{anch}}{L_{tot}/2} \tag{5.1}$$

We plot the resonator frequency of the different modes of vibration as a function of anchor position f_{anch}. We distinguished five different modes of vibration. The mode marked on violet in figure 5.3.3 potentially brings the highest capacitive signal, as both extremities are moving in phase. Subsequent simulations are given for this mode.

Figure 5.3.3 shows the distance between modes as a function of the anchor position. Multimode behaviour will be manifested the most in areas circled in red (figure 5.3.3) and areas where the distance between the modes is less than 1 kHz (minimal distance). However, one needs to keep in mind that minimal distance will depend on the quality factor of each mode.

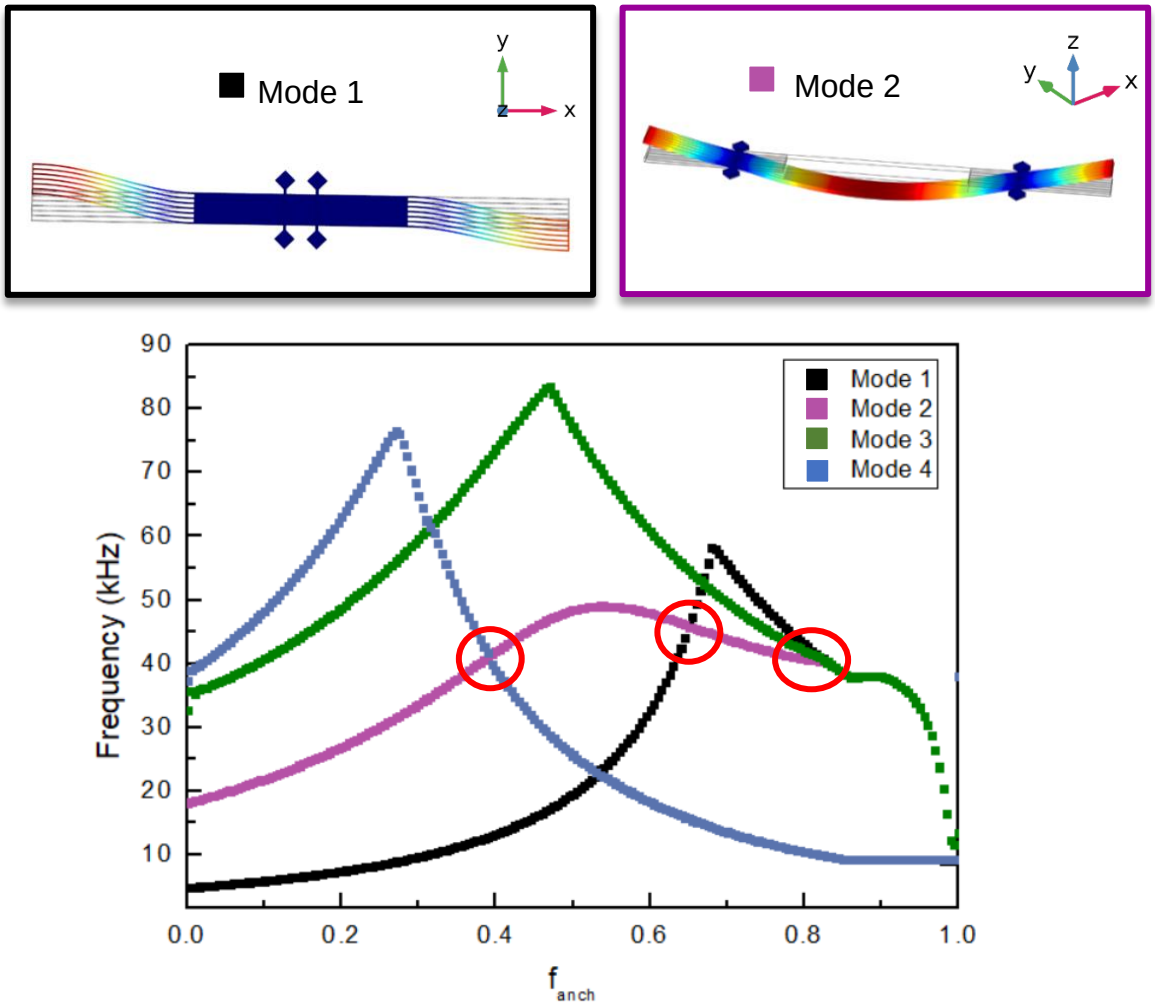

Figure 5.3.3: a) b) Deflection for some of the vibration modes of the H-resonator. c) Results from COMSOL simulation of resonator frequency response for different modes of vibration as a function of anchor position expressed with the factor f_{anch}. Parameters of H-resonator used in the simulation: device thickness 75 µm, L_{tot} 4000 µm, center size 500 µm, support size 250 µm, anchor width 40 µm, number of arms 7.

For the chosen vibration mode (mode 2 figure 5.3.3), we want to increase the ratio of displacement, quality factor and decrease the effective mass. This study for different resonator

parameters is presented in figure 5.3.4. Marked in the figure M_{ratio} refers to the ratio between effective mass m_{eff} and total mass m_{tot} calculated in the following manner:

$$M_{ratio} = \frac{m_{eff}}{m_{tot}} \tag{5.2}$$

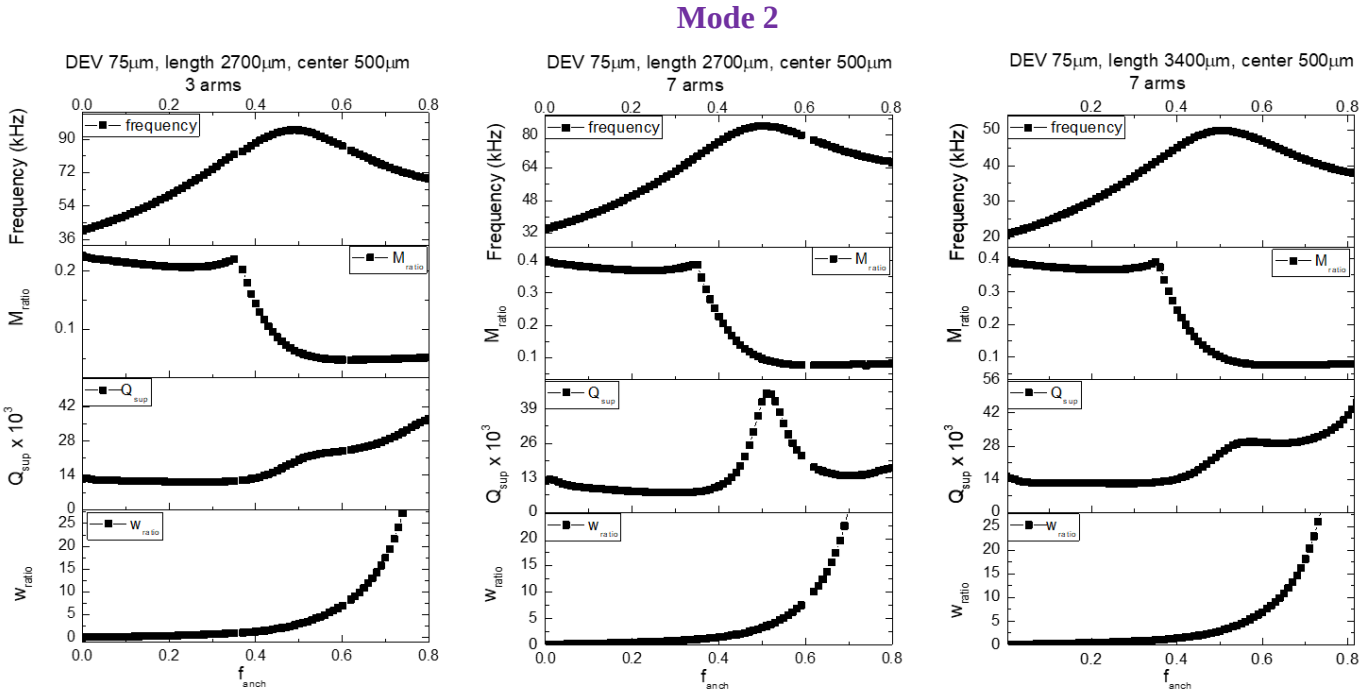

Figure 5.3.4. Results from the COMSOL simulation of chosen H-resonator as a function of anchor position expressed with factor f_{anch} . Parameters of H-resonator included above the graphs; where DEV informs about a device thickness, length is L_{tot}, center is center size, M_{ratio} is the mass ratio given by equation (5.2), Q_{sup} is a support quality factor, w_{ratio} is the ratio of displacement between extremity of zone 2 and center of zone 1 introduced in chapter 4.

The effective mass and ratio of displacement exhibit the same trends in all graphs in figure 5.3.4. A clear transition point for effective mass is visible for f_{anch} 0.45. The displacement w_{ratio} rises with f_{anch}. The low ratio of displacement suggests that most of the movement is centred in the heavy central section of the resonator. As a result, effective mass is large in this situation. As the anchor position value grows, so does the ratio of displacement, implying that more and more movement is provided by arms that are relatively light and, therefore, effective mass decrease.

Nevertheless, the distance between the modes decreases for higher values of f_{anch}. To avoid overlapping of the modes, f_{anch} cannot exceed value 0.6 for presented resonators. Therefore, values of f_{anch} ranging between 0.43 and 0.6 appear to be promising.

The distance of the modes in the frequency changes with changing different parameters of resonators, like center size or a number of arms. This study will be presented in the following sections.

5.3.2. Center part

This section discusses a study concerning the effect of the center part (zone 1) marked in figure 5.3.1. The size of zone 1 (center size) is of great importance for photoacoustic energy collection. However, all the parameters are interconnected, and proper structure optimization requires simulation that combines permutation over the resonators' parameters. In other words, it is necessary to verify how altering one parameter affect other parameters.

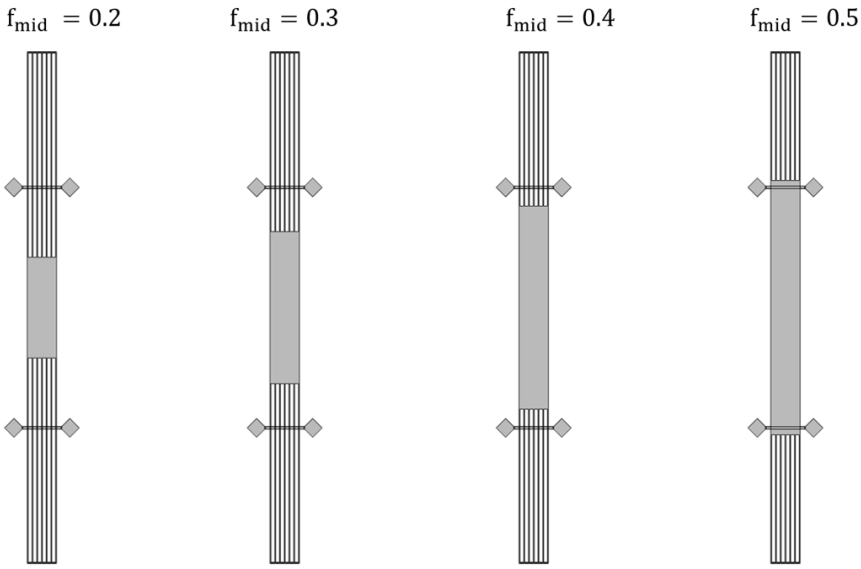

Figure 5.3.5: Graphic depiction center size using a factor f_{mid}. Anchor position is equal to factor $f_{anch} = 0.47$.

That is why we conducted a study that combines a sweep over zone 1 (center size) of the resonator and anchor position f_{anch}. For easier visualization of the results, we used factor f_{mid} which represents the size of zone 1 in comparison to a total length L_{tot} of the resonator. It is presented in figure 5.3.5 and can be mathematically described with the following equation:

$$f_{mid} = \frac{center\ size}{L_{tot}} \tag{5.3}$$

The results are presented in figure 5.3.6. Red points indicate the values of $f_{anch,}$ for which the distance between modes is less than 1 kHz, while hatched fields indicate possibly the most

favourable anchor position. We have chosen this range due to the transition point for effective mass. As a transition point, we refer to the value of $f_{anch} \approx 0.45$ where there is a visible drastic decrease of the effective mass.

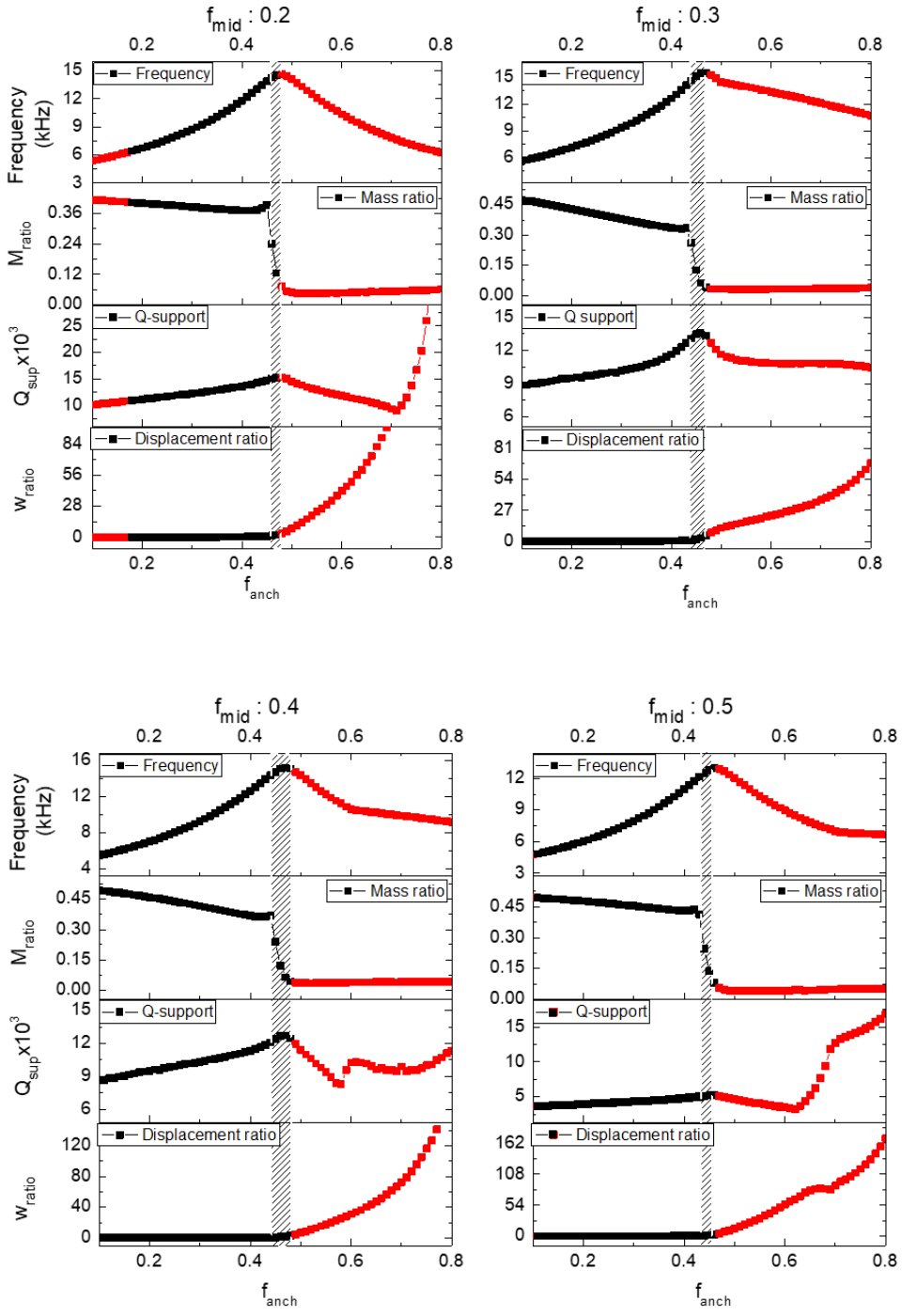

Figure 5.3.6: Results from COMSOL simulation for H-resonators with different center sizes indicated at the top of the graphs with a factor f_{mid} given by equation (5.3). In red, we marked areas where the distance between the mode of interest and others is less than 1 kHz.

To investigate transition point range more profoundly, we plot the effective mass, total mass and the ratio of displacement for different f_{mid} as a function of anchor position.

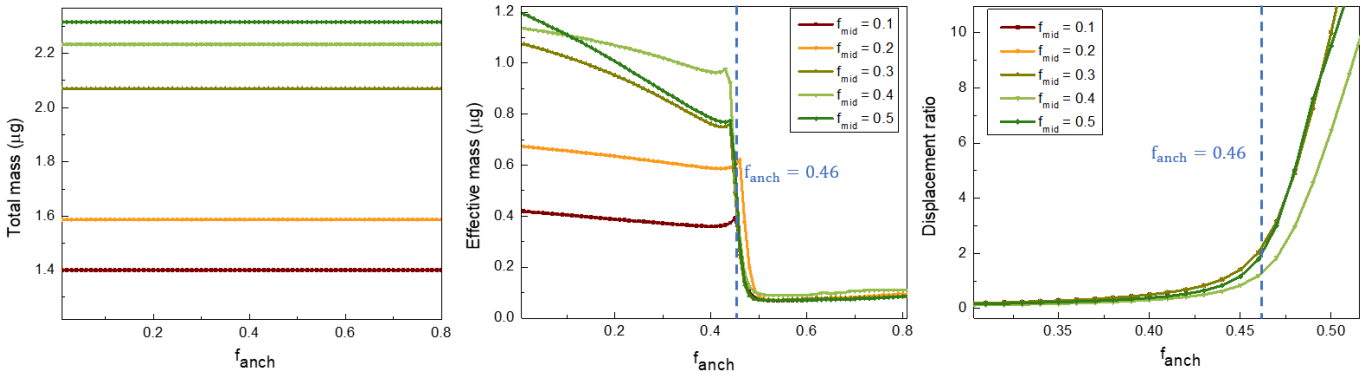

Figure 5.3.7: Total mass (left panel) and effective mass (middle panel) and the ratio of displacement w_{ratio} (right panel) as a function of anchor position f_{anch} and for different sizes of center part f_{mid}.

As presented in figure 5.3.7, effective mass significantly decreased for **all the investigated center parts (all f_{mid})** at the **transition point**, which we estimated at anchor position $\mathbf{f_{anch} = 0.46}$.

This transition point is advantageous because it allows us to expand the central part (zone 1) of the structure without increasing the effective mass. Additionally, the ratio of displacement is unaffected by the anchor position (for the studied range). To maximize the ratio of displacement and minimize the effective mass, we should work in the area for the f_{anch} >0.46.

The analysis demonstrates that the middle part's transition point for different sizes is at f_{anch} = 0.46. Therefore, the area of interest for anchor position is above f_{anch} = 0.46.

5.3.3. Number of arms

This section aims to present how effective mass, the ratio of displacement, and support quality factor change with changing the number of arms. It could be favourable to increase the number of arms for two reasons :

a) increasing area for photoacoustic energy collection (favourable)
b) increase area of the nominal capacitance

However, as all the parameters are interconnected, we conducted a parametric study by changing the number of arms for a resonator with anchor position f_{anch} = 0.48. These results are presented in figure 5.3.8a. To support our choice for anchor position, we plot the mass ratio for a resonator with 3 and 7 arms, which is presented in figure 5.3.8b. The curves for 3 and 7 arms are characterized by the same trend and same value for a transition point.

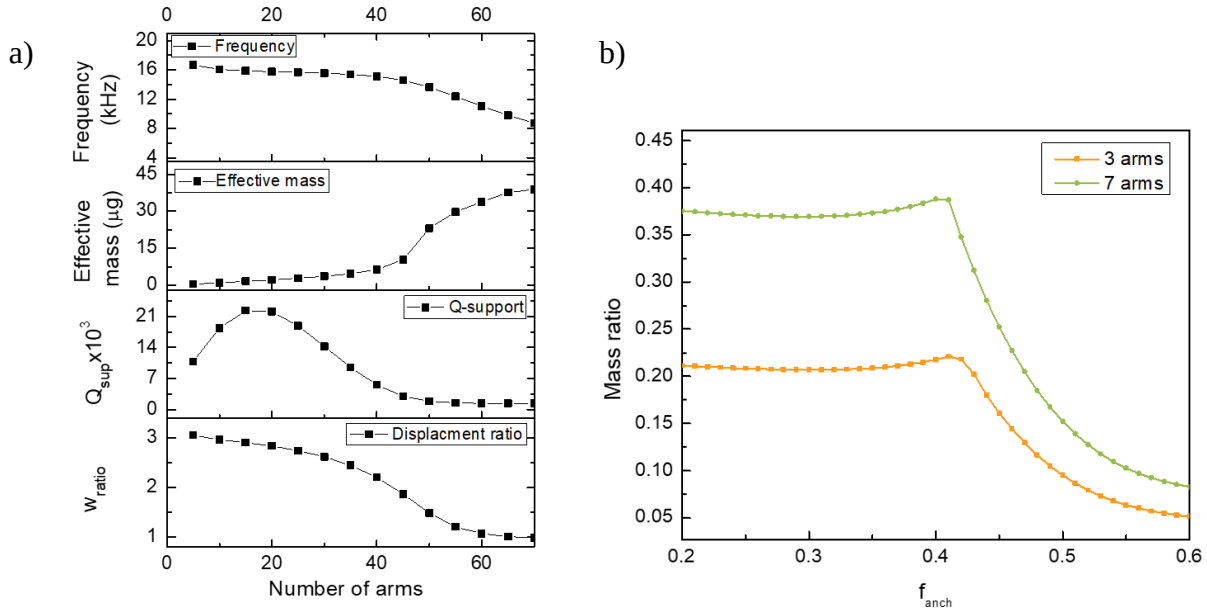

Figure 5.3.8: a) Results from COMSOL simulation of H-resonator as a function of the anchor position for H -resonator. Parameters of H-resonator are following: f_{anch} = 0.48, f_{mid} = 0.4, L_{tot} = 9000 μm. b) Plot of mass ratio as a function of anchor position for resonator with 3 and 7 arms.

Moreover, we verified if changing the number of arms influences the multimode behaviour, which is presented in figure 5.3.9.

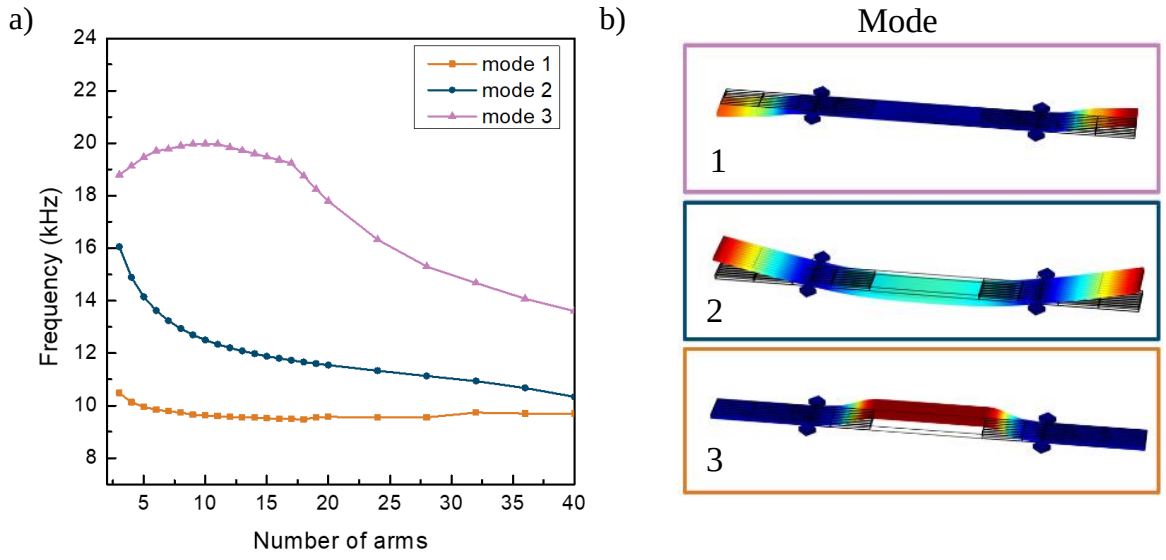

Figure 5.3.9: a) Results from COMSOL simulation of resonator frequency response for different vibration modes as a function of the number of arms. b) Visualization of first three modes of vibration. Parameters of H-resonator are following: f_{anch} = 0.46, f_{mid} = 0.4, L_{tot} = 9000 μm

As seen in figure 5.3.9a, increasing the number of arms is disadvantageous since it increases the effective mass, decreases the ratio of displacement, causes the multimode behaviour and increases fabrication difficulties. We assume that the crosstalk between the modes will be significant if the distance between mode 2 (the mode of interest) and the other modes is lower than 1 kHz. According to the data and assumption, multimode behaviour will manifest for the number of arms above 36. Therefore, we decided to use the design with a **number of arms below 10**. In this case number of arms will not lead to a multimode behaviour.

Finally, an increasing number of arms will increase the stress and total mass. If the mass is raised, it is likely that larger support (zone 4) will be required. This would consequently lead to an increase in parasitic capacitance.

5.4. Data selection

We have designed and fabricated a set of resonators (appendix A5), consisting of 66 resonators of the device thickness 75 μm. Parameters that differ between resonators, their values and their expected impact on resonator performance are presented in table 5.4.1. Based on the analytic model provided in chapter 2 and the study reported in section 5.3, we expect resonators with the lowest frequencies, the largest surface of zone 1 and the highest number of arms (but below 10) will be characterized with the best performances.

Manufactured resonators turned out to be fragile. The most fragile were resonators characterized by the lowest frequencies and center size of 500 μm. The examples of damaged resonators are presented in figure 5.4.1. Resonators with a low frequency are characterized by the longest arms. Long and thin arms exhibit poor stiffness, which means they are more prone to damage (red circle, figure 5.4.1).

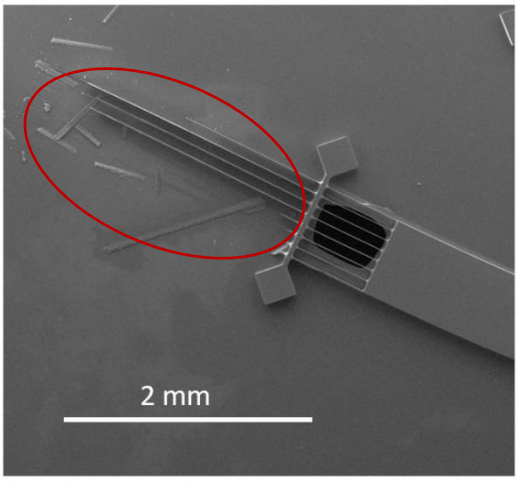

Figure 5.4.1. SEM pictures presenting an example of damage resonators due to the long arms.

Table 5.4.1. Parameters of fabricated H-resonators with their value and influence on the performance (figure 5.3.1).

Parameters	Value	Consequences
center part	f_{mid} = 0.4 and 500 μm	Increasing this factor (value) will increase the area of zone 1 and consequently the photoacoustic force. This parameter is essential in photoacoustic measurement.
f_{anch}	0.48	This parameter has the most significant impact on multimode behaviour, effective mass and ratio of displacement. We establish 0.46 to be a transition point for effective mass. It is more favourable to move the f_{anch} to a higher value. However, to avoid the multimode behaviour, we chose to work with f_{anch} = 0.48.
number of arms	2,3,4,5,6,7,8,9,10	This parameter will increase the nominal capacitance and width of the center part leading to higher photoacoustic force.
anchor width	40 μm	It defines the size of zone 3. This parameter affects mainly the support quality factor $Q_{support}$. There is a slight dependence on effective mass, frequency, the ratio of displacement and multimode behaviour. We establish 40 μm being an optimal value.
support size	250 μm	It defines the size of zone 4. This parameter influences the support quality factor and holds the whole structure.
out	100 μm	This parameter influences the support quality factor and gives uncertainty for back etching alignment. It is favourable to increase the parameter. However, the limit exists strains (too long out will be unable to hold the structuredue to strains).
resonance frequency	15 kHz, 45 kHz, 65 kHz	This parameter allows optimizing for the photoacoustic force. It is more favourable to decrease the resonance frequency.

Fabricated resonators were characterized with LDV using piezoelectric and photoacoustic excitation. Due to the vastness of data, table 5.4.2 presents results from resonators characterized by the best performances. The nomenclature of the samples can be found in appendix A5.

Table 5.4.2. Results for Laser Doppler vibrometer measurement for selected resonators.

SAMPLE	LDV						
	Piezoelectric			Photoacoustic**			
	Date	f_0 (kHz)	L_{max}* (Vrms)	Date	f_0 (kHz)	Q	L_{max}* (mVrms)
H75R15M500N8	07.2020	22.6	0.12	11.2020	22.3	280	3.5@100%
H75R15M500N10	07.2020	14.2	0.1	11.2020	13.8	340	2@100%
H75F15F4N7	07.2020	15	0.11	07.2020	15	660	0.15@400ppmv
H75F15F4N9	07.2020	15.8	0.14	11.2020	21.3	320	8@100%
H75R45F4N6	07.2020	45.34	0.014	04.2021	45.35	250	3.6@100%
H75R45N10	07.2020	45.3	0.015	04.2021	45.3	270	4.8@100%

Table 5.4.2. Photoacoustic characterization with capacitive detection for selected resonators.

SAMPLE	Capacitive			
	Photoacoustic**			
	Date	V_{DC} (V)	f_0 (kHz)	L_{max}* (mVrms)
H75R15M500N8	12.2020	20	22.3	0.1 @ 0.1%
H75R15M500N10	12.2020	20	13.8	0.2@400 ppmv
H75F15F4N7	12.2020	20	20.6	0.3@100%
H75F15F4N9	12.2020	20	21.2	0.24@0.1%
H75R45F4N6	04.2020	30	44.1	2.1@100%
H75R45F4N10	04.2020	30	44.7	3.5@100%

*L_{max} is a maximal amplitude of the Lorentzian peak in mVrms

** Photoacoustic excitation was performed with the laser NORCADA emitting at 2.3 μm with output power 3.9 mW and at a methane concentration indicated in the table.

It is worth noting that for some resonators, performances decreased in time. For instance, just after fabrication of the samples, we obtained a clear photoacoustic signal from H75R15F4N7 resonator with a methane concentration of 400 ppmv. However, this signal was unattainable after two months. We identified similar problems with other resonators. We hypothesize two major reasons for the device degradation:

a) pollution of the sample (presented in figure 5.4.2)
b) too high polarization voltage, which caused irreversible micro-deformation of the structure

In the next section, we present results for the resonator, which demonstrated the best performance over a long term use.

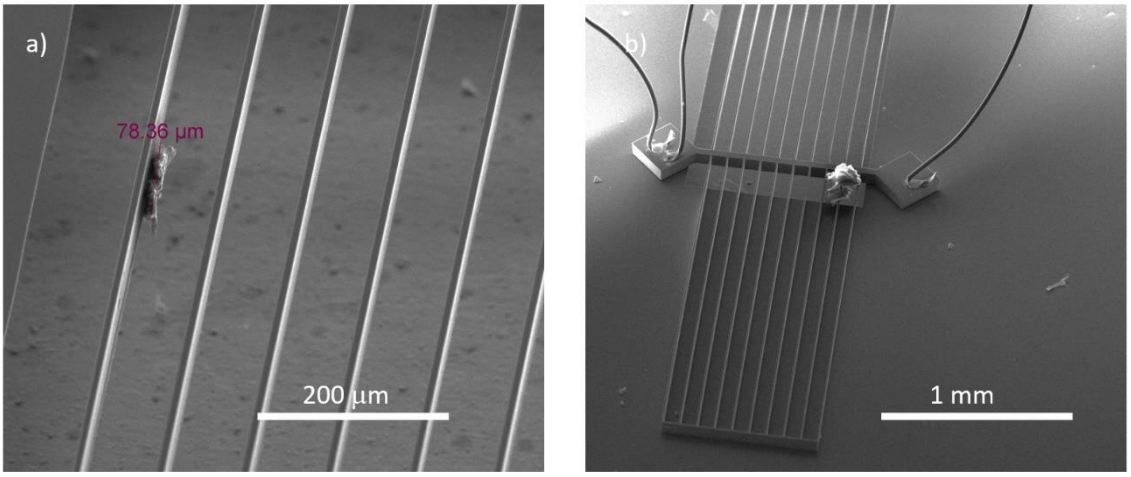

Figure 5.4.2: SEM picture presenting pollution on the sample.

5.5. Photoacoustic gas detection results

This section aims to present a photoacoustic gas detection performed on a resonator, which demonstrated the highest performance and stability over long term use. We start with a description of the resonator. Secondly, we present a setup on which photoacoustic detection will be performed. The characterization of the resonator is achieved with photoacoustic excitation via capacitive transduction. Subsequently, we will perform 1f and 2f detection to prove that the signal comes from photoacoustic and not photothermal excitation.

For gas detection, we used methane and laser NORCADA emitting at 2.3 µm

5.5.1. H-resonator

In this section, we present a chosen resonator for photoacoustic gas detection: H75R45F4N10. The resonator is illustrated in figure 5.5.1. The figure shows that the resonator is not perfectly aligned with a back hole (marked in red in figure 5.5.1). We believe that this misalignment might cause more energy losses as the air is trapped between the resonator and substrate, causing squeeze film damping.

The total length of the resonator is L_{tot} = 4700 µm, the length of center size is 1880 µm, the width of center size is 775 µm, number of arms is ten and calculated resonance frequency is 45 kHz. The contacts were made by micro soldering with aluminium wires. To prevents Schottky contact, we used highly doped silicon. It lowers barrier height at the interface

metal-semiconductor. Due to the low work function and maturity, most commonly is used aluminium and tungsten. It assures low impedance for the flow carriers in both directions.

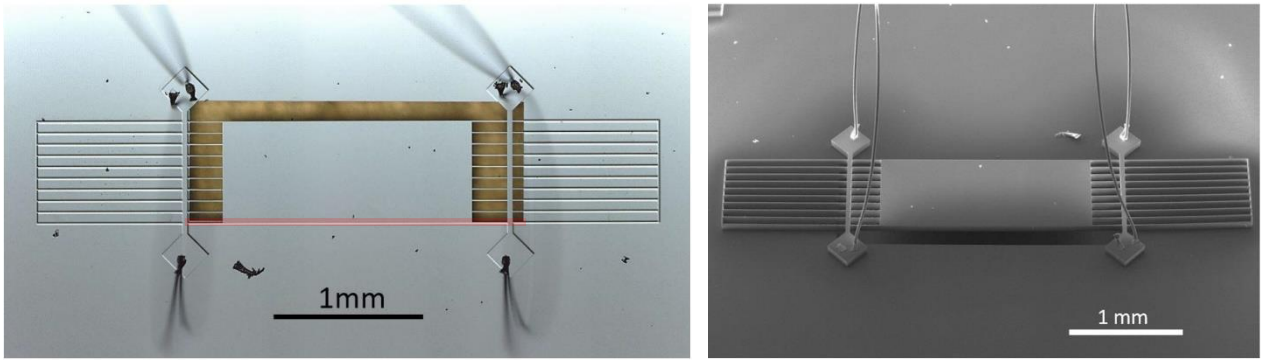

Figure 5.5.1. Optical (right panel) and scanning electron microscopy (left panel) pictures of the H-resonator with its wire bonding.

5.5.2. Setup

To achieve photoacoustic excitation used a setup presented in figure 5.5.2. The cell is filled up with methane. To target one of the methane lines, we used a DFB laser NORCADA emitting at 4294.55 cm^{-1} (2.3 μm) in a continuous wave regime. The current threshold of the laser reaches 40 mA at a temperature of 25°C.

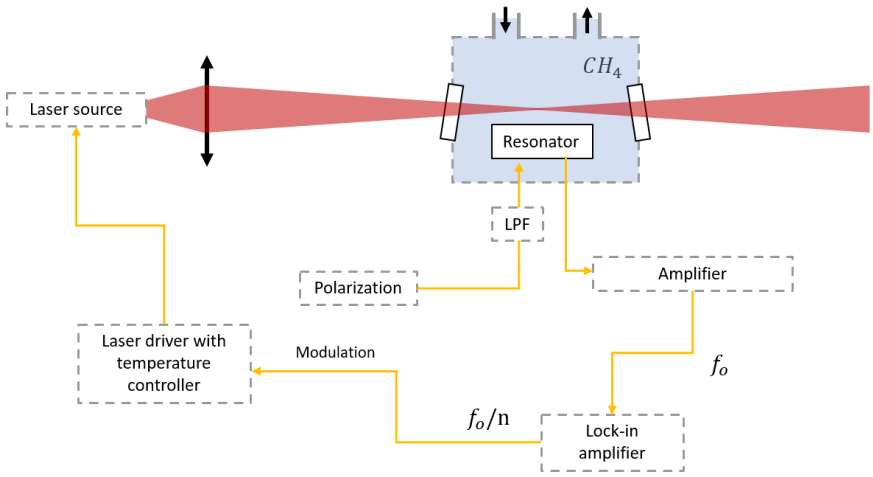

Figure 5.5.2. Scheme of the experimental photoacoustic setup with capacitive detection. The laser current is modulated at n-harmonic (n=1 for 1f detection, n=2 for 2f detection). The signal from the resonator is amplified and demodulated by the lock-in amplifier. LPF indicates a low pass filter.

Based on the HITRAN database [1], in this range of wavelength exists a strong and isolated methane transition at ν = 4300.36 cm-1 with absorption cross-section $\sigma = 8.62 \cdot 10^{-21} cm^2 . molecules^{-1}$. This absorption cross-section is presented in figure 5.5.3 together

with absorption spectra obtained from the photodiode by the measurement with NORCADA laser at 100% concentration of CH4. The maximum of the absorption peak

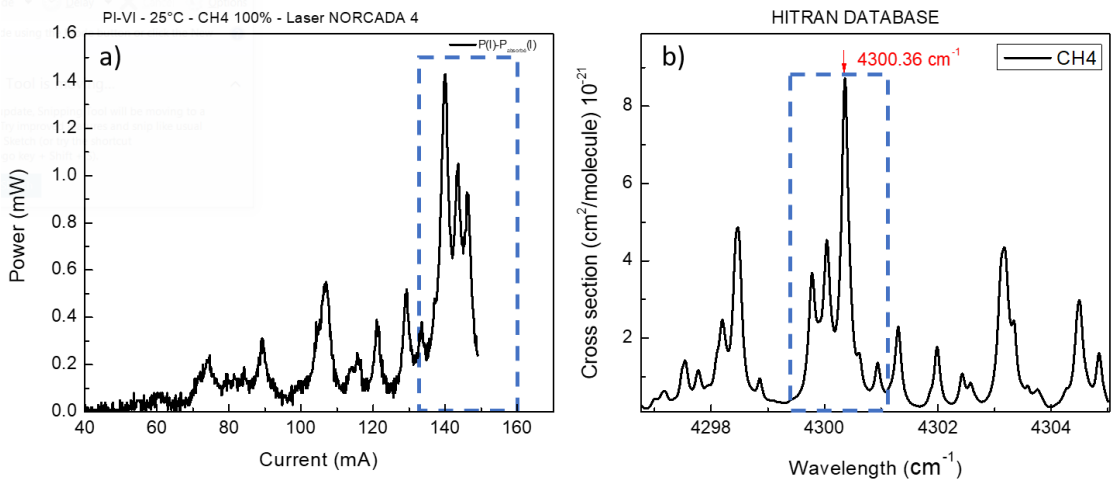

Figure 5.5.3: a) Absorption spectra of methane obtained by photodiode measurement with 100% CH_4 and without gas. b) Methane cross-section in the atmospheric pressure obtained using HITRAN database. With blue squares, we marked the corresponding absorption areas.

In comparison to initial setup presented in chapter 4, we improved the electrical circuit. To decrease the parasitic capacitance, the length of the connections were reduced. The concept was to decrease the distance between the electronics and sample. Therefore, we created a two stage circuit presented in figure 5.5.4.

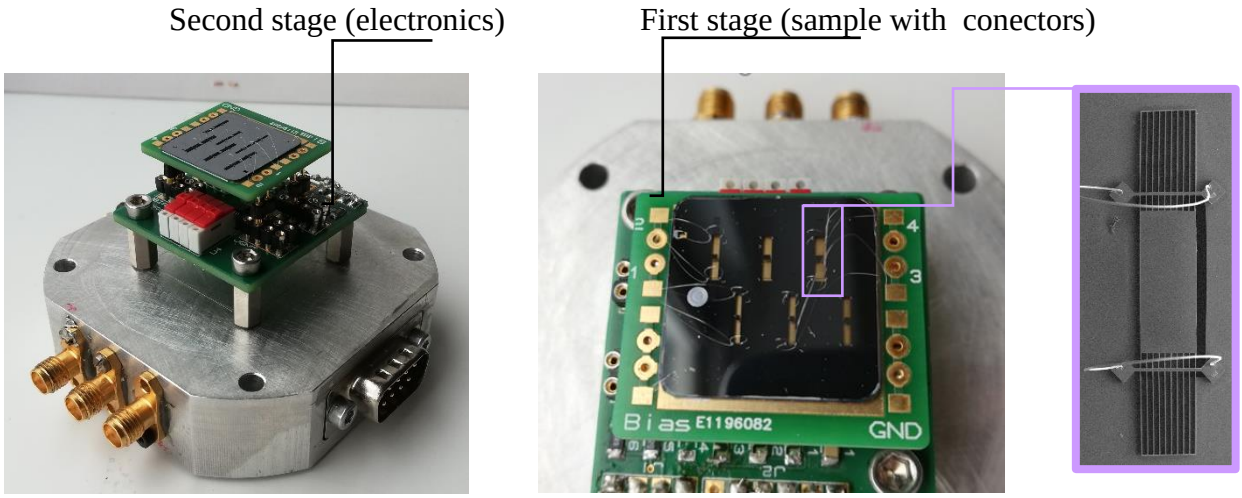

Figure 5.5.4: Pictures of the electronic stage with various resonators (left panel). The first stage of the circuit with a sample. There are six resonators present on the sample, from which four are connected (left panel).

We employed two printed circuit board (PCB) plates (figure 5.5.5) that interlock with each other using pin connectors. These connectors provide both mechanical stability and electrical signal transmission. The first stage (figure 5.5.4 right panel and figure 5.5.5 right panel) holds the sample with resonators and provides an electric contact. The second stage (figure 5.5.5 left

panel) contains the rest of the circuits and got equipped with a connector that allows switching between resonators.

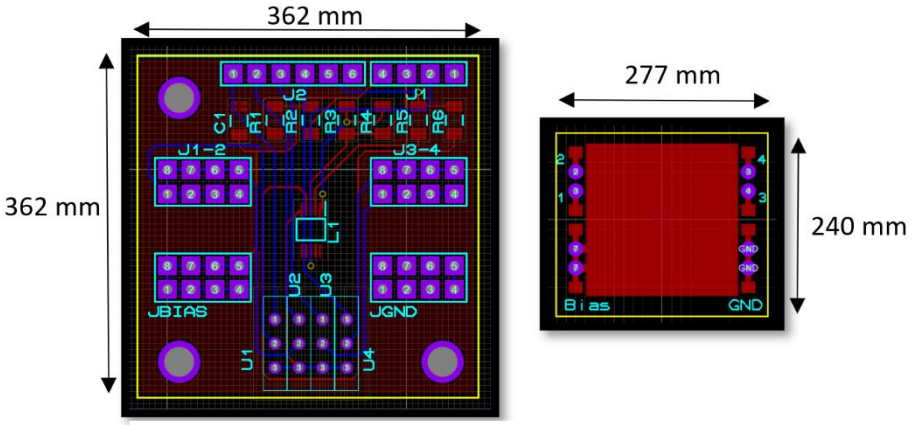

Figure 5.5.5: Bottom stage (left panel) and top stage (right panel) diagram of the PCB used for the electric circuit presented in figure 5.5.4.

For the measurements, we used polarization voltage in range 10 V and 30 V, and a FEMTO current amplifier LCA-40K-100M.

5.5.3. Characterization

To characterize the H-resonator with capacitive transduction, we target a methane absorption peak at ν= 4300.36 cm. For this, the laser temperature is fixed at 25°C and current at 138.5 mA. The frequency response of the H-resonator is acquired by sweeping the laser modulation frequency. The experiment was run with varying values of polarization. The outcomes are shown in figure 5.5.6.

As predicted, the electrical signal is proportional to the polarization voltage. For low polarization voltages, the response of the H-resonator may be represented by a Lorentzian curve. Thanks to Lorentzian fit, we estimate a quality factor Q and resonance frequency f_0 which for H-resonator Q=266 and f_0= 44.79 kHz, respectively. The shift in resonance frequency with polarization voltage results from a change in spring constant caused by the electrostatic force acting on the resonator. The following experiments are done with a polarization voltage of 30 V to optimize the electric signal from the H-resonator. It is worth noting that a high polarization voltage may cause the resonator to collapse [2].

The viscous quality factor for this structure should be 705, based on the analytic model presented in chapter 2 and the model for calculation of quality factor for a complex structure presented in chapter 4, section 4.5.2.2. We believe that the experimental value is lower due to the misalignment marked in red in figure 5.5.1.

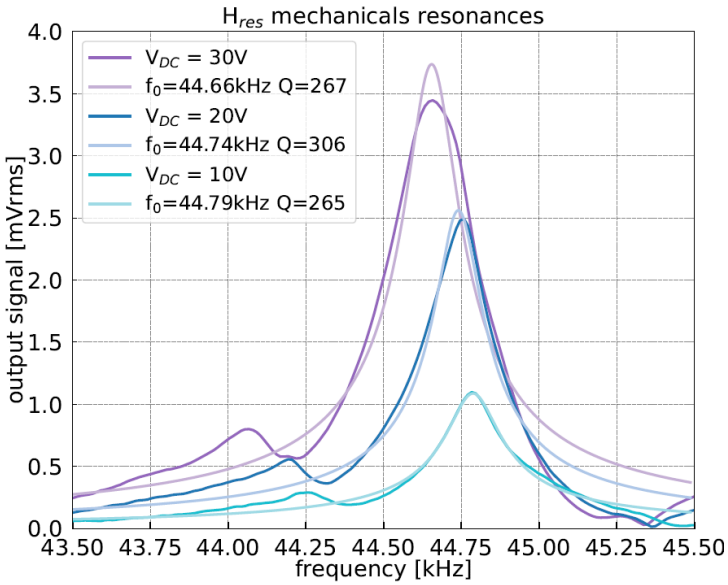

Figure 5.5.6. Capacitive measurement of H-resonator frequency response with under photoacoustic excitation with 100% CH_4 for different polarization voltage V_{DC}. The quality factor and the resonance frequencies were obtained via Lorentzian fit.

5.5.4. Modulation amplitude

To generate the harmonics of the absorption signal and thus identify the signature of the gas absorption spectrum, we perform wavelength modulation spectroscopy WMS. The main idea behind the WMS approach is to change the laser wavelength to scan the gas absorption profile while simultaneously modulating the laser wavelength with a sine wave.

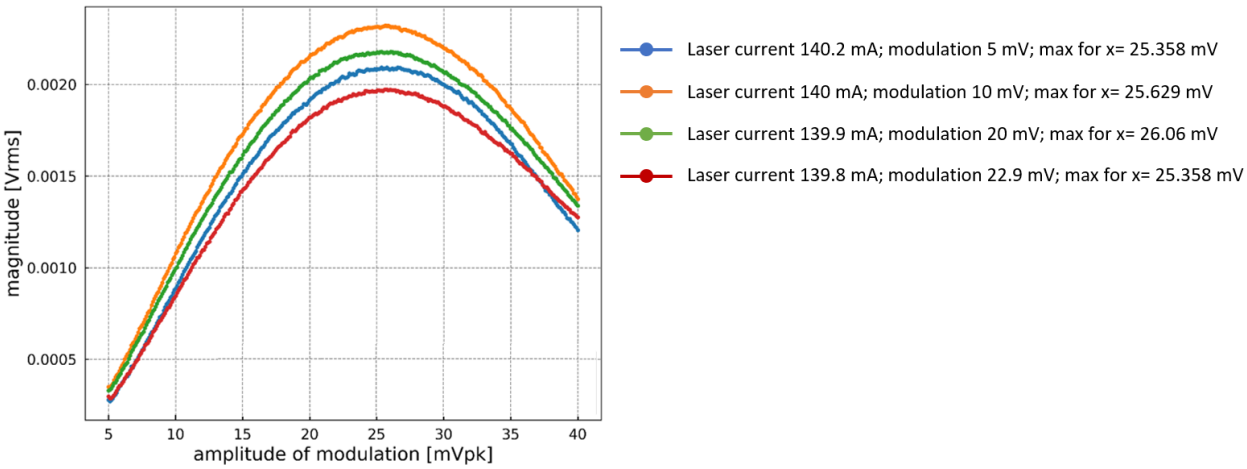

Figure 5.5.7. Optimization of the modulation amplitude for the 2f detection for laser current ranging between 139.8 mA (red curve) to 140.2 mA (blue curve). Maximum obtained for current 140 mA and modulation amplitude 25.659 mV (orange curve). The methane concentration 100%.

According to the wavelength modulation theory, there is an optimal modulation amplitude for 1f and 2f detection. The calculation of the optimal modulation amplitude requires recalculation for different frequencies as the response from the laser driver is not constant with frequency. To avoid this problem, we created a program in Python that allows retrieving an optimal modulation amplitude while changing both modulation amplitude and laser current. The results for 2f detection are presented in figure 5.5.7. The maximum is obtained for laser current 140 mA, and amplitude modulation set on lock-in amplifier 25.66 mV, corresponding to 9.3 mA of current applied on the laser. Subsequently, the modulation amplitude of value 9.1 mA for 1f detection was calculated using the theoretical model presented in appendix A1.

5.5.5. Gas detection

As recalled in chapter 4, the silicon micromechanical resonator is sensitive to photothermal excitation. When the resonator moves under this type of excitation, it can provide a false positive electrical signal even with the absence of the gas. Detection of the first and second derivatives of the gas spectrum allows confirming that the signal is a result of photoacoustic excitation.

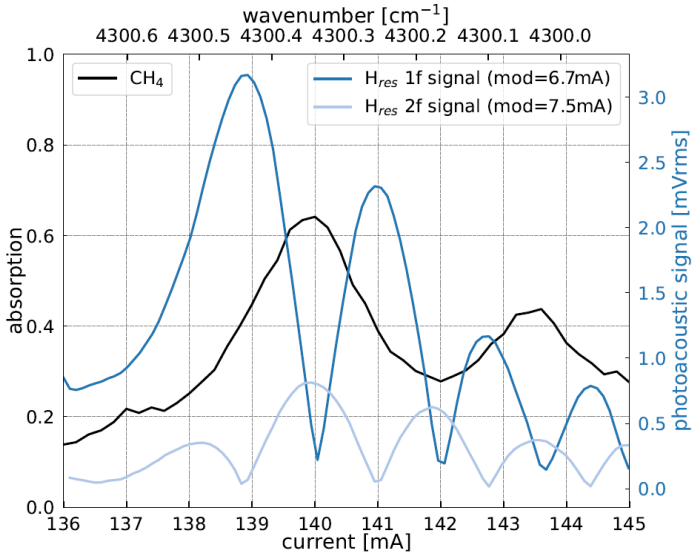

Figure 5.5.8: Absorption spectra of methane obtained by photodiode measurement with 100% CH4 and without gas (black curve). The absolute value of 1st (light-blue) and 2nd (dark blue) harmonic - WMS signal obtained by the absorption of 10% CH4 at atmospheric pressure, using a DFB laser emitting around 2.3 µm with an output power of 3.9 mW for a current of I=140 mA at a temperature of 25°C.

Especially useful for photothermal noise detection is second harmonic detection (2f detection). In 2f detection, the signal is proportional to the curvature of the detected absorption profile. This is a reason why a second-derived signal contribution of a broad absorption is minimized. The thermal absorption of materials is much larger than absorption of the targeted gas.

We detected the 1f and 2f signals of target gas absorption using a spectral scan obtained by adjusting the driving current of the laser. These results, along with an absorption spectrum, are shown in figure 5.5.8. We used photodiode measurements with and without gas to get the absorption spectra. This figure proves the resonator's photoacoustic excitation as 1f (light blue curve, figure 5.5.8) and 2f (blue curve, figure 5.5.8) signals correspond to the absolute value of first and second derivate of the absorption (black curve figure 5.5.8). According to [3], a lower modulation amplitude results in a more precise derived shape of the absorption signature. As a result, the modulation amplitude for this test was less than the optimum value in order to clearly distinguish 1f and 2f signatures.

5.6. Comparison with QTF

This section presents the technique of photoacoustic gas detection that uses a quartz tuning fork (QTF). As described in chapter 1, Quartz Enhanced Photoacoustic Spectroscopy (QEPAS) stands as one of the best techniques in terms of sensitivity in photoacoustic gas sensing. Furthermore, this technique is the most similar to ours as it does not require a photoacoustic cell. Therefore, we determined that comparing our approach to a bare QTF in on-beam mode would be the most trustworthy because of the lack of acoustic cell or other components that might confine the acoustic wave

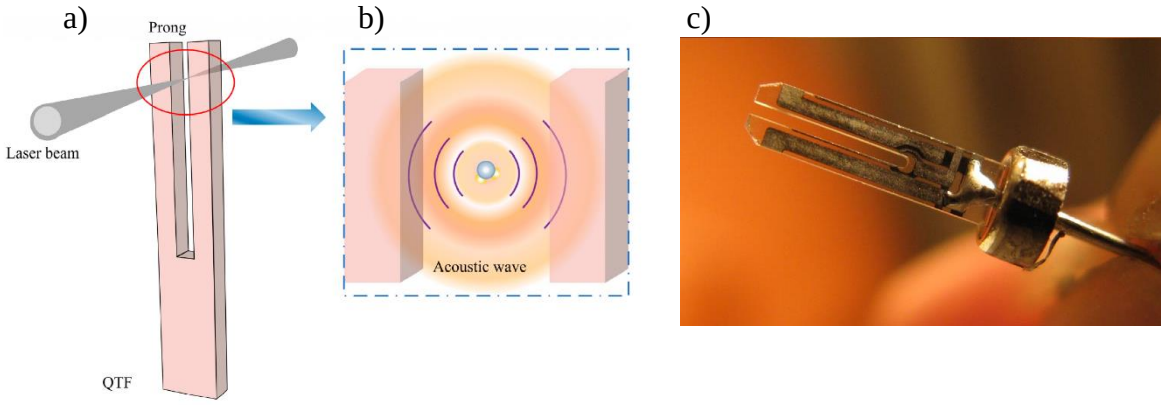

Figure 5.6.1. a) Scheme of the QTF with a laser beam in the on-beam configuration, b) photoacoustic wave created between the prongs on QTF [4], c) picture of a QTF.

In the on-beam configuration, the laser is focalized between the two prongs of QTF, as schematically presented in figure 5.5.5. Due to the reaction between modulated laser light and gas, a photoacoustic wave is created between the prongs of the QTF. This photoacoustic wave acts on the prongs setting them in motion. The movement of the prongs is translated into an electrical signal via the piezoelectric effect.

5.6.1. Characterization

Before performing the experiment of gas detection, it is necessary to know the characteristic of the studied quartz tuning fork: resonance frequency and quality factor. It is expected that QTF is characterized by the quality factor (around 10000) and resonance frequency around 32 kHz. For the characterization, we studied the frequency response of the QTF under electrical excitation. Lock-in amplifier acts as a function generator that sends a signal at a fixed frequency to the quartz tuning fork. One end of the QTF is connected to the excitation source and the second to the output. The output signal is amplified by the transimpedance amplifier and demodulated with the lock-in amplifier. The response from the lock-in amplifier is presented in figure 5.6.2. As pointed out in chapter 4, the time constant and distance between the points need to be well adjusted to obtain a reliable measurement. In the presented measurement (figure 5.6.2) the time constant was set for $\tau = 500$ ms, the time between two measurements: 1.5 s, distance between two points: 0.15 Hz.

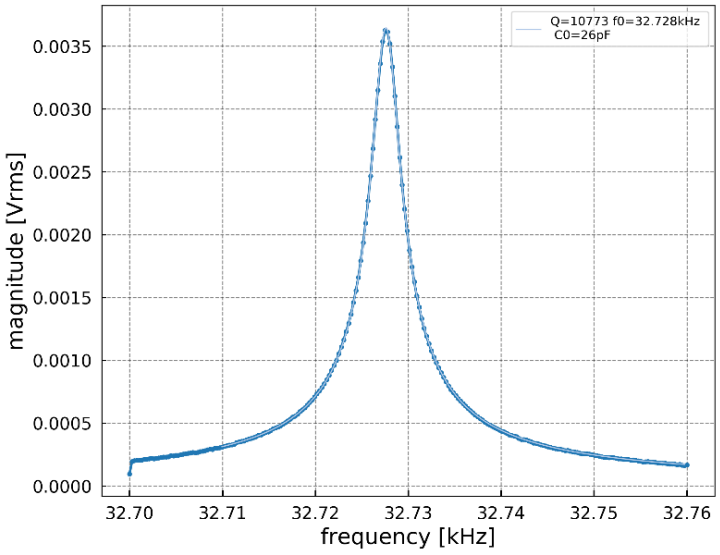

Figure 5.6.2: Frequency response of QTF under electrical excitation. Bidirectional sweep with a step of 0.15 kHz, time constant 500 ms and distance between the measurement 1.5 s, excitation voltage V_{ac} = 1 mV. The quality factor of the QTF is around 10800, and resonance frequency f_0 = 32.73 kHz.

The studied QTF is characterized by a quality factor of 10800 and a frequency of 32.729 kHz. The value of QTF's quality factor is above average, which is beneficial in photoacoustic sensing since it increases the displacement of the quartz tuning fork and, as a result, the voltage output. The same photoacoustic force will cause the highest displacement of the QTF characterized by a quality factor of 10800 than one at Q=10000. Furthermore, a high quality factor enhances immunity to noise that raises the signal-to-noise (SNR) ratio, which is essential in the limit of detection.

5.6.2. Results and comparison

This section aims to compare the QTF with H-resonator. To assure the reliability of measurement, the conditions were the same, and the modulation amplitude of the QTF was optimized, as in the case of the H-resonator. Characterization of the QTF was performed before each measurement in order to verify if the QTF did not degrade. Due to the high quality factor of the QTF, it was necessary to track the resonance frequency between each measurement to ensure that the photoacoustic measurement was performed under the best conditions.

5.6.2.1 Linearity of the measurement

As a first comparison between the QTF and H-resonator, we compare the linearity of the photoacoustic signal. It was performed on a calibrated dilution of CH_4 obtained using a mass flow controller Alytech GasMix Aiolos II. This measurement allows retrieving information about the proportion between photoacoustic and photothermal excitation. The signal recorded in the absence of absorbing gas provides information regarding photothermal noise.

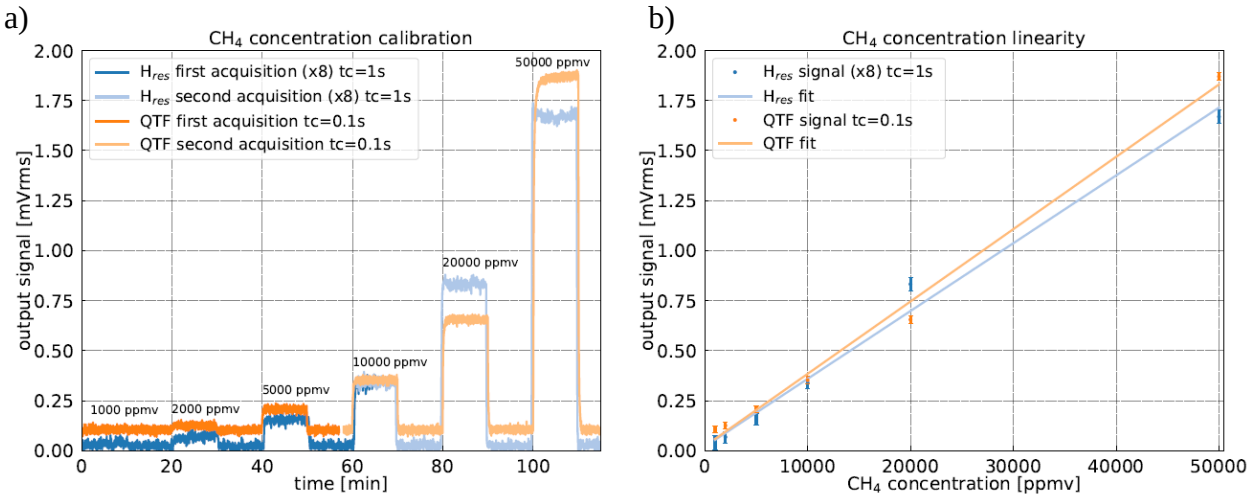

Figure 5.6.3: a) 1f QEPAS (orange) and H-resonator (blue) signal during continous measurement with a gas step cycle. Concentration was ranging from 1000 ppmv to 50000ppmv. After injecting a known concentration of methane for 10 minutes, the cell is flushed with pure N_2 for 10 minutes. (b) Signal form QEPAS (orange) and H-resonator (blue) as a function of injected methane concentration with a linear fit of the response. The integration time is 0.1 s for QEPAS and 1 s for H-resonator.

The curves shown in figure 5.6.3 on the left panel were assessed by monitoring the 1f signal from both the QTF and the H-resonator in dynamic measurement at 950 Nml/min gas flow rate. To test the recovery of the zero signal, the cell was sequentially filled with a

calibrated gas concentration and flushed with N_2 between stages. Methane concentration ranged from 1000 ppmv to 50000 ppmv. Each step was carried out for 10 minutes, and the measurement was taken constantly. Both curves exhibit reasonable and comparable linearity (figure 5.6.3, right panel), indicating a lack of sensor non-linearity induced by high voltage bias. The QTF data has a considerable offset as a result of thermal excitation. This photothermal excitation was reduced in subsequent measurements by improving the setup alignment.

5.6.2.2. Allan variance and NNEA

To evaluate the sensor stability, and more precisely to calculate the limit of detection and NNEA, we used an Allan variance analysis covered in chapter 4.

Allan-Werle analysis presented in figure 5.6.4 was performed for data series collected during 30 min at CH_4 concentration of 10% and time constant of 100ms. Allan variance was calculated by monitoring 1f and 2f signals for the quartz tuning fork and the H-resonator at optimum modulation amplitudes of 9.1 mA and 9.3 mA, respectively. To achieve the best signal, the current was set to I=138.5 mA for 1f detection and I=140 mA for 2f detection. The laser power reaches 3.86 mW and 3.92 mW under these circumstances.

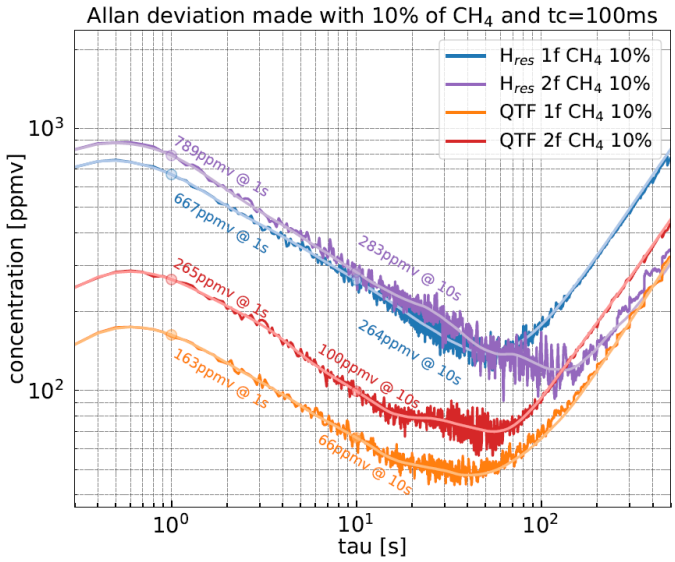

Figure 5.6.4: Allan-Werle deviation for QTF and H-resonator calculated from a 30 minutes acquisition for the 1f and 2f mode with 10% of CH_4 concentration and time constant of 100ms.

The slope of the curve in figure 5.6.3 at integration time τ <1s does not follow the predicted classical $t^{-1/2}$ slope behavior. The reason behind it is connected to the cut-off frequency of the lock-in amplifier's low pass filter. More precisely, the signal from the lock-in amplifier may be seen as an average of many measurements. The time of averaging is dictated

by the time constant. The measurement is considered to be trustworthy for τ at least 5 times greater than the time constant. It implies that if the Allan variance was applied to data with a time constant, such as 100ms, the findings would be trustworthy and would show the traditional $t^{-1/2}$ slope for τ greater than 500 ms. As a result, the curves in figure 5.6.4 have a standard $t^{-1/2}$ slope for τ > 1 s. Long-term drift appears after 40 s for QTF and after 55 s and 105 s for 1f and 2f detection, respectively, for H-resonator.

For silicon micromechanical resonators, the CH_4 limit of detection is 667ppmv at 1s integration for 1f detection and improves to 264ppmv with 10 s of integration according to the 1σ criterion. For 2f detection, the LOD corresponds to 789 ppmv for 1s of integration and 283 ppmv for 10s of integration.

For QEPAS on-beam setup, LOD for 1f detection equals 163ppmv and 66ppmv for integration times of 1s and 10s, respectively; whereas for 2f detection, it amounts to 265ppmv and 100ppmv for integration times of 1s and 10s, respectively.

5.6.3. Discussion and conclusions

The H-resonator LOD for 1f detection at 1s integration time results in a normalized noise equivalent absorption coefficient (NNEA) of $5.5 \cdot 10^{-7}\, W.cm^{-1}\sqrt{Hz}$. On the other hand, the QEPAS NNEA at 1s integration is $1.3 \cdot 10^{-7}\, W.cm^{-1}\sqrt{Hz}$. The value of NNEA for on-beam QEPAS is similar to the literature value, which is $1.2 \cdot 10^{-7}\, W.cm^{-1}\sqrt{Hz}$ for on-beam QEPAS [5]. Presented above NNEA for QEPAS shown superior performance over NNEA for resonant MEMS by a factor of four. Both measurements were made under identical circumstances, indicating a high degree of reliability.

On-beam QEPAS performance is equivalent to that of the silicon-based microresonator, even though it is still in the early stages of development.

5.7. Conclusions

We began this chapter by presenting a new design of resonator: simplify version of X-resonator presented in chapter 3. The geometry the new resonator, called H-resonator was designed in a way to overcome the problems encountered with the previous resonator. Secondly, we studied the optimization of the physical parameters of the H-resonator:

a) photoacoustic force
b) avoid energy losses
c) capacitive signal enhancement

We described the applied procedure to increase each of the physical parameters. The optimization was performed based on COMSOL finite element simulation as well as the analytic model presented in chapter 2. Through the simulations, we have proved a hypothesis concerning the multimode behaviour and anchor position. Subsequently, we have determined the anchor position, for which the ratio of displacement w_{ratio} is increased and effective mass decreased simultaneously, providing good separation between the modes (>1 kHz) in order to avoid crosstalk. Based on the results, we created a set of resonators with different parameters (table 5.4.1)

We fabricated a set of resonators using deep reactive ion etching that reduced the destructive squeeze film effect compared to wet etching and increased reproducibility. From the set of resonators we chose the one characterized by the best performances over a long term use. The chosen resonator is characterized by the resonance frequency of f_0 = 44.8 kHz and quality factor of Q = 266. Subsequently, we employed it in photoacoustic gas detection via capacitive transduction. In methane detection with laser NORCADA emitting at 2.3 μm the output power of 3.9 mW for a current of I=140 mA, we obtained a reproducible limit of detection (LOD) 667ppmv at 1s integration for 1f detection (1σ). This LOD led to a Normalized Noise Equivalent Absorption coefficient (NNEA) of $5.5 \cdot 10^{-7}\, W.cm^{-1}\sqrt{Hz}$.

The results for photoacoustic gas detection with H-resonator were compared to on-beam Quartz-Enhanced Photoacoustic Spectroscopy (QEPAS) technique, which stands as a reference for compact and selective gas sensors. NNEA and LOD at 1s of integration for 1f detection measured with bare QTF in on-beam configuration is $1.3 \cdot 10^{-7}\, W.cm^{-1}\sqrt{Hz}$ and 163 ppmv, respectively. This stands only four times higher than for H-resonator.

Even though we used an H-resonator for gas detection due to its high performance over the long term, its performance was far from the resonators with the greatest performances at their initial state. Therefore, expect that some of the fabricated resonators should present better LOD and NNEA than H75R15F4N5.1.

Future sensor improvements will concentrate on design modifications to improve the quality factor and photoacoustic energy collecting and reduce the fragility of the device. With the design improvements, it appears that obtaining the same or greater sensitivity to QEPAS-based sensors is indeed feasible.

The invention of the silicon microresonator described in this work opens the way for a new generation of integrated gas sensors.

Bibliography

[1] I. E. Gordon *et al.*, "The HITRAN2016 molecular spectroscopic database," *Journal of Quantitative Spectroscopy and Radiative Transfer*, vol. 203, pp. 3–69, 2017, doi: 10.1016/j.jqsrt.2017.06.038.

[2] N. Tas, T. Sonnenberg, H. Jansen, R. Legtenberg, and M. Elwenspoek, "Stiction in surface micromachining," *Journal of Micromechanics and Microengineering*, vol. 6, no. 4, pp. 385–397, 1996, doi: 10.1088/0960-1317/6/4/005.

[3] S. Schilt, L. Thévenaz, and P. Robert, "Wavelength Modulation Spectroscopy: Combined Frequency and Intensity Laser Modulation," *Applied Optics*, vol. 42, no. 33, p. 6728, 2003, doi: 10.1364/ao.42.006728.

[4] Y. Ma, "Review of recent advances in qepas-based trace gas sensing," *Applied Sciences (Switzerland)*, vol. 8, no. 10, 2018, doi: 10.3390/app8101822.

[5] A. Kosterev, Yu. A. Bakhirkin, R. F. Curl, "Quartz-enhanced photoacoustic spectroscopy," *Optics Letters*, vol. 27, no. 21, pp. 1902–1904, 2002, doi: 10.3969/j.issn.1001-0548.2015.06.025.

Conclusions and perspectives

Conclusions

The studies described in this thesis addresses the issue of lack of gas sensors characterized by excellent selectivity and high sensitivity provided in real-time measurement combined in a portable and low-cost device. Photoacoustic gas detection is one of the most promising methods to achieve a sensor with all features mentioned above. This thesis aimed to provide a new technique in photoacoustic gas sensing to boost the market and research for innovative, new generation gas sensing. Table 6.1.1 shows which component of the resonator is in charge of the selected characteristic.

Table 6.1.1: Required characteristics of the senor with an assigned component that are responsible for required features.

Selectivity	Sensitivity	Real-time measurement	Compactness
- **photoacoustic**: use of a laser with a linewidth smaller than the width of the absorption line	- **photoacoustic** - **capacitive** readout mechanism - **design**	- **photoacoustic**: (technique itself) - **instrumentation** and **electronics** for capacitive sensing	- **silicon** technology - **photoacoustic** - **capacitive** readout mechanism

The sensor proposed in this thesis is based on photoacoustic gas detection. We studied and realized a silicon microelectromechanical (MEMS) resonator characterized by a well-defined resonance with high quality factor (compared to the standard microphone). Subsequently, to detect the photoacoustic wave, we used silicon with capacitive readout mechanism, which allows avoiding any material deposition, is highly compatible with CMOS technology and can provide sub-femto-farad resolution [1]. To reach the objective, the work was divided into several parts.

In chapter 1, we presented our choice of technique: laser-based infrared absorption spectroscopy. Our choice was motivated by the possibility of achieving excellent selectivity. From laser absorption-based technique, we choose photoacoustic detection as it is potentially the best for compactness. Subsequently, we presented the three most common photoacoustic transducers used in gas sensing: standard photoacoustic based on microphones (PAS), QEPAS techniques and its variation, CEPAS.

One of the main challenges in achieving our goal was posed by capacitive transduction itself. Namely, the presented sensor needs to be a good photoacoustic transducer and a good capacitive transducer. A good photoacoustic transducer should be characterized by a high

overlap between the acoustic force and mechanical mode. For this, the surface for photoacoustic energy collection should be maximized. On the other hand, a good capacitive transducer needs to be characterized by a small distance between electrodes and high displacement. The small distance between the electrodes causes the squeeze film damping, which decrease the sensitivity of the device. To decrease this damping, the surface should be minimized. This creates a dilemma as for photoacoustic force energy collection, the surface should be maximized, and for capacitive transduction, the surface should be minimized. We called this dillema 'opposite trends dilemma'. Chapter 2 addresses this problem. Namely, we attempt to create a model that would provide a resonator's geometry allows to enhance the capacitive signal under the photoacoustic force and simultaneously provide a high signal-to-noise ratio. The model was created on a simple cantilever which allowed us to provide a fully analytic model. However, this model showed that a simple cantilever would not reach the state-of-the-art performances of photoacoustic gas sensors.

The model presented in chapter 2 showed that to create a resonator that would present the state-of-the-art performances, we need to apply another approach. In chapter 4 we proposed an orignial geometry of the resonator. Further, thanks to the original desing, we focused on the separation of the problems through dividing function into different sections of the resonator. Thanks to this approach, each part of the resonator can be optimized independently towards a specific function. In chapter 4, we present the first generation of the resonator: X-resonator, where this approach has been applied. Based on this design, we managed to obtain a good photoacoustic transducer characterized by NNEA of $1.6 \cdot 10^{-7} \mathrm{W} \cdot \mathrm{cm}^{-1} \mathrm{Hz}^{-1/2}$ with interferometric measurement. However, this resonator was not a good capacitive transducer. Based on the results, we identified the weaknesses of X-resonator design: high viscous damping more generally the design restrictions imposed by wet etching. Moreover, geometry of X-resonator was not optimized for the photoaocusitc energy collection.

To overcome the issues which occurred with X-resonator, in chapter 5, we proposed a new design: H-resonator realized using deep RIE to achieve good reproducibility, decrease viscous damping and give the possibility to create an design without restrictions imposed by wet etching. Finally, based on new design optimized using COMSOL simulation and analytic model presented in chapter 2, we reach NNEA of $5.5 \cdot 10^{-7} \mathrm{W} \cdot \mathrm{cm}^{-1} \mathrm{Hz}^{-1/2}$ under capacitive detection. Subsequently, we compared results to bare QTF in on-beam configuration for which we got NNEA of $1.3 \cdot 10^{-7}\ \mathrm{W} \cdot \mathrm{cm}^{-1} \mathrm{Hz}^{-1/2}$.

Finally, to provide batch production possibilities, we developed a relatively cheap and simple fabrication process, described in detail in chapter 3.

To conclude, we reached our objective, which was developing a high-performance silicon microresonator with capacitive transduction for photoacoustic gas sensing. Although the silicon-based microresonator is in its early stage of development, its performances are comparable to the on-beam QEPAS performances. We believe that the work presented in this thesis paves the way for a new generation of integrated gas sensors.

Short term perspectives

Even though H-resonator presents satisfying performances, some improvements can be achieved. First of all, the frequency is not optimized. As presented in chapter 2, to increase the photoacoustic force, the frequency should be around 11 kHz (for CH_4 detection). We have made attempts to lower resonator frequency. However, long and thin arms (low rigidity) cause the fragility of the resonator. To overcome this problem, we propose to add perpendicular arms to the structure, as presented in figure 6.2.1. This perpendicular arms are beneficial as they:

a) decrease the device fragility.
b) increase the rigidity and help to suppress the multimode behavior.
c) helps to increase the attenuation factor and consequently capacitive signal.

Figure 6.1.1: Scheme of H-square resonator with perpendicular arms anchor position moved to the center part.

Under the middle part of the resonator (zone 1) there is a hole. The purpose of the hole is the reduction of squeeze film damping. Additionally, the hole can increase the pressure difference between the top and bottom sides of the resonator, which is favourable as it will increase the photoacoustic force according to the following equation:

$$F_{PA} = \int_0^L \int_{-\frac{b}{2}}^{\frac{b}{2}} (p_A - p_B)\phi_n(x,y)dxdy \tag{6.11}$$

where $L, b, p_A, p_B, \phi_n(x)$ are length of the resonator middle part, width of the resonator middle part, pressure at the top side of the resonator, pressure at the bottom side of the resonator (figure 6.2.2c) and mode shape function, respectively.

To maximize the photoacoustic force, one needs to maximize the pressure difference. In H-resonator, the pressure difference is low due to gap and holes marked in yellow in figure 6.2.2d. By the gap, we mean the distance between the resonator and the hole in (x,y) plane in figure 6.2.2a,b,c. To overcome this problem, the anchor was moved towards the middle part and size of the back hole is going to be decreased.

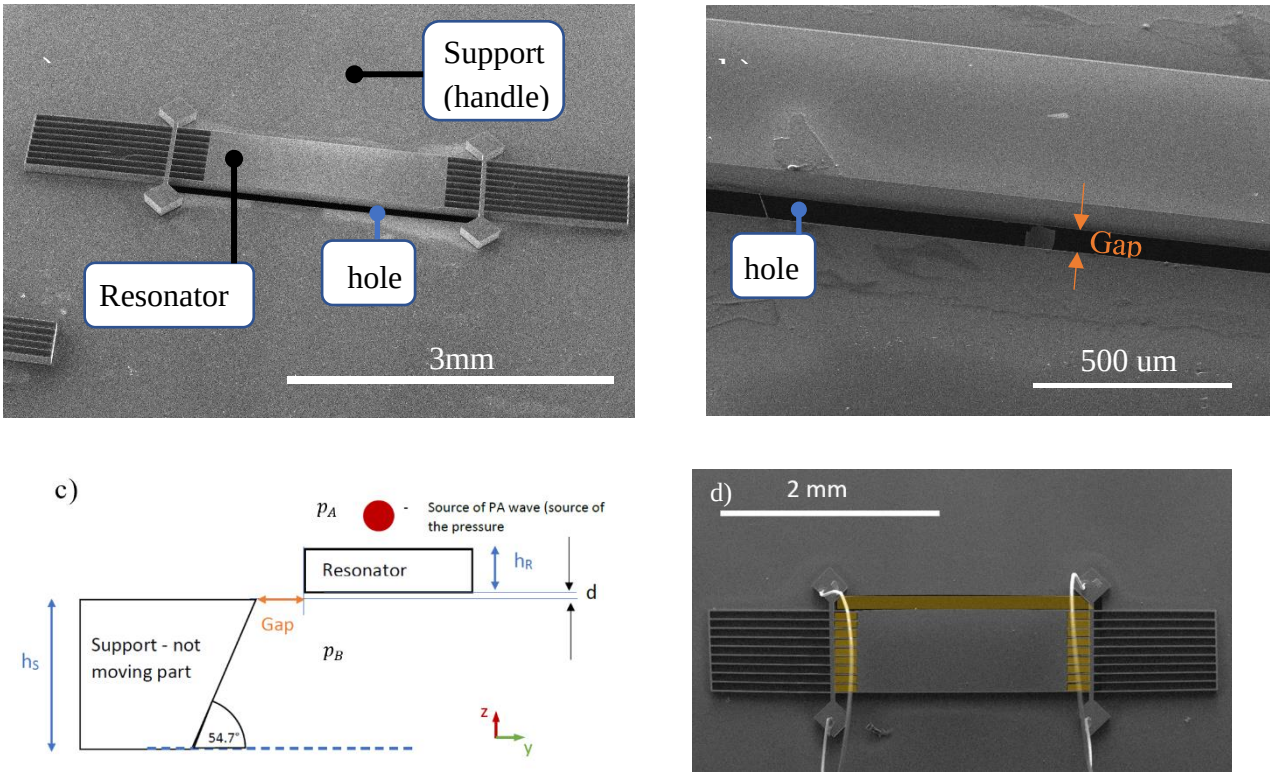

Figure 6.2.2: Figure .1. a), b), d) Picture from scanning electron microscopy of the device (plane x,y), c) sketch of the device cross-section (plane y,z). Where p_A is the pressure at the top of the resonator, p_B is the pressure at the bottom of the resonator (in a hole under the resonator), h_R is the thickness of the resonator, h_D is the thickness of SOI handle (support), d is the vertical distance (on z axis) between resonator and support (d corresponds to silicon oxide thickness).

Long term perspectives

A long time perspective is to integrate a whole sensor; thus, to fabricate all the elements, including electronics and laser, on a silicon wafer. The size of the H-resonator, which we compared with QTF, is around 2.5 mm x 1.5 mm x 0.5 mm (figure 6.3.1), while the size of the QCL laser with mounting fabricated in group NanoMIR (figure 6.3.1) has the size of 0.6 mm x 0.5 mm x 0.3 currently mm.

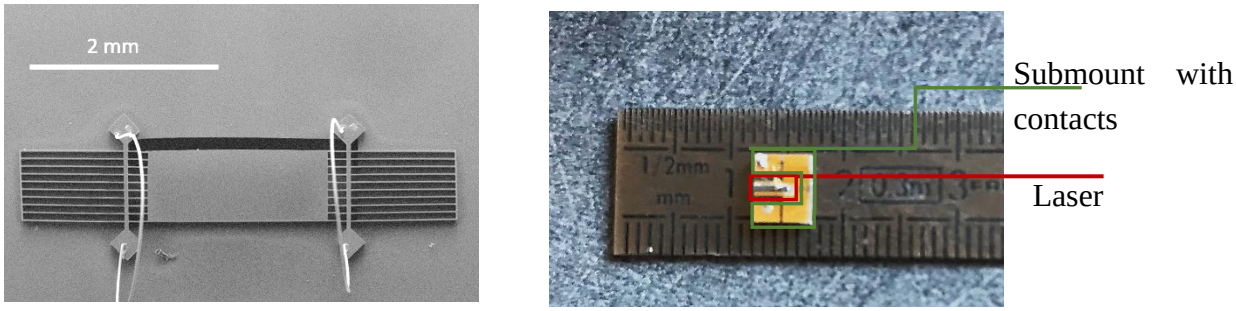

Figure 6.3.1: SEM picture of H-resonator (left panel) and picture of QCL laser with its submount on the millimetric scale (right panel)

Today's MEMS microphones with electronics have a size of 2.5 mm x 3.35 mm x 0.98 mm and cost less than 1 euro. We believe that in the long term perspective, it will be possible to enclose a resonator with a laser with mounting and create a gas sensor as small as 4 mm x 3 mm x 2 mm if feasible.

To increase the sensor sensitivity, other techniques might be used together with a microresonator—for instance, an optical cavity.

Finally, for a multipass gas sensor several resonators can be used together with lasers targeting a certain gas. Moreover, the resonator can be used with a cylindric-shaped acoustic chamber. Both resonator and chamber frequency can be optimized, including thermal relaxation time of the molecules and consequently improving resonator sensitivity.

Bibliography

[1] U. Ferlito, A. D. Grasso, S. Pennisi, M. Vaiana, and G. Bruno, “Sub-Femto-Farad Resolution Electronic Interfaces for Integrated Capacitive Sensors: A Review,” *IEEE Access*, vol. 8, pp. 153969–153980, 2020.

Appendix 1

A1.1. Modulation spectroscopy

Modulation techniques have been developed to reduce the noise contribution in the measurement, consequently leading to an increase of the signal-to-noise ratio. By modulating a specific parameter, the signal is transformed into a periodic signal. In spectroscopic measurement, the modulated parameter is usually the frequency or emission wavelength of the tunable laser diode. Modulation spectroscopy allows to make a measurement in higher frequency and, therefore, reduces commonly present in the electronics 1/f noise.

The most common techniques of modulation spectroscopy are wavelength modulation spectroscopy WMS and frequency modulation spectroscopy FMS, which allows decreasing 1/f noise by moving the detection band to higher frequencies. Frequency modulation and wavelength modulation differ only with the order of modulation frequency in comparison to the width of the absorption line.

Wavelength modulation spectroscopy is based on the modulation of the laser wavelength at a high-frequency range (higher than 1kHz) but with frequency modulation f_m lower than absorption linewidth ν_{line} ($f_m \ll \Delta\nu_{line}$) while frequency modulation is characterized with modulation frequency higher than half width of absorption ($f_m \gg \frac{\Delta\nu_{line}}{2}$). In both techniques, laser light scans the absorption line linearly by changing the output wavelength $\lambda(t)$ of the laser through the current sweep. These techniques generate a signal $\tilde{L}(\lambda, t)$, which consist of periodic components with the modulation frequency f_m and higher harmonics of the spectrum, which can be later on detected using a lock-in amplifier.

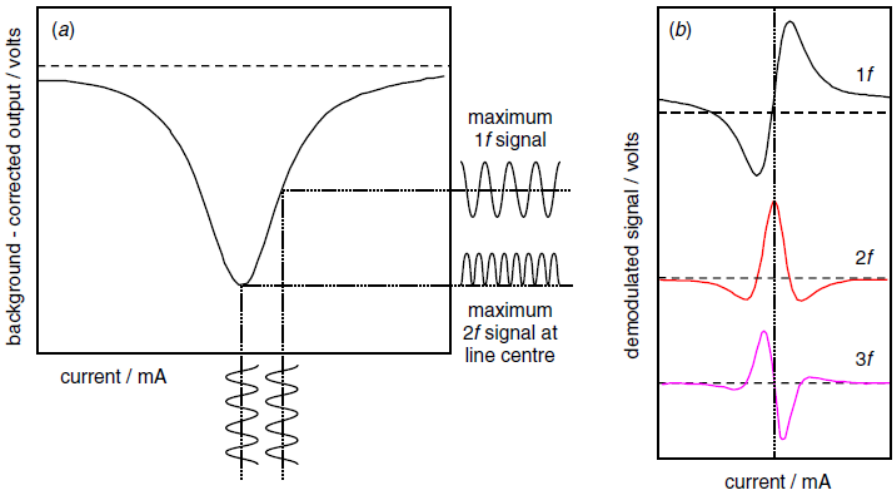

Figure A1.1.1: Generation of different harmonic signals in wavelength modulation spectroscopy. a) DC scan through a single gas line, *b*) Form of 1*f*, 2 *f* and 3 *f* harmonics as a function of position in the current scan. [1]

Wavelength modulation technique generates harmonics of the absorption spectrum, as presented in figure A1.1.1.

Absorption and transmission line shape can be ideally described with the Lorentzian line shape function. However, the experimental line shape change with an ambient conditions like pressure, temperature, and phase. The Lorentzian function, presented in the figure A1.1.2 is given by:

$$L(\lambda) = \frac{1}{\pi} \frac{\frac{1}{2}\Gamma}{(\lambda - \lambda_0)^2 + \left(\frac{1}{2}\Gamma\right)^2} \tag{A1.1}$$

where Γ is full width at half maximum (FWHM) and λ_0 correspond to the center for which the function takes maximal value equal to $L(\lambda_0) = \frac{2}{\pi\,\Gamma}$. In the presented model $L(\lambda_0) = 1$, which indicates that the maximum absorption is equal to 1.

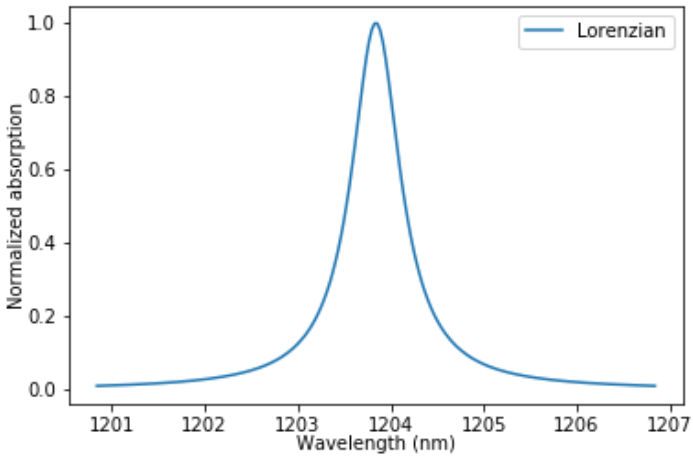

Figure A1.1.2: Lorentzian line shape function with a maximum at $L(\lambda_0) = 1$.

We use wavelength modulation. The laser is modulated around the central wavelength λ_c by:

$$\Delta\lambda = \lambda_{amp}\cos(\omega t) \tag{A1.2}$$

Laser emission can be modeled as follow :

$$\lambda(t) = \lambda_c + \lambda_{amp}\cos(\omega t) \tag{A1.3}$$

where λ_{amp} is the modulation amplitude.

If the absorption spectrum of the gas is described by the equation (A1.4), then absorption of modulated laser radiation can be described by :

$$\alpha(\lambda(t)) = L(\lambda(t)) = \tilde{L}(t) \tag{A1.4}$$

Therefore, modulated absorption function (modulated Lorentzian) will be given now by the following expression :

$$\tilde{L}(t) = \frac{1}{\pi} \frac{\frac{1}{2}\Gamma}{\left(\lambda_c + \lambda_{amp}\cos(\omega t) - \lambda_0\right)^2 + \left(\frac{1}{2}\Gamma\right)^2} \tag{A1.5}$$

The line shape function at the modulation $L(\lambda, t)$ can be expanded into Fourier series with a complex coefficient around the operating point (section A1.2) :

$$c_n = \frac{1}{T}\int_{-\frac{T}{2}}^{\frac{T}{2}} \tilde{L}(t) e^{-in\omega t} dt \tag{A1.6}$$

where n is the successive Fourier series coefficients (n = 1 for 1f detection, n = 2 for 2f detection). Using the convention $\omega t = \phi$

$$c_n = \frac{1}{2\pi}\int_{-\Pi}^{\Pi} \tilde{L}(t) e^{-in\phi} d\phi \tag{A1.7}$$

$$c_n = \frac{1}{4\pi^2}\int_{-\Pi}^{\Pi} \frac{\Gamma}{\left(\lambda_c + \lambda_{amp}\cos(\phi) - \lambda_0\right)^2 + \left(\frac{1}{2}\Gamma\right)^2} e^{-in\phi} d\phi \tag{A1.8}$$

Function given by equation A1.8 can be used to estimate optimized modulation amplitude λ_{amp} to maximize the effective absorption signal. For this we use the dimensionless modulation index :

$$\beta = \frac{\lambda_{amp}}{\Gamma} \tag{A1.9}$$

Subsequently, we plot real part of first and second Fourier coefficient C_1 and C_2 for differnt modulation index. The graphs are presented on the figure A1.1.3. C_1 and C_2 corresponds to the first and second harmonics. Next, we plot maximum of the real part of C_1 and C_2 as a function of the modulation index β .

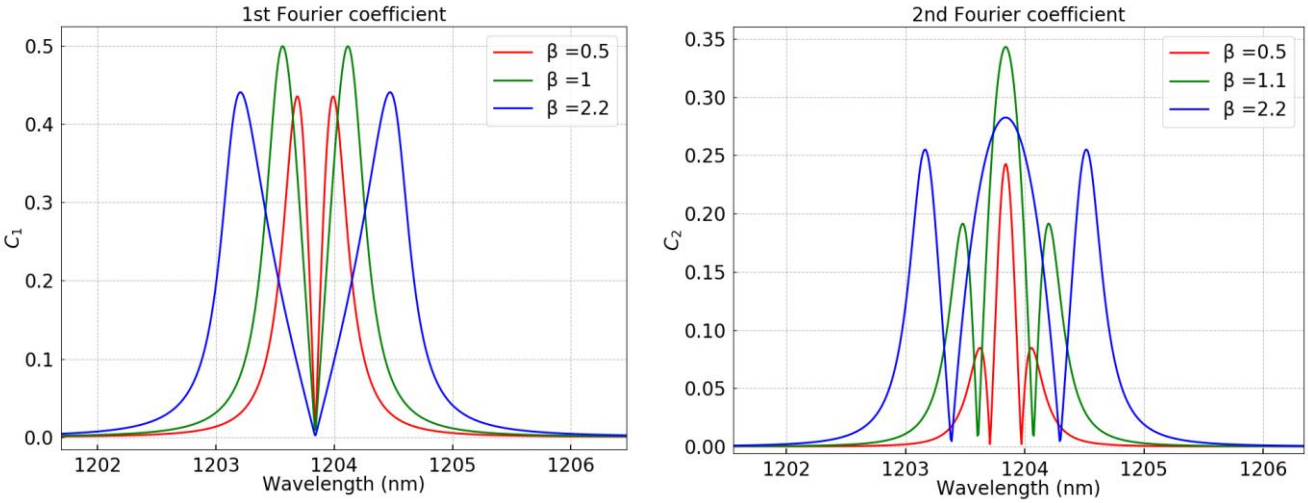

Figure A1.1.3: Absolute value of first (left panel) and second (right panel) derivative of a Lorentzian line shape function for different modulation index β.

This calculation is presented on the figure A1.1.4. From the results we find that the optimal modulation index, which allows to maximize an effective absorption coefficient. Figure A1.1.4 shows that for 1f real $C_1(max)$ is maximal for β = 1 and for 2f detection real $C_2(max)$ is maximal β = 1.11:

$$for\ 1f \qquad \lambda_{amp} = 1\ FWHM$$

$$for\ 2f \qquad \lambda_{amp} = 1.11\ FWHM$$

Coefficients of Fourier series can be use to calculate an effective absorption coefficient $\alpha_{eff}(n)$.

Using the convention of Fourier serie given with sin and cos term (appendix A1.2). The effective absorption coefficient will be given as a real part of c_n

$$\alpha_{eff}(n) = real(c_n) = \mathrm{a_n} \tag{A1.10}$$

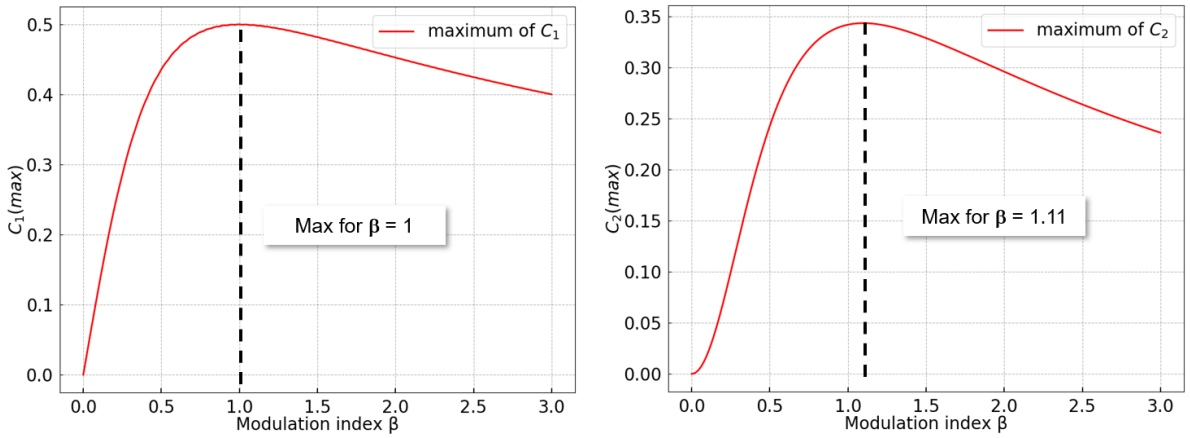

Figure A1.1.4: Maximum of the first C_1 (max) and second C_2 (max) Fourier coefficient as a function of modulation index β.

Therefore, for modulation amplitude $\lambda_{amp} = 1FWHM$ and 1f detection $\alpha_{eff} \approx 50\%$ while for 2f detection and modulation amplitude $\lambda_{amp} = 1.11FWHM$ $\alpha_{eff} \approx 35\%$

We take the real part because we modulate with cos form. If the λ will be modulated with sin, one needs to take a imaginary part (b_n)

A1.2. Mathematical description of Fourier transform

According to any function $f(\alpha)$ can be written as Fourier series (in certain period or hole function if it is periodic) as follow:

$$f(\alpha) = a_0 + \sum_{n=1}^{\infty} a_n \cos n\alpha + \sum_{n=1}^{\infty} b_n \sin n\alpha$$

Where :

$$a_0 = \frac{1}{2\pi}\int_{-\pi}^{\pi} f(\alpha)d\alpha$$

$$a_n = \frac{1}{\pi}\int_{-\pi}^{\pi} f(\alpha)\cos n\alpha \, d\alpha$$

$$b_n = \frac{1}{\pi}\int_{-\pi}^{\pi} f(\alpha)\sin n\alpha \, d\alpha$$

It is possible to complexify the Fourier series even if series, even if $f(\alpha)$ is real

$f(\alpha)$ is real but it can be represented in a complex terms with a Fourier series as follow :

$$f(\alpha) = a_0 \sum_{n=1}^{\infty} \frac{a_n}{2}(e^{in\alpha} + e^{-in\alpha}) + \sum_{n=1}^{\infty} \frac{b_n}{2}(e^{in\alpha} + e^{-in\alpha}) = a_0 + \sum_{n=1}^{\infty} \frac{a_n - ib_n}{2} e^{in\alpha} + \sum_{n=1}^{\infty} \frac{a_n + ib_n}{2} e^{-in\alpha}$$

Term $\frac{a_n+ib_n}{2}$ is a complex conjugate of $\frac{a_n-ib_n}{2}$. The third term of $f(\alpha)$ we can write with following form:

$$\sum_{n=1}^{\infty} \frac{a_n + ib_n}{2} e^{-in\alpha} = \sum_{n=-1}^{-\infty} \frac{a_{-n} + ib_{-n}}{2} e^{in\alpha}$$

which indicates that summation is from $-\infty$ to -1 . Therefore :

$$f(\alpha) = a_0 \underbrace{+}_{c_0} \sum_{n=1}^{\infty} \underbrace{\frac{a_n - ib_n}{2}}_{c_n} e^{in\alpha} + \sum_{n=-\infty}^{-1} \underbrace{\frac{a_{-n} + ib_{-n}}{2}}_{c_n \, for \, negatige} e^{in\alpha}$$

Finally, function $f(\alpha)$ can be written with just one coefficient c_n as follow:

$$f(\alpha) = \sum_{-\infty}^{\infty} c_n e^{in\alpha}$$

While the coefficient c_n we obtain by the following equation :

$$c_n = \frac{1}{2\pi}\int_{-\pi}^{\pi} f(\alpha)e^{-in\alpha} \, d\alpha$$

Bibliography

[1] J. Hodgkinson and R. P. Tatam, “Optical gas sensing: A review,” *Measurement Science and Technology*, vol. 24, no. 1, 2013, doi: 10.1088/0957-0233/24/1/012004.

Appendix 2

A2.1. Nomenclature and design details

Figure A2.1.1 presets the manner samples of X-resonator of 1st and 2nd generation were named. The name incudes type of resonator (X-resonator), a geometry and series

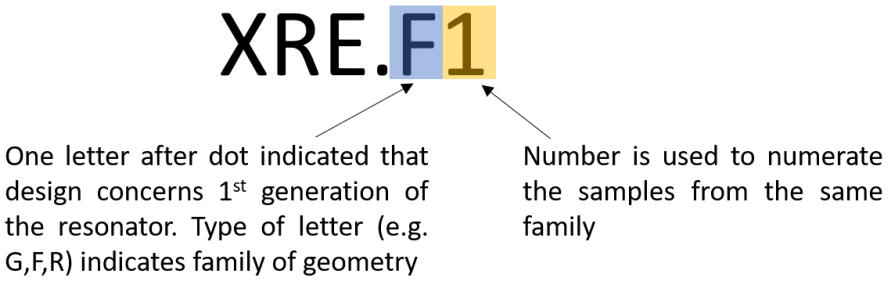

number.

Figure A2.1.1: Scheme presenting the explanation for samples' name.

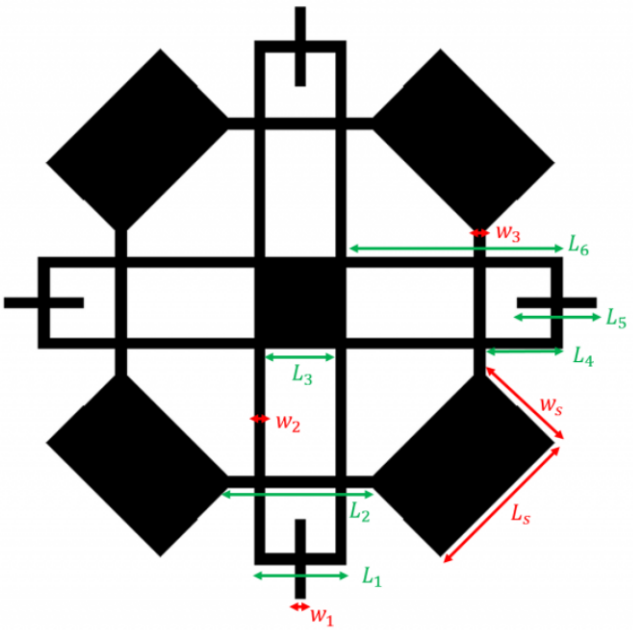

Figure A2.1.2: Geometry scheme of XRE.F presented on the photolithography mask

Table A2.1.1: dimensions of families of X-resonator presented in figure A4.1.2.

name	Frequency (kHz)	w1,w2,w3 (µm)	L1 (µm)	L2 (µm)	L3 (µm)	L4 (µm)	L6 (µm)	Ls (µm)	Ws (µm)
XRE.A	31	89.4	394.7	608.9	284	404	1100	1060	460
XRE.B	34	89.4	327.7	640	280	400	1156	1116	542
XRE.C	37	89.4	394.7	607.5	256	376	953	913	460
XRE.D	41	89.4	327.7	542	257	377	997	957	460
XRE.E	47	89.4	394.8	607.6	233	353	795	755	460
XRE.F	31	89.4	394.7	608.9	284	404	1101	1061	260
XRE.G	50	102.8	394.7	448.9	244	364	1159	1119	451.5
XRE.H	51	102.8	461.6	676	311	431	1017	977	450.7
XRE.K	59	102.8	461.6	676	263	383	896	856	451.5
XRE.L	63	102.8	394.7	608.9	251	371	960	920	451.5
XRE.M	77	102.8	461.6	676	314	434	635	595	450
XRE.N	81	102.8	394.7	608.9	259	379	760	720	451
XRE.R	33	129.5	729.5	943	580	700	1395	1355	432
XRE.S	68	129.5	595.5	810	300	420	938	898	432
XRE.T	72	129.5	528	742	308	428	973	933	432
XRE.U	85	129.5	528	742	256	376	857	817	433
XRE.V	31	89.4	394.7	608.9	284.2	404.2	1100	1060	460

For all resonators L5 (µm) 402µm

A2.2. Methane absorption

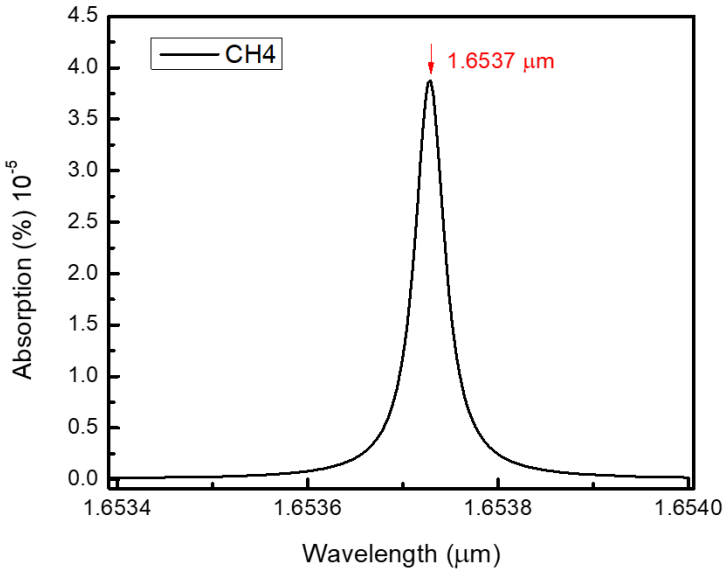

Figure A2.2.1: Methane absorption calculated for 1mmpv and 1cm of optical path centered at 1.6537 µm in the atmospheric pressure obtained using HITRAN database [1]

Bibliography

[1] I. E. Gordon *et al.*, “The HITRAN2016 molecular spectroscopic database,” *Journal of Quantitative Spectroscopy and Radiative Transfer*, vol. 203, pp. 3–69, 2017, doi: 10.1016/j.jqsrt.2017.06.038.

Résumé

Le marché des capteurs de gaz est en constante croissance. Cette croissance est dominée par un large éventail d'applications et des contraintes législatives croissantes sur la surveillance de l'air. Malgré la grande variété des capteurs de gaz, il est difficile de trouver celui qui offre un bon équilibre entre sensibilité, sélectivité, stabilité, compacité et coût. De plus, un marché en expansion continue exige le développement de nouvelles solutions qui se traduiront par davantage d'innovations technologiques.

Cette thèse fait partie d'un projet de recherche qui vise à développer un capteur de gaz compact, intégré et portable avec une excellente sélectivité, une haute sensibilité (ppb) et un temps de réponse rapide. Il se concentre principalement sur le développement d'un composant permettant la réalisation de capteurs compacts et sensibles.

Le capteur proposé dans cette thèse est basé sur la détection photoacoustique. Nous avons étudié et réalisé un micro-résonateur mécanique en silicium (MEMS) caractérisé par un facteur de qualité élevé comparé aux microphones commerciaux. L'emploi de silicium et la transduction capacitive rend le capteur compatible avec la technologie CMOS.

Le résonateur développé nous a permis d'atteindre un NNEA de $5.5{\cdot}10^{-7}$ $\mathrm{W{\cdot}cm^{-1}Hz^{-1/2}}$ en détection capacitive. Nous avons confronté ces résultats à un diapason en quartz en configuration "on-beam" pour lequel nous avons obtenu un NNEA de $1.3{\cdot}10^{-7}$ $\mathrm{W{\cdot}cm^{-1}Hz^{-1/2}}$montrant que le résonateur fabriqué atteint l'état de l'art.

Dans cette thèse, nous avons proposé une approche innovante basée sur un micro-résonateur mécanique qui permet d'intégrer et de miniaturiser les capteurs de gaz faisant progresser la recherche et le marché du capteur.

Abstract

The gas sensors market is constantly growing. This growth is driven by a wide range of applications and increasing legislative constraints on air monitoring. Moreover, gases play a vital role in many aspects of the people's life. Despite the wide variety of gas sensors, it is challenging to find the one that provides a good balance between sensitivity, selectivity, stability, compactness and cost. Furthermore, a continuously expanding market demands the development of new solutions that will result in more technological innovations.

This thesis is a part of a research project which aims developing a compact, integrated and portable gas sensor with excellent selectivity, high sensitivity (ppb) in fast and continuous response. It primarily focuses on the development of an active sensor component that is responsible for compactness and high sensitivity measurement.

The sensor proposed in this thesis is based on photoacoustic gas detection. We studied and realized a silicon microelectromechanical (MEMS) resonator characterized by a well-defined resonance with high quality factor, compared to the standard microphone. Subsequently, to detect the photoacoustic wave, we used silicon with a capacitive readout mechanism, which allows avoiding any material deposition and CMOS compatibility.

With fabricated resonator we reach a NNEA of $5.5{\cdot}10^{-7}$ $\mathrm{W{\cdot}cm^{-1}Hz^{-1/2}}$ under capacitive detection. Subsequently, we compared the results to bare quartz tuning fork in on-beam configuration for which we got a NNEA of $1.3{\cdot}10^{-7}$ $\mathrm{W{\cdot}cm^{-1}Hz^{-1/2}}$. Thus we can claim that the fabricated resonator presents the state-of-the-art performance.

In this thesis we proposed an innovative approach based on microelectromechanical resonator which, we believe, will allow to integrate and miniaturize gas sensors while advancing the sensor's research and market.